Calibration of the MEGA Prototype

Hardware and Performance of a Combined Tracking Compton and Low-Energy Pair Creation Telescope

Robert Andritschke

Technische Universität München

Max-Planck-Institut für extraterrestrische Physik
Garching bei München

Calibration of the MEGA Prototype

Hardware and Performance of a Combined Tracking Compton and Low-Energy Pair Creation Telescope

Robert Manfred Andritschke

Vollständiger Abdruck der von der Fakultät für Physik der Technischen Universität München zur Erlangung des akademischen Grades eines

Doktors der Naturwissenschaften

genehmigten Dissertation.

Die Dissertation wurde am 20.11.2006 bei der Technischen Universität München eingereicht und durch die Fakultät für Physik am 05.12.2006 angenommen.

Vorsitzender:		Univ.-Prof. Dr. Andrzej Jerzy Buras
Prüfer der Dissertation:	1.	apl. Prof. Dr. Volker Schönfelder
	2.	Univ.-Prof. Dr. Franz von Feilitzsch

Zusammenfassung

In den vergangenen Jahrzehnten entwickelte sich die γ-Astronomie zu einem wichtigen Zweig der Astrophysik. Insbesondere im Energiebereich von wenigen 100 keV bis zu einigen 10 MeV läßt sich eine große Vielzahl physikalischer Prozesse beobachten — zum Beispiel die Nukleosynthese, die Positronenannihilation, Synchrotronstrahlungs- und Bremsstrahlungsemissionen, der Pionenzerfall und die inverse Comptonstreuung. Eine erste Himmelsdurchmusterung wurde mit dem COMPTEL Teleskop auf dem Compton Gamma-Ray Observatory (1991-2000) durchgeführt. Tiefe Einblicke in eine Reihe von Objekten erhalten wir derzeit von INTEGRAL. Um die hochenergetischen Prozesse und die Zyklen, die Materie im Universum durchläuft, weiter zu verstehen, wird eine neue Satellitenmission benötigt.

Dieser Aufgabe wird ein Instrument namens MEGA (Medium Energy Gamma-ray Astronomy) gerecht. Sein Detektorkonzept vereint die Abbildungs- und Spektroskopieeigenschaften eines Compton- und Paarerzeugungsteleskops im Energiebereich von 0.4 bis 50 MeV. Am Max-Planck-Institut für extraterrestrische Physik wurde ein Prototyp von MEGA gebaut und seine Eigenschaften einerseits mit radioaktiven Laborquellen und andererseits anhand einer Beschleunigermessung bestimmt.

Das Instrument besteht aus einem Spurdetektor und einem Kalorimeter. Der Spurdetektor stellt den zentralen Teil des Detektors dar. Hier findet die primäre Wechselwirkung (Comptonstoß oder Paarerzeugung) statt. Er besteht aus elf Lagen doppelseitiger Siliziumstreifenzähler. In diesen Lagen können die Spuren geladener Teilchen aufgezeichnet werden, so wie es sowohl für einen spurverfolgenden Comptonstoßdetektor als auch ein Paarerzeugungsinstrument notwendig ist. Im Mittel beträgt die Energieauflösung des Spurdetektors 9.7 keV (1σ bei 122 keV und Raumtemperatur).

Der Spurdetektor ist an seinen Seiten und seinem Boden von 20 Kalorimeterblöcken umgeben. Das Kalorimeter absorbiert die sekundären Teilchen, die aus den Spurdetektor verlassen. Jeder Block umfaßt eine 10×12 Matrix aus CsI(Tl) Szintillatorkristallen, die an Silizium-PIN-Dioden gekoppelt sind. Die Blöcke am Boden erlauben eine dreidimensionale Auflösung der Wechselwirkungsposition, die durch zweiseitige Auslese der Kristalle erreicht wird. Ein neu entwickelter Algorithmus erlaubt eine Eichung der Energie und der Position von Wechselwirkungen in einzelnen Kristallen auch auf Basis von Kalibrationsdaten mit niedriger Statistik. Im Mittel ergibt sich eine Energieauflösung des Kalorimeters von 38 keV (1σ bei 662 keV) und eine Tiefenauflösung von unter 2 cm für Energiedeposits oberhalb von 3 MeV.

Die Detektoren werden von einem System ausgelesen, das eigenständig auf die $\approx 10\,000$ Detektorkanäle reagiert. Die Datenrate wird durch einen flexiblen Ereignisfilter begrenzt, der in der Ausleseelektronik implementiert ist.

Eichmessungen mit radioaktiven Laborquellen decken nur den niederenergetischen Teil des Energiespektrums ab. Deshalb wurde der Prototyp an der High Intensity Gamma-ray Source (HIGS) der Duke University (Durham, N.C., USA) mit monoenergetischer, vollständig polarisierter γ-Strahlung im Bereich von 0.7 bis 50 MeV bestrahlt.

Aus diesen Messungen wurden die Charakteristika des Prototypen, d.h. seine Eigenschaften als Compton- und Paarerzeugungsteleskop, ermittelt: Seine Energieauflösung beträgt 41 keV (1σ bei

0.7 MeV), das Gesichtsfeld ist größer als 160° und der Prototyp hat eine effektive Fläche von typisch $1 - 2$ cm^2.

Abschließend werden die mit dem Prototypen gesammelten Erfahrungen zusammen mit Verbesserungsvorschlägen diskutiert. So wurde die Elektronik als schwächstes Glied des Gesamtsystems identifiziert, aber auch Änderungen an den Detektoren (z.B. Siliziumdriftdetektoren zur Auslese der Kalorimeterkristalle) versprechen eine Leistungssteigerung des Teleskops.

Dieser Prototyp hat eindeutig bewiesen, dass das neue Konzept eines kombinierten Comptonstoß- und Paarerzeugungsteleskops realisierbar ist. Detaillierte Simulationen stimmen gut mit den Messungen überein. Der instrumentelle Hintergrund ist noch experimentell zu überprüfen, z.B. durch einen Stratosphärenballonflug mit dem Prototypen. Danach wären die Eigenschaften eines größeren Instruments mit hoher Genauigkeit vorhersagbar und die Konfiguration des Instruments für eine Satellitenmission könnte auf ihre Sensitivität hin optimiert werden.

Abstract

In the last decades γ-ray astronomy has evolved into an important branch of astrophysics. Especially in the energy range between a few 100 keV and several 10 MeV a large variety of physical processes in cosmic sources can be observed — such as nucleosynthesis, positron annihilation, synchrotron emission, Bremsstrahlung, pion decay, and inverse-Compton scattering. A first all-sky survey was performed by the COMPTEL telescope aboard the Compton Gamma-Ray Observatory (1991-2000). Detailed insights to selected objects are currently given by INTEGRAL. For a deeper understanding of the energetic processes and the life cycle of matter in our Universe a new mission is desirable.

This could be fulfilled by an instrument called MEGA (Medium Energy Gamma-ray Astronomy). The detector concept combines the imaging and spectroscopic capabilities of a Compton and a pair creation telescope for the energy range of 0.4 – 50 MeV. At the Max-Planck-Institut für extraterrestrische Physik the MEGA prototype has been built, its properties have been determined through measurements of radioactive laboratory sources and in an accelerator measurement.

The instrument makes use of an electron-tracking device ("tracker") and a calorimeter. The tracker is the central part of the detector. Here the primary interaction (Compton scatter or pair creation) takes place. It consists of eleven layers of double-sided silicon strip detectors. This setup allows to track charged particles as required for a tracking Compton instrument as well as for a pair creation detector. The average energy resolution of the tracker is 9.7 keV (1σ at 122 keV and room temperature).

The tracker is surrounded on the sides and at the bottom by 20 calorimeter blocks. The calorimeter absorbs secondary particles leaving the tracker. Each block houses a 10 by 12 array of CsI(Tl) scintillator crystals coupled to silicon PIN photodiodes. The bottom blocks feature a three dimensional resolution of the position of interaction by means of a two-sided readout. A new algorithm for calibrating the energy and position for individual crystals based on low-statistics data has been developed. The average energy resolution of the calorimeter is 38 keV (1σ at 662 keV), the average depth resolution is better than 2 cm for energies above 3 MeV.

The detectors are read out by a self-triggering system in response to $\sim 10\,000$ detector channels. In order to limit the data rate a flexible event selection hardware has been implemented.

Calibration measurements with radioactive laboratory sources cover only the lower part of the prototype's energy range. At the High Intensity Gamma-ray Source (HIGS) at Duke University (Durham, N.C., USA) the prototype was exposed to mono-energetic, fully polarized radiation in the range of 0.7 to 50 MeV.

From these measurements the characteristic parameters of the prototype, i.e. its Compton and pair creation telescope properties, are derived: an energy resolution of 41 keV (1σ at 0.7 MeV), a field-of-view larger than 160°, and an effective area of typically $1 - 2\,\mathrm{cm}^2$.

Finally, lessons learned from the prototype and possible improvements are discussed. The electronics subsystem has been identified as the weakest point of the system but also modifications of

the detectors (e.g. silicon drift diodes for the calorimeter readout) promise improved performance of the telescope.

This prototype clearly demonstrated that the new concept of a combined Compton and pair creation instrument is feasible. Detailed simulations are in good agreement with the measurements. After experimental validation of the instrumental background e.g. in a stratospheric balloon flight of the prototype, the performance of a full scale space telescope could be predicted with good accuracy and the instrument configuration could be optimized in terms of its sensitivity to astronomical sources.

Contents

Part I

Introduction and Overview

Chapter 1

From a Darkened Photographic Plate to an Imaging γ-Ray Detector

The history of γ-ray measurements started 1896, when an experiment of Henry Becquerel resulted in a mysteriously darkened photographic plate. After thorough cross-checks he deduced that the illumination of the photographic plate was caused by an unknown radiation, later called radioactivity. Two years later two components of this radiation, α and β rays, were isolated. Another two years passed by until the γ rays were discovered as a third, very penetrating component of radioactivity. They were later identified as high-energy electromagnetic radiation and "γ ray" got the collective term for radiation with higher energies than X rays without respect to the origin (radioactive decay, annihilation radiation, bremsstrahlung, etc.).

In the 1940s first γ-ray imaging detectors were built for diagnostic purposes in medicine. Roughly at the same time γ rays were identified as a component of cosmic rays. The following decades were full of discoveries resulting in the rich variety of celestial γ-ray sources known today. Highly relativistic electrons can be observed by their synchrotron radiation, inverse Compton effect, or bremsstrahlung; π^0-decays occur in regions where high-energy hadrons interact with matter; and de-exciting nuclei and decaying isotopes mark the sites of nucleosynthesis. For this upper end of the electromagnetic spectrum a series of different imaging telescopes has been built and new telescopes are on the way. A candidate for such a new instrument for the energy range of 0.4 – 50 MeV is the Medium Energy Gamma-ray Astronomy telescope MEGA. At these energies the dominating photon interaction changes from Compton scattering to pair creation with the transition taking place at several MeV, depending on the scattering material. Thus it seems ideal to design an instrument which is able to measure both types of interaction. A prototype realizing such a concept of a combined tracking Compton and pair creation telescope has been developed, built and calibrated, and is described in this thesis.

1.1 Properties of γ Rays

1.1.1 The Discovery of γ Rays*

Henry Becquerel wanted to investigate if the previously found X rays by Konrad Wilhelm Röntgen in November 1895 could be generated by phosphorescence. He set up an apparatus consisting of a phosphorescent substance (an uranium salt), a small cross of thin copper and a photographic plate wrapped in a light-tight envelope. A darkening with a cross shadow should indicate phosphorescent radiation *after* exposure to sun light. However due to cloudy weather in Paris on February 26 and 27, Becquerel left his setup in a dark cupboard. In spite of the setup not being exposed to sun light he developed the photographic plate and was surprised that it was darkened. Obviously the radiation had nothing to do with phosphorescence. It was originally called "uranic rays" or "Becquerel rays". The term "radioactivity" was introduced by Marie and Pierre Curie, who isolated other radiating materials such as Thorium†, Radium, or Polonium. Two components of radioactivity (α and β rays) were separated by Ernest Rutherford in 1898 in an experiment using magnetic fields to deflect the charged particles. In 1900 Paul Villard reported the third, most penetrating component, called γ rays.

The identification of the nature of the X and γ rays took several years. The final proof that X rays are "ultra-ultra-violet" light was delivered by Max von Laue in 1912 when he discovered refraction patterns using crystals as grids. In 1913 Rutherford and E. N. da C. Andrade observed reflections of γ rays from crystal surfaces showing that γ rays are light with even shorter wavelengths than X rays.

1.1.2 Waves or Particles?

Since interference and diffraction were observed, it was commonly accepted that light is an electromagnetic wave. Physicists were puzzled by the properties of black-body radiation, as the experimentally derived spectra could not be explained by classical thermodynamics. Max Planck succeeded in finding a well-fitting description by postulating a quantization of energy (1900). Albert Einstein followed upon this idea and introduced the photon concept in 1905 to explain the photoelectric effect, a discovery by Heinrich Hertz in 1887. In 1923 Arthur Holly Compton observed that the conservation laws for the scattering of two particles are also valid when a photon scatters off an electron — the Compton effect proving the particle nature of light [Compton, 1923, Compton and Simon, 1925].

Accepting and interpreting the wave-particle duality was an important step in quantum mechanics. At high energies the particle character of light dominates — photons interact with matter via photoelectric absorption, Compton effect, or pair creation. The latter process is closely connected to the discovery of the positron. Here the experimental evidence was provided after the theorists postulated the existence of the positron. The processes $e^+ + e^- \leftrightarrow \gamma + \gamma$ (annihilation and $\gamma - \gamma$ collisions) and $\gamma + N \rightarrow e^+ + e^- + N'$ (pair creation, N is a nucleus) were discussed in the years 1930 - 1935. The conservation laws again have to be fulfilled, with each photon having the energy and the momentum of a particle, so that the pair creation process needs a nucleus‡ N to transfer

*Pais [1986] illustrates in great detail the developments in physics in a historical context beginning 1895 with the discovery of X-rays.

†Schmidt [1898] found Thorium being radioactive independently from the Curies and published it half a month earlier.

‡The conservation laws can also be fulfilled with other scatter partners. Also electrons or other photons can be the scatter partner.

momentum onto. Charged particles can be visualized in a cloud chamber where condensing clouds are formed around their ionization path. In order to identify the type of particle a magnetic field is applied bending their tracks. Early photographs are published in Blackett and Occhialini [1933].

Generally speaking, the particle nature of light dominates if the wave length is smaller than the typical distances of the atoms in media which is clearly the case for photon energies above 1 MeV, i.e. wave lengths < 0.01 nm. Nevertheless the wave character is not completely hidden, γ rays can be Bragg and Laue diffracted.

1.1.3 Sources of γ Rays

The sources of γ rays can be divided into two main groups. On the one hand there are processes with discrete energies, i.e. transitions between energetically discrete nuclear states or annihilation lines. On the other hand continuum energy portions are released as photons when high-energy charged particles convert parts of their kinetic energy into electromagnetic radiation.

1.1.3.1 Radioactive Isotopes

The discovery of the radioactivity of Uranium by Becquerel and finding even stronger radiating substances such as Thorium, Polonium or Radium was the starting point of nuclear physics. With the identification of protons and neutrons as constituents of the nucleus, a schema of the different nuclei was established and called the table of isotopes[§]. The table is further populated by isotopes which were artificially generated in collisions of protons, neutrons, α- or even more massive particles with target nuclei. Also the list of reactions emitting radioactive rays got longer: Besides α, β^- and γ decay also the β^+ decay, electron capture (EC), fission, and far from the valley of stable isotopes[¶] emission of neutrons or protons was found.

A selection of radioactive isotopes, which have astrophysical significance or which are commonly used as calibration sources, is listed in appendix A together with decay mode, half-lifes, and prominent γ lines. As one example ^{40}K is naturally occurring on Earth being the most prominent contributor to the non-anthropogenic environmental radioactivity. Due to its long lifetime it is still present from a former supernova.

1.1.3.2 Nuclear Reactions

Discrete transitions between nuclear states occur in collisions of energetic particles with nuclei. Excited nuclei relax by emitting characteristic γ rays. For example

$$\alpha + {}^{9}_{4}\mathrm{Be} \rightarrow {}^{12}_{6}\mathrm{C}^{*} + \mathrm{n}$$

generates an excited Carbon nucleus which emits a 4.44 MeV photon in order to relax into its ground state. For laboratory use there are sources which contain a mixture of $^{9}_{4}$Be and the α-emitter ^{241}Am and serve as neutron and high-energy γ ray sources.

[§]Isotopes are nuclei having the same number of protons, i.e. they have the same atomic number and have identical chemical properties, i.e. they belong to the same element. The difference is the neutron number resulting in different atomic masses and different nuclear properties such as excitation levels and life times (respectively stability).

[¶]Isotopes having too many or too few neutrons are not stable. The stable ones form a continuous line in the table of isotopes called the valley of stable isotopes.

Neutron capture processes such as

$$\mathrm{n} + {}^1\mathrm{H} \rightarrow \gamma + {}^2\mathrm{H}$$

generate γ-ray lines (here 2.22 MeV). Moreover the reaction given as example is used to find hydrogen (and thereby water) on planets [Boynton et al., 2002].

1.1.3.3 Meson Decay

High-energy nucleons colliding with ambient matter produce π-mesons or even K-mesons, which decay into πs [Stecker, 1971]. The charged $\pi^{\pm}$ decay into leptons contributing to the γ-ray spectrum by annihilation, bremsstrahlung and other effects (see below). The neutral π^0 has a very short decay time (8.4×10^{-17} s) and ends up in two γ rays. The kinetic energy of the π^0s is transferred to the two created γs — they are highly-energetic and beamed in the moving direction of the original π^0, forming a continuum spectrum with an maximum at half the π^0 rest mass ($\sim 68\,\mathrm{MeV}$), the "pion bump" [Schönfelder, 2001, Fichtel and Trombka, 1997].

1.1.3.4 Annihilation

The electron-positron pair annihilation is the most prominent example of particle–antiparticle annihilation. When an electron and a positron attract each other and finally collide, they annihilate into photons. This could happen directly, resulting in two (antiparallel) photons of 511 keV, or indirectly via a bound state, the positronium. The spins of the electron and positron can be arranged either in a singulet configuration leading to two annihilation photons of 511 keV each, or a triplet configuration, leading to three annihilation photons with a continuum energy distribution below 511 keV.

Most positrons annihilate after thermalization with the ambient matter. In the interstellar medium annihilation "in-flight" is a significant effect (see Guessoum et al. [2005] for a detailed treatment), where positronium is formed by charge exchange with (atomic or molecular) hydrogen, helium, or other atoms and molecules after losing most of the energy by Coulomb collisions down to $\sim$ 10–100 eV.

1.1.3.5 Inverse Compton effect

The inverse Compton effect is principally the Compton effect, where a photon transfers parts of its energy to an electron as described in chapter 1.1.4.3. The only difference is the frame of reference; while in the Compton effect the electron is at rest before the scatter and gains energy, the inverse effect has a high-energy electron losing energy to a photon. The inverse Compton scattered photon has a maximum energy (head-on collision) of approximately $E_\gamma \approx 4\gamma^2 E_i$, with γ the Lorentz factor of the electron and E_i the energy of the original photon [Litvinenko and Madey, 1995].

This effect is used for example in the High Intensity Gamma-ray Source (HIGS) as described in chapter 7.2.1 to produce mono-energetic γ rays. In astrophysical environments the inverse Compton effect plays a dominant role where a stream of high energy particles (e.g. in jets from pulsars, active galactic nuclei, gamma-ray bursts, etc.) exists. Low-energy photons from star light, synchrotron light, light of a nebula or cloud, or the cosmic microwave background are boosted up to X- and γ-ray energies by scatters with high-energy electrons.

1.1.3.6 Synchrotron radiation

Synchrotron radiation is emitted by relativistic charged particles (mostly electrons and positrons) spiraling around magnetic field lines. γ rays can be produced if these fields are sufficiently strong.

The maximum emission occurs at energies of $E_{\gamma,\max} = 5 \cdot 10^{-13}\frac{\text{eV}}{\text{T}} \cdot B_\perp \left(\frac{E_e}{m_e c^2}\right)^2$, with $B_\perp$ the magnetic field strength perpendicular to the electron's path, E_e and $m_e c^2$ the electron's energy and rest mass [Murthy and Wolfendale, 1993]. Radiation of up to 1 MeV is produced in synchrotron facilities, even more energetic photons can be produced by highly relativistic electrons in the strong magnetic fields of neutron stars (especially magnetars) or in jets.

1.1.3.7 Curvature radiation

Curvature radiation adds to synchrotron radiation if the electrons are bound to a strong magnetic field. Then the electrons are additionally accelerated when they follow bent magnetic field lines.

1.1.3.8 Bremsstrahlung

Bremsstrahlung occurs while electrons traversing matter are decelerated in the electric field of nuclei. A commonly used application is the X-ray tube where electrons are accelerated onto a metal anode releasing their kinetic energy as bremsstrahlung (besides characteristic X-ray lines).

The maximum energy of a bremsstrahlung photon is the energy of the radiating electron so that at accelerator facilities such as HIGS (High Intensity Gamma-ray Source, chapter 7.2.1) bremsstrahlung up to few hundreds of MeV can be observed as result of collisions of the storage ring electrons with the rest gas.

1.1.4 Interaction of γ-Radiation with Matter

In order to detect γ rays, they have to interact with detector materials. The dominant interaction process changes twice in the keV to GeV range — from photoelectric to Compton effect and then to pair creation. Figure 1.1 shows the cross sections for the materials of interest in this work. Elastic scattering seems to play a minor role since its cross section contributes less than 10% to the total one. This is true for detectors, but focusing optics (chapter 1.2.7) rely on this interaction.

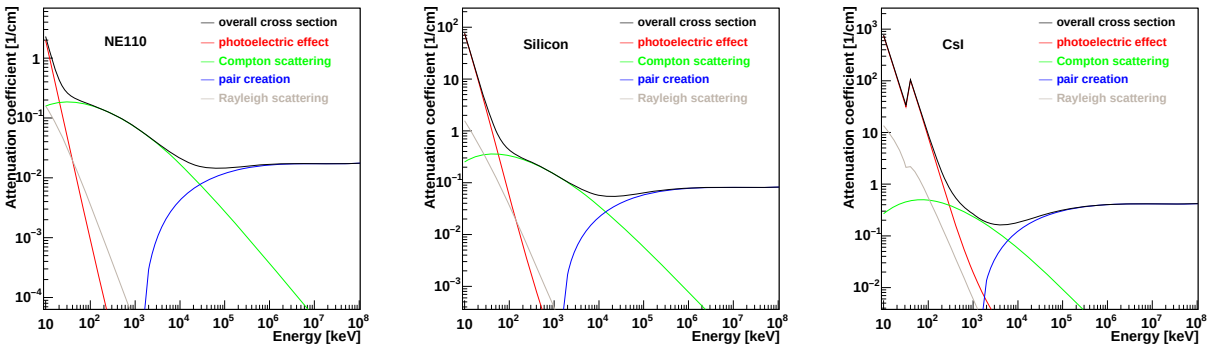

Figure 1.1: Attenuation coefficients (cross sections) for interactions of photons in plastic scintillator (NE110, left), Silicon (middle) and CsI (right). The numbers are taken from the simulation tool GEANT3 [GEANT3].

1.1.4.1 Elastic Scattering

Elastic scattering is dominated by Rayleigh scattering for X- and low-energy γ-ray energies. The cross section drops similarly to the photoelectric effect, but is roughly one order of magnitude

smaller. If the scattering occurs in a crystal lattice, constructive and destructive interference lead to Bragg reflections and Laue diffraction patterns [Friedrich, Knipping, and von Laue, 1912].

1.1.4.2 Photoelectric Effect

Photons can be absorbed completely while transferring their energy to a bound electron which is knocked off the atom*. The kinetic energy of the electron is the photon's energy reduced by the electron's binding energy† E_b. The remaining free state recombines and characteristic X rays or Auger electrons with a total energy of E_b are generated.

The probability of absorption via the photoelectric effect drops by orders of magnitude from X rays to MeV γ rays. A crude approximation for the cross section is given in Evans [1955]:

$$\sigma_p \simeq \text{const} \frac{Z^4}{E_i^3} \tag{1.1}$$

with Z the atomic number and E_i the energy of the incoming photon. Due to the complex structure of atomic shells there exists no analytical description of the cross section. For example, it is difficult to model the most obvious feature in the cross section, the K-edges. Instead, experimental values are tabulated.

The photoelectric effect can also occur in a nucleus. This nuclear photoelectric effect results in a photodissociation of a nucleus where a neutron or a proton is released. In heavy nuclei the absorption of a γ photon can destabilize the nucleus so that it breaks into pieces (photofission).

1.1.4.3 Compton Effect

At MeV energies the dominant interaction is the Compton effect. The incoming photon with energy E_i is scattered by an angle φ while transferring a portion of its energy E_e to an electron in the material. The scattered photon keeps the energy $E_g = E_i - E_e$ and emerges with its direction changed by the scattering angle φ, while the recoil electron's path has an angle ε to the direction of the incoming photon:

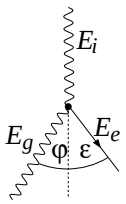

Figure 1.2: Compton effect

$$\cos\varphi = 1 + m_e c^2 \left(\frac{1}{E_i} - \frac{1}{E_g} \right) \tag{1.2}$$

$$\cos\varepsilon = \frac{E_e(E_i + m_e c^2)}{E_i \sqrt{E_e^2 + 2E_e m_e c^2}} \tag{1.3}$$

The angular distribution of scattered γ rays has been calculated by O. Klein and Y. Nishina [1929]. It depends on the polarization of the incoming photon. The differential cross section $d\sigma_c/d\Omega$ per electron could be described as (details can be found in Davisson and Evans [1952], Evans [1955])

$$\frac{d\sigma_c}{d\Omega} = \frac{r_e^2}{2} \left(\frac{E_g}{E_i} \right)^2 \left(\frac{E_i}{E_g} + \frac{E_g}{E_i} - 2\sin^2\varphi \cos^2\chi \right) \tag{1.4}$$

with χ the angle between the plane of polarization of the incoming photon and the scatter plane, and $r_e = 2.818 \cdot 10^{-15}$m the classical electron radius. The expression for unpolarized radiation follows by integrating over all polarization angles as

$$\frac{d\sigma_c}{d\Omega} = \frac{r_e^2}{2} \left(\frac{E_g}{E_i} \right)^2 \left(\frac{E_i}{E_g} + \frac{E_g}{E_i} - \sin^2\varphi \right) \tag{1.5}$$

*In order to fulfill the energy and momentum conservation laws momentum needs to be transferred to a third particle, here the atom. Again the particle character of light is obvious.

†The energy transfer associated with the momentum transfer to the atom is negligible.

Equations 1.2 and 1.5 can be reformulated to describe the Compton cross section differential in the electron's energy:

$$\frac{\mathrm{d}\sigma_c}{\mathrm{d}\underline{E}_e} = \begin{cases} r_e^2\pi\frac{1}{\underline{E}_i^2}\left[\frac{1}{1-\frac{\underline{E}_e}{\underline{E}_i}}\left(1-\frac{2}{\underline{E}_i}-\frac{2}{\underline{E}_i^2}+\frac{1}{\underline{E}_i^2\left(1-\frac{\underline{E}_e}{\underline{E}_i}\right)}\right)\right. & \text{for } 0 \le \underline{E}_e \le \frac{2\underline{E}_i^2}{1+2\underline{E}_i} \\ \left. +1-\frac{\underline{E}_e}{\underline{E}_i}+\frac{2}{\underline{E}_i}+\frac{1}{\underline{E}_i^2}\right] & \\ 0 & \text{else} \end{cases} \tag{1.6}$$

with $\underline{E}_x$ the energies in units of electron masses $m_e c^2$. The distribution of scattered photon energies is

$$\frac{\mathrm{d}\sigma_c}{\mathrm{d}\underline{E}_g} = \begin{cases} r_e^2\pi\frac{1}{\underline{E}_i^2}\left[\frac{\underline{E}_i-2}{\underline{E}_g}+\frac{\underline{E}_g+2}{\underline{E}_i}+\left(\frac{1}{\underline{E}_i}-\frac{1}{\underline{E}_g}\right)^2\right] & \text{for } \frac{\underline{E}_i}{1+2\underline{E}_i} \le \underline{E}_g \le \underline{E}_i \\ 0 & \text{else.} \end{cases} \tag{1.7}$$

Since the (differential) cross section is defined as the number of scattered particles with energy E_x per second and per incident particle flux, the spectral component looks like

$$\frac{\mathrm{d}N}{\mathrm{d}E_x} = n \cdot \frac{\mathrm{d}\sigma}{\mathrm{d}E_x} \cdot \frac{\rho}{m_{atom}}$$

with n the number of incident particles during the measurement time per unit area, ρ the material's density and m_{atom} the mass of one atom.

All formulae given for a Compton interaction are derived under the assumption that the electrons are free. In the realistic case of bound electrons small deviations occur. Since a bound electron has no fixed momentum, the momenta in the Compton scatter process — and hence the distribution of the incoming energy onto the electron and scattered photon — are not sharply defined any more. This effect is called Doppler-broadening and is discussed in great detail in Zoglauer [2005]. The introduced error in the case of Silicon as scatter material is equivalent to up to a few keV uncertainty in the energy measurement.

1.1.4.4 Pair Creation

If the photon's energy exceeds twice the rest mass of an electron, pair creation processes can occur on target nuclei and electrons. The scatter partner is needed to fulfill the conservation laws. The energy of the incoming photon is divided into the rest mass of the electron and positron ($m_e c^2$ each), the kinetic energy of both particles E_e, E_p and a small energy E_n, which is transferred to the scatter partner: $E_i = 2\,m_e c^2 + E_e + E_p + E_n$. The cross section is zero for energies below $2\,m_e c^2$ (for nuclei as scatter partner, $4\,m_e c^2$ for electrons) and reaches significant values above ~ 10 MeV where it also becomes the dominant interaction. For high energies it is nearly constant. The Z-dependence of the cross section can be approximated by [Evans, 1955]:

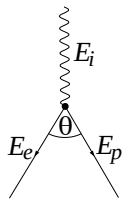

Figure 1.3: Pair creation

$$\kappa = \kappa_{Pb}\frac{\rho}{11.35}\frac{207.2}{A}\left(\frac{Z}{82}\right)^2$$

with κ the attenuation coefficient of an element with density ρ and atomic number Z, κ_{Pb} is the (tabulated) attenuation coefficient of lead. This approximation does not take into account the effect that outer electron shells are partially shielded from the field of the core by inner electrons. For that reason extrapolating from lower-Z materials will deliver slightly too large values.

1.1.4.5 Quantized Absorption

γ-radiation can not only be absorbed by an atom but also by a nuclus or even a nucleon. If the γ-ray energy matches an allowed transition of two states, the absorption is resonant and the cross section for this interaction is increased. Resonance energies for different isotopes are at a few to several MeV (pygmy dipole resonance [Igashira et al., 1986]), at 10–30 MeV (giant dipole resonance [Berman and Fultz, 1975]) — both are collective effects between the nuclons. The Δ-resonance at 330–350 MeV is an internal excitation of a nuclon ([Ahrens et al., 1988]).

Another mechanism resulting in absorption lines at γ-ray energies occurs in the case of electrons captured in a strong magnetic field, which leads to discrete states of the bound electrons similar to atoms (Landau levels).

1.1.5 γ–γ Interactions

A further γ-ray loss mechanism is the inverse process of the (electron–positron) annihilation, also called "photon–photon pair creation". In this interaction two photons collide and generate preferably an electron–positron pair. Depending on the radiation fields which supplies the lower-energy scatter partner the thresholds for the second photon are quite high — $\sim 4 \cdot 10^{14}$ eV for the 2.7 K background radiation, $\sim 10^{11}$ eV for (visible) starlight, and $\sim 3 \cdot 10^{8}$ eV for 1 keV X rays [Murthy and Wolfendale, 1993].

A γ photon can also interact with a strong magnetic field (e.g. from magnetars) resulting in two photons [Weise, 2004].

1.1.6 Interaction of Secondary Particles with Matter

Many of the mentioned γ-ray interactions generate energetic charged particles, usually electrons. Measuring γ rays relies on understanding the energy deposits of these charged particles. Mostly the energy of the charged particles is transfered by interactions with the Coulomb field of the atoms in the detector material.

Collisional Ionization and Excitation is the dominant interaction of charged particles in matter at lower energies where no significant bremsstrahlung is generated. The energy deposit per unit length is described by the Bethe-Bloch relation for particles heavier than electrons (e.g. muons and protons) and by a modified relation for electrons and positrons[‡]. In figure 1.4 the differential energy loss due to collisions and excitations is plotted versus the electron's kinetic energy (see Evans [1955], Grupen [1993], Schopper [2002], Zoglauer [2005] for details). It has a minimum for kinetic energies E_{kin} around twice the rest mass m of the secondary particle ($E_{kin} \approx 2\,mc^2$). Above $E_{kin} \approx mc^2$ there is only a slight dependence on energy, which gives reason to call charged particles with a larger energy than their rest mass "Minimum Ionizing Particles" (MIPs). A crude estimate for the energy deposit of MIPs per unit length $\frac{dE}{dx}$ is given by [Grupen, 1993]

$$-\left.\frac{dE}{dx}\right|_{min} \approx 2\,\frac{\mathrm{MeV}}{\mathrm{g/cm^2}} \cdot \rho$$

[‡]The modifications to the Bethe-Bloch relation are necessary because the colliding particles have the same masses. Also, electron–electron scattering differs slightly from positron–electron scattering due to the indistinguishableness of the scatter partners.

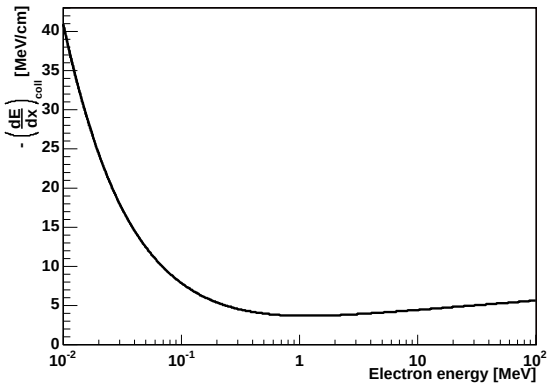

Figure 1.4: Collisional energy losses of electrons in silicon.

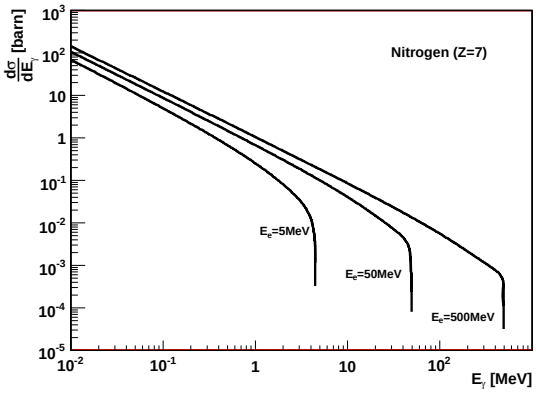

Figure 1.5: Bremsstrahlung cross section for one electron with energies $E_e = 5$, 50, 500 MeV interacting with one nitrogen atom according to equation 1.8.

δ rays are electrons which got enough energy transferred in a Coulomb collision that they also generate ions on their path through the medium.

Bremsstrahlung which is already mentioned in chapter 1.1.3.8 becomes important at higher energies.

The ratio of energy losses due to bremsstrahlung and (Coulomb) collisions is given approximately by [Knoll, 1988]

$$\frac{dE_{bremsstrahlung}/dx}{dE_{collisional}/dx} \cong \frac{E_e \cdot Z}{700 \text{ MeV}}$$

with E_e the electron's energy and Z the atomic number of the absorbing material. For MEGA's detector materials Silicon and CsI, both energy losses are equal at energies of 50 MeV and 13 MeV respectively.

Bremsstrahlung photons show a spectrum which is dominated by low-energy photons, the cross section $\frac{d\sigma_{brems}}{dE_\gamma}$ has coarsely a $1/E_\gamma$ behavior (E_γ the energy of the bremsstrahlung photon, figure 1.5). An approximation is [Koch and Motz, 1959][§]

$$\begin{aligned}\frac{d\sigma_{brems}}{dE_\gamma} &= \frac{Z^2 r_0^2}{137}\frac{\underline{p}'_e}{E_\gamma \underline{p}_e}\left\{\frac{4}{3} - 2\underline{E}_e\underline{E}'_e\left(\frac{\underline{p}'^{\,2}_e + \underline{p}^2_e}{\underline{p}'^{\,2}_e\,\underline{p}^2_e}\right) + \frac{\epsilon\underline{E}'_e}{\underline{p}^3_e} + \frac{\epsilon'\underline{E}_e}{\underline{p}'^{\,3}_e}\right. \\ &\quad - \frac{\epsilon'\epsilon}{\underline{p}_e\underline{p}'_e} + L\left[\frac{8\underline{E}_e\underline{E}'_e}{3\underline{p}_e\underline{p}'_e} + \frac{\underline{E}^2_\gamma(\underline{E}^2_e\,\underline{E}'^{\,2}_e + \underline{p}^2_e\,\underline{p}'^{\,2}_e)}{\underline{p}^3_e\,\underline{p}'^{\,3}_e}\right. \\ &\quad \left.\left. + \frac{\underline{E}_\gamma}{2\underline{p}_e\underline{p}'_e}\left(\frac{\underline{E}_e\underline{E}'_e + \underline{p}^2_e}{\underline{p}^3_e}\epsilon - \frac{\underline{E}_e\underline{E}'_e + \underline{p}'^{\,2}_e}{\underline{p}'^{\,3}_e}\epsilon' + \frac{2\underline{E}_\gamma\underline{E}_e\underline{E}'_e}{\underline{p}^2_e\,\underline{p}'^{\,2}_e}\right)\right]\right\} \qquad (1.8)\end{aligned}$$

$$\text{with } L = 2\ln\frac{\underline{E}_e\underline{E}'_e + \underline{p}_e\underline{p}'_e - 1}{\underline{E}_\gamma};\ \epsilon = \ln\frac{\underline{E}_e + \underline{p}_e}{\underline{E}_e - \underline{p}_e};\ \epsilon' = \ln\frac{\underline{E}'_e + \underline{p}'_e}{\underline{E}'_e - \underline{p}'_e}.$$

Here $\underline{E}_e$ and $\underline{p}_e$ is the energy and momentum of the electron before, $\underline{E}'_e$, $\underline{p}'_e$ after the emission of a bremsstrahlung photon of energy $\underline{E}_\gamma$, where all energies are given in units of electron masses $m_e c^2$ and all momenta in units of $m_e c$; Z is the atomic number of the traversed material.

[§]In Koch and Motz [1959] a collection of different approximations is given. The formula given here has the number "3BN"; it uses Born–approximation and neglects screening effects of the electric field of the atom core by the electrons.

Molière-scattering theory describes the change in direction of charged particles passing through matter [Bethe, 1953]. Multiple small-angle scatterings on the Coulomb potentials of nuclei and electrons make the path of the passing particle chaotic. The distribution of scatter angles widens with decreasing energy and can be approximated for small scatter angles by a Gaussian. Its width projected on the scatter plane is [Group, 2004]:

$$\delta_{0,proj} \approx \frac{13.6\ \text{MeV}}{\beta cp}\sqrt{\frac{x}{X_0}}\left(1 + 0.038 \ln \frac{x}{X_0}\right) \tag{1.9}$$

with $\beta cp = \frac{E_e^2 + 2E_e m_e c^2}{E_e + m_e c^2}$ the electron's velocity times its momentum, $X_0 \approx \frac{716.4 \cdot A}{Z(Z+1)\ln(287 \cdot Z^{-1/2})}\ [\frac{\text{g}}{\text{cm}^2}]$ ($X_0(\text{Si}) = 21.82\ \text{g/cm}^2$) the radiation length, and x the traversed thickness of the scatter material. For example, 1 MeV electrons traversing 0.5 mm (0.3 mm) silicon have a scatter angle distribution width of $\delta_{0,proj} = 34°$ (11°).

Annihilation of positrons produces (mostly) two 511 keV photons (compare chapter 1.1.3.4). This happens after a positron has lost nearly all of its kinetic energy through the above mentioned effects, especially through Coulomb collisions.

Showers of particles occur when the impinging photon exceeds several GeV. In that case there is enough energy to generate several electron–positron pairs or even heavier particle – anti-particle pairs such as pions in a cascade of reactions.

Čerenkov Radiation appears, if the charged particle is faster than the speed of light in the medium. The Čerenkov light is beamed in the moving direction of the particle (opening angle $\Theta_C = \arccos(c/nv)$ with c the speed of light in vacuum, n the refractive index, and v the speed of the particle). Since these photons are only generated above a threshold velocity $v_{thr} = \frac{c}{n}$ and since the particle is rapidly slowed down in the medium, the light pulse is short.

1.2 Imaging γ Rays

Imaging of γ rays was pioneered in nuclear medicine. There patients incorporate tracer molecules labeled with short-lived radioactive isotopes (e.g. ^{99m}Tc, ^{131}I) which accumulate selectively in specific tissues such as the thyroid gland or cancer. In the 1940's and 1950's spatial information about the distribution of tracers was gained by positioning a single detector at various locations by hand or later by a scanner[Sorenson and Phelps, 1987]. In 1953 Hal O. Anger introduced a lead pinhole to image the source distribution on a film. Later he replaced the film by a solid NaI crystal coupled to a photomultiplier array [Anger, 1958], the Anger camera (appendix. B.1). This camera principle is widely used in many variations and different contexts (a few will be mentioned below).

The pinhole camera is a simple and direct imaging method but requires long exposure times. More sophisticated methods are in use today in different fields such as nuclear medicine, radioactive waste imaging, and high-energy astrophysics. In the following the focus lies on the astrophysical applications; examples for nuclear medicine and other fields are given in appendix B.

Each energy range from hard X rays to the very hard γ rays has its peculiarities due to the changing dominant interaction process (from photoelectric absorption over Compton effect to pair creation, figure 1.1):

1.2.1 Collimators and Modulators

For photon energies up to several hundreds of keV the photoelectric effect dominates (at least in high-Z materials). Focusing systems built on current satellites (Wolter telescopes) work up to $\sim$ 10 keV, ongoing developments in X-ray mirror optics aim at an upper limit of $\sim$ 80–100 keV (for lenses see chapter 1.2.7). The remaining spectral band dominated by the photoelectric effect is the domain of collimators and modulators.

Collimators consist of a high-Z (mostly lead) brick with an array of parallel holes that shield the detector from all radiation not co-axial to the collimating holes (ideally by the photoelectric effect).

This technique is a well established tool in astrophysics. OSSE (Oriented Scintillation-Spectrometer Experiment [Johnson et al., 1993]) aboard the Compton Gamma-Ray Observatory (CGRO) actually combines two variants. On the one hand a NaI crystal has a passive collimator made from tungsten on the front side. On the other hand an active shield consisting of NaI and CsI at the sides and the bottom respectively, defines the field of view ($3.8° \times 11.4°$ FWHM) and rejects background. There are four of these detector systems, each individually rotatable by 192° around the y-axis of the spacecraft. OSSE allowed quite quickly the determination of the regions of positron annihilation in our Galaxy [Kinzer et al., 2001].

A more recent collimating instrument operates as one of three instruments onboard the SUZAKU (ASTRO-EII) satellite [SUZAKU]. The hard X-ray detector (HXD) has an active BGO collimator and passive fine collimators which becomes transparent at around 100 keV (Field of view $34' \times 34'$below and $4.5° \times 4.5°$ above $\sim$ 100 keV). With two layers of sensors the HXD is sensitive in the $\sim$ 10–600 keV band. The lower part of the band is covered by silicon PIN diodes, the upper one by a phoswich arrangement of GSO and BGO scintillators read out by photomultipliers.

Collimators have a field of view which is also the resolution element. Observing larger fields requires reorientation of the instrument. This can be overcome with modulation techniques:

Temporal multiplexing modulates the source flux impinging on the instrument's detector in the time domain which does not need any spatial resolution. Scanning collimators are a simple example for this method. A more sophisticated representative is the Reuven Ramaty High-Energy Solar Spectroscopic Imager (RHESSI [Lin et al., 2002, Hurford et al., 2002]). Radiation from the sun has to pass two identical and parallel grids separated by 1.55 m before reaching the Ge-detector. While the spacecraft continuously rotates, the flux of a point source onto the detector is modulated by a characteristic frequency. RHESSI consists of nine of these grid–detector combinations, each having another grid pitch. The achieved field of view is 1.0°–7.5° and the angular resolution ranges from $2.26''$ to $183.2''$, both numbers depending on the grid geometry.

A variant of temporal multiplexing is the **occultation** method. Uncollimated detectors see step-like features in their count rates if a source crosses the Earth's (or Moon's) limb. This technique has for instance been applied to BATSE [Harmon et al., 2002] and RHESSI [Smith, 2004].

Spatial multiplexing modulates the source flux geometrically by a coded mask, i.e. a unique shadow for each source position is cast onto a (position sensitive) detector plane. Current instruments of this type are the spectrometer SPI (fully coded field-of-view 16°, angular resolution 2.5° FWHM [Vedrenne et al., 1999]), the imager IBIS (fully coded field-of-view 9°, angular resolution $12'$ [Ubertini et al., 1999]), and the X-ray monitor JEM-X (fully coded field-of-view 4.8°, angular resolution $3'$ [Lund et al., 1999]) aboard the INTEGRAL observatory and the BAT telescope [Barthelmy et al., 2005] aboard the SWIFT satellite. SPI has the highest spectral range (20 keV – 8 MeV), featuring a mask of 63 opaque hexagonal elements (Densimet¶, 60 mm flat-to-flat, 3 cm

¶Densimet is a tungsten alloy.

thick) and a detector plane of 19 hexagonal germanium detectors (56 mm flat-to-flat, ~ 69 mm long). The in-flight performance of the SPI instrument is investigated in Roques et al. [2003] (e.g. a FWHM energy resolution of 2.5 keV); a dedicated effort was invested in the high-energy range and for extended sources (on ground, by Wunderer [2002]).

1.2.2 Triangulation

For monitoring (single) bright sources which exceed the background and the celestial sources in the light of γ rays such as gamma-ray bursts or solar flares, triangulation techniques can be used. Sources showing temporal fluctuations in flux can be localized by triangulation of the arrival times at different satellites (e.g. the first gamma-ray bursts by the VELA satellites).

1.2.3 Oriented Detectors

Source positions can be calculated from the count rates of thin scintillator modules which have different orientations (the count rate is proportional to the projected area of the detector perpendicular to the source direction). BATSE (Burst And Transient Source Experiment, [Fishman et al., 1994b]) aboard CGRO and GBM (Glast Burst Monitor, [von Kienlin et al., 2004]) aboard GLAST is based on this technique.

1.2.4 Compton Scattering

In the energy range of ~ 100 keV to several MeV Compton scattering is the dominant photon interaction process (figure 1.1). If both the energy of the scattered photon and electron is measured along with the interaction positions, the incoming photon can be reconstructed as illustrated in figure 1.6. The scatter angle φ is calculated according to equation 1.2 from the energy of the scattered photon and the recoil electron. If the electron's path is not known (this is the case for many scatter detectors — such systems are sometimes called "classical Compton cameras"), the photon's origin can be restricted to an event circle. If the electron track is known ("tracking Compton cameras"), the origin can be further restricted to an arc. Event reconstruction methods including options if the measured information is incomplete, are described in great detail in Zoglauer [2005].

An early Compton telescope was placed in the OSO-1 satellite [Peterson and Howard, 1961], but it suffered severely from background [Peterson, 1965]. The Compton system proposed by Volker Schönfelder et al. [1973] features a time-of-flight (TOF) measurement for suppressing the background. The scatter detector and the absorber have a sufficient large distance ($\gtrsim 1$ m) to allow for resolving the travel time of the scattered photon between the two detectors. This system was flown several times in stratospheric balloon flights with continuously improved instrumentation. Finally the Compton Telescope COMPTEL was one of the four instruments aboard the Compton Gamma-Ray Observatory CGRO (launched in 1991, deorbited in 2000, figure 1.7, [Schönfelder et al., 1993, 2000b]). Its scatter detector consisted of seven liquid scintillator Anger cameras surrounded by a plastic anticoincidence shield. The calorimeter which should absorb the scattered photon was located 1.5 m below the scatter detector and had 14 NaI Anger cameras. The telescope operated in an energy range from 0.75 to 30 MeV (energy resolution 5% – 10% over the whole energy range, 8.8% FWHM at 1.27 MeV) and had a field-of-view of about 1 steradian (source location accuracy $\sim 1°$).

COMPTEL's scatter detector cannot resolve the electron track, so it belongs to the "classical" Compton telescopes. A representative of a tracking Compton telescope is MEGA. The prototype of this instrument is subject of this work.

1.2.5 Pair Creation

Photon interaction processes at energies above the Compton regime are dominated by pair creation until the Universe gets opaque due to γ–γ interactions (chapter 1.1.5). The incoming photon of a pair creation event can be coarsely reconstructed by the bisecting line between electron and positron track (figure 1.8). A more careful reconstruction takes into account an asymmetric distribution of the kinetic energy onto electron and positron and the measurement uncertainty from the unknown recoil on the scatter nucleus.

A simple form of a pair telescopes recognizes the particle cascade which is released by the electron and positron from the primary interaction if the total energy exceeds $\sim 100\,\mathrm{MeV}$. The cascade is mainly oriented in the flight direction of the incoming photon. A stack of particle detectors with suitable coincidence can detect these cascades. This was realized in the instruments Explorer 11 (1961) [Kraushaar et al., 1965] and OSO-3 (1968) [Kraushaar et al., 1972]. Explorer 11 detected high energy γ rays from space and from the Earth's atmosphere; OSO-3 measured emission above 100 MeV from the Milky Way. Both instruments had no imaging capabilities so that the position resolution was on the order of the field-of-view (1 sterad and 0.15 sterad, respectively).

The following pair creation telescopes were imaging systems containing spark chambers which track the path of the charged particles and have foils as conversion material. A first generation was represented by the satellites SAS-2 [Fichtel et al., 1975] and COS-B [Bignami et al., 1975], a second by EGRET (Energetic Gamma-Ray Experiment Telescope, figure 1.9, [Kanbach et al., 1988]). EGRET had a calorimeter below the spark chamber (the Total Absorption Spectrometer Crystal TASC made up from 435 kg NaI) which allowed to determine photon energies of up to several tens of GeV. Background was suppressed by a time-of-flight system and an anti-coincidence shield. Currently a new generation of imaging pair creation telescopes is awaiting launch, AGILE (Astro-rivelatore Gamma a Immagini LEggero) [Pittori, 2003] with its Gamma-Ray Imaging Detector GRID (energy range 30 MeV – 50 GeV) and GLAST (Gamma-ray Large Area Space Telescope) [Michelson, 1996] with the Large Area Telescope LAT (energy range $\sim$ 20 MeV – $>$ 100 GeV). Characteristic for this third generation is the tracking by several layers of silicon strip detectors instead of spark chambers. Both instruments are expected to enlarge the field-of-view by a factor of 4 – 6 and improve the angular resolution by approximately a factor of 2. Since AGILE is a small mission, its sensitivity will be a factor of 2 better than EGRET, whereas GLAST will outperform EGRET by a factor of a few tens.

The tracker of the MEGA instrument consists — similar to AGILE and GLAST — of silicon strip detectors, but has no conversion foils (they would spoil the tracking of the Compton electron). Its tracking capability enables MEGA to measure pairs in addition to Compton scatters so that it can be also seen as belonging to this third generation of pair creation telescopes.

1.2.6 Direct and Indirect Air-Shower Detection

Imaging in the energy range from $\sim$ 10 GeV to 5 TeV is the domain of the Imaging Atmospheric **Čerenkov Telescopes** (IACT) [Aharonian and Akerlof, 1997]. Here the Earth's atmosphere is used as conversion medium where the pair creation takes place. The pairs generated in the primary interaction have energies high enough to produce a cascade of secondary particles. The charged particles in the cascade emit Čerenkov radiation which can be measured from the ground. Images of the air showers (by the Čerenkov light) are recorded with optical telescopes in moon-less nights. The direction and energy information of the incoming photon can be derived from the shape and flux of the showers. Current examples for this type of instruments are HESS [Hofmann et al., 2001], MAGIC [Baixeras et al., 2004], CANGAROO [Enomoto et al., 2006], and VERITAS [Holder et al., 2006].

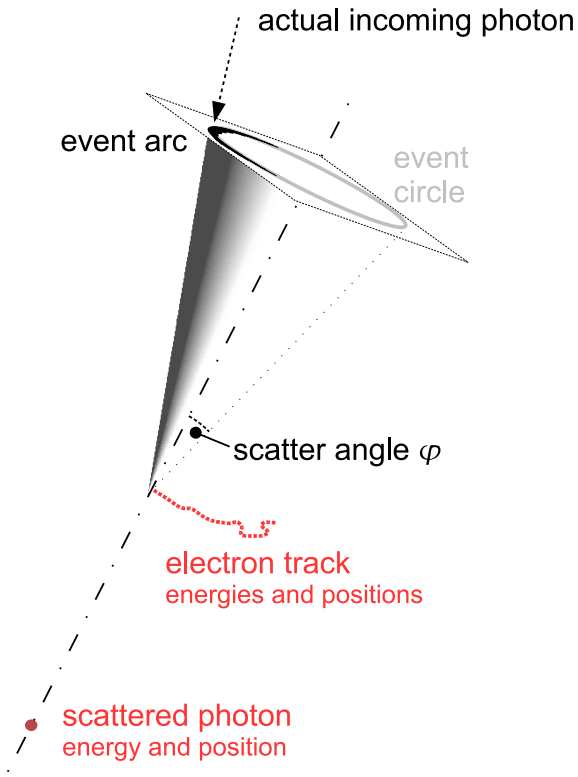

Figure 1.6: Event reconstruction scheme of a Compton scatter interaction

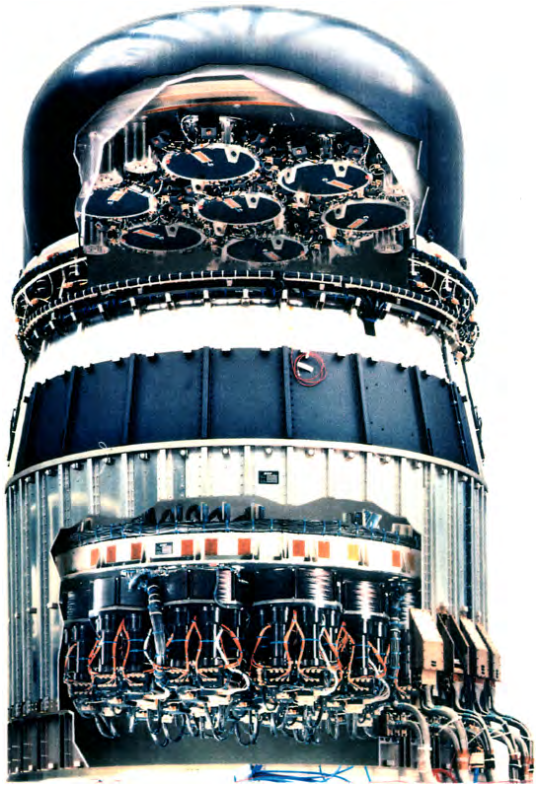

Figure 1.7: Photomontage of the COMPTEL instrument

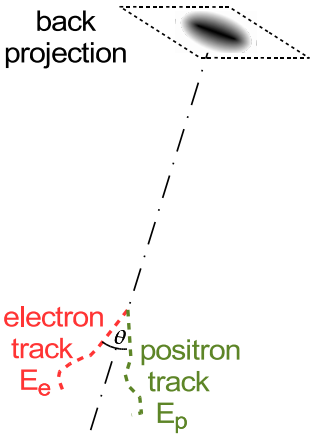

Figure 1.8: Event reconstruction scheme of a pair creation interaction

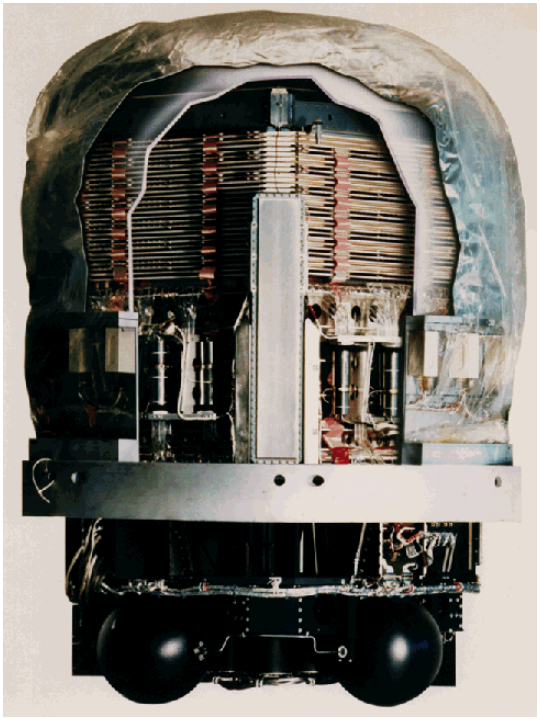

Figure 1.9: Photomontage of the EGRET instrument

Above 10 TeV the secondary particles in the air shower are energetic enough to reach the ground. They can be detected with large **air-shower arrays** of particle detectors such as CYGNUS [Alexandreas et al., 1992] or MILAGRO [Atkins et al., 2000b]. Since these instruments do not detect light from the atmosphere but the high-energy particles, they can also be operated during daylight. The direction of the converting γ ray in the atmosphere is derived from the arrival times of the detected (secondary) particles by reconstructing the incident particle wave front.

1.2.7 Diffraction

All above-mentioned methods with exception of the Čerenkov telescopes have in common that the area of active detector material directly governs the instrument's effective area. In contrast, at X-ray energies and below celestial photons are focused from a large collection area to a much smaller detection area, reducing the impact of detector backgrounds and enabling direct imaging. Up to medium X-rays focusing with mirrors is the established method for imaging; current mirror developments aim at up to 80–100 keV. Another imaging tool are lenses which could even work at higher energies. For the energy range of 1–2 keV Braig and Predehl [2004] propose a Fresnel zone plate. At γ-ray energies a method in a conceptual stage for astrophysics purposes is based on phase Fresnel lenses [Skinner, 2001]. An experimentally advanced method for focusing γ rays up to 1 – 2 MeV uses Laue diffraction in crystals to focus the incoming radiation onto a small detector volume [Smither, 1982]. A demonstrator instrument called CLAIRE proved already the applicability of the concept in a balloon flight in June 2001 [Halloin, 2003]. Further steps towards a satellite mission are ongoing, the envisioned instrument is the Gamma-Ray Imager (GRI, Knödlseder [2006]), which evolved from an earlier, smaller concept called MAX [v. Ballmoos et al., 2004].

1.2.8 Limits of the Different Imaging Methods

Different physical as well as technical limits are inherent to each of the imaging methods. There is no "universal" method; thus the choice of a particular detector concept (which could even combine different methods) is a trade-off between measurement goals and feasibility. Table 1.1 gives an overview over the main tradeoffs.

1.3 Current Imaging γ-Ray Telescopes

Figure 1.10 shows the sensitivities of a selection of instruments. In the hard X- and low γ-ray energies collimators such as OSSE aboard CGRO and HDX aboard SUZAKU as well as coded masks such as the two main instruments IBIS and SPI aboard the INTEGRAL observatory are used. Some of these instruments cover also a large part of the Compton dominated energy range. However, better sensitivities were achieved at these energies with the Compton telescope COMPTEL. Since the deorbiting of CGRO no instrument with better or even comparable MeV sensitivity has been available in space. At energies above a few tens of MeV, three pair creation telescopes are included in figure 1.10: COS-B as representative of the first generation, EGRET aboard CGRO being a second generation instrument and GLAST (to be launched end of 2007) as the third. For even higher energies ground-based Čerenkov-telescopes such as MAGIC and HESS are used.

The lack of instrumentation for MeV energies with a sensitivity comparable to EGRET is obvious. Different ideas exist to bridge the observational gap: One aims at the transition region between the Compton and pair creation regime. It combines the Compton-scatter principle used in COMPTEL and the charged particle tracking capability of a pair creation telescope such as EGRET. This is the operating principle of MEGA, its prototype is subject of this work. Very similar to MEGA is

	Energy Range	Angular resolution	Field-of-view	Background rejection methods
Collimator	governed by detector range and collimator thickness; feasible below few MeV	no imaging in field-of-view	governed by collimator aspect ratio, extended by scanning	active and/or passive shielding
Mask	governed by detector range, mask thickness; feasible below several MeV	depends on mask and detector element size, detector–mask distance, e.g. IBIS and SWIFT: ∼arcmin, SPI: ∼deg	medium – large, depending on geometry	active and/or passive shielding
Compton telescope	Compton regime (few 100 keV – few 10 MeV)	∼deg, Doppler limited, depending on energy resolution and geometry	large, depending on geometry	active shielding against charged particles and other suppression methods (e.g. TOF, tracking)
Pair-creation telescope	Pair regime (above few 10 MeV)	∼ deg down to few arcmin, limited by detector position resolution, at low energies by scatters in conversion detector	large, depending on geometry	active shielding against charged particles, TOF (in EGRET)
Čerenkov telescope	very high energies (few 10 GeV – >10 TeV)	arcmin and better	few degrees	discrimination algorithms between photon and hadron induced showers
Laue lens	up to a few MeV	arcsecs, depends on focal length, crystal size, mosaicity	few resolution elements, extendible by scanning	intrinsically low background due to a decoupling of collection and detection area, probably additional detector shielding
Phase Fresnel lens	governed by detector range	extremely high (sub μarcsecs), depends on focal length	milli arcsecs	intrinsically low background due to a decoupling of collection and detection area, probably additional detector shielding

Table 1.1: Comparison of the gamma-ray imaging methods

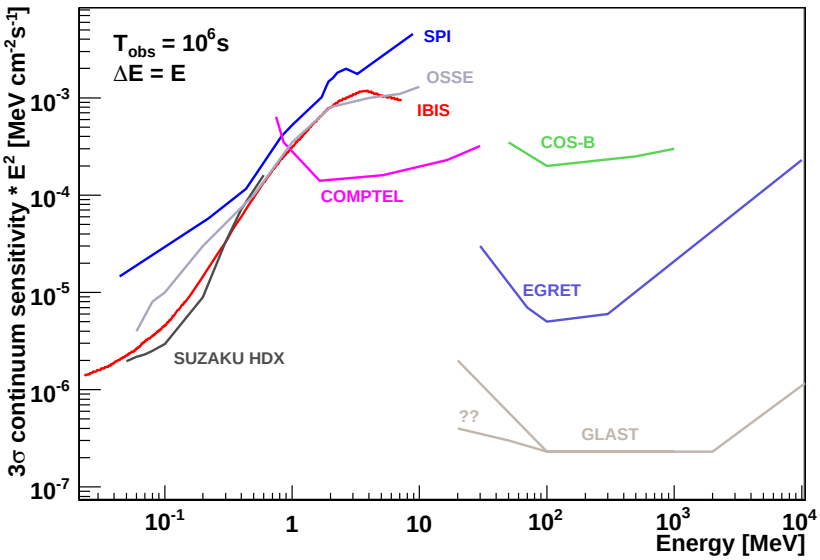

Figure 1.10: Sensitivity curves of selected recent, current, and near future astrophysical telescopes (mostly pre-flight values). The sensitivity is given here as the minimum flux of a source, which is needed to get a 3σ-detection in 10^6seconds observation time in a broad energy band ($\Delta E = E$), multiplied by E^2 (as it is done for comparing multiwavelength spectra [Gehrels, 1997]).

TIGRE [Bhattacharya et al., 2004], whose prototype is still under construction. The goal of these instrument concepts is to achieve a sensitivity 10 times better than COMPTEL, i.e. a sensitivity advance comparable to that of EGRET with respect to COS-B. A variety of approaches for realizing a Compton telescope are studied for the Advanced Compton Telescope (ACT) [Boggs, 2005] which range from solid state detectors (Ge, Si, CdZnTe) with or without a crystal calorimeter (CsI or $LaBr_3$) over time projection chambers (liquid Xe or Ar) to gas microwell detectors. These efforts concentrate on an instrument with a sensitivity 100 times better than COMPTEL aimed primarily at nuclear astrophysics observations. They are in a conceptual stage and should complement the GLAST sensitivity to the MeV range, but the launch date will be post 2015.

1.4 The γ-Ray Window to the Universe

The past γ-ray missions opened a window to the most energetic phenomena in the Universe. The sky is full of (point-like and extended) objects emitting γ rays at all distance scales — as near as the outer atmosphere and as far away as to the most distant sources known:

1.4.1 Earth's Atmosphere and Solar System

Earth's Atmosphere as a target of Cosmic Rays is "glowing" in γ rays due to bremsstrahlung and the decay of secondaries. This is non-instrumental background radiation for γ-ray telescopes in an earth orbit. Petry [2005] imaged this atmospheric emission (100 – 300 MeV) with EGRET.

Terrestrial γ-ray Flashes (TGFs) originating from the Earth's atmosphere were first detected by BATSE [Fishman et al., 1994a]. The flashes last between a fraction of a millisecond and several

milliseconds. Photon energies of up to 20 MeV are measured [Smith et al., 2005]. They are correlated with thunderstorms from which optical discharge phenomena above the storm clouds such as sprites are known. RHESSI data in combination with magnetic field measurements confirms the connection of TGFs to lightnings [Cummer et al., 2005, and references therein]. The production mechanism of the high-energy radiation is unclear, it is suspected that it is generated by a relativistic runaway electron avalanche mechanism.

Gamma rays from the Moon and from planets are induced by impinging cosmic rays which generate bremsstrahlung and secondary particles (e.g. π^0, neutrons, electrons, positrons, etc.) in the surface layers [Fichtel and Trombka, 1997]. Photons emitted as result of captures of (moderated) neutrons especially on hydrogen but also on silicon, chlorine, or iron reflect the elemental composition of the surface layers [Reedy et al., 2003]. For instance, two regions have been found near Mars' poles which are hydrogen-rich below the surface [Boynton et al., 2002] indicating the existence of ice by the 2.2 MeV radiation of the neutron capture reaction on hydrogen. The overall flux, however, is only intense enough to be measured with current instrumentation directly at the surface or by nearby passing/orbiting satellites.

Solar Flares are one of the brightest γ-ray transients observable. They exhibit a complex spectrum of bremsstrahlung, nuclear lines, positron annihilation, the neutron capture line and decaying secondary particles from collisions (especially π^0). The composition of ions, their acceleration processes, their energies and the surrounding medium are all convolved into the overall observable γ-ray emission [Murphy et al., 1997]. Instruments such as SMM (Solar Maximum Mission) or RHESSI [SolPhys] are dedicated instruments for investigating the sun during activity maxima.

1.4.2 Galactic Objects

Massive Stars in their late burning stages, especially Wolf-Rayet (WR) stars, have strong stellar winds. These carry away nucleosynthesis products, including radioactive isotopes (e.g. ^{26}Al) into the interstellar medium. The kinetic energy in the winds gives rise to Fermi acceleration of cosmic rays in wind-wind collisions in star forming regions such as OB associations.

Binary Systems can be sources of high-energy emission if one of the two companions is a compact object (white dwarf, neutron star, or a black hole). Accretion flows from the "normal" star onto the compact object over the Roche-lobe or via a strong stellar wind release large amounts of gravitational energy. The varying intensities from these compound objects as seen in X rays (therefore they are called X-Ray Binaries, XRBs) is believed to result from variations in the accretion rate. The accreting matter heats up and emits a thermal spectrum up to X rays. Black hole systems often develop jets and therefore are called microquasars [Fender and Maccarone, 2004]. If such a system has a jet pointed toward the observer, the system is seen as **microblazar** [Cui, 2005]. Very-high-energy photons (> 100 GeV) have been found associated with an X-ray binary (LS 5039) by the HESS collaboration which seems to have also an EGRET counterpart [Aharonian et al., 2005]. Low to very-high-energy γ rays are expected to be generated by two mechnisms where the dominant process is unknown: (a) inverse Compton scattering of low-energy photons on relativistic electrons and positrons; (b) relativistic protons interacting with low-energy photons and protons.

A white dwarf in a binary system accretes matter in form of a hydrogen shell. If the energy generated by nuclear burning exceeds the cooling by radiation, a runaway starts and the hydrogen shell burns explosively as a **nova**. According to standard models, nucleosynthesis takes place

in this explosion. It leads to a characteristic mixture of elements where also the composition of the white dwarf (CO or ONe) is imprinted [Hernanz and José, 2004]. CO novae are expected to bring measurable amounts of ^{7}Be to the surface while ONe novae can be identified by ^{22}Na emission. With an accurate measurement of the prompt γ-ray emission of the radioactive isotopes (prominently the positron annihilation radiation from β^+ decaying isotopes) lasting for some hours, theoretical models could be constrained in terms of the dynamics in the envelope and the mixing of materials (metals) from inner parts into the envelope.

Supernova (SN) explosions mark the end of life of stars. They produce most of the heavy elements in the Universe. The explosion process is a key for understanding the current composition and distribution of the elements in the Universe. There are two fundamentally different explosion mechanisms, the thermonuclear explosion (SN Type Ia) and the core collapse (such as types II, Ib, Ic).

The first type is believed to originate from binary systems with a white dwarf. The matter density in the white dwarf is high so that carbon burning efficiently releases energy. This energy cannot be radiated away and the white dwarf is disrupted. Three possibilities triggering the carbon burning are commonly discussed [Hillebrandt and Niemeyer, 2000]: (1) The white dwarf exceeds the Chandrasekhar mass ($\sim 1.4 M_\odot$) by accretion of matter from the companion star (Roche-lobe overflow). The contraction of the core due to the large gravitational pressure ignites by compression heating and explosive carbon burning disrupts the white dwarf. (2) In sub-Chandrasekhar mass white dwarfs, an ignition of their CO cores can be triggered by a shock when an accreted He layer detonates. (3) Two white dwarfs merge. In addition to the fundamental uncertainty of the precursor scenario, the detonation process itself is also unclear. Possibilities include prompt or delayed detonation and others. The investigations of SN type Ia are of particular interest since the empirical data suggest that SN Ia are very homogeneous and can be used as standard candles, i.e. as measure of distance on cosmological scales [Phillips, 2005].

The explosion of a star heavier than $\gtrsim 8\,M_\odot$ in a core collapse supernova is the result of the contraction of the core after silicon burning [Woosley and Janka, 2005]. When there is no more fusion energy available, the radiation pressure can no longer balance the gravitational forces. The electrons are squeezed into nuclei forming a neutron-rich proto-neutron star. The stages finally leading to the explosion are not well understood (see e.g. Burrows et al. [2005]). It is clear that neutrinos are responsible for energy transport from the inner parts to the infalling matter and for cooling. After the explosion a neutron star or black hole, possibly with a jet, and an expanding shell forming a nebula (the supernova remnant) remains.

The different types of supernovae leave traces by long-lived radioactive isotopes which are found in the diffuse galactic emission (^{26}Al and ^{60}Fe, see below). The expelled amounts of relatively short-lived isotopes (^{44}Ti and ^{56}Co) give hints for the masses and explosion types and can be found in the supernova remnants (see below).

Pulsars are rotating neutron stars with strong magnetic fields left over from such a core collapse supernova. During the collapse the magnetic flux as well as the angular momentum of the precursor must be conserved. Thus the magnetic field strength as well as the angular frequency increases by a factor of $\sim 10^{10}$. This results in magnetic fields on the order of 10^8 T and rotation periods of milliseconds to several hundreds of milliseconds. These strong magnetic fields accelerate particles leading to non-thermal radiation. In the case of the so-called spin-down pulsars the accelerator is powered from the rotational energy, the emission is periodic with a slight slow down. Pulsars with an accretion flow (in a binary system) are "recharged", but the pulsation are often irregular. In either case, pulsed emission can be observed from radio to the high-energy γ rays as it is the case

for the Crab pulsar. Such clear multi-wavelength detections are available only for a fraction of other pulsars. Most pulsars are apparent only at radio wavelengths [Wielebinski, 2002]. Different emission scenarios for radiation are in discussion, such as the polar cap, the outer gap or, to account for the polarized radiation, the two-pole caustic model [Dyks et al., 2004, and references therein]. In these models vaccuum gaps with high potential drops are postulated and high-energy particles can produce strong radiation. Additionally to the light curve and the relation between the different wavelengths, polarization measurements are an important tool for discriminating between the scenarios.

Supernova Remnants are the expelled outer shell from a supernova. The hot matter moves with high speed into the interstellar medium. At the transition between the interstellar medium and the expanding shell a shock front forms in which charged particles are Fermi accelerated. These particles can be observed in γ rays by their inverse Compton scattered radiation and the decay radiation of pions from proton collisions. As more and more interstellar medium is swept up, the shell slows and cools down.

The remnant contains radioactive isotopes produced in the progenitor and the explosion. One interesting isotope is ^{44}Ti. Its yield is very sensitive to the mass of the progenitor [Timmes et al., 1996]. Up to now a detection at γ-ray energies succeeded only for Cas A [Iyudin et al., 1994, Schönfelder et al., 2000a]. Another significant isotope is ^{56}Co which is prominently produced in supernovae Type Ia (e.g. Diehl and Timmes [1998]). This isotope has been measured clearly from the core-collapse SN 1987A [Matz et al., 1988] and from the type Ia SN 1991T [Morris et al., 1997].

Diffuse Galactic Emission originates from sources in our Galaxy which are either truly extended or cannot be resolved by current telescopes. Enrichment of the interstellar medium with long-lived radioactive isotopes (e.g. ^{26}Al or ^{60}Fe) leads to spatially extended line emission. ^{26}Al is expelled from nucleosynthesis sites such as massive stars with strong stellar winds (Wolf-Rayet stars), supernovae and novae. Significant contributions to galactic ^{60}Fe are only expected to be produced by massive stars and expelled in core-collapse supernovae: Whereas ^{26}Al can already be produced in H-burning zones, the ^{60}Fe production can only take place deep down in the He-burning zones. The different types of sources can be differentiated by the abundances of these two isotopes. The distribution of ^{26}Al is known from COMPTEL [Plüschke, 2001]. The spectrometer SPI has recognized the Doppler shifts resulting from the rotation of our Galaxy [Diehl et al., 2006] and detected ^{60}Fe [Harris et al., 2005].

Radioactive isotopes such as ^{26}Al, ^{44}Ti, ^{56}Co, and many others decay via emission of a positron (β^+–decay). These positrons and the ones produced by other processes populate the galaxy and are observable by their annihilation radiation (511 keV line and positronium continuum emission). INTEGRAL images of both components [Knödlseder et al., 2005, Weidenspointner et al., 2006] show a large positron population in the galactic bulge whose spatial distribution and intensity cannot be explained with known populations of galactic sources. A plethora of sources have been proposed to account for the excess radiation, from astronomical objects to dark matter (Bertone et al. [2006] presents a long list of possibilities in his introduction). Also a transport mechanism by magnetic fields has been proposed by Prantzos [2006] carrying the positron from the disk into the bulge.

Positrons and lines from radioactive isotopes are not the only contributors to the diffuse galactic radiation. Continuum γ rays resulting from bremsstrahlung, inverse-Compton radiation, and pion decays (produced by baryonic particle collisions) are known to originate from the interstellar medium [Strong et al., 2005].

1.4.3 Extragalactic Sources

Active Galactic Nuclei (AGN) are galaxies whose emission is variable and most of them show strong emission lines. A zoo of types developed historically (e.g. Seyfert galaxies, Quasars, BL Lacertae objects) showing different properties such as bright cores, some times overshining the rest of the galaxy, broad and / or narrow emission lines, polarized emission, and emission maxima in the IR, UV, or even X and γ rays. Variability on the time scale of days restricts the origin of the radiation to the nucleus, where only gravitational energy from accreting matter can serve as energy source. Typical (but not always observed) for accreting systems is the jet outflow perpendicular to the accretion disk. Despite these large differences it is currently believed that such objects have a common structure [Urry and Padovani, 1995] and the observed properties result from observational, e.g. the viewing angles onto the object, and physical properties, e.g. mass and spin of the central black hole. According to this unified AGN model there are different structures around a massive black hole: An accretion disk is formed around the black hole. This nucleus is surrounded by molecular clouds which rotate faster in the vincinity of the black hole (broad line region) and slower at larger distances (narrow line region). These regions are additionally filled with an electron gas. An extended molecular torus absorbs radiation from the inner regions. Perpendicular a jet structure extents into the interstellar medium which is sometimes strong (radio-loud) and sometimes weak (radio-quiet). The observed spectrum is compounded of non-thermal and thermal radiation. The non-thermal results from inverse Compton scatters in the jet and the thermal radiation originates from the accretion disk and the molecular clouds. The extended molecular torus can hide parts of the accretion disk and the fast-rotating part of the molecular cloud depending on the viewing angle onto the accretion plane. Many questions are open concerning the central engine and its connection to the jet [Madejski and Sikora, 2006] such as the conversion process of potential energy to acceleration energy in the jet, or which particles are accelerated in the jet (dominantly hadrons or leptons). Especially blazar* models lack more precise and sensitive measurements in the sub-MeV and MeV range, which would help to disentangle e.g. the the various inverse-Compton processes taking place in the jet — synchrotron self-Compton (SSC) or external Compton (EC) components. Moreover the extragalactic component of the EGRET unidentified sources may be composed of blazars [Bloom, 2006] which could be tested by extending their spectra to lower energies.

Gamma-Ray Bursts (GRBs) are cosmological† phenomena being extreme in several aspects, e.g. they are the brightest and most variable sources in the γ-ray sky. It is not surprising that they were the first point-like γ sources discovered. They can be observed at extreme cosmological distances. A redshift of 6.29 has been repored from GRB 050904 by Sakamoto et al. [2006]. Two classes of GRBs are distinguished, short bursts (duration $\sim 0.1-2\,\mathrm{s}$) with hard spectra and long bursts (duration $\sim 2-200\,\mathrm{s}$) with soft spectra [Kouveliotou et al., 1993]. The short bursts are believed to originate from the merging of two neutron stars or a neutron star and a black hole (e.g. Ruffert and Janka [1998]). The established model for the long bursts is the collapse of a massive star to a black hole (MacFadyen and Woosley [1999], where the connection to core collapse SN Ic has been shown in several cases (e.g. by Stanek et al. [2003]).

Long GRBs are found to be usable as "standard candles", i.e. as cosmological distance indicators [Lazzati et al., 2006]. In order to substantiate this up to now empirical property, observationally verified models of their central engines and jets are desirable. γ rays are an invaluable tool for constraining GRB models, since the prompt emission, which peaks at hundreds of keV or above,

*In the unified AGN model blazars are the objects where the jet points towards the line-of-sight so that a predominantly a non-thermal spectrum is observed.

†BATSE observed a homogeneous distribution all over the sky excluding a galactic origin [Meegan et al., 1992].

is expected to originate from close to the central engine. Optical polarization [Malesani et al., 2005] and a high energy component (10 – 200 MeV, González et al. [2006], even evidence for TeV emission Atkins et al. [2000a]) has been found in the afterglow.

The Extragalactic Gamma-ray Background seems to have two main contributors: Unresolved Seyfert galaxies with emission in the X- and hard X-ray band and blazar-type AGNs in the γ rays [Comastri, 1999]. In the MeV range, it is unclear if AGNs can account for most of the background radiation or if an additional component is present (most likely SN Type Ia, Zdziarski [1996], Watanabe et al. [1999]). However, it is speculated that there might be also an additional (diffuse) component such as annihilation radiation from pions, positrons or exotic particles as expected e.g. from light dark matter [Rasera et al., 2006].

Absorption Features in the observed spectrum reflect properties of the *traversed* matter instead of the *emitters*. Absorption lines in blazar and GRB spectra due to nuclear resonant absorption mechanisms allow (in principle) to determine the red shifts of objects even in γ rays and provide some constraints on the column density and composition of the traversed material in the line-of-sight [Iyudin et al., 2005].

Chapter 2

MEGA - an Instrument based on a Combination of Compton Scatter and Pair Creation Interactions

Medium-energy gamma-ray photons provide an unique view of the energetic Universe (chapter 1.4): In this energy band one finds the nucleosynthesis lines, there is the transition region between the domincance of hot thermal and non-thermal emission, and there is the positron annihilation. COMPTEL provided the first all-sky survey in this energy range [Schönfelder et al., 2000b] and INTEGRAL gives detailed insights (in terms of spectral and angular resolution) to selected objects, especially on our Galaxy. In order to understand further the energetic processes and the life cycle of matter in our Universe the MeV regime needs to be deeper explored, a new mission with improved sensitivity is desirable.

2.1 Goals of a Satellite Mission in the MeV Range

For a closer look to the known γ-ray sources and a deeper view into the Universe to discover and identify many more high-energy objects, a new mission has to achieve an **improved sensitivity**. The advances in sensitivity between successive generations of telescopes is usually one order of magnitude as seen in the pair creation telescopes (figure 1.10), so a new mission aims at a factor of ten higher sensitivity compared to COMPTEL.

The sensitivity at this level should be provided throughout a **wide energy range** from several hundreds of keV to several tens of MeV. Thus the gap between INTEGRAL at the lower energies and EGRET and GLAST at the higher ones is closed.

A large fraction of the γ sources detected by COMPTEL [Schönfelder et al., 2000b] are variable (approximately half of them are gamma-ray bursts and a quarter are Blazars, see also Collmar [2006]). The outbursts of these and other objects (e.g. supernovae and novae) are not predictable so that most of them can only be recognized by a continuously monitoring instrument requiring a **wide field-of-view**.

Pulsar models as well as GRB models often predict large differences in the polarization properties of the γ-ray emission. Sensitive **polarization** measurements add a novel tool to γ-ray astrophysics.

The sites of nucleosynthesis are identified by the decays of radioactive isotopes produced in stars and explosions. Conclusions about the progenitor and the explosion can be drawn from the abundances of some key isotopes (e.g. ^{44}Ti or ^{56}Co) compared to the yield of ^{26}Al. **Good energy**

resolution and the capability of **imaging** to locate and disentangle **point-like** and **extended sources** are required here.

More precise and sensitive measurements of the diffuse cosmic γ-ray background in the MeV range should give tighter constraints on the necessary components of this background (are Seyfert galaxies and blazars the only constituents or are there additional sources such as supernovae Ia or light dark matter annihilation [Rasera et al., 2006]?).

Many more interesting targets could be investigated such as solar flares, the Orion region with its nuclear interaction lines, probably resonant absorption features from matter along the line of sight to distant objects.

2.2 The Principle

The Medium Energy Gamma-ray Astronomy telescope (MEGA) is a candidate for a surveying space mission as a second generation Compton telescope fulfilling the needs discussed in the previous chapter. Its design goal is to provide a sensitivity level of 10 times better than COMPTEL for energies from 0.4 to 50 MeV.

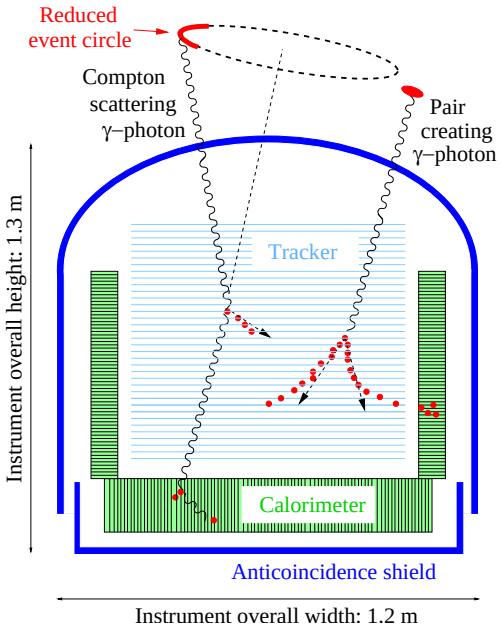

Figure 2.1: Schematic view of the working principle of MEGA. The detector is shown in a cross-sectional view. A Compton and a pair creation event is over-plotted.

Since the energy range extends from the Compton regime into the lower pair creation regime, an improved sensitivity is achieved by combining the Compton imaging capability and the tracking of charged particles needed to detect pair creations as in EGRET. This in turn is advantageous for Compton imaging (compared to COMPTEL), since the electron track information reduces the classic Compton cone to a segment of a cone.

The threepart design found in COMPTEL as well as in EGRET is retained in MEGA as shown schematically in figure 2.1: The first subsystem is the tracker (called D1) where the primary interaction — Compton scatter or pair creation — takes place, the second is the calorimeter (D2) which measures the secondaries leaving the tracker, and the third is the Anti Coincidence Shield (ACS) which recognizes charged particles impinging on the detector. However, MEGA's detailed detector geometry differs significantly from previous designs: The layout is much more compact,

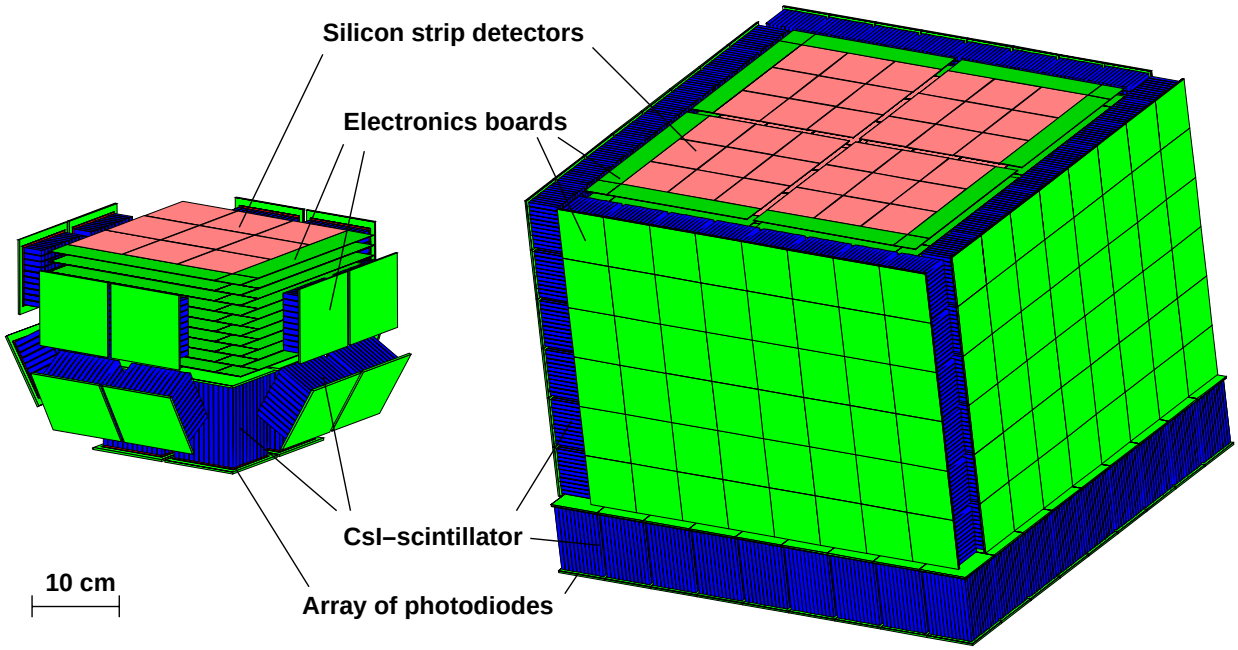

Figure 2.2: Simulation models for the prototype (left) and an envisioned satellite instrument (right)

i.e. the tracker and the calorimeter are close together. This makes it feasible to surround the tracker with the calorimeter except for the entrance window which results in high efficiency, a wide field of view ($\sim$ 160°), and good polarization sensitivity. It comes at the cost of losing the possibility of measuring the time of flight (TOF) for Compton interactions. The required time resolution would be smaller than 1 ns which is not achievable with current detector systems offering an acceptable energy resolution (but new developments are promising, see chapter 10). TOF was the most important tool for background suppression in COMPTEL; its absence is compensated in MEGA by the electron tracking capability.

The path of charged particles is recorded by the tracker of MEGA consisting of double-sided silicon strip detectors (chapter 3) stacked upon each other. The layers are thin enough for electrons to traverse several of them (for electron energies above $\sim$ 1 MeV) and the strip pitch is small enough to provide sub-mm position resolution of the individual interactions. MEGA's calorimeter consists of scintillating CsI(Tl) crystals with Silicon-PIN-diode readout (chapter 4). It is finely segmented to separately record all particles escaping from the tracker. In case of the scattered photons from a Compton interaction the cross section for photoelectric absorption of these photons often is still low (compare figure 1.1). It is very likely that (one or more) Compton interactions will occur in the calorimeter before the final photoelectric absorption. MEGA resolves the individual interactions, and their sequence is reconstructed from the interaction information (see appendix I.1 for details on the algorithms used). In contrast, it was sufficient for COMPTEL with its less compact design (1.5 m distance between tracker and calorimeter) to measure the center of gravity in both (scatter and absorbing) detectors with Anger cameras (figure B.1). Due to the large baseline the direction of the scattered photon was determined sufficiently accurate from individual interaction positions know to a few cm.

2.3 The MEGA Prototype

In order to prove the principle of operation and to address the technical challenges, a prototype of the MEGA instrument has been built, tested and calibrated. It is a scaled down version of the

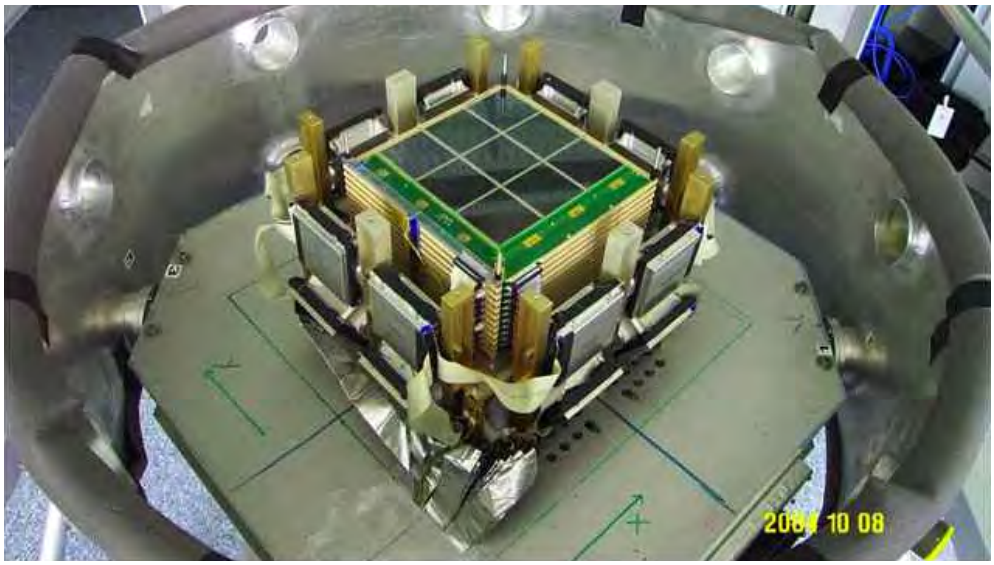

Figure 2.3: The MEGA prototype with opened cover of the tracker layers

envisioned satellite instrument and features a third in tracker depth, a quarter in tracker area, and the calorimeter covers the lower hemisphere of the tracker only to ∼30%.

The prototype has been calibrated with two kinds of calibration sources — radioactive laboratory sources and a polarized γ-ray beam. In addition tests with muons have been performed. Since laboratory sources cover only the lower part of MEGA's energy range, a calibration up to 50 MeV using the accelerator γ-ray beam of the HIGS facility (chapter 7.2) has been performed. The response to polarization could also be determined with this fully polarized beam.

A crucial aspect for a satellite mission is the background suppression. There are several sources of in-flight backgrounds: Charged particles such as electrons and protons cross the instrument in a space environment. Therefore the ACS (appendix G) surrounds the tracker and calorimeter and rejects the readout of these events. Neutrons impinging on the satellite most easily activate the structure (especially the aluminium) if they are moderated (for example by fuel tanks). Also cascading isotopes such as ^{22}Na are produced. Additionally the Earth's atmosphere radiates in γ rays because of the bombardment with cosmic rays making it a strong γ-ray source to satellites in a low-earth orbit. Since a time-of-flight measurement in MEGA is impossible with current electronics due to the compact design, the rejection of the latter background sources has to be achieved with the electron track information and the redundant information available in the case of multiple Compton interactions.

The individual components of the MEGA prototype are described in detail in the following chapters.

Part II

MEGA — The Subsystems

Chapter 3

The Tracker

The central part of the MEGA prototype is the tracker. It serves three main purposes:

- It is the scatter medium for Compton scatters.
- It is the conversion material for pair creation events.
- It measures the energy and interaction positions of electrons and positrons.

3.1 Design

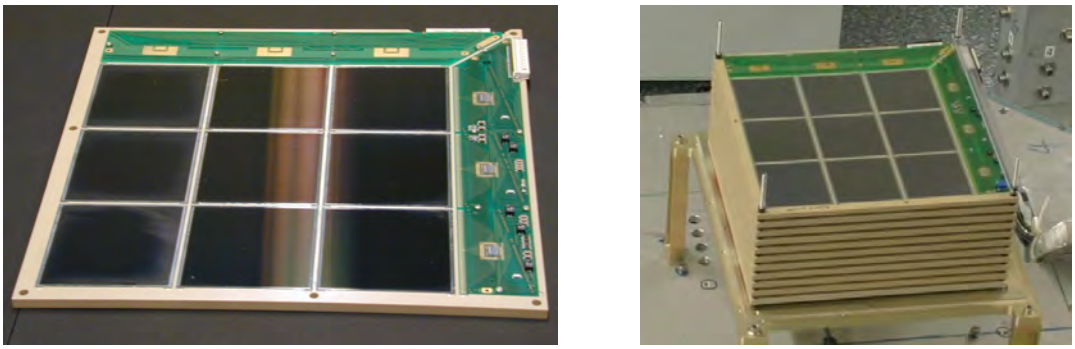

Figure 3.1: The tracker. Left: single layer. Right: the full stack of 11 layers

The MEGA prototype tracker is a stack of 11 layers of double-sided Silicon strip detectors with 1 cm vertical spacing between the layers. Every layer is composed of a 3×3 array of wafers* (500 μm thick) and front-end electronic boards for both sides (figure 3.1). Top and bottom sides of each individual wafer are structured in 128 readout strips (orthogonal directions on opposite sides) and a surrounding bias ring (figure 3.2). The top surface structures are implemented by p-doping (therefore called p-side), the bottom surface by n-doping (n-side). The decoupling capacitor of the readout electronics is integrated on the wafers themselves by a silicon oxide (1500 Å) and silicon nitride (900 Å) layer between the p- and n-doped strips and the aluminium readout wires. This oxide causes a problem on the n-side: Unavoidable positive fixed charges in the oxide and at the Si–SiO_2 interface attract electrons to the Si surface and form an electron accumulation layer†. Such

*The silicon strip detector wafers were designed by the Max-Planck-Institut Halbleiterlabor and fabricated by Eurisys (Strasburg), now CANBERRA.

†An electron accumulation layer as occuring in n-type material cannot be avoided by using p-type material where the amount of positive charges is large enough to generate an inversion layer.

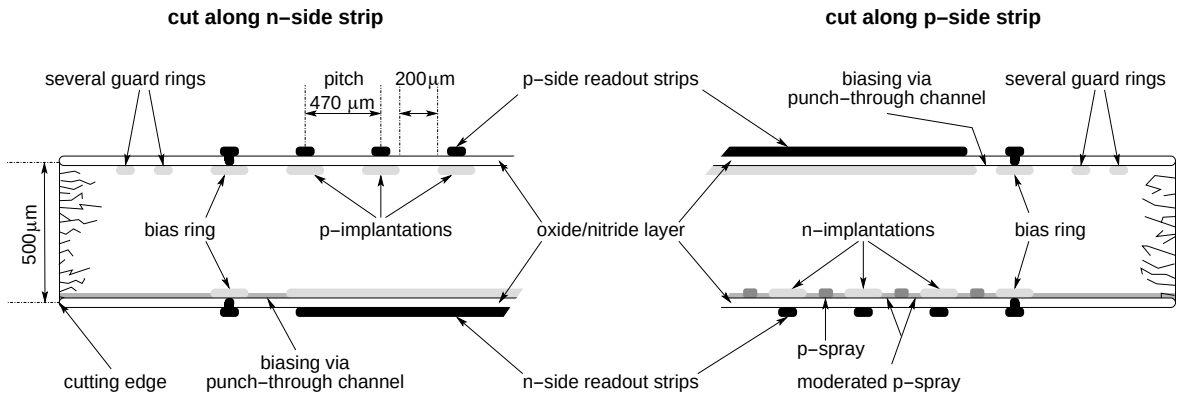

Figure 3.2: Sectional drawing of a MEGA double-sided silicon strip wafer

an electron layer interconnects the n-implants. In order to separate the n-strips of the MEGA strip detectors a moderate p-doping (the so-called p-spray) is introduced binding the attracted electrons and blocking the connection between the strips. The biasing resistors are integrated as well by means of the so-called punch-through mechanism where a current flows over a potential barrier between two highly doped regions. In order to avoid large currents flowing over the cutting edges, the p-side features several guard rings (high resistivity structures) outside the bias ring which isolate the p-side bias potential from the wafer edges.

The bias voltage is applied to the bias rings. The wafers start to deplete from the p-side (since the bulk material is slightly n-doped the initial pn-junction is on the p-side). On the n-side, the bias ring is low ohmic contacted to the strip implants as long as the wafer is not fully depleted so that also the small gap between the implants is not depleted. Once the gap is depleted, the punch through effect sets in, which forms a high ohmic channel over the gap - the bias resistor. This explains, why the p-strips show their final noise behavior already before full depletion, whereas the n-side strips still remain interconnected by the undepleted region.

A more detailed description, measurements with individual wafers, and discussions can be found in [Schopper, 2002].

A major goal for the design of the layers was to minimize the fraction of passive material. The holding structure is a light-weight frame and the (front-end) electronic boards are thin printed circuit boards (0.5 mm) holding bare silicon chips, i.e. without package. This design results in $\sim 40\%$ of the total mass of a layer being active (excluding the electronics at the two edges, this fraction increases to $\sim 60\%$).

3.2 Tracking of Charged Particles

Measuring the path of a charged particle with double-sided strip detectors is in principle very simple: Every passage through a wafer generates a signal on one p-side and one n-side readout strip, pinpointing the interaction location. Complications arise, when reconstructing the track from real measured data. They are discussed extensively in [Zoglauer, 2005] and will be summarized here briefly.

- The order of interactions cannot be measured since the necessary time resolution (< 0.1 ns) cannot be achieved. The only indication for the order, especially the track orientation, are the energy deposits. There the start and end points are crucial. Since the electron track

starts somewhere within a layer and does not need to pass the full wafer thickness, this first energy deposit is most often comparatively low. Low energy thresholds, i.e. low noise, is important in this respect.

- Due to increasing Molière-scattering U-turns appear at the end of a track, i.e. the scatter angle is large enough so that the particle's path changes from downward to upward motion. On the one hand this helps distinguishing front from back of the track. On the other hand the resulting ambiguity, which p-side signal corresponds to which n-side signal, can be solved on a single-layer basis only by correlating the energy informations of both sides.
- In case of a pair creation, there are two tracks, i.e. two (or even more) hits in one layer. Again, it is ambiguous which p- and which n-side signals belong to the same hit.
- The charge generated by an interaction may be distributed over several strips, especially if a charged particle crosses the wafer diagonally. Then neighboring signals are combined to so-called clusters and treated as single hits.
- Defective strips need to be taken into account by the tracking algorithm.

The tracking algorithm needs to handle all these problems. Obviously a good energy measurement is crucial for the tracking as well as a good correlation of p- and n-side energies. Furthermore a low energy threshold helps to not lose the first interaction.

3.3 Calibration and Characteristics of Individual Layers

In the following sections the individual strip detector layers are characterized. Table 3.1 gives an overview of the discussed parameters. The detector called Hermes is not included, because the electronics on the n-side were defective. It was put on top of the stack and used as an anticoincidence layer for charged particles in the accelerator measurements described in chapter 7.

3.3.1 Bias Voltages and Leakage Currents

The prototype tracker layers are divided into three groups of different bias voltages, 45V, 65V, and 140V, since the voltage for full depletion varies widely. The appropriate measurements are described and discussed in [Schopper, 2002] and [Bloser et al., 2003]. The leakage currents at room temperature lie between 9.8 and 35.1 μA per layer ($30 - 108\ \frac{\mathrm{nA}}{\mathrm{cm}^2}$)[‡] as stated in table 3.1. Most wafers showing low depletion voltages break through (avalanche multiplication) already at voltages lower than the depletion voltage of the high voltage wafers. This results in the requirement that there must not be a mixture of wafers with different voltage characteristics on the same layer. This prevents to have a working twelfth layer. For the same reason, a simple bias supply featuring one voltage of 140 V does not work.

Despite the decoupling capacitors that are already implemented on the detector wafers, the potential of the aluminium readout strips needs to be the same as that of the implanted strips. Otherwise the resulting electric field would attract charges (electrons or holes, depending on the polarity) at the silicon-oxide boundary. These additional charges enhance the noise, and in the worst case they from a conductive channel between the strips. Measurements have shown that the voltage drop across the punch-through structure is about 6 V, and the inputs of the front-end

[‡]For comparison, the double-sided strip detectors (10 cm$\times$10 cm$\times$300 μm) of the TIGRE prototype are reported to have leakage currents of typically 20 nA/cm^2 [Bhattacharya et al., 2004].

chips lie around 1 V below the chips' ground, thus a difference of 5 V between chip ground and bias potential needs to be maintained. Without additional external capacitors (as it is the case here) this (and the different bias voltages) enforces a design having several galvanically separated grounds. Such a ground concept is very sensitive to induced noise.

3.3.2 Calibration

For the calibration of the individual tracker layers two kinds of radiation are used — radioactive laboratory sources and atmospheric muons. Fully absorbed photons from laboratory sources deposit a fixed amount of energy from which the energy calibration is derived. The atmospheric muons generate straight tracks with large energy deposits in the tracker. They are used for the position calibration.

The calibration data presented here are taken with the fully integrated prototype during the measurements at the HIGS facility (chapter 7.2). Because the front-end electronics are highly sensitive to temperature, the gains of the individual readout channels vary when changing the environment or even when rotating the instrument from an upward position onto its side. Deviations of 10% in gain are observed comparing laboratory data taken at MPE with data taken at HIGS. The calibration data of the setup at HIGS are given here for reference (an overview over all available data is given in appendix H.1).

Since the parameters of 7680 readout channels needed to be evaluated, automatic procedures were developed. They need to cope with gains and thresholds fluctuating widely over the numerous front-end chips and also over the channels within each chip.

3.3.2.1 p-Side

In order to calibrate the p-side, pulse height spectra of the energy deposits of the two radioactive laboratory sources ^{241}Am (59.5 keV) and ^{57}Co (122 keV[§]) are taken (the characteristic X rays also emitted by the sources are neglected since they are below the detector threshold). The whole detector is read out on every trigger of a tracker channel. The data is corrected with respect to offset and common mode, reduced to channels containing signals (chapter 5.2), and histogrammed. The photopeak position (full absorption peak) in units of the analog-to-digital converter is determined from these histograms, yielding the energy calibration.

Every tracker channel (i.e. strip) is processed individually using the spectrum fitting algorithm described in appendix D which accounts for photopeak and an exponential noise continuum. Figure 3.3 shows an example of a fitted tracker channel. An overview over the results for the 122 keV line of ^{57}Co is shown in figure 3.4 (a channel-by-channel view can be found in appendix E). The photopeak positions are spread over a large range, but for many layers a separation into two or three groups can be observed. This reflects the varying operating parameters between the three connected front-end chips on a printed circuit board as described in appendix 5.1.5.

The photopeak positions determined from the two sources give only limited information to compensate the non-linearities of the front-end electronics (chapter 5.1). Other radioactive laboratory sources which would have been strong enough and which feature a single γ-ray line in the required energy range ($\sim$ 60 – 150 keV) were not available during the measurement campaign (e.g. ^{109}Cd with a line at 88 keV). In order to account for the non-linearities an artificial point is introduced as described in chapter 5.1. The full range calibration is derived from these points by linear inter-

[§]^{57}Co emits a 122 keV as well as a 136 keV γ-ray line. In order to keep the calibration simple, the 136 keV line has been neglected. This is reasonable, since the 136 keV has a low probability (10.7%) compared to the 122 keV line (85.6%) (appendix A), and the detector cannot resolve both lines.

detector name	U_b [V]	I_l [μA]	σ_p [keV]	ENC_p [e$^-$]	σ_n [keV]	ENC_n [e$^-$]	noise threshold p-/n-side [keV] (6×RMS$_{\text{noise}}$)	trigger threshold [keV]	saturation p-/n-side [MeV]	defective strips p-/n-side	rise time p/n-side [μs]
Bachus	45	26.0	8.2	840	17.4	1970	46±8 / 63±4	> 37	0.40 / 0.69	7 / 13	2.6 / 2.1
Apoll	45	15.1	7.7	1090	20.1	1740	47±4 / 65±7	> 32	0.29 / 0.60	45 / 29$^+$	2.9 / 2.0
Neptun	45	13.5	6.3	1070	22.0	1910	44±2 / 66±3	> 28	0.52 / 0.29	10 / 14	3.1 / 2.0
Vulkan	45	15.7	9.4	970	28.5	1820	47±9 / 69±8	> 37	0.27 / 0.66	55 / 102	2.4 / 2.0
Poseidon	65	13.5	8.6	1290	20.4	1990	49±3 / 65±4	> 31	0.29 / 0.60	25 / 12	2.7 / 2.1
Sisyphus	65	35.1	10.9	1130	20.2	2050	51±3 / 93±8	> 37	0.32 / 0.93	72 / 90	2.5 / 2.1
Achilles	65	22.6	11.6	1820	25.4	2510	54±3 / 72±4	> 26	0.38 / 0.47	34 / 12	2.6 / 2.4
Ikarus	65	9.8	10.1	910	19.6	1760	60(19±3) / 80(46±11)*	-**	0.36 / 0.96	42 / 47$^+$	2.6 / 2.0
Merkur	140	12.0	11.2	1300	25.0	1890	52±7 / 63±4	> 38	0.42 / 0.69	23 / 20	1.6 / 1.9
Odysseus	140	16.0	13.0	1550	29.4	1970	60(34±5) / 80(63±13)*	-**	0.35 / 0.75	76 / 33	1.9 / 1.4
Hermes	140	23.0	-	-	-	-	- / -	-	- / -	- / -	3.0 / -
average		18.3	9.7	1200	22.8	1960	51±11 / 72±10	> 33	0.36 / 0.66	39 / 37	2.5 / 2.0

Table 3.1: Performance of the 11 tracker layers at $\sim 20^\circ$C. U_b = bias voltage, I_l = leakage current at room temperature, σ_p = average width (standard deviation) of photopeak at 122 keV (^{57}Co) measured on p-side, ENC_p = average equivalent noise charge on p-side in electrons, σ_n = upper limit for the average energy resolution at 122 keV on n-side (see text), ENC_n = upper limit for the average equivalent noise charge on n-side in electrons, * - noise threshold too low because of bad low energy calibration due to indeterminable ^{241}Am photopeaks, these values are not included in the average values, ** - bad low energy calibration leads to senseless values, $^+$ - one wafer is not connected on the n-side because of incomplete depletion resulting in increased dead area (see appendix E).

and extrapolation as plotted in figure 3.5. In the cases, where only one calibration point at 122 keV is available, the straight line between zero and the calibration point is used (dashed line).

The energy resolutions represented by the widths of the photopeaks show a broad distribution around 10 keV (1σ for the 122 keV line, figure 3.4 on the right)[¶]. Several factors are responsible for this behavior, including the inhomogeneous operating parameters between the front-end chips, varying quality of the strip detector wafers (especially obvious in the extreme differences in the depletion voltages), as well as surface effects on the wafers leading to areas with increased noise. An analysis of the noise is given below in chapter 3.3.3.

3.3.2.2 n-Side

As reported in [Schopper, 2002] the n-side shows nearly two times the noise of the p-side. This automatically translates into a higher noise threshold of around 60 keV which deforms or even cuts away the ^{241}Am line (59.5 keV). Since calibrating on the basis of one measurement point is unreasonable, a different method is used for the n-side. It takes advantage of the fact that the p-side and the n-side measure the same amount of charge, i.e. they are fully correlated. Consequently the n-side energy is derived by evaluating its correlation to the p-side (once the p-side is calibrated). This method matches the requirement of giving good correlations between p- and n-side as mentioned in chapter 3.2 per definitionem. Additionally the data basis for this method is comparatively large, since all measured data can be used instead of being restricted to dedicated calibration measurements of single-line sources.

The procedure starts with generating for each n-strip channel a histogram as shown in figure 3.6. It includes from all data sets[‖] only events which have exactly one signal on the n-side and one on the p-side. This ensures that no ambiguities appear and that there is at most minor charge sharing between strips. The filtered data are evaluated in the next steps: The range of sufficient statistics is determined, outliers are coarsely eliminated; for every n-signal histogram bin the mean of the p-energies is calculated; finally the values of groups with 16 bins are averaged into one value. An upper limit for the energy resolution can be gained by selecting a small energy range (for example 122 keV $\pm$ 10 keV) and fitting an Gaussian over the selected data.

The results for 122 keV is shown in figure 3.7, the channel-by-channel numbers are plotted in appendix E. The ADC bin numbers for an energy of 122 keV are in the same range as the p-side. The energy resolution is a factor 2–3 worse due to the higher noise as well as the fact that all uncertainties of the p-side calibration influence the n-side results.

3.3.3 Energy Resolution

Several mechanisms limit the energy resolution of semiconductor detectors as described in appendix C. When assembling and calibrating the instrument a significant contribution has been observed from not quantifiable noise sources. They result mainly from interferences with the environment due to imperfect shielding, grounding and crosstalk; for example:

- Due to the properties of the strip detectors used, the readout electronics need to run with their ground at bias potentials rather than instrument ground. This means that the n-side electronics have floating grounds with respect to the detector housing. The resulting severe

[¶] Bhattacharya et al. [2004] reported a value of 4.5 keV (1σ for the 122 keV line) for the TIGRE strip detectors.

[‖] To be precise the data sets including coincident data and calibration data for the tracker are used. Since the tracker is not read out in calibration measurements for the calorimeter, these files are useless here.

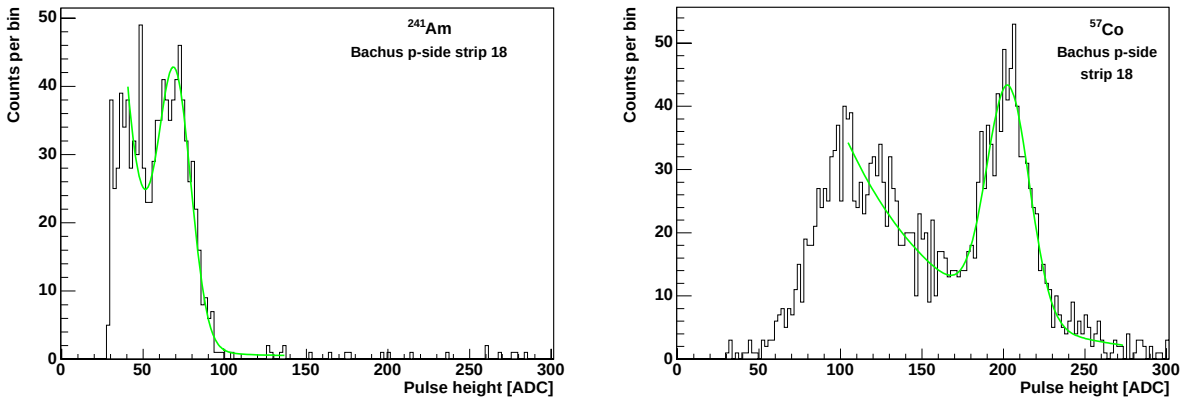

Figure 3.3: Example for a fitted tracker channel on p-side; left ^{241}Am, right ^{57}Co spectrum.

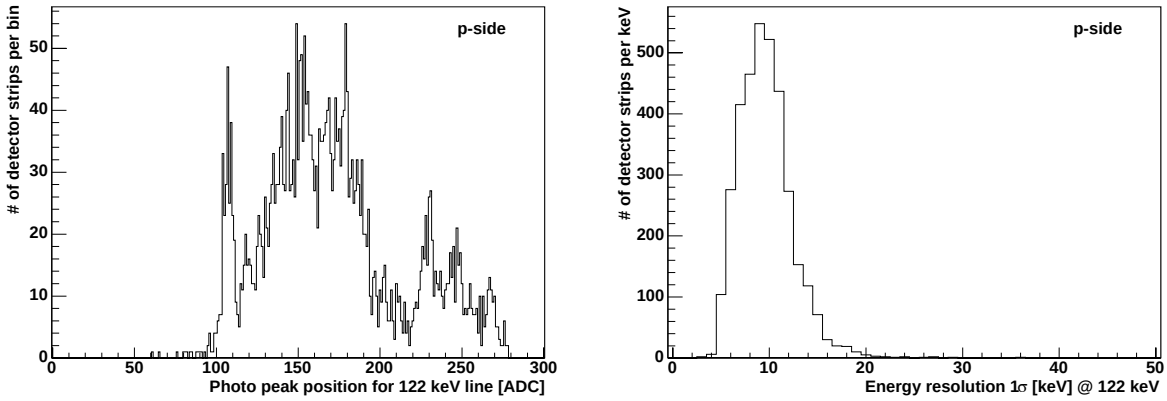

Figure 3.4: Distribution of photopeak positions (left) and energy resolutions (right) for the 122 keV line (^{57}Co) for the p-side tracker channels.

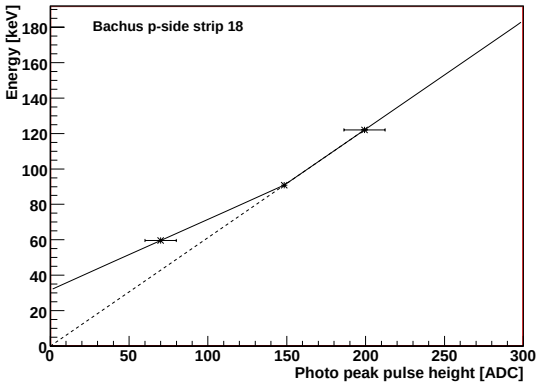

Figure 3.5: Result of an energy calibration on the p-side. The middle point is introduced artificially to account for non-linearities (see text). The error bars indicate the peak width ($\pm 1\,\sigma$).

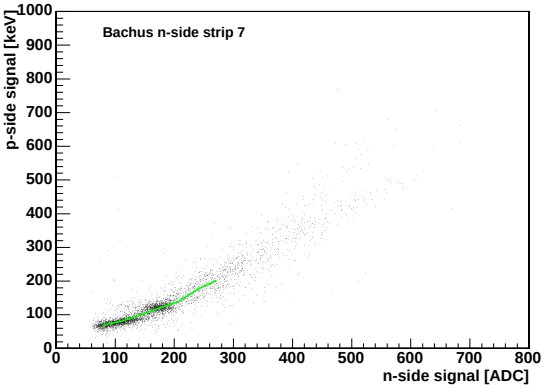

Figure 3.6: Scatter plot used to determine the correlation between the individual (uncalibrated) n-side strips and the (already calibrated) p-side. The green line indicates the calibration result. Above a value, where the statistics gets low (here $\gtrapprox$ 270 ADC), the algorithm stops to avoid false values.

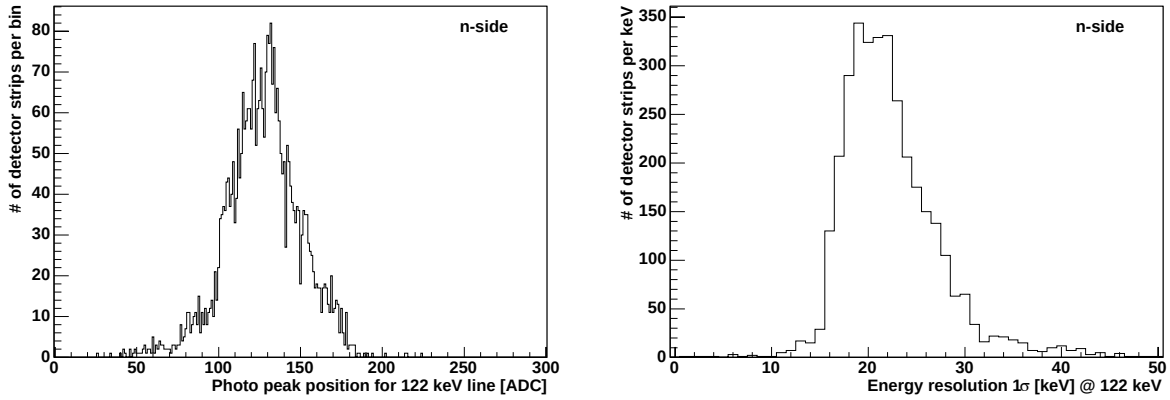

Figure 3.7: Distribution of photopeak positions and energy resolutions for the 122 keV line (^{57}Co) for the n-side tracker channels. Due to the calibration method, the n-side energy resolution values are only upper limits.

complications of the ground concept could be significantly reduced by properly placed noise suppression capacitors, but not completely eliminated.

- A separate setup for debugging the electronics of defective detector units never could be used to measure a spectrum due to interferences.
- Problems occurred while assembling the cable harness between the tracker layers and their dedicated repeater cards (compare chapter 5.2). The flat band cables of the various layers needed to be stacked in a way that lines with the same functionality lie on top of each other. Otherwise increased noise due to cross talk was observed in spite of a aluminium foil covering each cable individually.
- On the analog output of the front-end chip switching edges during operation of the VME bus can be observed.

A systematic problem arises from the two facts that the whole tracker stores in the FEE's sample-and-hold stages the current pulse heights at the same time (there is only one common HOLD signal for the whole tracker), and that only the p-side triggers are used. Thus the shaped pulse of a given n-side channel is not held (i.e. sampled) always in the same phase of its shaped pulse (because the timing is derived from a p-side channel which triggered, and of course this is not always the same p-side channel — thus the timing varies). This additionally smears out the n-side spectra.

A large fraction of the induced noise is eliminated by subtracting the common mode, i.e. the mean of the signals from a front-end ASIC after offset subtraction. This way the noise components seen by all channels (e.g. cross talk on the chip's supply lines) can be almost completely eliminated. Histograms of the resulting values for one p- and one n-side chip are shown in figure 3.8. That the induced disturbances on the n-side are larger is typical for all layers and results from the grounding concept ("floating" n-side grounds as described in chapter 5.2.2). The shift of the distribution by few ADC units in negative direction for both p- and n-sides can be explained by the crosstalk of the trigger pulses onto the first two or three channels of each chip: The readout in the initialization phase, during which the base line of each channel is determined, is triggered by the readout electronics, i.e. there is no correlated trigger. During the actual measurement every readout is triggered and crosstalk (e.g. from the trigger signal onto the analog signal) occurs shifting the common mode distribution. In order to get an overview over the common modes of the various layers, figure 3.9 shows the rms (as measure of the widths) of the distributions. The importance of this correction becomes obvious when the gain in the order of 1 $\frac{\text{keV}}{\text{ADC}}$ (compare figure 3.4 and 3.7) is

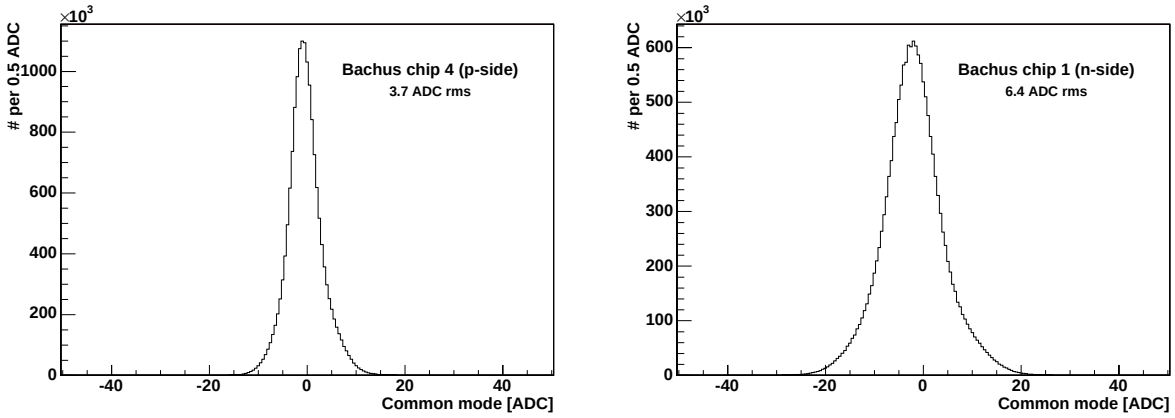

Figure 3.8: Examples for common mode distributions on p- (left) and n-side (right) for one sample chip each.

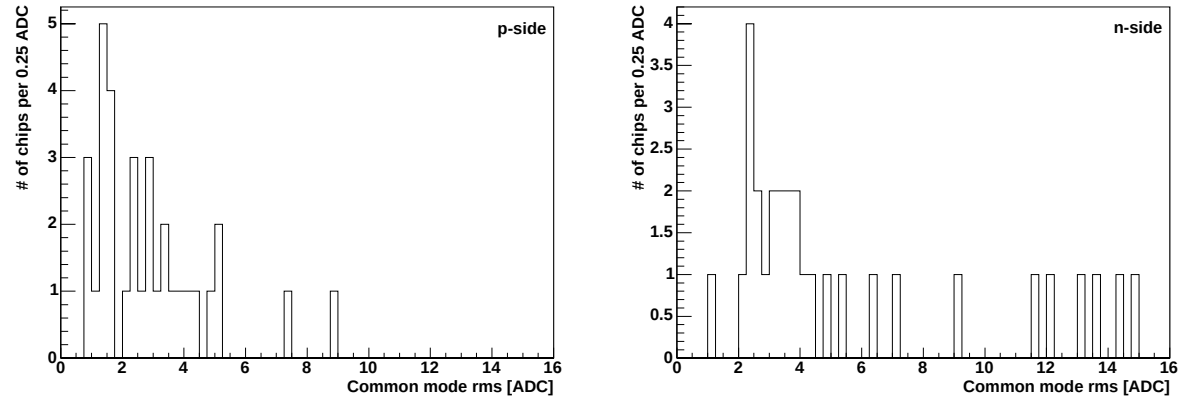

Figure 3.9: Spread of the widths of the common mode distributions for all p-side (left) and n-side (right) chips.

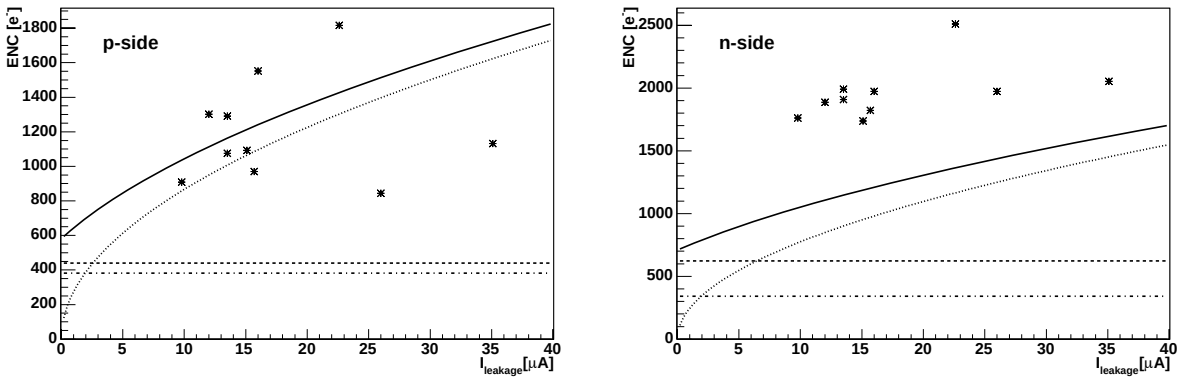

Figure 3.10: Average noise values in equivalent noise charge (ENC) in dependence of the leakage current for the p- and n-side of various tracker layers (data points). The lines show the expected values: the dotted one indicates the contribution of the leakage current, the dashed line the preamplifier noise, the dash-dotted line the (bias) resistor noise, and the solid line the square sum of these. A capacitance of 45 pF on the p-side and 75 pF on the n-side taken from measurements is used for calculating the preamplifier noise. That the p-side measurements show lower values than expected is due to a selection effect (see text).

taken into account. Without common-mode correction the energy resolution would be broadened by several keV.

There is another systematic problem connected with the common mode that arises in the context of the trigger mechanism: The trigger threshold is an external voltage applied to the the front-end

ASIC which is compared to the output of the shapers. Since the threshold voltage is not influenced by the common mode fluctuations, the actual trigger threshold varies. Moreover, the timing is smeared out (time-walk) and for large (positive) common modes the trigger threshold can even be lower than the noise threshold (events may show no hits in triggered detectors).

For all these reasons, the noise due to leakage currents and due to the preamplifier constitutes a lower limit on the overall noise. The measured noise (in equivalent noise charge ENC) is shown in figure 3.10. The expected numbers are calculated according to equations 5.1 and 5.2; the capacitances of the strip detectors are taken from Schopper [2002] (i.e. $3 \times 15\,\mathrm{pF}$ on p-side and $3 \times 25\,\mathrm{pF}$ on n-side). The noise is plotted against the leakage current (the given values are for a whole layer) with the associated noise calculated under the assumption that the current of the layer spreads homogeneously over the strips (i.e. it is divided by 384 to obtain leakage current per strip). The measured values (averaged over the whole layer) are derived from the baseline fluctuations of a readout channel according to equation C.1.

On the p-side the measurement appears to be inconsistent with the prediction since many layers show less noise than expected. This can be explained by two effects. The first arises from a selection: because very noisy strips cannot be calibrated, and thus their noise cannot be expressed in ENC, these channels do not contribute to the mean noise. The second effect is due to the fact that there is a current flowing over the guard ring structure and the detector edges which is measured as bias current. Hence the leakage current is lower than measured.

On the n-side a large gap between the observed and calculated values is obvious which is, as reported in [Schopper, 2002], due to an unknown noise source intrinsic to the detector. It is suspected that the biasing method via punch-through structures on the detector wafer causes an additional noise contribution on the n-side.

Besides the electronic noise described above in terms of ENC, the charge generation statistics and charge collection efficiencies also contribute to the energy resolution of the detector (equation C.2). Adding up the individual components (for the mean p-side values listed in table 3.1: $\Delta E_{leakage\,current} = 4.22$ keVrms, $\Delta E_{preamp} = 1.58$ keV rms, $\Delta E_{bias\,resistor}$ negligible for reasonable resistances, $\Delta E_S = 660$ eV rms for the statistical charge generation of a 122 keV signal, and a negligible contribution from the charge collection) gives 4.57 keV rms which is significantly lower than the determined average of 9.7 keV rms. Thus systematic uncertainties play a major role in the energy resolution of the tracker.

The individual strips of one layer exhibit a wide variation in their energy resolutions (figure 3.4, 3.7 right). The spread originates from the detector, presumably from defects and impurities of the surfaces which are localized and affect neighboring strips (compare appendix E)*. It is worth mentioning here that noisy strips on the p-side do not show up in most plots since the triggers of noisy channels are blocked! These blocked p-side channels show very few signals†, thus they are treated as defective and do not appear in the figures. Such a selection effect cannot take place on the n-side channels since all n-side triggers are deactivated due to the large common-mode and noise.

Since the energy resolution of the p-side is significantly better than that of the n-side, the energy information is taken from the p-side. Only in the case of an overflow on the p-side the n-side energy information is used (if not also in overflow).

---

*In the tests of the front-end electronics (before they are connected to the detectors) the individual channels show homogeneous noise characteristics.

†The only way for measuring a signal from a blocked p-side channel, is if a coincidence occurs between a signal over the noise threshold in this channel and another triggering channel. This is a rare condition especially for calibration measurements.

3.3.4 Dynamic Range

The lower limit of the dynamic range is determined by the noise and trigger thresholds. The noise threshold is set by the data acquisition software to six times the rms of the baseline fluctuations. This limit is calculated in an initialization phase at the beginning of every measurement and in housekeeping phases during measurements (appendix E shows the channel-by-channel values). The distribution of the noise thresholds (figure 3.11, layer-by-layer averages included in overview table 3.1) appears to be split into two parts, below and above $\sim$ 40 keV (50 keV) on p-(n-)side. This is an effect originating from the energy calibration — the channels with threshold values in the lower part had no usable peak in the ^{241}Am spectra (59.5 keV), and the calibration delivers too low values as a consequence of the effects discussed in chapter 3.3.2.1. Of course this effect translates to the n-side when the majority of channels lacks the ^{241}Am peak, as it is the case for the layers "Ikarus" and "Odysseus".

Besides the noise threshold, which is set in hardware, the trigger threshold of the hardware limits the dynamic range. If no energy deposit exceeds this threshold, no readout takes place (chapter 5.1): The level discriminator in the FEE compares an externally applied voltage level with the output of the shaper. Since especially the strip detectors show a large common-mode component, as explained above, the trigger levels vary with respect to the base of the signal. This smears out the low-energy cutoff in the spectra. Consequently no "hard" value can be determined for the trigger threshold. In the overview table 3.1 as well as in figure 3.12 a lower limit is given. Even worse, it is possible that the noise threshold determined in the detector initialization phase exceeds the trigger threshold (when the common-mode is such that the trigger threshold is very low). This results in spurious events where a chip has triggered and started a readout but no corresponding signal has been found in the chip.

The other end of the dynamic range is determined by saturation effects. In spite of a series of bottle necks while transferring the analog signals along the readout chain to the ADC modules (compare chapter 5.2) the electronics is adjusted such, that the upper limit for a signal is defined by saturation effects in the TA1 front-end chip. However, it cannot be excluded that a small fraction of channels, which show large baseline offsets, saturate at a point further down the chain. Apart from the offsets, the spread of the operating parameters such as the amplification factor has a large impact on the overflow values as can be seen in figure 3.13 where the maximum measured signals during the HIGS campaign of each individual tracker channel are histogrammed. Again some splitting into groups of channels (i.e. the chips) can be observed like for the photopeak positions. The group of p-side channels showing overflow values below 100 keV are either channels with a bad energy calibration or channels which are blocked early after the first calibration measurements. On the n-side a few channels show only low, spurious signals. These account for the overflow values below 100 keV on the n-side. The group of n-side channels around 300 keV results from the tracker layer "Neptun". Its chips saturate already at lower levels than others. Compare the uncalibrated saturation point shown in figure E.4 with the corresponding gains shown in figure E.6). The reason for this behavior is unknown; presumable it is an electronics problem in setting the operating parameters of the chips. Anyhow the overflow numbers should be taken with some care since extreme extrapolations needed to be done while converting from the units of the ADCs to energies.

Overall the dynamic range covers the important range around one MIP (minimum ionizing particle, chapter 1.1.6, traversing 0.5 mm silicon resulting in an energy deposit of $\sim$ 0.2 MeV).

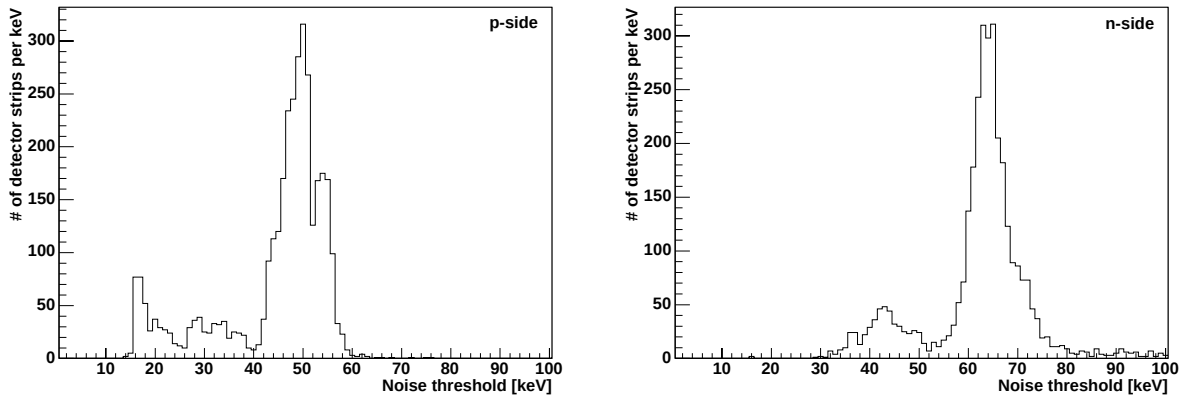

Figure 3.11: Distribution of noise thresholds for the p- (left) and n-side (right) channels. The entries below $\sim$ 40 keV (50 keV) on the p-(n-)side results from a bad low energy calibration, see text.

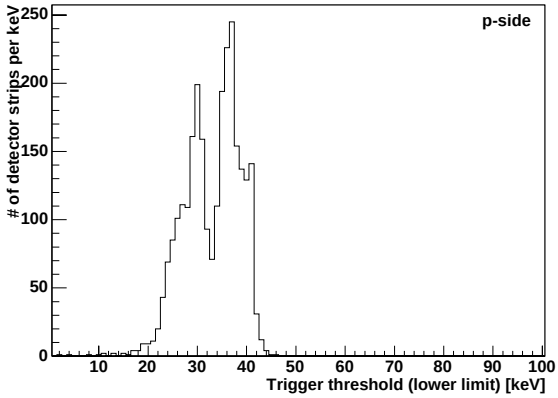

Figure 3.12: Distribution of the trigger thresholds

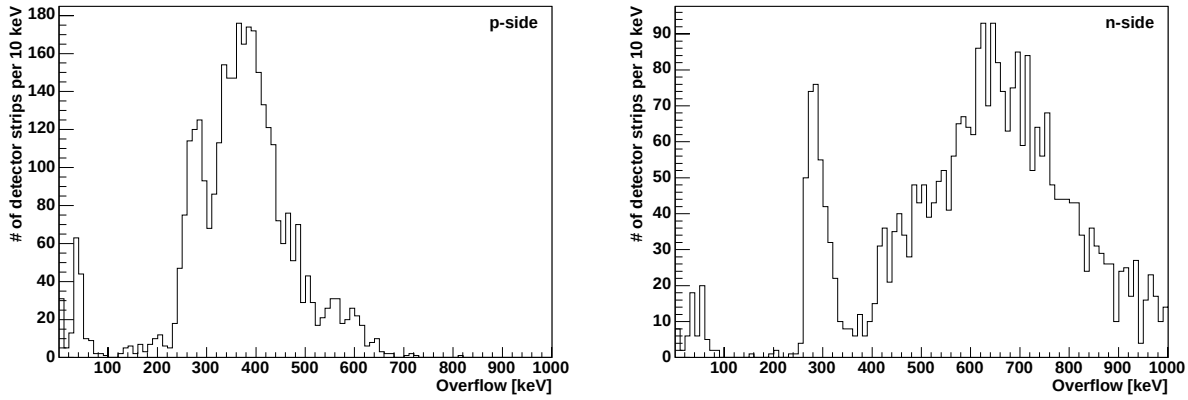

Figure 3.13: Distribution of the overflows for the p- (left) and n-side (right) channels. For the entries below $\sim$ 100 keV an the group of n-side channels around 300 keV, see text.

3.3.5 Spatial Calibration

The charges generated by an event can be distributed over two or even more strips. This provides the possibility of determining the point of interaction with higher precision than the strip pitch. Adjacent strips showing signals are combined to clusters. Within such a cluster an interpolation between the strips can be done using either the center of gravity or the so-called η-method, as discussed in Schopper [2002]. The achieved spatial resolution is published in Bloser et al. [2003]; the measured position resolution is 290 μm FWHM as derived from muon tracks (figure 3.17).

If there is more than one hit in one detector layer, it is ambiguous which p- and n-side signals belong together. In principle, this problem is solved by searching for the combinations with the best-matching energies [Schopper, 2002]. This is especially important for reconstructing pairs. A more sophisticated approach has been implemented by Zoglauer [2005]. It takes into account additionally that neighboring strips (or even the same strip) could have signal contributions either from a single interaction or from two interactions. For either method of matching p- and n-signals, the energy information is — on a single-layer level — the *only* available indication for the correct combination. Considering the whole tracker, higher level methods can use information such as the track geometry to find the particle's path through the detector [Zoglauer, 2005].

3.3.6 Shaping Time and Time Resolution

The time resolution of a detector is closely connected to its shaping time and the trigger mechanism. Shorter shaping times result in an improved time resolution, but also in a degraded spectral resolution. In the present prototype the spectral performance is emphasized in the tracker as the calorimeter is inherently slower than the tracker due to its crystal's time constant. The rise times of the strip detectors (their measurement is described in chapter 5.1.6) are 2.5 ns and 2.0 ns on p- and n-side respectively (figure 3.14, channel-by-channel appendix E). The wide spread of the values are again due to the varying operating conditions of the front-end chips (compare table 3.1 and appendix E).

Due to the trigger mechanism of the front-end electronics (chapter 5.1) the time resolution is limited by time walk. The trigger time can be delayed by the full rise time, however, for most detector signals the delay will be shorter. A time resolution measurement with a tagged source (^{60}Co) has been performed. The measurement setup is described in chapter 7.1.2. The FWHM of the time spread in the tracker (figure 3.15) is 0.33 μs, but there is a tail towards late trigger times extending up to 4.5 μs.

3.4 The Stack of Layers

The 11 layers are stacked up and switched together (i.e. read out simultaneously) to form the tracking detector.

3.4.1 Compton Scatter Events in the Tracker

It is illustrative to plot the spectral data of a ^{57}Co measurement in two ways (figure 3.16). In the left plot every measured interaction is counted separately, in the right one simultaneous energy deposits are summed up. Comparing both plots shows the following: The entries at small energies (below 30 keV) disappear, i.e. they are signals below the trigger threshold, which is around 50 – 70 keV, but above the noise threshold (which is as low as $\sim$ 15 keV for some strips). It is very likely that these signals are noise excesses which did not trigger the readout (in the plot of the

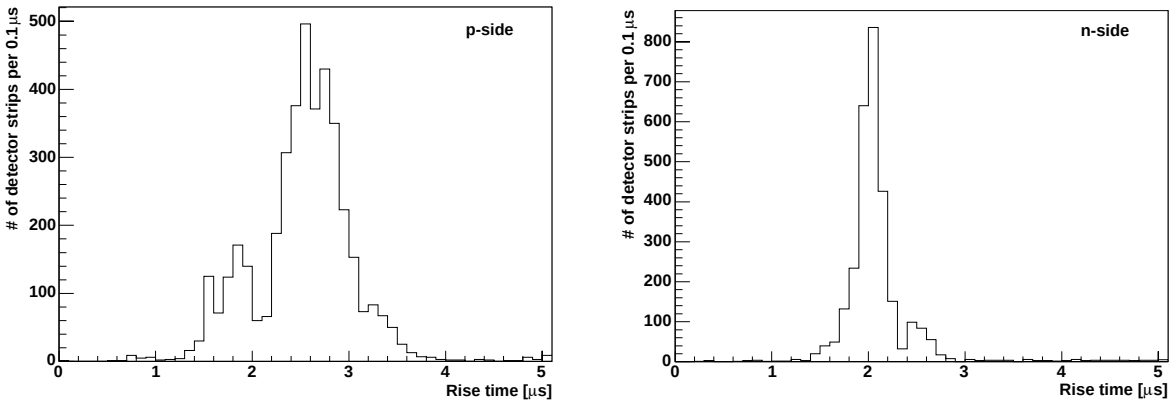

Figure 3.14: Rise times of the shaped pulses.

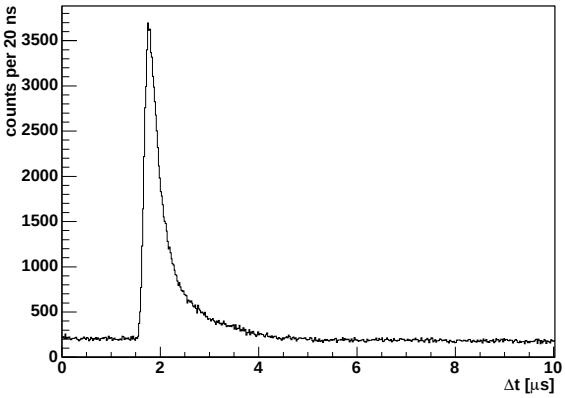

Figure 3.15: Time resolution of the strip detectors measured with a tagged source. The peak has a width of 0.33 μs FWHM. The notes on the measurement given in chapter 9.3 apply as well here.

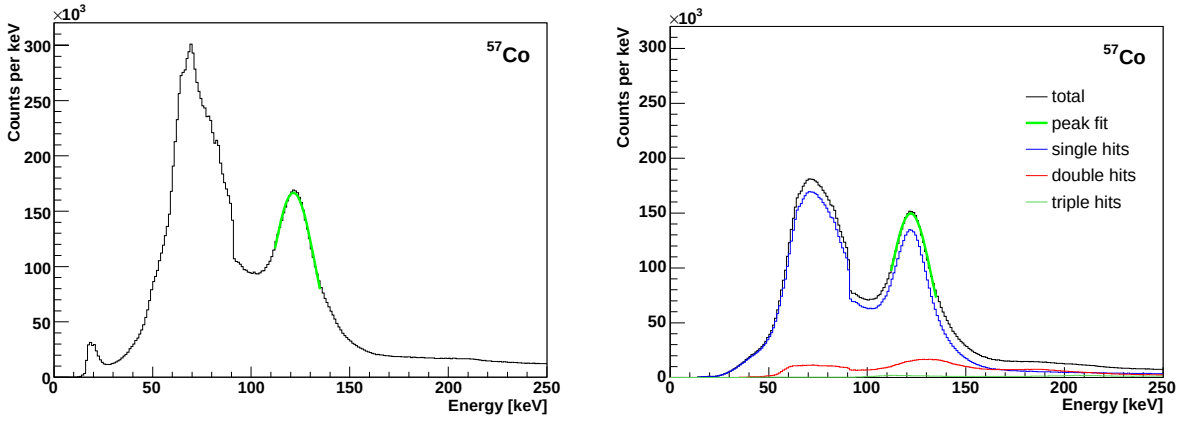

(a) each interaction taken into account individually

(b) coincident interactions summed up

Figure 3.16: Calibrated ^{57}Co spectrum taken with the full tracker including the complete set of ^{57}Co calibration measurements. In case (a) the energy of every hit is added individually, i.e. without respect to any other hit in the event. The peak position is 121.5 keV and its width 11.0 keV (1 σ). In case (b) the sum of the energies in one event is filled in and the overall, single, double, and triple hit spectrum plotted. The (overall) peak position is 122.1 keV and its width 10.7 keV (1 σ).

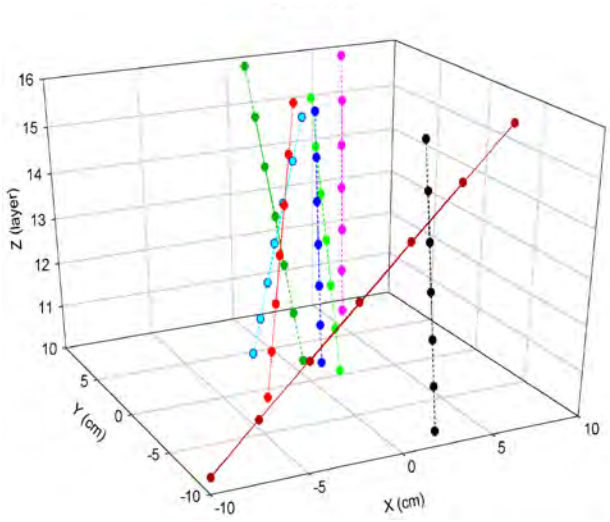

Figure 3.17: Muon tracks (from an early measurement with seven layers), figure from [Bloser, 2002]

summed energies, these events are almost gone). These spurious hits and chance coincidences are responsible for the shift to higher energies by $\sim$ 50 keV and broadening of the photopeak in the double spectrum. The individual energy resolutions average to an overall resolution which is 11 keV for the 122 keV line. The peak positions and resolutions differ marginally between the two spectra since the single hits clearly dominate the photopeak. Background events (especially the ^{40}K line at 1.46 MeV) contribute to the energy deposits above 170 keV.

3.4.2 Tracking Capability

The tracker's capabilities to trace individual charged particles is shown most easily by recording muon tracks (figure 3.17). Reconstructing the paths of single and multiple charged particles not moving in a straight line from the measured interaction points and energies is a challenging task especially in case of Compton scatters, but also for pair creations. The algorithm implemented by Zoglauer [2005] achieves better than 70% correctly reconstructed tracks, for tracks with 7 or more interactions the efficiency is around 90% as evaluated for the baseline satellite geometry. Also the pair recognition efficiency is above 70%.

3.5 Possible Improvements of the Calibration

The main problem in calibrating the strip detectors of the prototype are the non-linearities of the front-end electronics. These could not be accounted for very well during the Duke campaign. Thus the biggest improvements could be achieved with additional calibration points:

- The low energy range of the calibration suffers from the non-linearities of the front-end electronics. This is even worse if the 59.5 keV line of ^{241}Am is close or below the (trigger) threshold so that it cannot be evaluated. An additional calibration source such as ^{109}Cd (88 keV) would improve the situation.

- For energies above 122 keV the calibration needs to extrapolate. Muons would deposit an energy of $\sim$200 keV if they cross one layer (0.5 mm) of the silicon tracker. If the muons are sorted by their incidence angle, a calibration could probably be derived. Also, blocked

channels could be calibrated since one trigger already starts a readout. In case of the measurements at the HIGS facility the dataset is too small since a dedicated muon measurement has not been performed and the background measurements do not contain enough muon data.

All mentioned calibration methods with muon tracks suffer from the fact that the fastest triggering channel starts the readout. Since the timing of the readout is a conceptual weakness of the prototype due to the time-walk problem (chapter 5.1.6), this will add an additional broadening. However, for calibrations with muons this effect will be low, since muons generate large signals which only have small time-walks.

For a future instrument, the necessity of improved detectors and much more advanced front-end electronics is obvious. Possible hardware improvements are described in detail in chapter 10.

Chapter 4

The Calorimeter

In the case of Compton interactions in the tracker, the calorimeter measures the energy and interaction position of the Compton-scattered photons leaving the tracker. Even for high-Z materials, the cross section for photoelectric absorption of photons becomes negligible above ~ 1 MeV compared to the total cross section. The most probable interactions are Compton scatters (until pair creations start dominating at several MeV) which result in events with more than one energy deposit in the calorimeter (ideally the last is a photoelectric absorption). For a compact detector such as MEGA the individual interactions need to be resolved. Resorting to the center of gravity of the deposited energies would lead to large angular uncertainties in the reconstructed event, because the distance between tracker and calorimeter is short (in contrast to COMPTEL which was briefly described in chapter 1.2.4). An Anger camera cannot easily resolve multiple simultaneous interactions in contrast to a pixellated detector. When measuring position and energy deposit for the individual interactions, their sequence must also be known to allow correct interpretation of the event. Since the time resolution of common high-energy detectors is far too coarse for sequencing by measured interaction times, software algorithms need to reconstruct the correct sequences afterwards using kinematical considerations. Zoglauer [2005] describes in detail the algorithms used for the prototype; a brief summary is given in appendix I.1.

In the case of pair creation events the position resolution of the calorimeter is less important. It helps to extend the electron/positron track from the tracker into the calorimeter, but the direction of the incoming photon is reconstructed from the first track elements of electron and positron only. Again, details of the algorithm are given in Zoglauer [2005]. Instead the calorimeter is used to determine the total energy of the photon requiring a high stopping power, i.e. the calorimeter needs to be thick (more than $50\,\mathrm{g/cm^2}$ of a high-Z material).

4.1 Design

The calorimeter of the prototype is divided into 20 blocks of three different sizes. Each block contains 120 CsI(Tl) crystal sticks which have a footprint of $5 \times 5\,\mathrm{mm^2}$ and vary in length from 2 cm to 8 cm (figure 4.1 and 4.2). The crystal surfaces are covered with reflective paper* to minimize light loss at the crystal surfaces. A 10×12 PIN-photodiode array† is optically coupled to the crystals by transparent silicone. In order to avoid crosstalk the coupling silicone is separated with a white silicone grid matching to the crystal spacing and diodes. Three versions differ in the length of the crystals. Eight blocks have 2 cm long crystals and another eight blocks have

*The crystals are separated by 3 – 4 layers of Millipore filter paper.

†fabricated by Hamamatsu Photonics, Japan, custom design

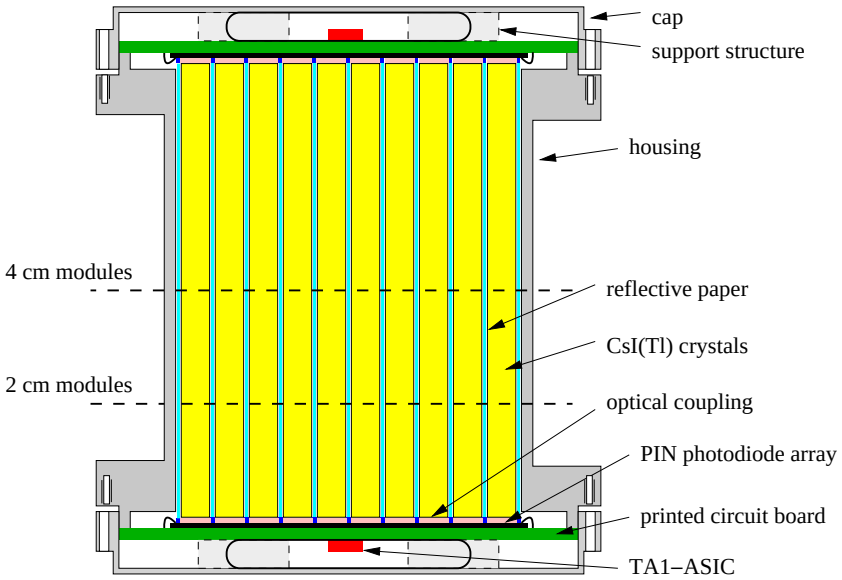

Figure 4.1: Schematic view of a 8 cm calorimeter block having readout electronics on both sides. The shorter 4 cm and 2 cm versions have readout on one side, on the other side the crystals are covered with reflective paper and the housing is closed.

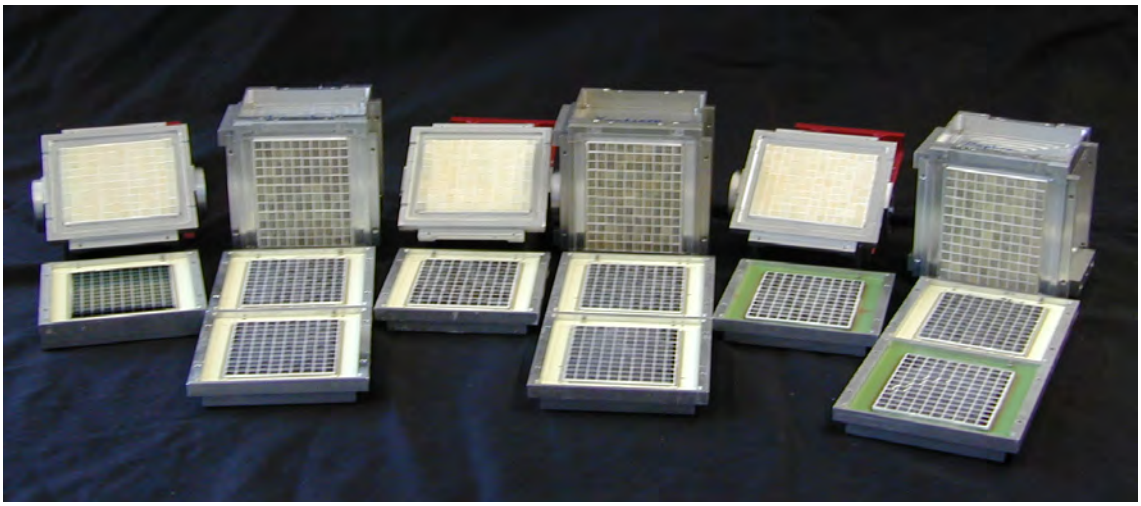

Figure 4.2: A sample of calorimeter blocks before mounting their caps which include the diode arrays and the front-end electronics.

4 cm crystals. They form the side walls of the calorimeter, the 4 cm blocks the lower half and the 2 cm ones the upper half (figure 2.2 left and figure 2.3). The readout array and front-end electronics are oriented towards the outside of the prototype. The third version has 8 cm long crystals. Four of these blocks are mounted below the tracker. Due to the length of these crystals position-resolution capability along the crystal is required in order to avoid large errors in the direction of the Compton-scattered photon. Therefore the 8 cm blocks are read out on both ends of the crystals. This allows to reconstruct the depth of interaction from the distribution of the light between both ends.

Due to the coupling method the mechanical structure needs to be stiff so that a high contact pressure can be achieved for coupling the crystals to the diode arrays. Approximately 40% of the mass of a block is passive material.

Further details concerning the design and manufacturing of the calorimeter blocks are described in Andritschke [2000] and Schopper [2002].

4.2 Characteristics of the PIN-Diodes

While characterizing the calorimeter, the properties of the silicon PIN-diodes (especially the electronic noise) can be determined separately from the complete detector with coupled crystals. Therefore measurements with an ^{241}Am source have been performed. The photon energy of 59.5 keV is below the detection threshold in the crystal; only conversions in the diodes are read out. Thus the diodes can be characterized separately even if the calorimeter blocks are mounted. From those measurements the gains of the front-end electronics channels are evaluated with the same algorithms as the tracker channels (appendix D). The photopeak positions (a measure for the gains, figure 4.3) vary widely as it is also the case for the tracker channels. The larger variations occur between the individual front-end chips (compare appendix F) which reflects the differing operating conditions of the individual chips due to their interconnection (chapter 5.1.5). The corresponding peak widths (energy resolutions, figure 4.4) cluster around 1.5 keV($1\,\sigma$) with some outliers above 2.5 keV($1\,\sigma$). Several components contribute to the energy resolution, as there are three sources of electronic noise, fluctuations in the number of charges (equation C.2), and systematic components as discussed in the following:

- The main contributor to the electronic noise (figure 4.5) is the preamplifier (equation 5.1[‡], detector capacitance $C_T = 15\,\mathrm{pF}$ as given by the manufacturer).
  Another contributor to electronic noise is the leakage current of the PIN photodiodes. Only the sum of the currents of the 120 diodes in an array can be measured. The results are listed in tables 4.1 and 4.2. The values exhibit a wide spread, but there is a group of wafers showing currents between 13 and 25 nA and a group at several hundred nA. The ones showing high currents are degraded due to the necessity of un- and remounting the diode arrays few times (due to electronics and other hardware failures). Only considering wafers without any connected defective diodes, the leakage current per pixel is around 84 – 210 pA.
  Finally, the noise contribution due to the biasing resistors ($\sim 500\,\mathrm{M\Omega}$) is negligible.
  The overall measured electronic noise (in equivalent noise charge) is between 240 and 300 e^-rms. Those detectors showing high leakage currents exhibit lower noise than expected, which is a selection effect: Most of the leakage current is flowing in one (or a few) defective pixels which are excluded from analysis and do not contribute to the measured average noise.

[‡]The shaping time constant is adjusted to the maximum value of $\approx 3\,\mu$s in the front-end chips. In the datasheet of the TA1.1 chip the preamplifier noise is only given for 1 and 2 μs. The tabulated values have been coarsely extrapolated to $ENC_{preamp} = (150 + 5.5 \times C_T[\mathrm{pF}])\,e^-$rms for the calculations here.

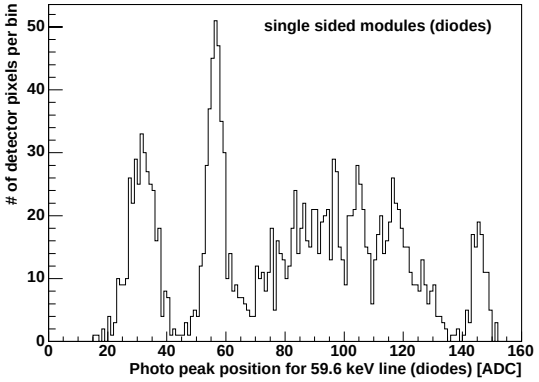

Figure 4.3: Distribution of photopeak positions for the 59.5 keV line of ^{241}Am

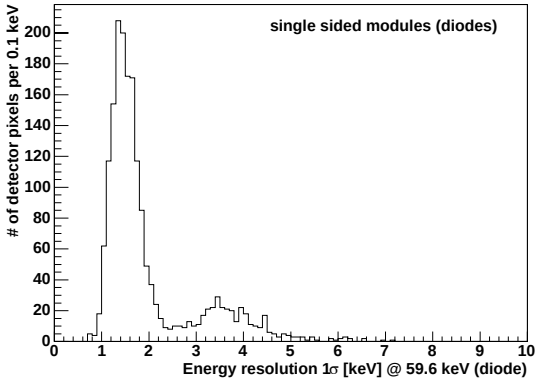

Figure 4.4: Distribution of peak widths for the 59.5 keV line of ^{241}Am

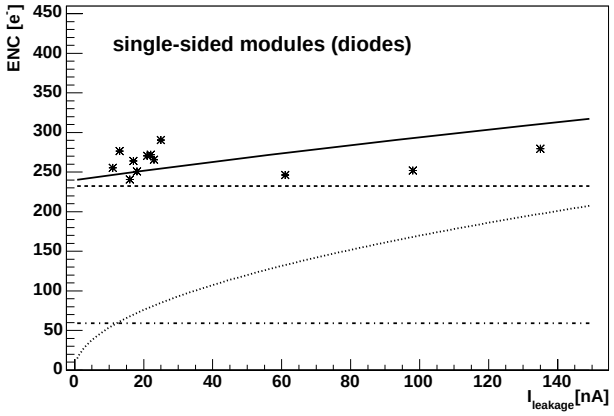

Figure 4.5: Electronic noise in equivalent noise charge (ENC) in dependence of the leakage current. The data points show the measured noise averaged over the channels of a diode array. The lines show the expected values: the dotted one represents the contribution of the leakage current, the dashed line the preamplifier noise, the dash-dotted line the (bias) resistor noise, and the solid line the square sum of these. The data points lying below the expectation result from a selection effect (see text).

- The contribution of the fluctuating number of generated charge carriers (Fano noise, $W_S/2.35 = 44\,e^-$rms according to appendix C.2 for 59.5 keV photons) is negligible here.

- The difference between the measured ($\sim$ 1.5 keV) and the expected (0.9 – 1.1 keV) peak widths results mainly from systematic errors introduced by the electronics. Here the arguments given for the p-side of the strip detector in chapter 3.3.3 hold analogously for the PIN diodes.

4.3 Calibration of Individual Crystals

The combination of a crystal coupled to a read out PIN diode of the monolithic diode array is characterized in terms of its gain, energy resolution, dynamic range, light yield, and time resolution. In case of the crystals of the bottom calorimeters with double-sided readout also the position resolution along the crystal axis is determined. Efficiencies of the calorimeter pixels could not be

determined since the readout in the special mode required[§] is already saturated by background (room background and electronic noise), resulting in 100% dead time (the evaluation of the life time would be impossible or at least very error-prone)[¶].

The calibration data for the presented results are taken in the fully integrated state of the prototype for the same reason as mentioned for the tracker (chapter 3.3.2), namely the high sensitivity of the operating parameters (especially the gain) of the front-end electronics on temperature. The individual channels of the calorimeter blocks are calibrated by exposing them to the radiation of the two radioactive laboratory sources ^{137}Cs and ^{22}Na (appendix A) and reading out after every trigger[‖]. The sources are placed at the four corners of the calorimeter. This reduces the shading (appendix F.3) of the lower side walls onto the bottom modules.

Since 1920 channels with single-sided readout and 480 with double-sided readout need to be evaluated, automatic procedures were developed. It is necessary to process each readout channel individually, because the number of entries in the spectra vary widely, the optical couplings are inhomogeneous, the front-end electronics are non-linear, and the offsets, gains, and thresholds vary between the readout channels. All this is taken into account in the calibration algorithm described in appendix D. Three peaks (662, 511 and 1275 keV) in the spectra provide three calibration points which allow for some correction of the non-linearities in the front-end electronics (chapter 5.1.6).

4.4 Characteristics of Crystals with Single-sided Readout

The gain is determined from photopeak positions. Fitted example spectra of the two calibration sources are shown in figure 4.6. The photopeak positions (figure 4.7) vary widely due to several reasons:

- The quality of the optical coupling between the crystals and the PIN-diode-array is inhomogeneous. Slightly different crystal lengths and hand-crafted silicone coupling grids lead to different contact surfaces influencing the light collection.
- The crystal wrapping with reflective paper determines the loss of scintillation light. It is hand-crafted and its properties, as well as those of the crystal surfaces vary.
- The front-end chips have widely varying operation parameters (chapter 5.1.5).

The three calibration points result in a calibration curve as shown exemplary in figure 4.8. They do not lie on a straight line due to the non-linearities of the front-end electronics (chapter 5.1.6). The three points are interpolated by a spline (interpolation with a polynomial of third order) because a simpler linear interpolation results in steps in the calibrated spectra at points where different slopes of the interpolation lines join. For energies below 511 keV linear extrapolation from the 662 and 511 keV calibration point is used, for energies above 1.275 MeV a linear extrapolation from the point of origin and the 1.275 MeV calibration point is applied (dashed line).

[§]For the measurements discussed here the detector is in calorimeter readout mode, where *every* trigger of the calorimeter starts a *full* readout.

[¶]Dedicated measurements with only a subset of the calorimeter, e.g. one block, could be performed where background does not already saturate the readout. With the current setup which records the dead time such a measurement has not been done due to timing constraints — especially at HIGS.

[‖]A trigger here is given by any interaction in the calorimeter, of course no coincidence with the tracker is required.

detector name	crystal length	leakage current [nA]	ENC [e^-]	light yield e^-/keV	σ [keV] @ 662 keV	noise threshold [keV]	trigger threshold [keV]	saturation [MeV]	defective pixels	rise time [μs]
Aetna	4 cm	61	247	15.2	50.5	255±36	327	5.7	11	3.5
Antigone	2 cm	13	277	17.2	37.1	169±35	301	3.9	3	4.9
Ariadne	4 cm	98	252	18.1	37.7	129±39	313	2.9	11	5.1
Circe	2 cm	16	241	17.9	39.4	255±27	367	4.7	4	3.8
Diana	2 cm	11	256	19.1	36.1	134±36	228	2.5	4	5.0
Europa	2 cm	17	264	17.4	38.1	163±30	236	2.4	7	4.5
Fortuna	4 cm	21	270	13.8	40.9	168±58	276	2.9	14	4.9
Helena	4 cm	530	267	19.2	34.6	171±28	276	2.8	13	4.0
Hydra	4 cm	530	269	17.2	41.0	209±31	331	4.5	11	3.8
Medusa	4 cm	22	272	14.6	39.4	211±43	246	4.4	14	4.5
Minerva	2 cm	135	279	21.1	28.5	115±27	238	3.3	11	4.5
Pallas	2 cm	23	266	16.6	38.2	154±44	335	5.1	5	5.5
Penelope	4 cm	380	438	16.9	34.0	176±28	295	3.2	13	4.8
Persephone	2 cm	25	290	15.5	42.2	188±42	278	2.5	13	4.3
Thetis	2 cm	18	251	17.3	36.0	240±32	323	4.2	8	4.4
Venus	4 cm	400	256	18.9	33.6	156±28	353	3.7	12	4.5
Average		144	275	17.3	38.0	181±54	301	3.7	9.6	4.5

Table 4.1: Performance of the 16 calorimeter blocks with single-sided readout at $\approx 12°$C. Leakage currents: sum of the currents of all pixels of a block, ENC: measured equivalent noise charge (block-by-block average), light yield: number of electrons measured in a readout diode per keV energy deposit in a crystal (block-by-block average),σ = energy resolution (1 standard deviation, block-by-block average), noise threshold: the values are given including their rms as measure for the width of the threshold distribution (block-by-block average).

The dynamic range is constrained by the noise thresholds and the overflows which are shown in figure 4.9. The detector-by-detector average is listed in table 4.1. On average, the noise threshold of the calorimeters with single-sided readout is 181 keV and the overflow 3.7 MeV. Since these values are calculated using extrapolation from calorimeter calibrations at intermediate energies, they should be taken with care given the non-linearities of the front-end electronics.

The light yield allows to compare the collection efficiencies of the scintillation light. It describes the number of photoelectrons generated in the diodes per energy deposit in the crystal. Two numbers need to be known, the signal amplitude of a defined energy deposit in the crystal determined with ^{137}Cs, and the calibration factor between the signal amplitude (which is given in analog-to-digital converter units) and the number of generated (photo)electrons determined with ^{241}Am. The interaction of a 59.5 keV photon of the ^{241}Am source deposits a defined amount of charge (16500 electrons) in the PIN diode (not measurable in the crystal because the energy threshold is too high) so that the light yield could be determined using the ^{137}Cs measurement by

$$Y = \frac{S(^{137}\mathrm{Cs})}{E_\gamma(^{137}\mathrm{Cs})} \cdot \frac{E_\gamma(^{241}\mathrm{Am})}{S(^{241}\mathrm{Am})} \cdot \frac{1}{E_{e-h}} = \frac{S(^{137}\mathrm{Cs})}{S(^{241}\mathrm{Am})} \cdot 25 \frac{e^-}{\mathrm{keV}}$$

with $S(\ldots)$ the signal amplitude in ADU, $E_\gamma(\ldots)$ the corresponding line energy, and $E_{e-h} = 3.6\,\mathrm{eV}$ the average energy to generate an electron–hole pair in the semiconductor.

According to figure 4.10 the light yield peaks at $\sim 18\,e^-/\mathrm{keV}$ which is low compared to reported values for CsI–PIN photodiode combinations of up to $40\,e^-/\mathrm{keV}$ [Kilgus et al., 1990] or 41 and $46\,e^-/\mathrm{keV}$ [Bird et al., 1993]. There is a list of parameters responsible for the low value achieved (measurements exploring the parameter space are performed in [Andritschke, 2000]):

- The shaping time of $3\,\mu\mathrm{s}$ is not matched perfectly to the large decay time of CsI. The optimum lies around $6\,\mu\mathrm{s}$ which cannot be achieved with the TA1.1 front-end ASIC (and would lead to even worse time walk effects).
- The geometry is not optimized for light output but for position resolution (fine pixellation). The aspect ratios of the prototype crystals are 4:1, 8:1, and 16:1, whereas the high light yields are achieved with 0.5:1 and lower.
- The method of optical coupling employed — pressing crystals in (hand-made) silicone cushions — gives rise to light loss by imperfect coupling. More reliable optical coupling can be achieved by gluing or optical grease, but it was and is important to be able to easily unmount the calorimeter blocks for repairs.

The energy resolution, given by the peak widths of the calibration measurements, is 38 keV at 662 keV on average over all channels. The block-by-block averages are listed in the overview table 4.1, and the channel-by-channel distribution is shown in figure 4.11. Calculating the terms contributing to the peak width according to equation C.3 (electronic noise $\Delta E_E = 16\,\mathrm{keV}$, statistical noise $\Delta E_C = 6.2\,\mathrm{keV}$), it becomes evident that the main contribution needs to be due to crystal-intrinsic fluctuations ΔE_I and systematic fluctuations ΔE_{sys} ($\sqrt{\Delta E_I^2 + \Delta E_{sys}^2} = 34\,\mathrm{keV}$). Inhomogeneities in the crystals (such as the Tl doping, impurities, or crystal defects) and light losses, which depend on the interaction location, compose the crystal-intrinsic fluctuations which could lead to deviations of $\sim 2\%$ ($\widehat{=}$ 13 keV at 662 keV) as measured in [Andritschke, 2000] for a 4 cm block. Systematic errors are the largest contributors to the energy resolution and arise

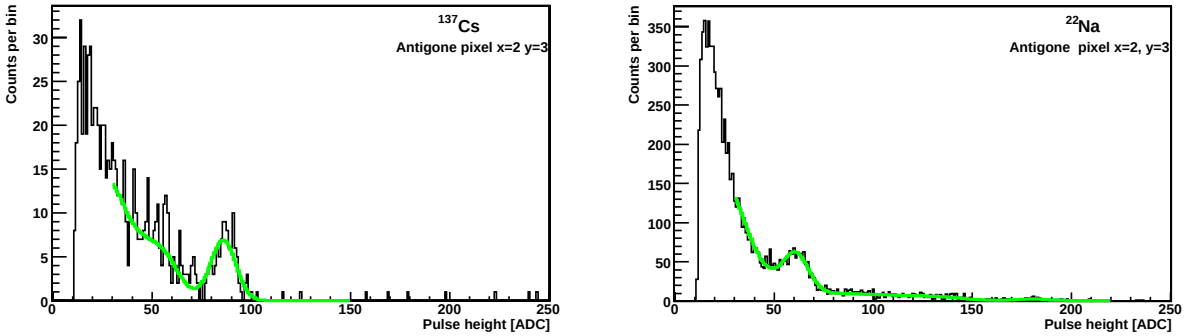

Figure 4.6: Fitted spectra of a ^{137}Cs (left) and a ^{22}Na (right) source

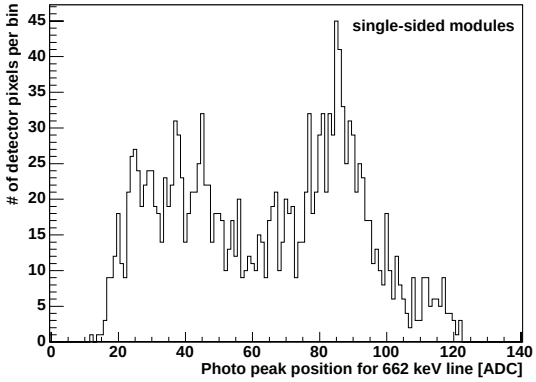

Figure 4.7: Distribution of the 662 keV peak positions

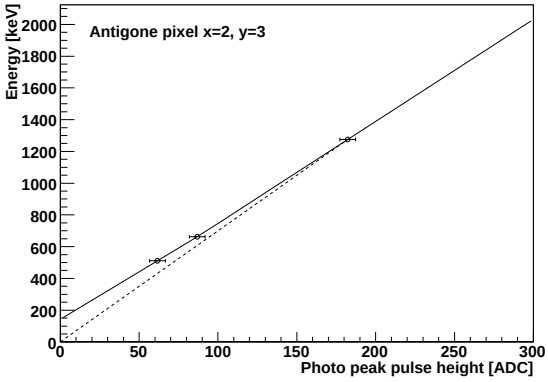

Figure 4.8: Energy calibration. The dashed line indicates the extrapolation line for energies above 1.275 MeV, see text.

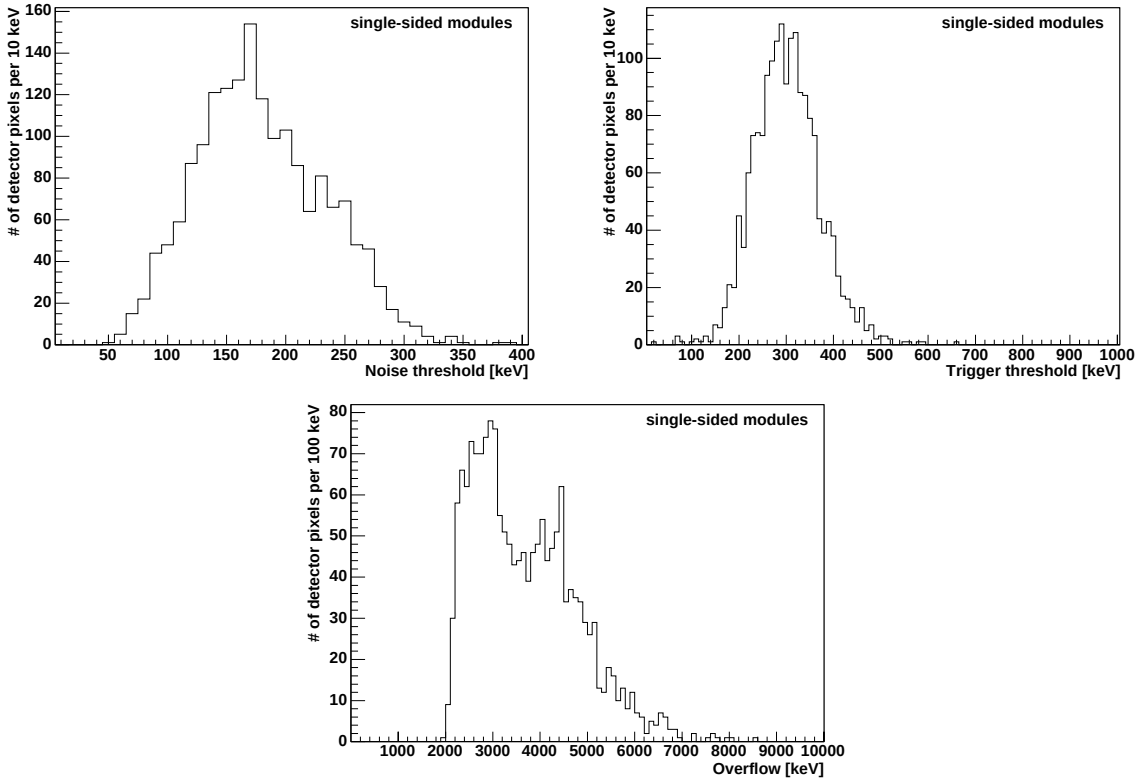

Figure 4.9: Distribution of noise thresholds, trigger thresholds and overflows of the single sided calorimeters

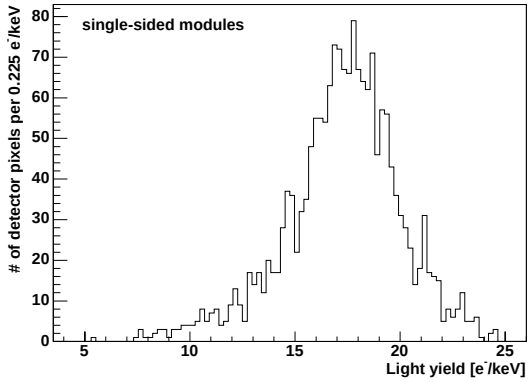

Figure 4.10: Distribution of the light yields

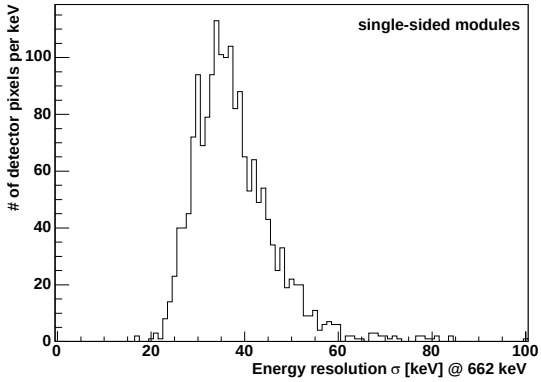

Figure 4.11: Distribution of the energy resolutions for the 662 keV line of ^{137}Cs

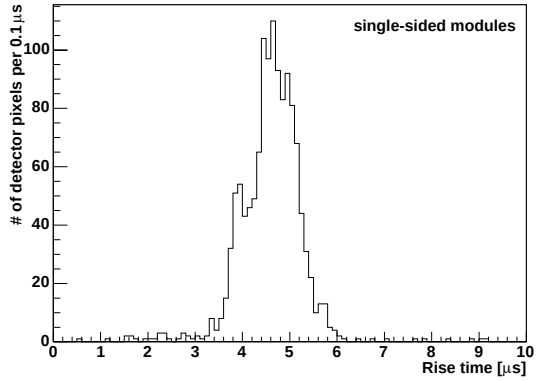

Figure 4.12: Distribution of the shaping times

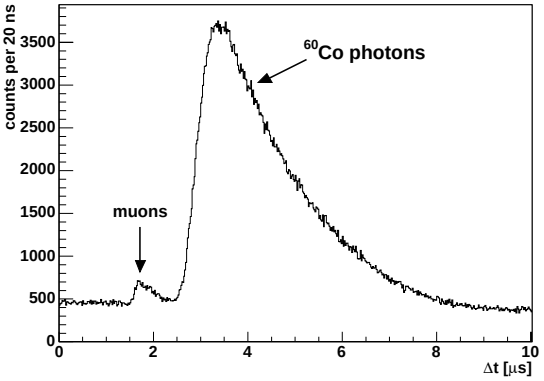

Figure 4.13: Time resolution of the calorimeter measured with a tagged ^{60}Co source. The peak of the source photons has a width of 1.9 μs (FWHM). The small peak at earlier times results from muons traversing both the tagged source's scintillator and the calorimeter. The notes on the measurement given in chapter 9.3 apply as well here.

mainly from electronics problems such as cross talk, the time walk problem (chapter 5.1.6) in combination with common-mode noise as already described in chapter 3.3.3, and temperature drifts. A systematic dependency of the energy resolution (as well as the other parameters) has not been observed which confirms that longer crystals increase the uncertainties only slightly compared to the other effects.

Shaping times and time resolution: The arrival time of a hit is signaled by the rising edge on the trigger line. It is influenced by the full time-walk described in chapter 5.1.6, which can be as much as the full rise time for low signals. For the calorimeters this is 3.5 – 5.5 μs (table 4.1 and figure 4.12). The resulting time resolution measured with the ^{60}Co tagged source setup (chapter 7.1.2) is shown in figure 4.13. In addition to the broad peak resulting from the tagged source photons there appears a small peak with shorter time walk. These events are due to muons passing the plastic of the tagged source as well as one of the calorimeters. Since they induce large signals their time walk is low.

detector name	leakage currents [nA]	σ [keV] @662 keV	noise threshold [keV]	trigger threshold [keV]	overflow [MeV]	defective pixels
Aphrodite	23 / 168	32.1	138 – 285	238	13.7	18
Athene	69 / 50	45.1	142 – 368	351	15.2	16
Daphne	92 / 42	31.0	135 – 314	220	10.1	7
Xantippe	92 / 56	42.9	58 – 333	277	13.1	16
Average	74	37.8	118 – 325	271	13.0	14

Table 4.2: Performance of the 4 calorimeter blocks with double-sided readout at $\sim 12°$C. Leakage currents: sum of the currents of all pixels in an array, the arrays of both sides are listed separately. Noise threshold: see 4.5.

4.5 Characteristics of Crystals with Double-sided Readout

In case of the bottom calorimeter blocks, reading out both ends of the crystal bars allows to determine the position of interaction along the crystal from the distribution of the scintillation light. In this respect it can be regarded as a kind of a small Anger camera (appendix B.1) where the readout elements are located at the sides. The resulting additional degree of freedom needs to be taken into account before an energy calibration can be performed. In the calibration algorithm, a model for the distribution of the light depending on the z-coordinate of the interaction is included (described in appendix D.3). Figure 4.14 shows an example for fitted spectra with z-dependence. Because of the additional dimension in the measurement data a surface has to be fitted. This fit surface is generated in three steps. First an one-dimensional spectrum is generated from the current fit parameters as in the single-sided case (appendix D.2.6, without noise, which is introduced in the third step). In the second step the z-model (appendix D.3) is calculated which gives for each bin along the crystal two numbers — the fraction of photons seen by the inner and the outer diode. Assuming a homogeneous distribution of the incoming photons the entries of the spectrum are distributed onto the inner and outer diodes according to the z-model. Finally the two-dimensional distribution is folded with noise, represented by a two-dimensional gauss distribution. The assumption of a homogeneous distribution is a reasonable approximation here, since the radioactive calibration sources are placed $\sim$ 9 cm away from the nearest 8 cm crystal. In the worst case there is a deviation of $\sim$20% from homogeneity along the crystal, which is neglected. Other distributions can be introduced at the cost of an even larger parameter set.

Different calibration methods have been used for previous calibrations [Andritschke, 2000, Schopper, 2002]; the advantages of the new one are:

- The (differing) energy resolutions of the two diodes are accounted for.
- All parameters are included in the final fit.
- No dedicated measurement to evaluate a z-calibration is necessary.
- This approach can handle data with lower statistics than the old ones.

It comes at the cost of a complex algorithm. Due to the extremely low statistics of the calibration data acquired during the accelerator campaign at the HIGS facility, manual intervention was still required in several instances.

Gain: The fit parameter representing the peak position in the one-dimensional spectrum (first step in calculating the calibration surface) is shown in figure 4.15.

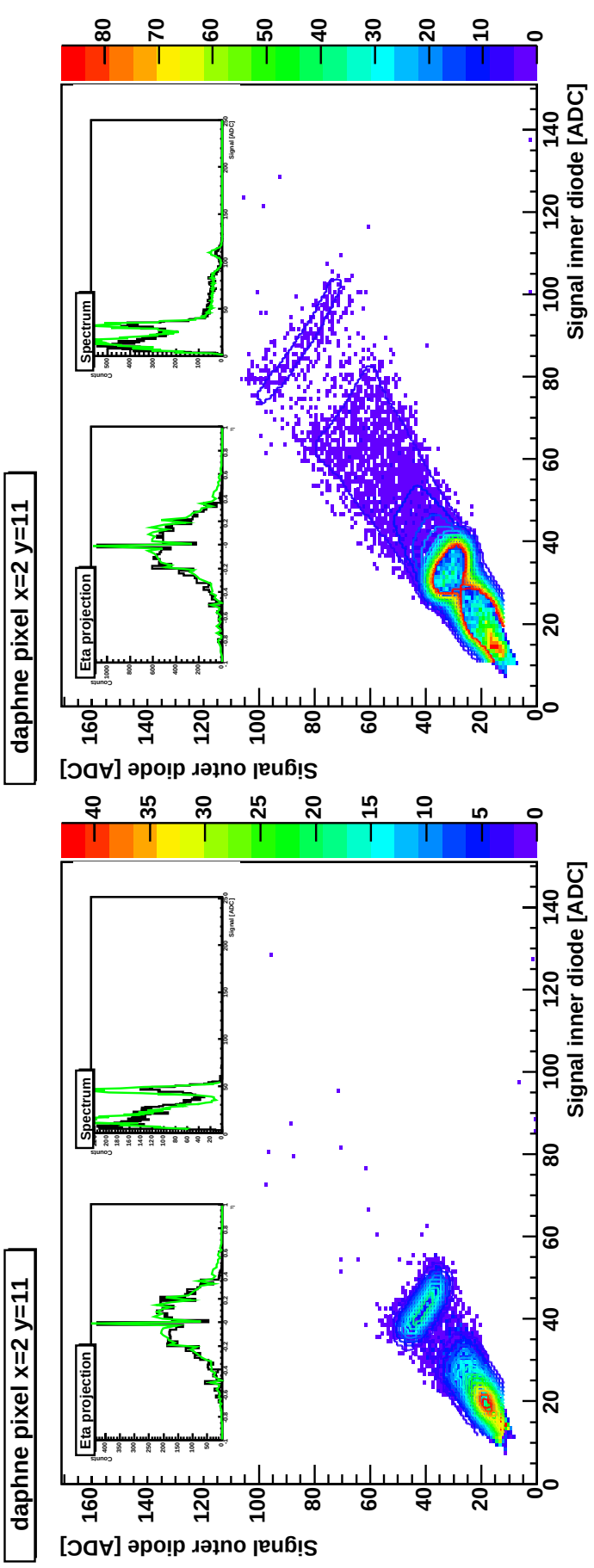

Figure 4.14: Fitted spectra with position resolution of a calorimeter crystal with double-sided readout. The left spectrum results from a ^{137}Cs source, the right from ^{22}Na. The color-coded pixels show the data bins, the overplotted lines indicate the contours of the fit (colors do not match for ^{22}Na since the fit display had to be rescaled in order to show also the contours around the 1275 keV "area"). In order to be able to inspect the quality of the fit by eye, two projections for each spectrum are inserted in the plot. The first is a projection onto the parameter $\eta = \frac{S_i - S_o}{S_i + S_o} \in [-1; 1]$ reflecting the z-dependence ($S_i =$ signal inner diode, $S_o =$ signal outer diode, the spike at 0 is an binning effect which also appears in the fit). The second is a projection onto the parameter $S = \sqrt{S_i^2 + S_o^2}$ which approximately eliminates the z-dependence resulting in a slightly smeared out energy spectrum.

In the calibration algorithm — as for the tracker calibration — it was necessary to introduce an artificial point between 662 and 1275 keV. Without this point, the calibration shifts the Compton edge of the 1.275 MeV line (^{22}Na) to higher energies. This problem results from the non-linearities of the front-end chip and was accounted for by introducing a point at 968.5 keV in the energy spectrum. The added point lies on the straight line between zero and the 1.275 MeV calibration point, analogously to the approach taken for the tracker.

Dynamic range: In the calorimeters with double-sided readout the noise threshold determining the lower limit of the dynamic range depends on the interaction position and is higher than for the blocks with single-sided readout. This is due to the fact that the scintillation light is distributed onto two diodes. Interactions taking place near a diode generate larger signals in this diode than interactions in the middle of the crystal introducing a dependency of the threshold onto the interaction position. The pulse heights of both sides of a crystal are included in the reduced data stream, even if only one is above its noise threshold. This situation prevents the existence of a sharp noise threshold. Instead a *range* for the noise threshold is given in table 4.2. The lower number is the lower edge of calibrated spectra, the higher number is the energy at which both diodes exceed their noise thresholds for all positions along the crystal. The latter value is histogrammed crystal-by-crystal in figure 4.16. The upper limits of the dynamic range (overflow) due to saturation effects are also given in table 4.2 and their distribution is plotted in figure 4.17. The overflows are more than the expected factor of two higher than in the single-sided case. Since these numbers are extreme extrapolations from the available calibration data, and the double-sided modules suffer even more severely than the single-sided ones from the non-linear energy response, the errors associated with these numbers are quite large.

The energy resolution in the case of crystals with two-sided readout depends not only on the noise of both diodes and the crystal quality but also on the reconstruction of the z-coordinate. Consequently the energy resolution of the individual crystals is determined from the data by generating a spectrum from energy- and z-calibrated data and fitting the photopeaks with a Gaussian plus a linearly approximated background. Figure 4.18 shows the distribution of the peak widths for the 662 keV line of ^{137}Cs and the block-by-block averages are listed in table 4.2.

The spatial resolution can be estimated from the calibration data as follows: For a given pair of measured signals S_i and S_o their position z is determined. Also the position $z + \Delta z$ is determined from $S_i + \sigma_i$ and $S_o - \sigma_o$ ($\sigma_{i,o}$ are the noise of the diodes in sigma ADC units). Δz is then approximately one sigma of the position resolution (an upper limit of 8 cm is set). These Δz depend on the deposited energy as shown in figure 4.20. The spread over the various crystals is shown in figure 4.19 for an energy of 1 MeV. The position resolution can be as good as $\sim$ 1 cm (as confirmed by a measurement of a collimated source [Andritschke, 2000]), but is not better than 4 cm for a large fraction of the crystals. In these cases the variation of the light distribution with the interaction position is smaller than the variation due to the noise of the readout diodes. This is the result of the high quality of the crystal surfaces. Improvements such as roughening the surfaces are described in chapter 10.3. At high energies (especially muon interactions) the z-resolution improves due to the lower (relative) influence of the measurement noise. The average resolution reaches $\sim$ 1 cm ($1\,\sigma$).

In principle the spatial resolution can be determined by the measurement of a collimated source as described in [Andritschke, 2000]. Due to a tight schedule this kind of measurement could not be repeated. Instead muon tracks are used to check the position resolution (see figure 4.23).

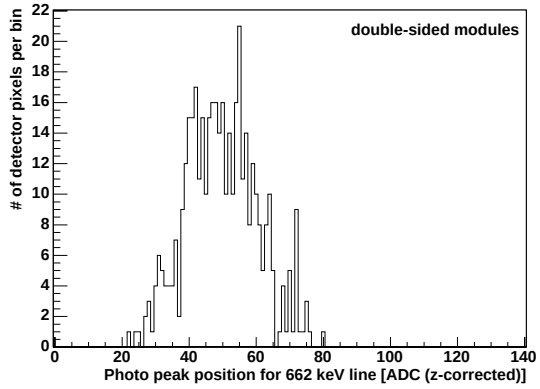

Figure 4.15: Distribution of the peak positions of the double-sided calorimeters for the 662 keV line of ^{137}Cs (corrected for z-dependence)

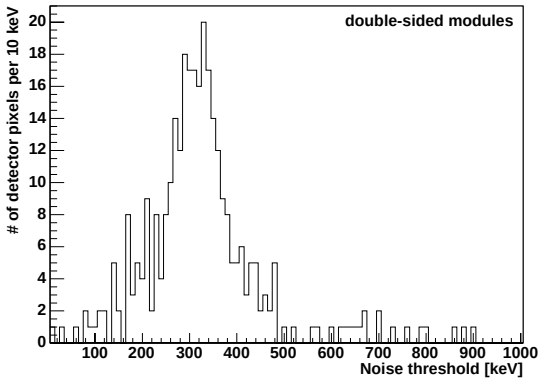

Figure 4.16: Distribution of noise thresholds of double-sided calorimeters (upper limit, see text)

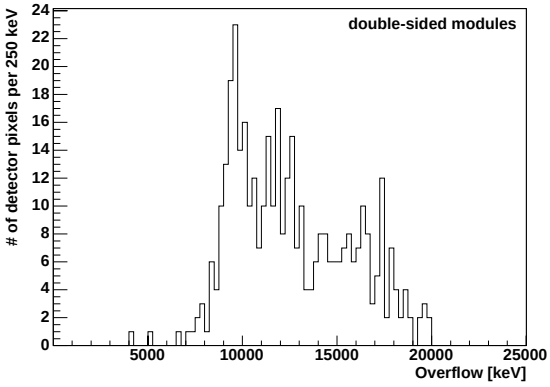

Figure 4.17: Distribution of overflows of double-sided calorimeters

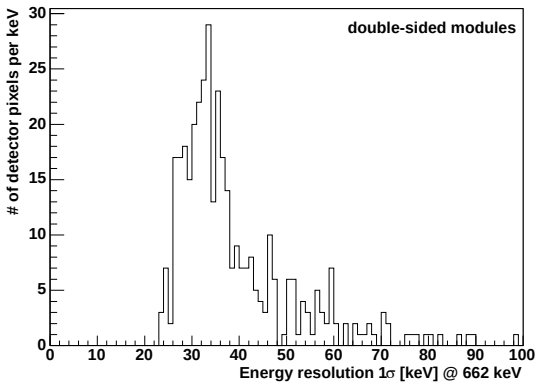

Figure 4.18: Distribution of the energy resolutions at 662 keV

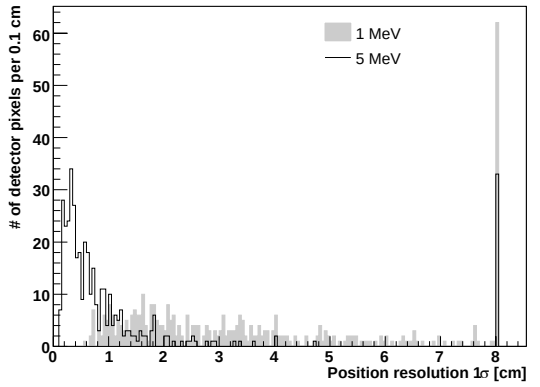

Figure 4.19: Distribution of the z-position resolutions along the crystals for 1 MeV and 5 MeV calculated from the fit parameters of all crystals with double-sided readout. Due to the method (see text) this is only a crude estimate

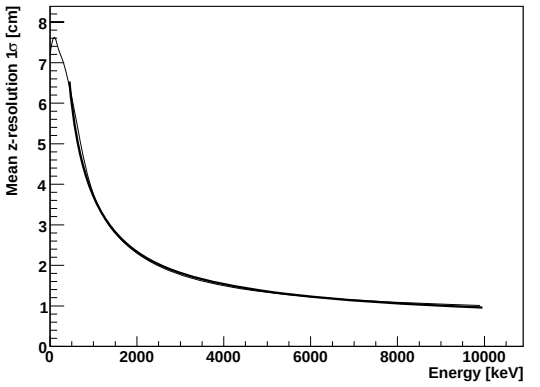

Figure 4.20: Dependency of the z-position resolution on the energy averaged over all 8 cm crystals calculated from the fit parameters. A function $\Delta z = 629 * E^{-0.760} + 0.383$ fits to the data.

The capability to filter interactions in the readout diodes is an additional advantage of the two-sided readout. It is possible to determine if an interaction in a diode has happened. This could be a photoelectric or Compton effect in a diode or a charged particle passing through a diode. In these cases the signals of both diodes do not match, i.e. the ratio of the outer and inner signal is out of the range expected from energy deposits in the crystal. The current software only takes into account that charged particles can reach the calorimeter. On recognizing such an event the z-coordinate is set to the end which is hit and the energy is calculated from the opposite diode only; the energy deposit from the hit diode is neglected. An improved calibration could treat diode hits separately with an own set of calibration parameters (e.g. from an ^{241}Am measurement) and add an additional hit to the event in the data stream.

4.6 The Calorimeter as Sum of Individual Crystals

The calorimeter is of course the assembly of the different crystal blocks, and thus its overall performance is a summation of the (widely varying) properties of the individual crystals and crystal blocks.

Figure 4.21 shows two spectra of the calibration sources and the ^{40}K 1.46 MeV line generated in two different ways: In the spectra on the left side each energy deposit is a separate entry in the histogram. This results in a distinct Compton edge. On the right side the (coincident) hits of an event are summed up suppressing the Compton edge. A ^{22}Na source emits three photons, two 511 keV photons from the β^+-decay — these are emitted in opposite directions — and a few picoseconds later a 1.275 MeV photon (relaxation of the resulting ^{22}Ne*). Coincidences between a 1.275 MeV and a 511 keV in an event decrease the number of entries in the (single-photon) photopeaks and form a very broad background distribution due to incomplete absorption of one or both photons. In addition, chance coincidences of two (or more) photons from (independent) deexcitations in the source result in a high energy tail as seen in the ^{137}Cs spectrum.

A table containing the widths of the photopeaks is included below the spectra (figure 4.21). The derived values mostly agree with the average value calculated from the single crystal calibrations as listed in tables 4.1 and 4.2. The fits are not very significant at low signal-to-background ratios as it is the case for the high-energy peak of ^{22}Na spectrum on the right side and the ^{40}K peak.

For simulation purposes [Zoglauer, 2005] overall characteristics of the peak width as a function of the energy are needed. The energy resolutions of the 20 calorimeter blocks (i.e. averages over the 120 crystals combined in one block) are plotted versus the energy in figure 4.22 (a)–(c). The slopes of a linear approximation for each block are histogrammed in figure 4.22 (d) (the 1.46 MeV line is excluded from this calculation due to its bad signal-to-background ratio). The mean value of the slopes is 18.6 keV/MeV.

The spatial resolution and the correct alignment of the bottom calorimeter blocks can be tested in coincidence with the tracker by measuring muon tracks. Hits in tracker and calorimeter must form one straight line, reflecting the passage of a high-energy minimum-ionizing muon such as the one shown in figure 4.23.

4.7 Possible Improvements of the Calibration

The lack of high energy calibration points could be taken care of by evaluating the energy deposits of muons. It is unclear, how well the expected Landau-distributions can be fitted with respect to the non-linearities of the front-end electronics. In particular for the HIGS runs the available

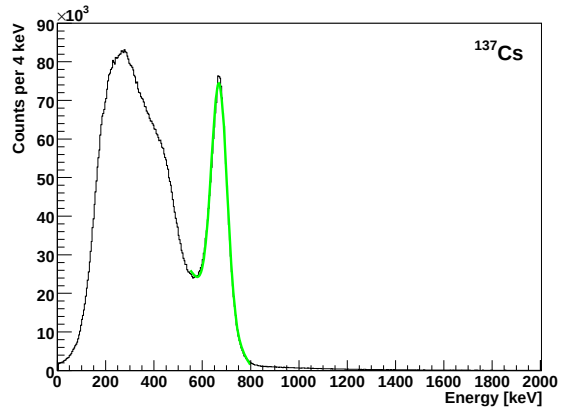

(a) ^{137}Cs, event hits separately

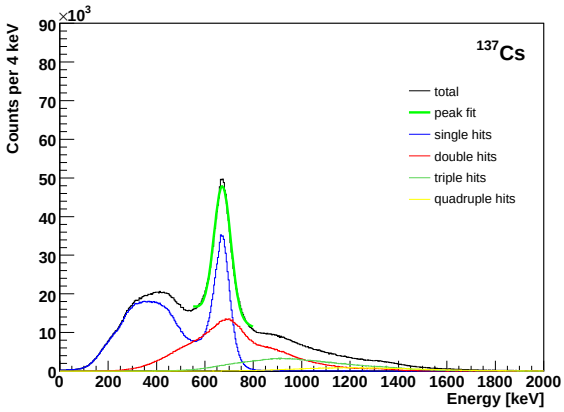

(b) ^{137}Cs, event hits summed up

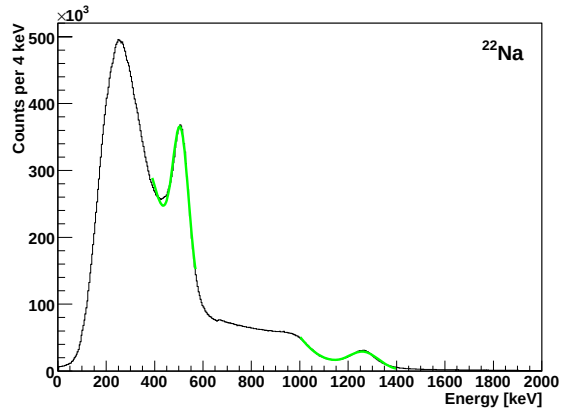

(c) ^{22}Na, event hits separately

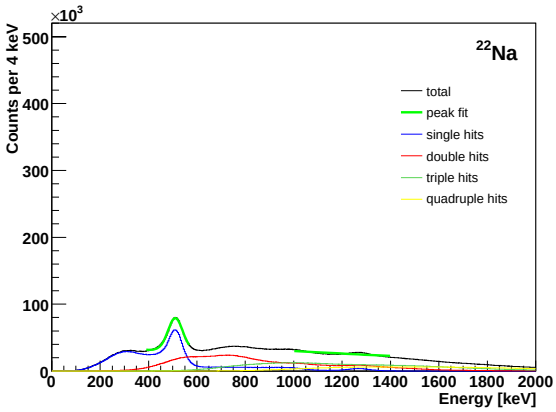

(d) ^{22}Na, event hits summed up

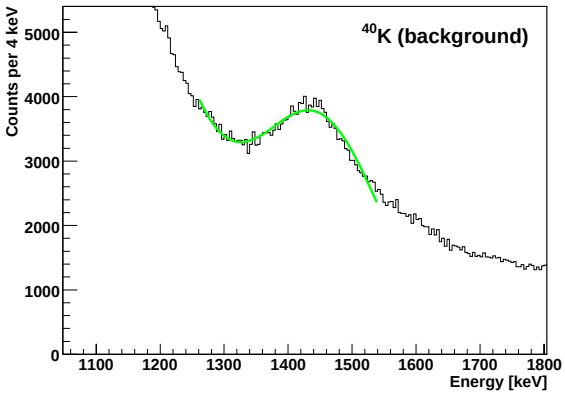

(e) room background (^{40}K), event hits separately

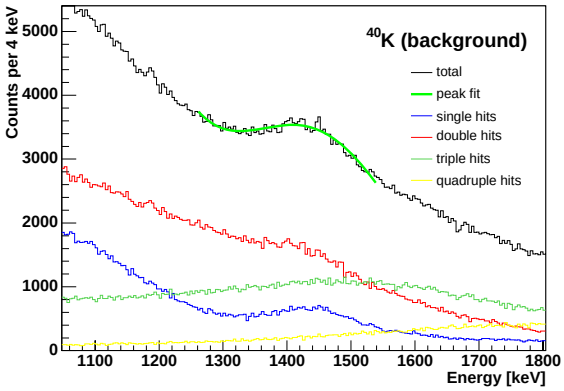

(f) room background (^{40}K), event hits summed up

figure	(a)	(b)	(c) 1	(c) 2	(d) 1	(d) 2	(e)	(f)
peak position [keV]	672	670	508	1264	510	1274	1447	1453
peak width [keV] (1σ)	36	32	32	63	31	42	68	96

Figure 4.21: Calibrated ^{137}Cs, ^{22}Na and background spectra measured with the full calorimeter including the complete set of the respective calibration measurements performed at the HIGS facility. In cases (a), (c) and (e) the energy of every event hit is inserted individually in the histogram. In cases (b), (d), (f) the sum of the energies in an event is used. Case (d) shows a very high background of chance coincidences. This reflects that one decay of ^{22}Na emits three (two 511 keV and one 1275 keV) photons, making chance coincidences likely. The fit functions are a Gaussian with a linearly approximated background in the fit range.

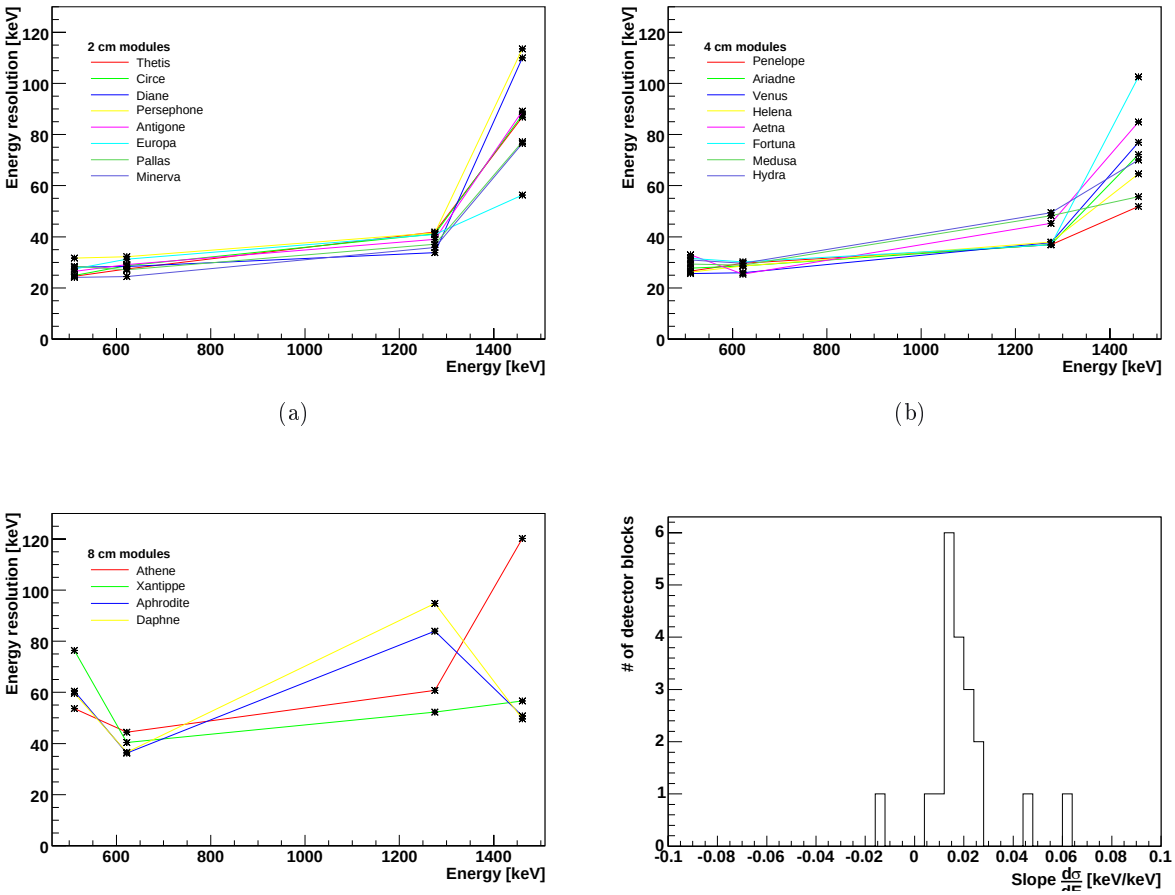

Figure 4.22: (a)–(c): Energy resolutions of all calorimeter blocks for different energies. (d): Slopes of a linear approximation of the energy resolutions. The data points at 1461 keV are not included since the respective photopeaks show too high backgrounds. The mean slope is 18.6 keV/MeV.

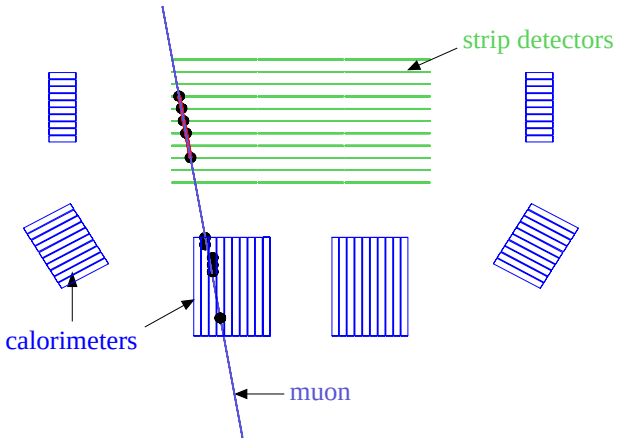

Figure 4.23: Measured muon track. In this schematic representation, only the active material of the prototype is shown, i.e. the tracker silicon and the calorimeter crystals. In addition the front and back calorimeter blocks are omitted.

statistics may be too low — of course, again only measurements of the same setup can be used (for reasons see chapter 3.3.2).

The z-calibration could also be improved with muons. The muon's path through the calorimeter could be extrapolated from the tracker and used for a z-calibration. In order for a sizeable fraction of muon tracks to have a well-defined z interaction position in a crystal bar, the crystals would have to lie parallel to the tracker layers contrary to the standard configuration, where the crystals point in direction to the tracker. This setup has been arranged once in the laboratory and a z-calibration has been successfully evaluated by Andreas Zoglauer. The setup at HIGS could not be changed into this configuration due to mechanical and time constraints.

Apart from deeper calibrations, of course improvements of the hardware resulting in a (more) linear energy measurement and a more precise timing information are desirable. These are described in the dedicated chapter 10.

Chapter 5

Electronics

The large number of detector channels of the prototype requires a readout system with a highly integrated front-end where the small signals (several thousands of electrons) are amplified, filtered, and directed to the digitalization stage. The readout mechanism needs to detect by itself that an interaction in the detectors has occurred (self-triggering system). Moreover it needs to classify the events (in the sense of take or discard) according to the patterns of individual interactions. The present chapter discusses the front-end electronics and the readout chain, chapter 6 is dedicated to the classification circuit, i.e. the coincidence electronics.

5.1 The TA1.1 Chip

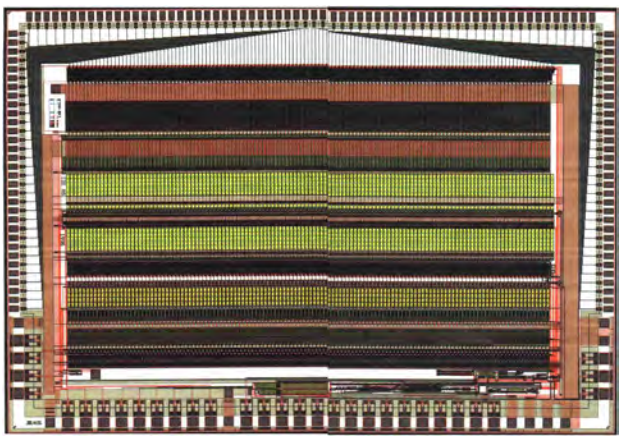

Figure 5.1: The TA1 ASIC

5.1.1 Block Diagram

The TA1.1 ASIC* (figure 5.1) is a 128-channel low-noise/low-power charge-sensitive preamplifier-shaper circuit built by Ideas, Oslo, Norway [IDE]. This chip features a simultaneous sample and hold and a multiplexed analog readout (figure 5.2). It is the first of a series of chips including a triggering unit. The trigger is implemented as level-sensitive discriminator.

*Application-Specific Integrated Circuit

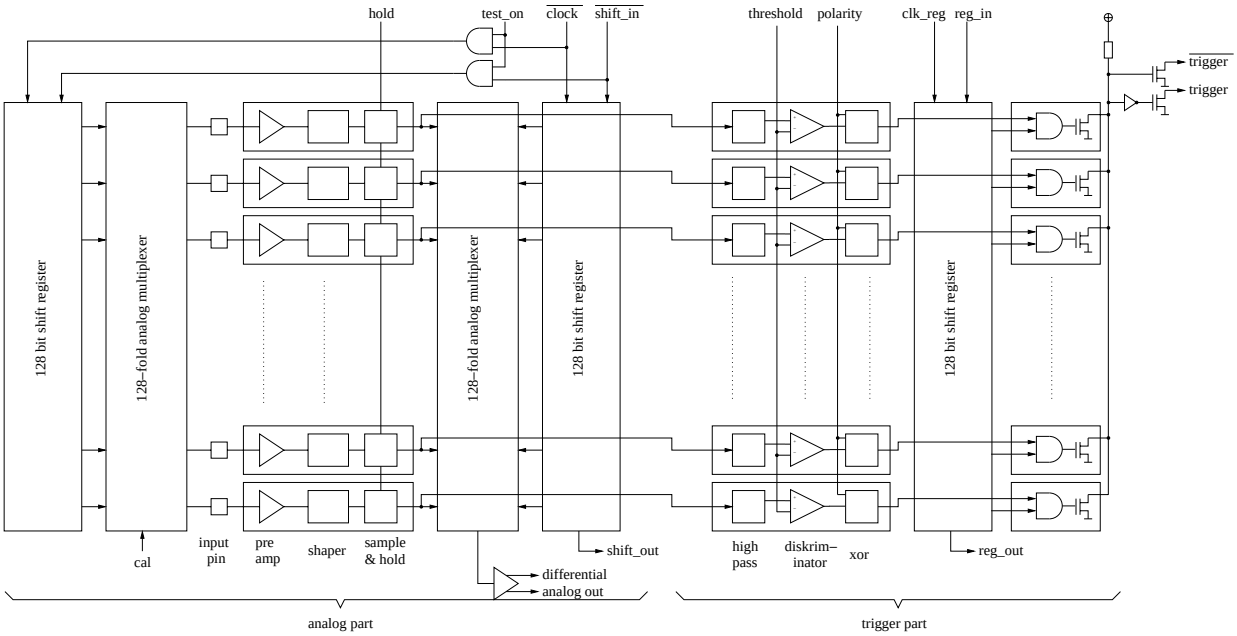

Figure 5.2: Block diagram of the TA1.1 chip (adapted from [IDE])

5.1.2 Principle of Operation

The recognition and readout of an event occurring in a detector connected to the TA1 chip is a process which has four phases:

1. The chip is continuously amplifying (charge sensitive) and shaping its input signals. When one of the 128 shaped signals exceeds the (externally applied) threshold level, this is signaled by the switching of a level discriminator.

2. After that it is necessary to wait until the shaped signal pulse reaches its maximum and to store the maximum amplitude for further readout. This is realized by waiting a fixed time defined by external electronics before applying the hold signal. On this signal the chip sets all its sample and hold units in hold state.

3. The values stored in the sample-and-holds are read out by multiplexing one channel after another to the analog output.

4. After readout a digital and analog reset is applied and the initial situation is restored.

Phase 2 is the critical step in this process. Principally, the implementation of the trigger as level discriminator and the storage of the pulse height in simple sample-and-hold stages leads to the time walk problem discussed in detail in chapter 5.1.6.

The TA1 offers a calibration feature by means of a test-pulse input. This feature is not used in the MEGA prototype since the observed pulse forms of the test pulses differ significantly from the pulses of the detectors. The test pulses are used for a functional test of the individual channels only.

5.1.3 Basic Data

In the MEGA prototype the chip is operated at lower currents[†] than recommended by Ideas:

[†]For a functional description of the voltages and currents see TA1 datasheet and [Schopper, 2002].

	VFP [mV]	VFS [mV]	PRE_BIAS [μA]	SHA_BIAS [μA]	OTA_BIAS [μA]	$IBUF$ [μA]
recommended	-200	700	500	22	45	140
tracker p-side	-270	100	100	15	50	50
tracker n-side	-270	100	100	15	50	50
calorimeter	-350	100	100	3	50	40

This results in a lower power consumption of ~ 0.5 mW per channel compared to 1.7 mW per channel for the recommended settings.

The upper limit for the linear range is given as 18 fC in the TA1 datasheet. In the prototype saturation is reached at 12.5 fC on average for the p-sides of the tracker layers. This deviation presumably results from the extremely low current settings.

5.1.4 Noise

The noise contribution of the chip's preamplifiers in Equivalent Noise Charge (ENC) is given by Ideas as

$$ENC_{preamp} = (165 + 6.1 \times C_T\,[\mathrm{pF}])\, e^- \mathrm{rms} \tag{5.1}$$

for a shaping time of $2\,\mu$s with C_T the total capacitance seen by the channel input, i.e. the capacitance of the detector and the lead-in wires. The TA1 has built-in CR-RC shapers which results in a noise contribution from the leakage current of the detector of [Toker et al., 1994]

$$ENC_{leakage\,current} = \frac{2.71828}{e}\sqrt{\frac{eI_nT_p}{4}} \tag{5.2}$$

with e the electron charge, I_n the leakage current of one detector channel and T_p the peaking time of the shaped pulse. The noise of the bias resistor can be calculated to [Toker et al., 1994]

$$ENC_{bias\,resistor} = \frac{2.71828}{e}\sqrt{\frac{T_pkT}{2R_p}} \tag{5.3}$$

with k the Boltzmann constant, T the absolute temperature and R_p the parallel resistance of the bias resistor of the detector and the feedback resistor of the charge sensitive preamplifier. The total noise thus is given by

$$ENC_{total} = \sqrt{ENC^2_{preamp} + ENC^2_{leakage\,current} + ENC^2_{bias\,resistor}}\,[\mathrm{rms}\ e^-].$$

5.1.5 Serial interconnection

The TA1 chips can be daisy-chained. This feature is used extensively in the MEGA prototype. There are always three chips connected to one repeater card, and up to five repeater cards are in turn serialized (figure 5.3). The serial shift registers are connected in series and the analog output lines are connected in parallel to a single differential line which means that the output currents of the chips in a chain are added. Since all daisy-chained chips should operate with identical settings, each of the six adjustment inputs (see table in chapter 5.1.3) of the three daisy-chained chips are directly connected to the same line. This is correct for the voltages, but for the currents this constitutes a design mistake — the currents do not necessarily divide up homogeneously due to tolerances in fabrication. This leads to a more or less spread of the operating parameters of the various chips (compare appendices E and F).

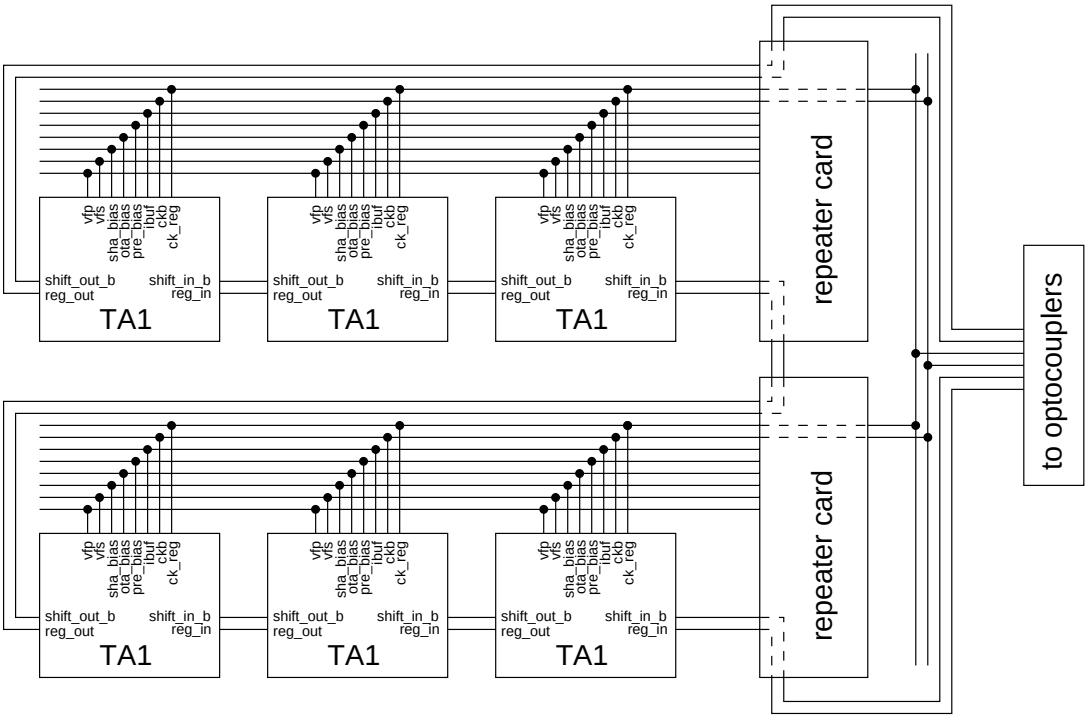

Figure 5.3: Scheme of connecting three TA1 chips and two repeater cards in series. Not all signals are included. The scheme is drawn up to the optocoupler connection. An overall view is shown in Figure 5.8.

5.1.6 Pulse Shapes and Time Walk

The response of a RC-CR shaper as implemented in the TA1 chip to a δ-impulse of charge is of the form

$$V_\delta(t) = \frac{A}{C_D + C_i} \frac{t}{\tau} e^{-t/\tau} \text{ for } t > 0 \tag{5.4}$$

with C_D the detector capacitance, C_i the input capacitance of the preamplifier (including lead-in capacitances), τ the peaking time and $\frac{A}{C_D+C_i}\frac{1}{e}$ the peak value at $t = \tau$. This function can be fitted to the measured pulse shape which is shown in figure 5.4. For the measurement the TA1 chip was switched into test mode where the signal amplitude of a single channel can be observed at the output of the chip.

The amount of charge seen by the preamplifier is proportional to the maximum voltage of the shaped pulse. Ideally the sample-and-hold stages are put into hold state exactly at the point in time when the pulse has reached its maximum. In order to determine the proper moment, a trigger signal is generated by the TA1 which is derived from the shaped pulse by a simple level discriminator. This combination introduces a timing problem[‡] (figure 5.5) which is referred to as "time walk" in this work: The rising edge of the trigger signal happens later for low pulse heights than for high ones relative to the actual interaction time in the detector. If the (fixed) delay time between trigger and hold is optimized for large pulses, the hold signal for low pulses is applied too late resulting in a measurement of a too-low pulse height. Thus what starts as a timing problem, results in increased errors on energy measurements. Obviously lower thresholds shift the problem to lower energies, thus increasing the (nearly) linear range, but the threshold level is limited by noise. Additionally, due to production tolerances of the chips there are varying threshold offsets

[‡]This problem is already addressed in [Andritschke, 2000, Schopper, 2002], but its implications for the performance of the MEGA prototype necessitates a detailed discussion within this work.

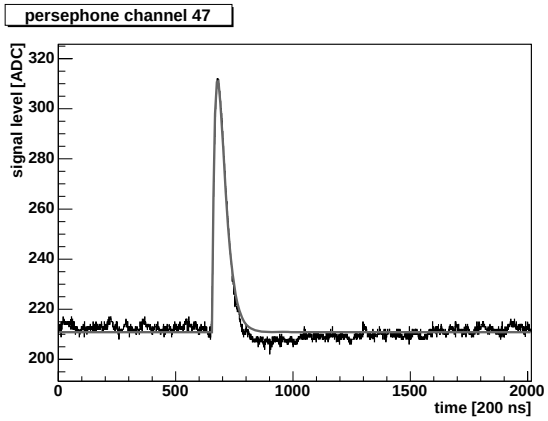

Figure 5.4: Sampled pulse (gained with an modified setup) of an interaction in a calorimeter channel including fit

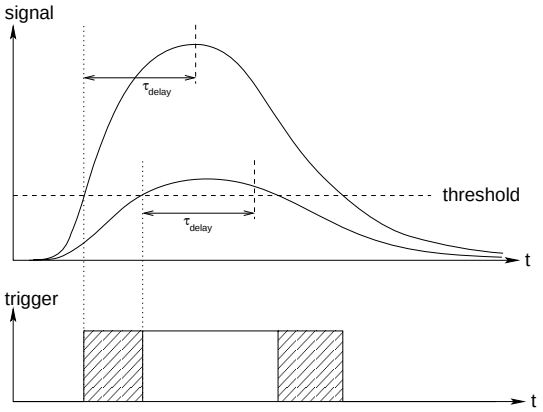

Figure 5.5: Time walk illustration. For small pulses the trigger signal is late compared to large pulses. A constant delay (τ_{delay}) ends up in too low sampled amplitudes for small pulses.

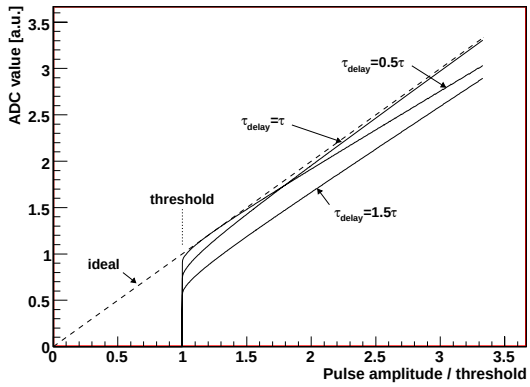

Figure 5.6: Deviation of the measured pulse height (ADC value) from the ideal value due to time-walk for three cases, a too short delay, an optimum delay, and a too long delay

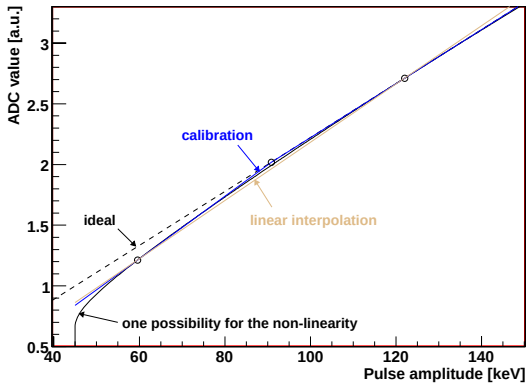

Figure 5.7: Comparison of the interpolation method used for the strip detectors with a simpler linear interpolation between the two calibration points (59.5 keV and 122 keV). The circles mark the two available calibration points and the artificially introduced point (see text).

between the individual channels (and there is only one threshold input per chip) necessarily leading to suboptimal thresholds for most of the channels.

A solution to overcome the time walk problem in the energy measurement is in principal to correct the measured pulse height. The necessary information (for every channel individually!) is the pulse form, the trigger threshold, the delay time, and for each event the measured pulse height. Initial test have shown that implementing and calibrating such a correction for the 10 000 channels of the MEGA prototype requires more effort and time than available and reasonable due to the large number of channels, varying pulse shapes with signal amplitude, and so on.

Instead of this complex approach, interpolation between the measured pulse heights is chosen to account for the time-walk induced non-linearities. Therefore some prior knowledge is used:

- Figure 5.6 shows three cases, how the measured pulse height could differ from an ideal linear behavior. In the case of a too short delay ($\tau_{delay} = 0.5\tau$ with τ the time constant of the pulse) the ideal curve is touched for that pulse amplitude, where the time-walk plus the delay end up in a hold during the maximum of the pulse. For all other amplitudes, too low values are measured. If the delay matches the time constant ($\tau_{delay} = \tau$), the ideal curve is asymptotically reached. Finally too long delays ($\tau_{delay} = 1.5\tau$) result in systematically too low values.
- The delay has been adjusted for the tracker such that for the detector "Bachus" (the first operating layer and at the same time the one with the best performance) the hold is applied at the maximum of a 122 keV (^{57}Co) pulse. The calorimeter delay is adjusted for the 662 keV line (^{137}Cs) with the detector "Helena".
- An additional effect worsens the situation — it has been observed on the oscilloscope that low pulses are shorter than high ones resulting from a not ideal shaper. This adds a shift of the pulse maxima.

With this information a typical dependence between the pulse amplitude and the measured value in the tracker could be as plotted in figure 5.7. Two interpolation methods are added in the plot, a linear interpolation between the two available calibration points, and the interpolation using an additional point. The additional point lies on the straight line through the point of origin and the 122 keV calibration point and in the middle between the two calibration points (due to the limited measured information no optimal position can be determined so that the middle has been chosen). This way a better approximation is achieved for the extrapolation to high energies as well as to lower energies compared to the simple linear interpolation, since the slopes of the calibration curve are better fitting in the calibration points.

In the calorimeter three calibration points are available (662 keV of ^{137}Cs, 511 keV and 1.275 MeV of ^{22}Na) and an artificial point has been introduced analog to the tracker between 662 keV and 1.275 MeV to account for a correct reconstruction of the energy of the Compton edge of the 1.275 MeV photons.

5.2 The Readout Chain

5.2.1 Components

An overview of the readout chain is given in figure 5.8. The detectors are connected to TA1 front-end chips. A series of three chips is supplied by one repeater card. The repeater card shifts the logic levels of the TA1 chip to TTL standard and regulates the supply voltages low-noise. Three

or four repeater cards are in turn serialized and connected to the galvanic decoupling (see next Section) consisting of two boards. The first decouples the analog signal and the control signals, the second the trigger signals. The analog signal is fed into an analog-to-digital converter (ADC) and the control signals are driven by a sequencer and a digital input-output module (DIO). The trigger signals are delayed[§] and stretched in the optocoupler cards. The stretching is necessary since the level discriminator generating the trigger signal sometimes switches twice or more due to noise when the shaped pulse crosses the threshold level. In particular at the falling edge this would generate false triggers. The trigger signals are further evaluated by the coincidence module. In the case of an accepted trigger pattern the sequencer is triggered which generates the readout sequence (chapter 5.2.3). The ADC, DIO, sequencer and coincidence are connected via a VME bus to a computer which controls the whole system and stores the data.

A picture of a test bench for functional testing of single modules is shown in figure 5.9; the different components are visible.

5.2.2 Ground Concept

The very sensitive front-ends are galvanically separated by optocouplers from the rest of the readout system so that there are nine separated grounds (eight of the front-ends and one of the VME bus). This separation not only reduces noise induced by crosstalk from the VME bus into the front-end electronics, but is also forced by the fact that the readout electronics of the strip detectors need to run at the corresponding bias potentials. Broken oxide / nitride layers on the strip detectors connect the inputs of the TA1 chips directly to the implants and thus to the bias potential, but the TA1 stops operating if one of its input channels sees too large a potential. Also, the strip detector itself must not see large potentials across the oxide / nitride layers; otherwise conductive channels could be induced due to the MOSFET-like structures so that the strips would be interconnected and the punch-through biasing (chapter 4.1) annulled. The galvanic separation of the front-ends bridges the potential gaps between the different grounds. One polarity of the bias voltages can be safely interconnected and tied to the potential of the detector housing and structure. This is done for the calorimeters (only one polarity of the PIN diodes is read out) and the p-sides of the tracker. Consequently the n-sides need to have "floating" grounds, which are only AC-coupled by large capacitors to the corresponding p-side grounds.

5.2.3 Readout Procedure

When the coincidence electronics accepts an event for readout (chapter 6.3), a readout sequence is started which runs completely independent from the instrument's CPU (figure 5.11). The first step in the sequence is that the two hold signals (one for the tracker and one for the calorimeter, accounting for significantly different timing behaviors) are applied (figure 5.11a). Upon the hold signal the analog signal levels of every detector channel are stored. After that the sequencer is started. It addresses channel after channel and generates the conversion signals for the ADCs (figure 5.11b). The eight front-end chains work in parallel, i.e. eight channels are sampled simultaneously. The ADCs have memories attached on their boards where the sampled data is stored. No action of the instrument's CPU is required up to this point. After the sequence has finished, the CPU gets an interrupt signal (via the VME bus) and starts fetching the data from the ADC modules (figure 5.11c and d). Once all data are read from the ADC modules the instrument is ready for the next event.

[§]There is an adjustable delay for the trigger signals implemented on the trigger optocoupler card. It was intended to adjust the trigger timings between the front-end chips. This feature was never used and set to a minimum value of 0.5 μs since the timing behavior turned out to be much more complex.

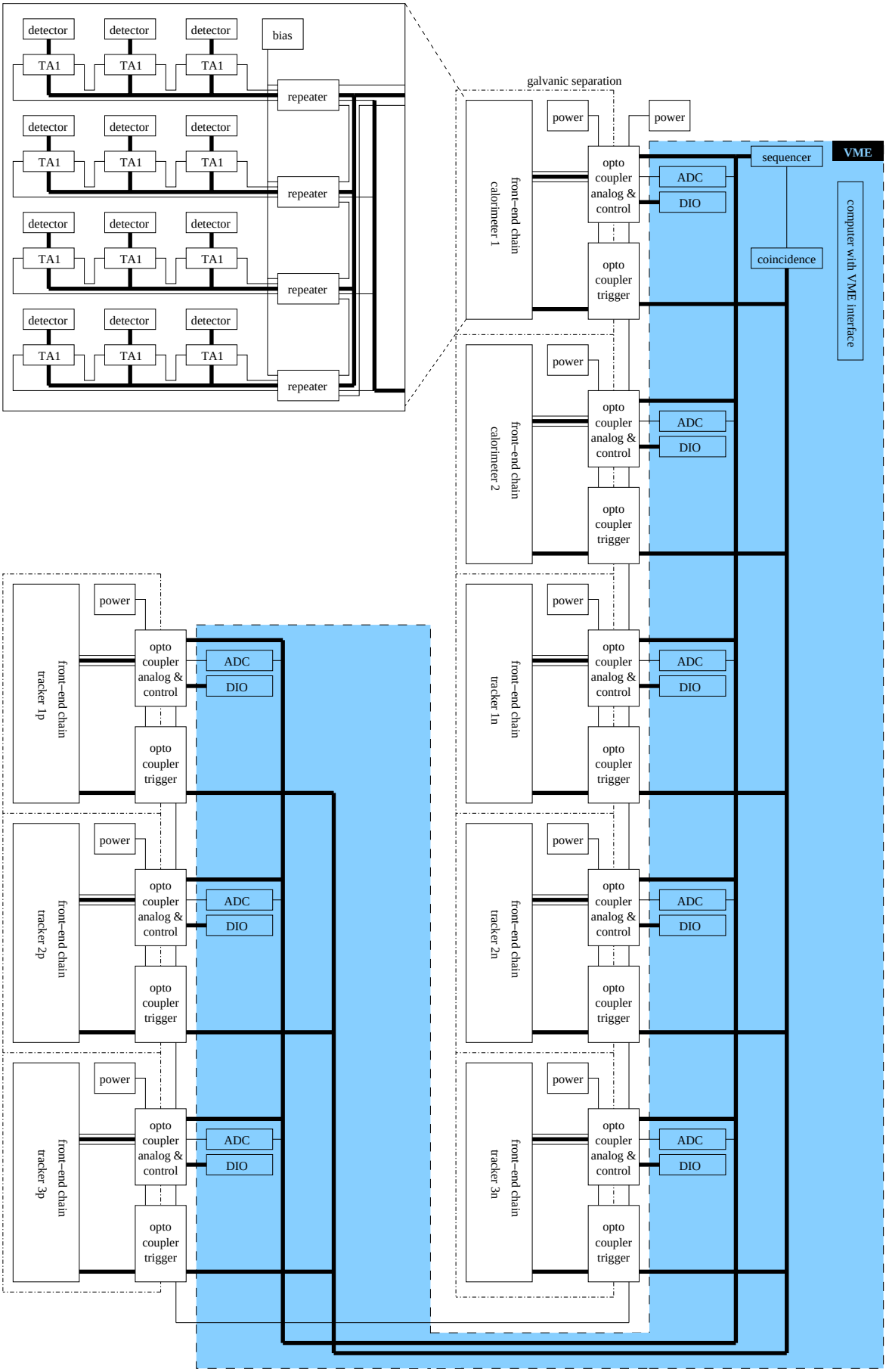

Figure 5.8: Schematic overview over the hardware components of the data acquisition system. Details of the front-end chain are shown only for "calorimeter 1".

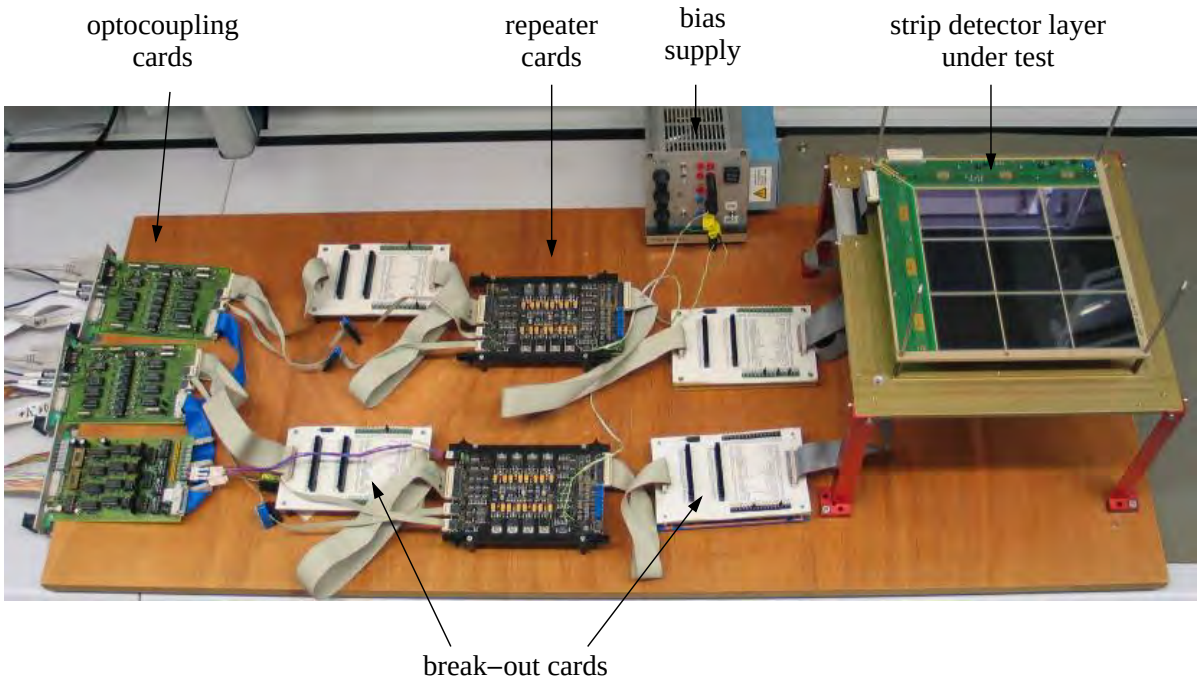

Figure 5.9: Test setup with a tracker layer

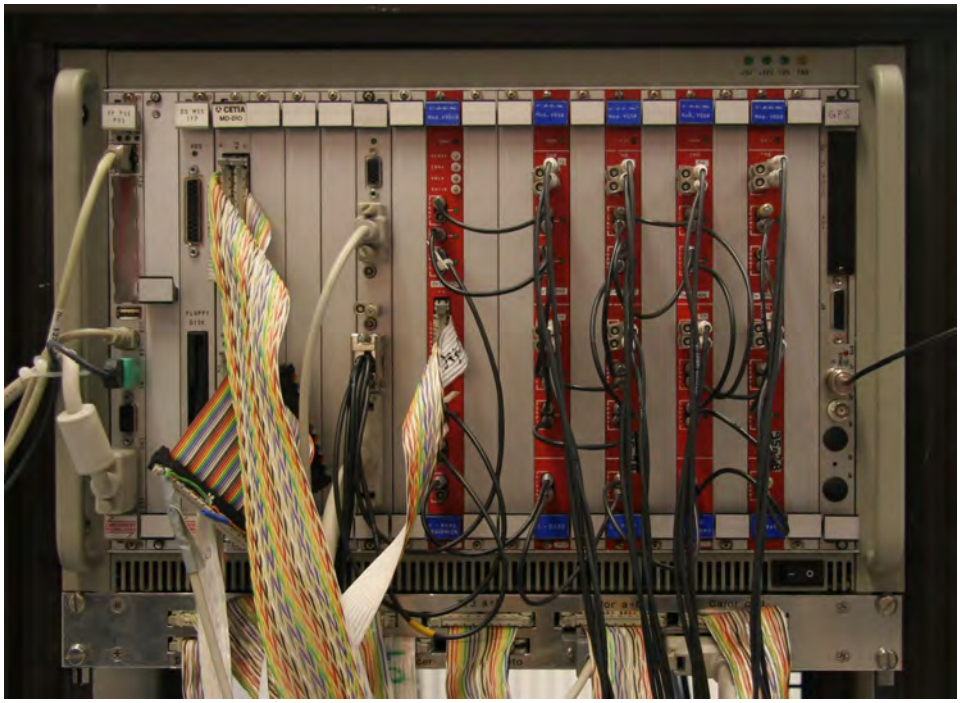

Figure 5.10: VME bus rack (from left to right): CPU card, harddisk slot with floppy, DIO, coincidence card, sequencer, four ADCs, and GPS

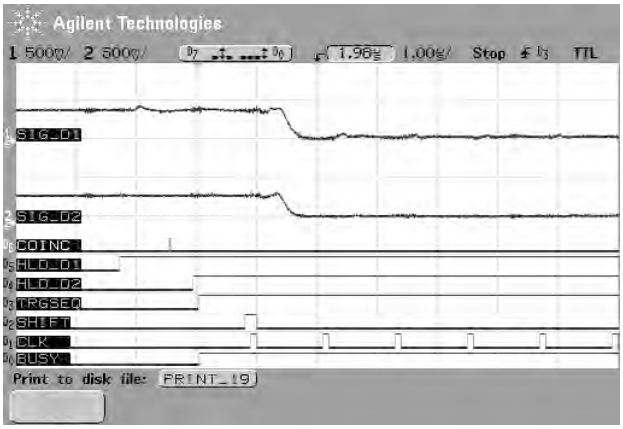

(a) Start of readout sequence

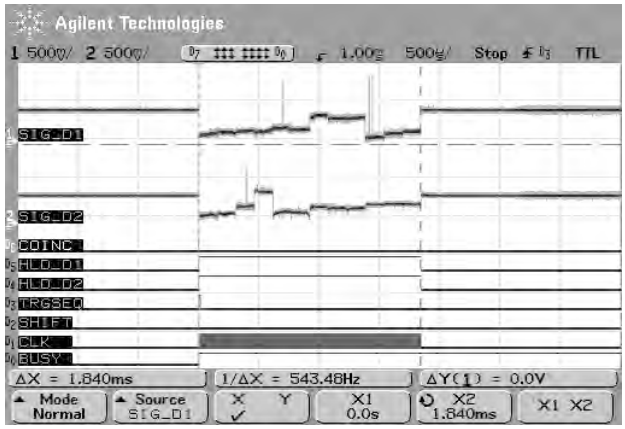

(b) Analog to digital conversion part, duration $\approx$ 1.8 μs

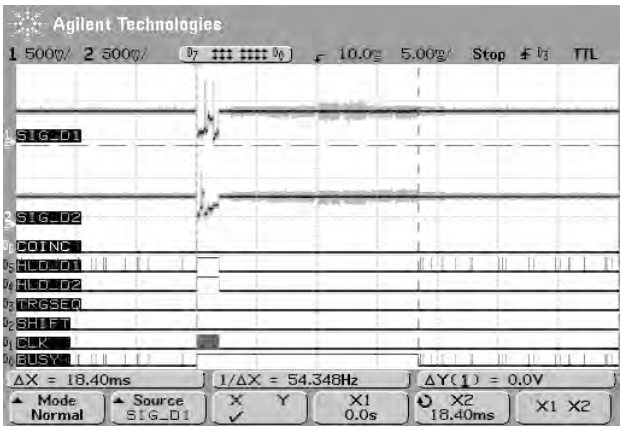

(c) Complete read-out sequence in full mode, i.e. no suppression of empty channels done in ADC modules; duration $\approx$ 18.4 μs

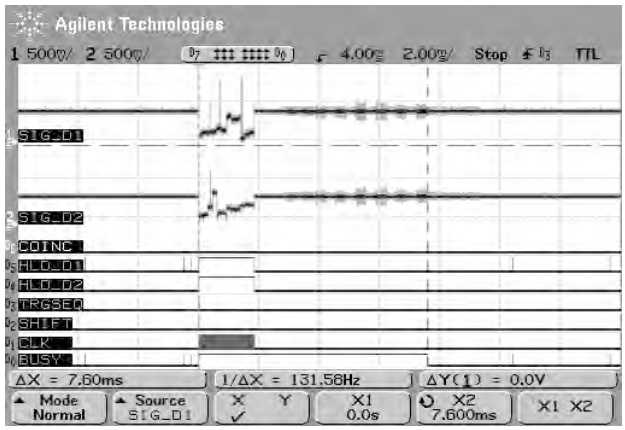

(d) Complete read-out sequence in semi-sparse mode, i.e. suppression is done for 90% of the channels, the rest is always read out for common-mode correction; duration $\approx 8\,\mu$s (average)

Figure 5.11: Readout sequence. SIG_D1 (SIG_D2) is the input of one of the six (two) ADCs of the tracker (calorimeter). COINC is the signal for a valid coincidence of triggers (see chapter 6). HLD_D1 (HLD_D2) is the hold signal for the tracker (calorimeter) channels storing the current pulse amplitudes in the sample-and-hold stages. TRGSEQ starts the sequencer generating the readout sequence. On the SHIFT line the bit is generated which moves throughtthrough the daisy-chained shift registers selecting one channel at a time. CLK is the corresponding clock. BUSY signals that some processing is ongoing, i.e. the coincidence electronics is looking for a coincidence, the sequencer is generating th readout sequence or the ADCs have data in their memories which are not yet read.

5.2.4 Dead Time

During the readout time (signal busy in figure 5.11c and d) the detector cannot accept any further event. If the hardware sparsification in the ADC modules is used, all channels below a programmable threshold are eliminated from the data stream (see next section). The dead time is shorter in this case ($\sim 8\,\mu$s on average) than without sparsification ($\sim 18.4\,\mu$s). Its duration is recorded by the coincidence electronics as described in chapter 6.6.

5.2.5 Software

For data reduction the incoming sampled values are processed as described in [Schopper, 2002]: In an initialization phase the offsets and noise are determined for each channel individually from data at random readout times, i.e. without correlation to any trigger signals of the detector units. The offset is calculated as the running average, the noise is the running variance after the common-mode for each chip (average of the 128 channels after subtracting the offset) is subtracted. After the initialization phase the actual data processing starts with reducing the data taken on a trigger pattern which is accepted by the coincidence electronics (next chapter). A valid interaction (hit) in a detector channel is recognized if the sampled value exceeds six times the noise after subtracting offset and common-mode.

The ADC modules already offer a (hardware) data reduction feature. The sampled values minus a (user given) offset are compared with a (user given) threshold and saved in the module's memory only if the data exceeds the threshold. Of course common-mode correction is no longer possible if this feature is used for all channels. A third mode which is a mixture of the non-reducing and the reducing mode is implemented to get common-mode correction and hardware data reduction at the same time: the data reduction is switched off for 10% of the channels. These are used to calculate the common-mode.

The structure of the data acquisition software can be seen in figure 5.12. The basic structures had been introduced at the start of the MEGA prototype assembly by F. Schopper; most of the coding work, especially the higher-level codes, have been written by A. Zoglauer. The basic idea is to represent each hardware component (e.g. ADC, sequencer, front-end chip, detector) with its properties in the software (as a so-called "object"). This approach has been chosen to generate a modular, object-oriented code which is easy to maintain, flexible, extendible, and highly configurable. Several layers have been necessary to implement the full functionality: The lowest level manages the hardware interfaces, i.e. the VME bus with its different modules, and the standard serial and parallel PC-interfaces. Based on this layer is the hardware abstraction layer. Here the individual functionalities of different physical units such as detectors, ADCs, or the coincidence system are represented. The data is further handed over to the data acquisition step which controls the collection and storing of event and housekeeping data. Since there are three "supervising" instances (the graphical user interface for interactive access, the macro for automatic runs and a network access via TCP/IP implemented in anticipation of a balloon flight), an interface layer is necessary to combine the different channels.

The natural implementation for this broad range of functionalities from very low level hardware access to top level functions is in the C++ language. For visualization and graphical user interface the C++ class library ROOT [Brun and Rademakers, 1997][¶] is used.

[¶] See also `http://root.cern.ch`

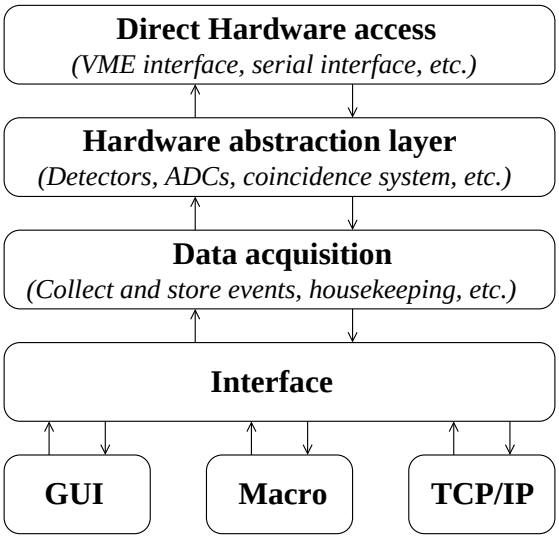

Figure 5.12: Software block diagram

5.3 Improvements

Given the current hardware nearly the full range of improvements has already been exploited. For example the early system had two sequencers, one for the tracker and one for the calorimeter. Since both worked in parallel without synchronization, cross-talk noise from the tracker's digital signals onto the analog signals of the calorimeter occurred and vice versa. The reduction to one sequencer solved the problem but required additional logic in the hold signal lines.

In future more homogeneous operating parameters all over the front-end chips — especially shaping times and gains — could be achieved only by supplying each chip individually with the corresponding currents and voltages instead of having three chips connected to common lines (chapter 5.1.5) which would be a major change in the layout of the front-end electronics boards.

Another point for improvements is the readout speed, i.e. the dead time. In the phase of digitizing the stored pulse heights of the front-end electronics the bottle neck is given by the rise times in the analog optocoupler (maximum rate 1 MHz). With faster optocouplers the readout speed could be improved up to a factor of five until the ADC's limit (5 Msamples/s). Another way of gaining speed would be to use more ADC modules so that the the digitalization is more parallelized. Both methods would decrease only the smaller fraction of the readout time (compare figure 5.11) since the data flow from the ADC's memories to the CPU memory over the VME bus consumes most of the time. Without redesigning the ADC modules the only way to speed up the data transfer is to use two (or even more) VME busses, each equipped with an own CPU — a major task in terms of hardware as well as software. In the extreme case each detector unit would be supplied with its own ADC and CPU (see also chapter 10.4).

In terms of induced noise, only a better ground concept could improve the situation, which automatically means to introduce external decoupling capacitors for the strips of the tracker. The large part of systematic uncertainties in the energy resolution and the problem of the non-linear energy response can only be eliminated with a different trigger and / or energy measurement concept as briefly presented in chapter 10.4 which means a different front-end electronics and thus a completely new system.

The only time critical step at the beginning of the readout procedure, i.e. until the holds for tracker and calorimeter are applied, is implemented in a dedicated electronics, the so-called coincidence electronics as described in the following chapter.

Chapter 6

Coincidence

In the three detector parts of the MEGA prototype, the tracker (chapter 3), the calorimeter (chapter 4), and the AntiCoincidenceSystem (ACS, appendix G), a variety of interactions can occur as there are photoelectric absorptions, Compton scatters, pair creations, and incident charged particles depositing energy along their path through the detector. Since MEGA's purpose is to image Compton and pair creation events, these have to be discriminated against charged particles (e.g. muons, electrons, or protons) and against events which deposit energy only in one readout channel (both photoelectric absorptions and Compton events where the scattered photon leaves the detector are useless). Filtering out unwanted events reduces the readout rate and consequently the data volume. The remaining interactions have in common that two or more readout channels have signals at the same time, i.e. they are coincident. In the MEGA prototype this filtering is accomplished by a custom-made electronic device called coincidence electronics.

6.1 Requirements

The detailed requirements on the coincidence electronics are the following:

1. Coincident events between tracker and calorimeter need to be recognized and processed, others discarded. In order to determine if individual hits are coincident, the different timing behavior of the tracker and the calorimeter has to be taken into account.

2. Due to the properties of the front-end electronic ASIC (chapter 5.1) correct timing of the hold signals for the sample-and-hold stages in the ASIC is crucial. It is closely connected to the coincidence timing.

3. A flexible method of event selection depending on the pattern of triggering chips is needed. It should allow a restriction to events which are expected in the current measurement situation. For example, long tracks of charged particles can be selected for muon measurements or high-energy pair creations.

4. The readout of events needs to be inhibited when the ACS recognizes a charged particle impinging on the detector, i.e. when the ACS sends a veto signal.

During the development process additional functions were integrated in the coincidence electronics:

- Different modes are implemented for calibration, test, health monitoring, and operation of single detector units.

- A command interface for the ACS was included.
- Pulses of the plastic detector of the beam monitor used at the accelerator measurement (chapter 7.2) were counted.
- Further features which are not detailed here, because they are either not used or of minor importance.

6.2 Specification

The input signals for the coincidence electronics are the trigger signals of the front-end chips (stretched and delayed, see chapter 5.2.1). The prototype is designed to have up to 12 tracker layers (11 are part of the prototype assembly) and 20 calorimeter blocks. Only the triggers of the p-side chips are used; this results in a maximum of 36 signals for the tracker. The calorimeter has 24 chips (4 blocks have double-sided readout). The ACS electronics combines its inputs to 4 veto signals. The triggers of the tracker (D1) are delayed at maximum by the rise times (1.5 – 3.5 μs), the ones of the calorimeter (D2) by 3 – 6 μs. Consequently, the coincidence window, i.e. the time after a D1 trigger where a D2 trigger is accepted as being coincident, needs to be on the order of several μs. When there is a coincidence between D1 and D2 the complete detector should be read out. Figure 6.1 shows the timing of such a coincident event. A D1 channel and a D2 channel have pulses exceeding their threshold levels, activating the trigger outputs. The trigger pulses are stretched to $\sim$ 7 μs (in the optocoupler cards for the trigger signals) to get a clean signal and to extend the pulse over the whole coincidence window. The coincidence window opens with the D1 trigger and closes after a programmable period "coincidence window". In the mean time the D1 pulse reaches its maximum; the holds of the D1 chips need to be activated already before the coincidence window ends, i.e. before it can be decided if a valid coincidence occurred. The D1 hold is applied with the delay "hold delay 1" (compare chapter 5.1.6) after the D1 trigger. At the end of the coincidence window the decision is made, if coincident or not. In the **coincident case** the hold for the D2 is generated with a delay "hold delay 2" after the trigger signal of D1. The hold timing of the D2 is also derived from the D1 because the time resolution of D1 is better, resulting in reduced time-walk in D2. After the D2 is in hold state the time critical phases are finished. Then a pulse is generated after a minimum time "readout delay"* to start the readout sequence. In the **non-coincident case** (figure 6.2) the hold of the D1 is released after the coincidence window has expired and no readout takes place; the circuit waits for the next rising edge on the D1 trigger lines.

Whether an event will be read out should be decided in a flexible way so that the user can select events according to the type of measurement. For example, it should be possible to select pairs, i.e. events with tracks in D1 (even if there is no D2 trigger), or just all coincidences (at least one D1 and one D2 trigger). At the same time it should be possible to allow high-energy pairs which triggered the bottom plate of the ACS in an anticipated balloon configuration, i.e. events which triggered the bottom of the ACS should be allowed only if they have long tracks in D1. This decision needs to be taken in hardware since the readout rate is very limited in the prototype. Therefore all trigger lines are fed into the coincidence electronics so that the decision — readout or no-readout — can be taken from the pattern seen on the trigger lines. Finally the pattern of triggered chips should be recorded that started a readout — not only for debugging purposes but also for detailed data analysis.

*The sequencer has a built-in delay before starting the readout sequence, which cannot be set lower than 500 ns.

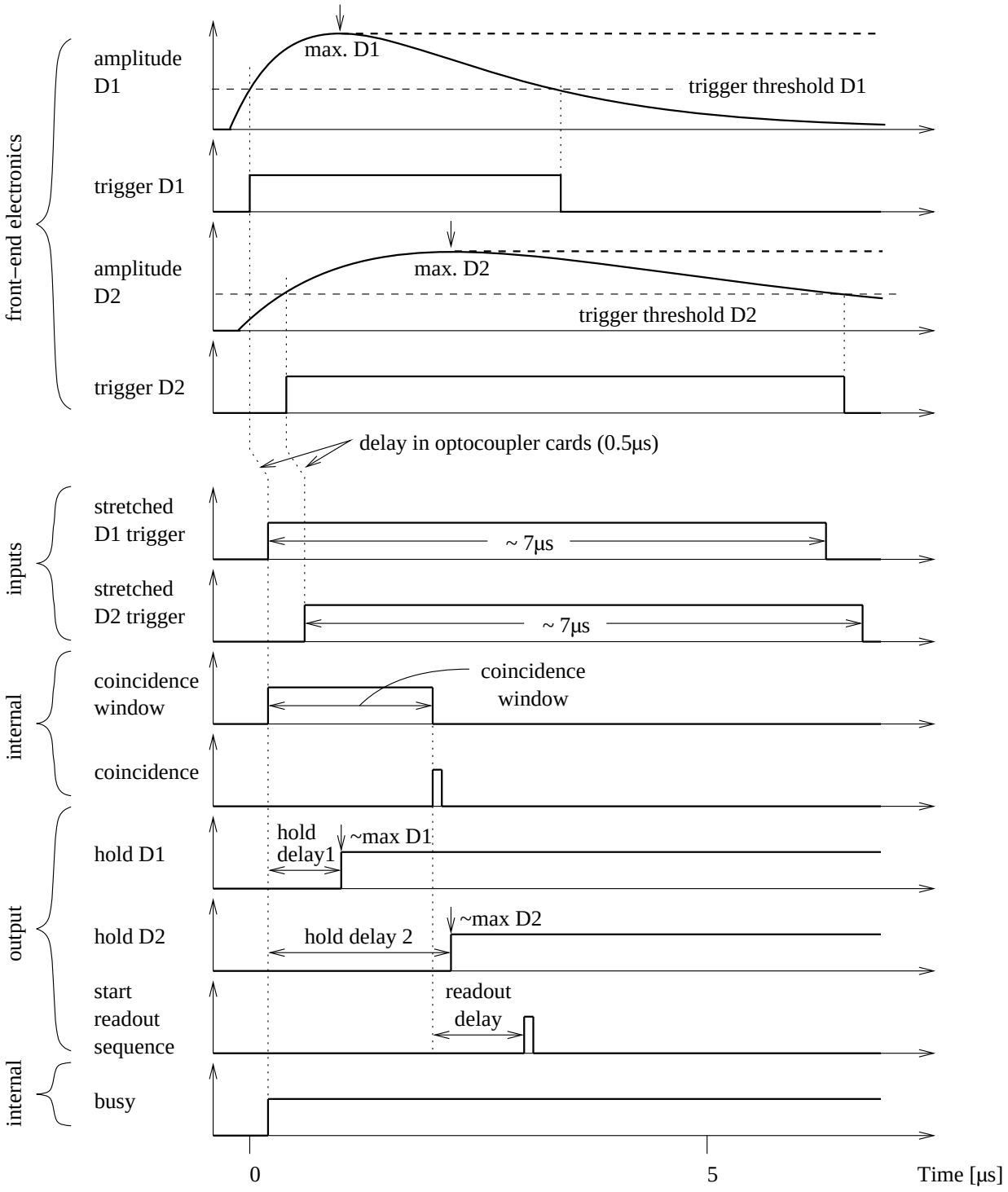

Figure 6.1: Timing diagram for a coincident event. A signal in one tracker and one calorimeter front-end channel (amplitude D1 and D2) is recognized by activating the front-end chip's trigger outputs (trigger D1 and D2). With a delay the stretched trigger pulses arrive at the inputs of the coincidence electronics (stretched D1/D2 trigger). The D1 trigger starts the coincidence window and after its expiration the trigger pattern is evaluated and — in this case — accepted. In the meantime the hold of the D1 detector is applied, the D2 hold is activated after a valid coincidence took place. Finaly the sequencer is started by a short pulse (start readout sequence). From the beginning of the sequence (i.e. D1 trigger arriving at the coincidence electronics) the busy flag is activated.

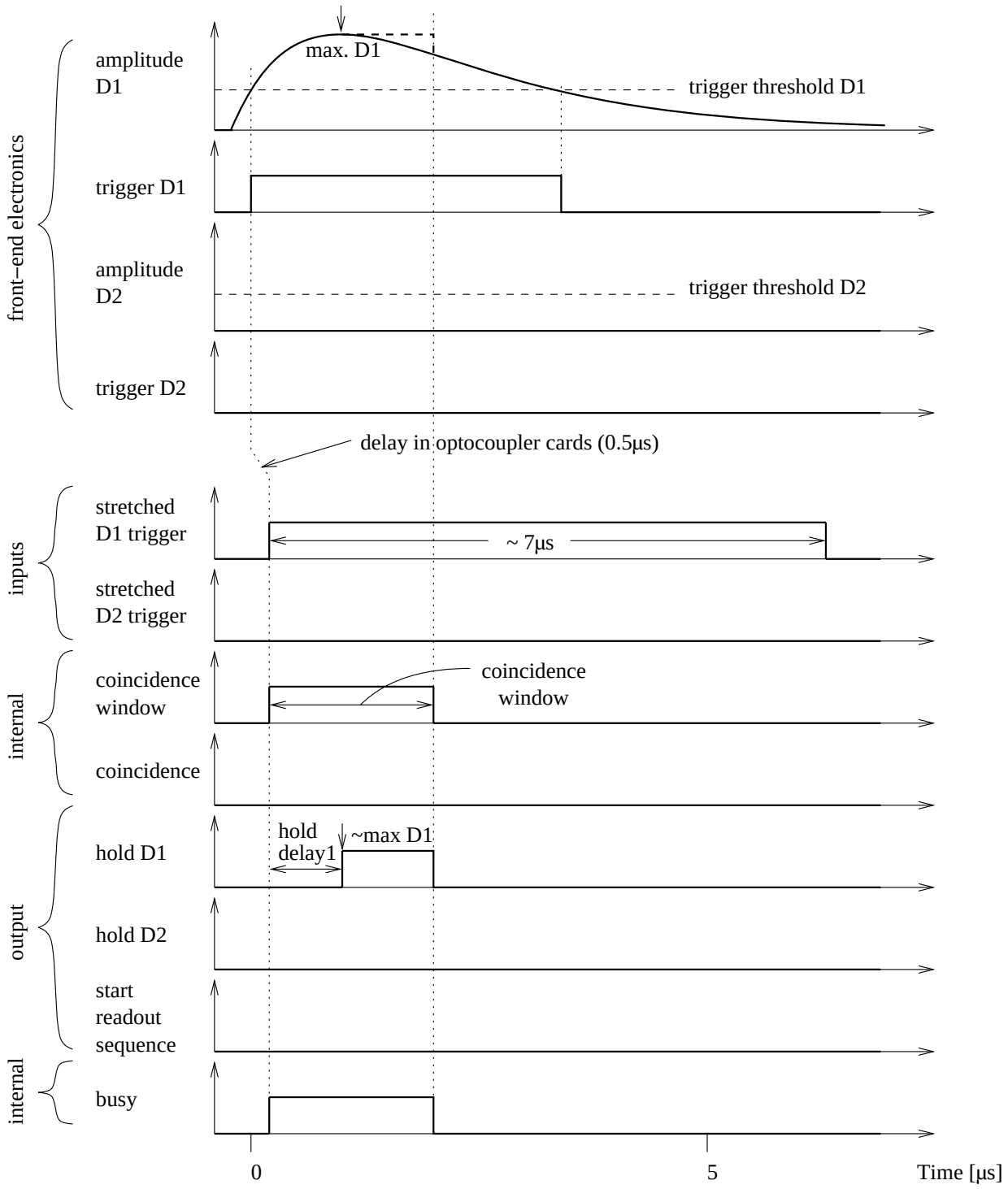

Figure 6.2: Timing diagram for a non-coincident event. The missing D2 trigger leads to an unvalid coincidence and the coincidence electronics returns into the state waiting for a D1 trigger immediately after the coincidence window has expired.

For debugging, health monitoring, and for adjustment purposes the trigger rates of the individual chips need to be monitored. Since all trigger signals are already available in the coincidence electronics, it is convenient to implement also this functionality in the coincidence electronics[†].

Various parameters and configuration data need to be set or read (delay times, trigger patterns, trigger rates etc.) necessitating a fast and versatile interface to the instrument CPU. The VME bus has been chosen, since it is already used by the sequencer, ADCs and other modules.

6.3 Realization

The first version of the coincidence electronics was set up with NIM modules [Schopper, 2002]. All settings were adjusted by potentiometers; no pattern recognition was implemented. As one part of the electronics development for this work, it was replaced by a VME bus card featuring a field programmable gate array (FPGA), random-access memories (RAM), a VME-bus interface, input receivers and output drivers (figure 6.3). All logic is implemented in the FPGA, a XILINX SpartanXL XCS40XL (figure 6.4). The FPGA is configured via the VME bus so that changes in the implementation such as debugging or additional features are a matter of changes in software. Since this FPGA stores its configuration in SRAM cells, it must be configured after power-up. The RAMs hold the trigger patterns. The input receivers and output drivers adapt the voltage levels to those required/provided by the FPGA[‡].

The board holds two 1 MBit RAM devices. Each bit contains the "valid coincidence"/"invalid coincidence" information for a given pattern of triggered detector units (trigger pattern). Since each bit's address consists of 21 bits, this requires reducing 64 trigger (36 × D1, 24 × D2, 4 × ACS) to 21 signals (figure 6.4). Therefore the three trigger signals of a D1 layer are combined (by a logic or) so that one address bit of the RAM is assigned to each layer. The D2 trigger signals are merged into eight address bits (one bit would have been sufficient; up to now there was no need to distinguish between different parts of the calorimeter). The four ACS veto signals are combined into two different veto signals: one absolute veto, which inhibits the start of the whole sequence described above, and one programmable veto, which is assigned to an address bit. The veto signals of the bottom part of the ACS are connected to the programmable veto so that such an event can still be accepted by the trigger pattern. This allows to avoid self vetos of high-energy pair-creation events (self vetos occur when the charged particles of the γ-induced shower pass the calorimeter and generate signals in the lower part of the ACS).

The time critical sequence (compare the theoretical sequence in figure 6.1 with a measured one in figure 6.5) begins at the rising edge of one of the D1 trigger inputs. This is 0.5 μs after a D1 chip triggered due to the delay in the trigger optocoupler cards. In order to reduce chance coincidences and pile-up effects, rising edges of the D1 trigger are ignored, if at the same time a D2 trigger is active. The sequence consists of a series of delays in the FPGA where all time-critical delays are programmable. The first delay is the "coincidence window". The "hold delay 1" runs in parallel to the coincidence window. After it expired the D1 hold is activated. At the end of the coincidence window the pattern of activated trigger inputs forms the address of one bit in the trigger pattern RAMs. If this bit is one, the hold signal for the D2 is generated and the readout is started (chapter 5.2.3). If the relevant bit of the trigger pattern RAMs is zero, the hold signal for the D1 is released and a new cycle can start immediately.

[†]Before the coincidence electronics had been introduced in the prototype, dedicated VME-bus modules (so-called pattern units) were used to record and monitor the trigger signals.

[‡]The XILINX SpartanXL family of FPGAs runs at voltage levels of 3.3V. They are tolerant to 5V input levels, but level shifters are required for the outputs to drive the connected TTL logic.

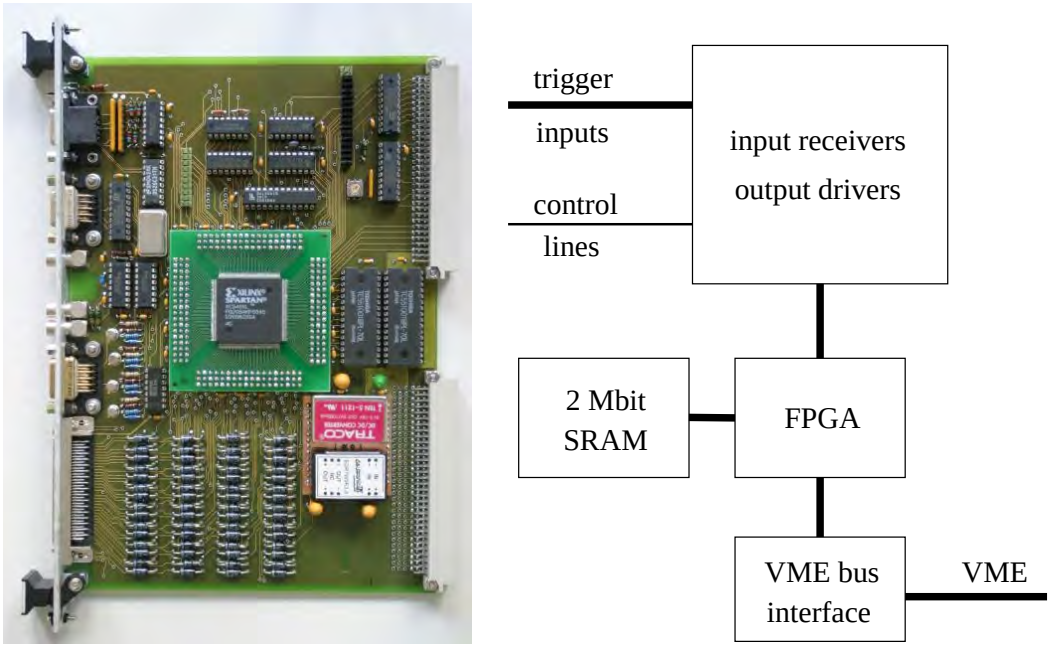

Figure 6.3: Left: Coincidence board. Right: Functional blocks of the coincidence board

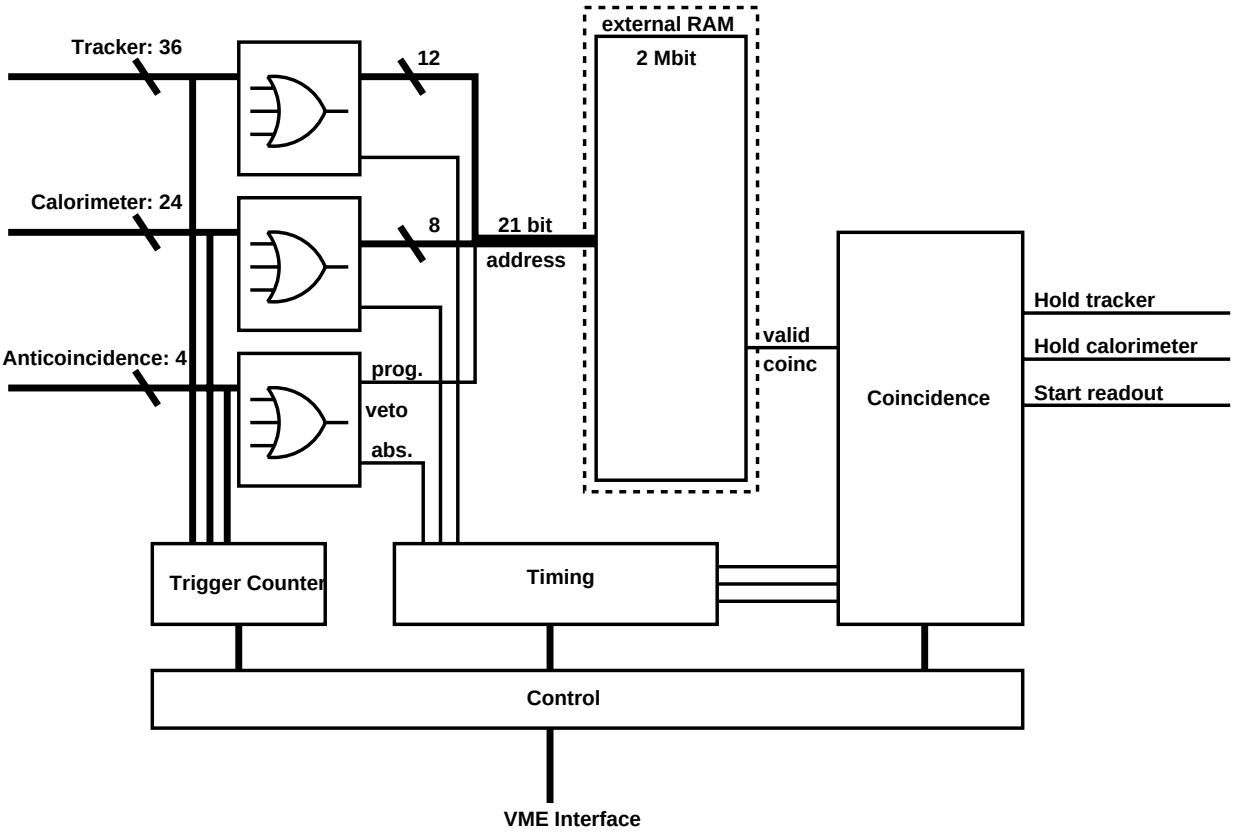

Figure 6.4: Schema of the coincidence electronics

At the beginning of the sequence the busy signal is set which inhibits the start of a new cycle. After the readout is finished or an invalid pattern has been detected, busy is released signaling that the coincidence electronics is ready for a new cycle.

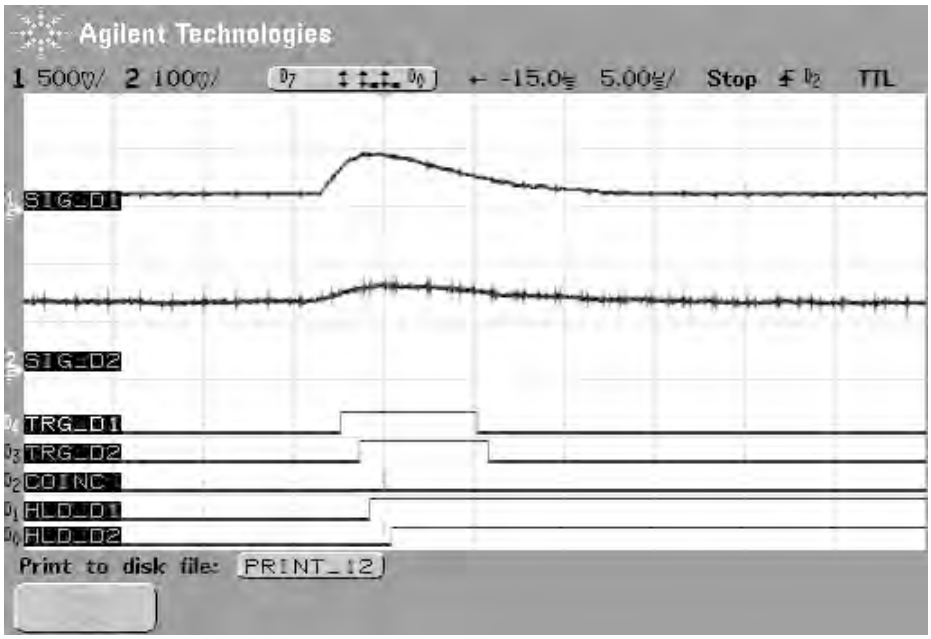

Figure 6.5: Measured coincidence. One channel in the tracker (D1) and one channel in the calorimeter (D2) have been selected. Their shaped signals (SIG_D1 and SIG_D2) are shown in the top two channels of the diagram. The second pair of signals show the corresponding trigger signals (TRG_D1 and TRG_D2 with the fixed duration as seen by the coincidence electronics). That there is a coincidence of a valid pattern is signaled by a short pulse on COINC. The hold signals used to store the current amplitudes are shown in the bottom pair of signals (HLD_D1 and HLD_D2). Note: The shown sequence is NOT a standard readout sequence! In normal operation the shaped signals are not directly accessible. Additionally the HOLD signals are disconnected from the front-end electronics for this measurement. Otherwise the shaped signals (SIG_D1 and SIG_D2) would have constant level after applying the hold signals.

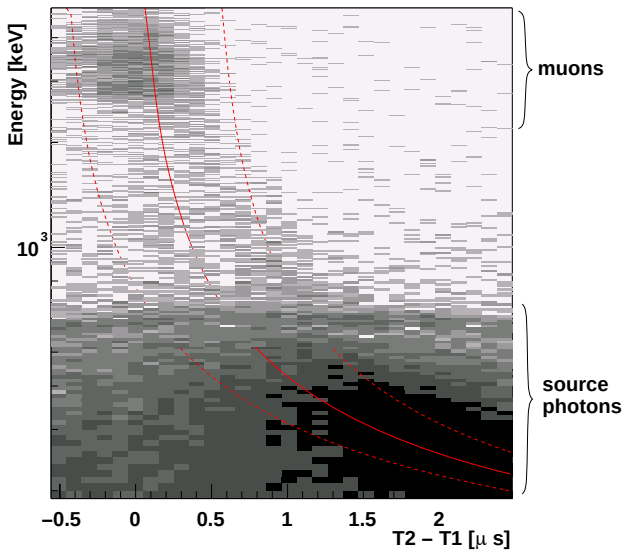

Figure 6.6: Possible reduction of chance coincidences, from [Schopper, 2002]. The difference in the trigger times of the calorimeter (T2) and the tracker (T1) has been determined with a time-to-amplitude converter. since the measurements has been performed at an early stage of the prototype where the coincidences are still selected by a setup of NIM modules.

6.4 Selection of the Coincidence Window

The coincidence window starts at the beginning of the timing sequence in the FPGA. Its duration needs to be set to the maximum rise time occurring in the D2, i.e. $\sim 7\,\mu$s. If it is shorter, events with low energy deposits in D2 (late trigger) are not read out. Large coincidence windows, however, increase the amount of chance coincidences which use up the limited readout capacity. The compromise chosen for the prototype is a duration of $2.2\,\mu$s for the coincidence window (see [Schopper, 2002] for details). The resulting low energy cutoff is around 500 keV as observed in chapter 9.1.

6.5 Trigger Patterns

Whether there is a valid coincidence is determined by the trigger pattern. Three patterns are commonly used in the MEGA prototype:

1. Simple coincidence: At least one D1 chip and one D2 chip triggers, no further restrictions.
2. Simple coincidence with top layer in anti-coincidence: During the accelerator measurements (HIGS, chapter 7.2) many charged particles crossing the detector polluted the data at a beam energy of 50 MeV. These are rejected by using the top layer in anti-coincidence. Otherwise scheme "1 " is used.
3. Long tracks in D1: Muon tracks are selected by a pattern which requires at least five triggered D1 layers. No requirements are placed on the D2 signals.

One could think of many variations depending on the measurement situation. The main driver for the implementation of this flexible trigger selection mechanism was the anticipated balloon flight. In order to be able to select "high quality" events such as pairs or Compton events with tracks, complicated trigger patterns need to be selected. If defective strips of the tracker layers are taken into account this results in patterns such as four or more triggering layers in a row, one layer may fail in between, and at least one D2 trigger. At the same time the self veto of high-energy pairs should be avoided. This results in allowed patterns, where the programmable veto has triggered, but the lowest few tracker layers need to be triggered.

Another set of allowed trigger patterns was needed when the tracker of the prototype was set up as demonstrator instrument for a medical PET camera. In this case only the tracker layers were used and coincidences between the upper and lower half have been selected for readout (this measurement is described briefly in appendix B.4.

6.6 Dead Time Measurement

In order to evaluate the efficiency of the detector, the knowledge of the instrument's dead time during the measurements is crucial. Due to the slow data acquisition process (chapter 5.2) the dead time of the prototype exceeds the lifetime (during the HIGS measurements dead times of 80% and more were accepted). The data acquisition system is ready for the next event after the ADC memories have been completely read out. Since the amount of data to be read varies[§] and since the reading operating system is a multitasking system (Linux), the readout time is not constant

[§]The amount of data to be read from the ADC memories depends on the data reduction method. The ADC modules already offer data sparsification in hardware (chapter 5.2.5) which reduces the readout time.

and needs to be measured each time. For this purpose, the coincidence electronics generates time stamps at the start of the coincidence sequence and at the end of the readout. Additionally the coincidence sequences which did not lead to a valid coincidence (i.e. no readout) are counted. The sum of both components reflects the prototype instrument's dead time.

6.7 Timing Issues

Some less-than-optimal properties of the MEGA prototype system result from the described timing which should be kept in mind while evaluating coincident data:

The data used for calibrating individual channels are acquired by reading out only the D1 or only the D2 respectively. The hold delay is set to a fixed value (individually set for D1 and D2) after the trigger. The single-channel calibration compensates this to some degree. When reading out D1 and D2 in coincidence the hold times are derived from the *earliest* D1 trigger. Considering an individual hit of an electron track in D1, its signal pulse is held earlier than would be the case if this channel had generated the first (or only) trigger, and the time-walk will be over-compensated. Thus a kind of double compensation takes place, the first by "correction" of the trigger time (the earliest D1 trigger defines the timing also for the other channels), and the second by the energy calibration. This also fully affects the D2 channels.

Besides the energy calibration another problem is induced by the time-walk problem. The coincidence window needs to have a very long duration in order to avoid losing low-energy events (chapter 6.4). This in turn increases the number of chance coincidences. There is no measure to recognize and skip in hardware chance coincidences occurring during the coincidence window. Instead these have to be filtered afterwards by the software. The following low-level method has not yet been applied to any data since the high-level cuts as described in Zoglauer [2005] are very powerful, thus a low-level filtering was not necessary. Nevertheless, this method should be briefly described here since it illustrates the relationship between signal amplitudes (energy deposits) and timing: The coincidence electronics measures the time between the first D1 and the first D2 trigger. This quantity could be used to suppress chance coincidences. A global method is described in [Schopper, 2002] where the time difference is correlated with the largest energy deposit in the D2. It keeps the events which have D2 trigger delays matching the pulse heights (figure 6.6 shows this correlation and a possible cut). Since the various channels differ in their timing behavior (rise times and trigger thresholds) a more accurate suppression could be achieved if the pulse shapes and the trigger times of each readout channel were known. The necessary measurement and evaluation would be very time consuming and significantly exceed the scope of this work. Additionally, complications are expected, for example from rise times varying with pulse height.

Part III

Calibrating the Full Prototype

Chapter 7

Prototype Calibration Measurements

Extensive calibration measurements have been performed with the MEGA prototype described in the previous chapters. The ACS was not needed for measurements of photon beams and thus omitted.

Since the front-end electronics of the tracker dissipate a power of ~ 4 W, the inside of the tracker housing heats up above room temperature ($\sim 30°$C). At these temperatures, the noise of the strip detectors is significantly elevated. We have therefore installed a cooling system. The detectors are covered by a box through which a flow of cold air from a standard mobile air conditioner is directed. An air temperature of $\sim 12°$C cools the inside of the tracker housing down to $\sim 20°$C.

7.1 In the Laboratory

7.1.1 Measurements with Radioactive Laboratory Sources

In the laboratory the radioactive sources ^{22}Na, ^{137}Cs, and ^{88}Y are placed in the field of view. The setup with a source holder as used before the Duke campaign is shown in figure 7.1. After the Duke campaign, the setup was mounted in the balloon mechanical structure (figure 7.2). Several point source measurements as well as measurements of extended sources have been performed. For each instrument configuration — in particular after each assembly / disassembly of the system and for different instrument environmental conditions — separate calibrations are necessary. Since this work concentrates on the prototype's response over its full performance energy range which can only be derived from HIGS data (chapter 7.2), most of the laboratory source measurements are not included in this work.

7.1.2 The Tagged Source

For time resolution measurements, a tagged source has been used (figure 7.3). It consists of a plastic scintillator covered with a ^{60}Co-doped foil; the scintillator is read out by a photomultiplier with attached electronics. ^{60}Co is a β^- emitter; in approximately 50% of the decays the electron is registered in the scintillator. The resulting pulse is converted into a digital signal, delayed, and given into the coincidence electronics. There an additional counter is implemented (in the FPGA) which counts the time between a time tag and the next valid coincidence (i.e. readout).

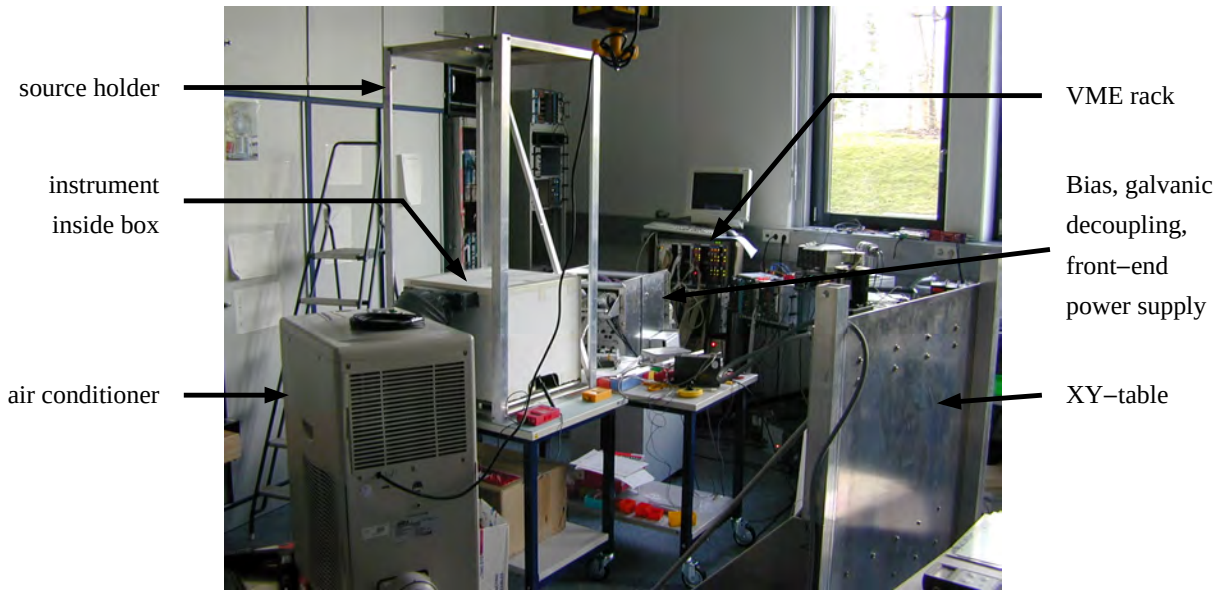

Figure 7.1: Measurement setup in the laboratory. The XY-table is set up in preparation for the accelerator measurement.

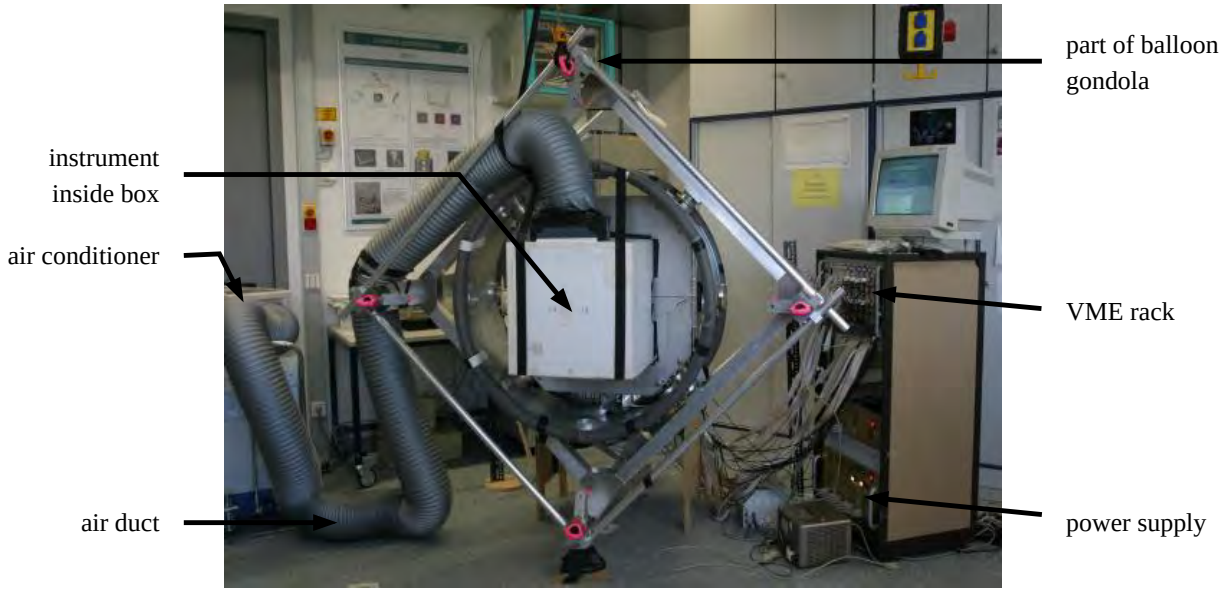

Figure 7.2: Measurement setup in the laboratory after the campaign at HIGS. The instrument is mounted in the balloon gondola structure.

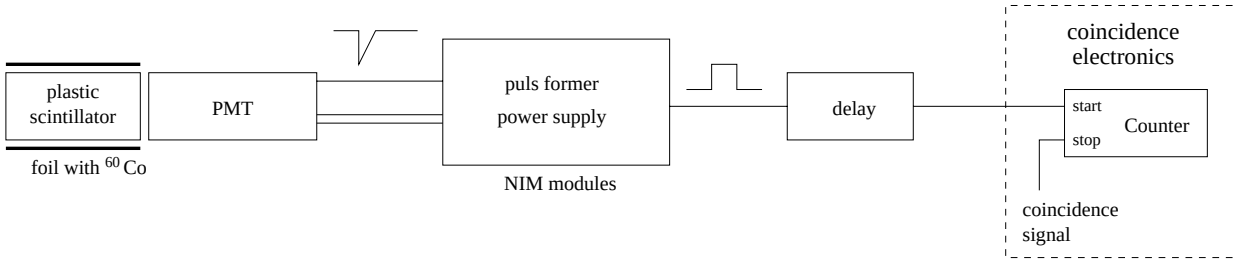

Figure 7.3: Extension to the MEGA prototype hardware for measurements with a tagged source. A counter determining the time between a trigger from the tagged source and a valid coincidence in the MEGA prototype is implemented in the FPGA of the coincidence card.

Figure 7.4: Setup with tagged source

7.2 At the High Intensity Gamma-ray Source

7.2.1 The High Intensity Gamma-ray Source (HIGS)

The High Intensity Gamma-ray Source (HIGS) is an inverse Compton beam driven by the Duke Free Electron Laser (FEL) [Litvinenko and Madey, 1995, Litvinenko et al., 1997, 2001]. Figure 7.5 schematically illustrates the FEL and HIGS facility: Electrons are injected into the electron storage ring as a single bunch. One side of the ring contains wigglers, i.e. many magnets generating an alternating magnetic field. This field forces the electrons on a sinusoidal trajectory, causing them to emit synchrotron radiation at wavelengths between IR and UV (determined by the electron energy, the wiggler geometry and the magnetic field strength). Two mirrors forming a laser cavity reflect the resulting photon bunch back and forth. Two different sets of mirrors were used, one for the IR to optical range of the FEL photons, and one for the optical to UV range. The distances in the storage ring and in the laser cavity are adjusted such that the electron and photon bunches are co-moving (overlapping) in the wiggler. This leads to resonant amplification (stimulated emission) of photons. The laser photons are boosted up to γ energies (0.7 – 50 MeV) when a second electron bunch is injected into the storage ring and collides with the photon bunch in a field-free zone. The IR-to-UV photons are backscattered in inverse Compton interactions forming the γ beam. Lead collimators (we used 2.54 and 1.27 cm diameters) restrict the photons to a pencil beam with an energy spread of 1 – 2%. The laser photons are fully polarized; this polarization is retained

through the inverse-Compton process resulting in a fully polarized γ-ray beam [Litvinenko and Madey, 1995].

Due to this generation process the γ-ray beam is pulsed with a repetition frequency of 2.7898 MHz which is the revolution frequency of the electron bunches.

A high-purity germanium detector was available to determine the energy profile of the beam. The spectra obtained for the 700 keV and the 5 MeV beam are shown in figure 7.6.

7.2.2 Measurement Setup

Experiments at HIGS are set up in an experimentation hall, the so-called γ-vault. A schematic view of the relevant collimators, walls, and detector placements is shown in figure 7.7. Since the MEGA prototype should ideally be illuminated over its complete area, it was mounted on a computer-controlled XY-table. This enabled moving the instrument accurately and repeatably across the γ-ray beam. To allow different incident angles, the XY-table was turnable (by hand). For the alignment two theodolites were used. This ensured a higher angular and lateral precision (several arcseconds and sub-mm) than needed (arcminutes and few mm). The pattern of the beam incidences is shown in figure 7.8. In order to decrease the amount of chance coincidences, the calorimeter channels which lay in the direct path of the beam were blocked, i.e. the trigger signals of these channels were switched off. However they still were read out.

The beam intensity is not stable due to operational aspects: Electrons may be scattered out, requiring a refilling of the storage ring from time to time. Thus the setup had to be extended by a beam monitor. It consisted of a 1 cm thick plastic scintillator (5 cm $\times$ 5 cm area) immediately behind the final collimators (figure 7.9 left). In order to calibrate its count rate over the different beam energies, a NaI detector (25 cm diameter, 12.5 cm thick, figure 7.9 right) was added as "stopping detector". While the NaI detector was placed behind MEGA during normal operation, it was moved in front of MEGA for the beam monitor calibration runs. The decay of the beam flux can be seen in the plastic detector rate (figure 7.10). During the gaps in the rate fresh electrons were injected into the storage ring.

The upper limit of the beam-photon rate, i.e. the rate after reinjection of electrons, is chosen to result in a readout rate of 120 events per second which is 80% of the saturation rate. This correponds to a photon rate in the beam of $\sim$50 000 γ rays per second.

Due to the pulsed nature of the γ-ray beam, background suppression can be achieved by gating the data acquisition system with an electrical signal synchronous to the beam pulses. Since the MEGA prototype has a coincidence window of 2.2 μs the individual γ-ray pulses cannot be resolved (only 0.36 μs between two pulses) and this method is not applicable.

Chapter 8 is dedicated to the beam monitor calibration including approach and challenges as well as results.

7.2.3 Performed Measurements

For every XY-table position 10 000 – 50 000 events were collected. A compromise between limited measurement time and statistics needed to be found. For example, there is no need to spend a lot of time on positions where the beam is directed onto passive material such as the electronic boards. During the measurement campaign from April 21st to May 6th a total of $15.5 \cdot 10^6$ triggered events were recorded, most above 8 MeV. An overview of angles and energies at which measurements have been performed is given in appendix H.2. A graphical illustration of the measurements is shown in figure 7.12.

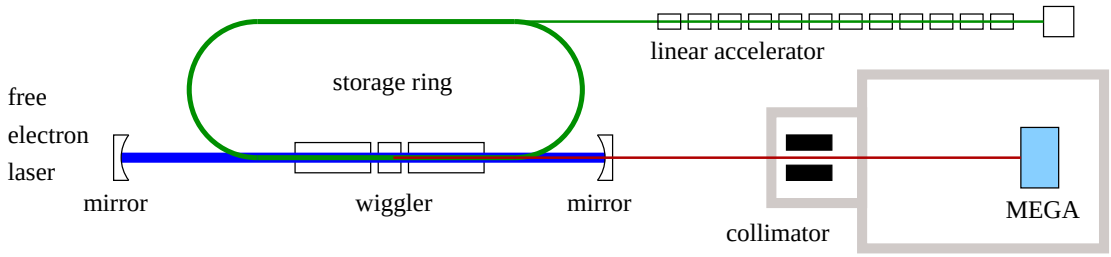

Figure 7.5: Schematic plot HIGS/FEL

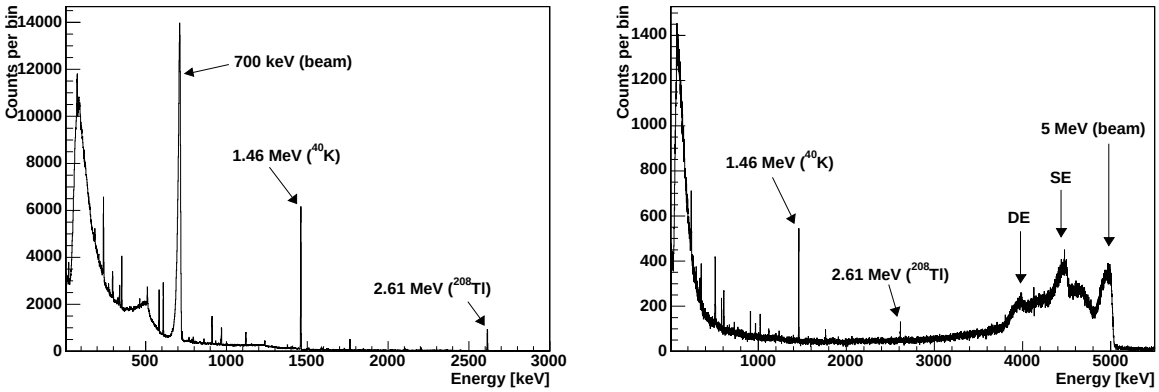

Figure 7.6: Beam (left: 700 keV, right: 5 MeV) spectra taken with a high-purity germanium detector. Background lines used for calibrating the detector are indicated. In the 5 MeV spectrum the single escape (SE) and double escape (DE) peaks are observed.

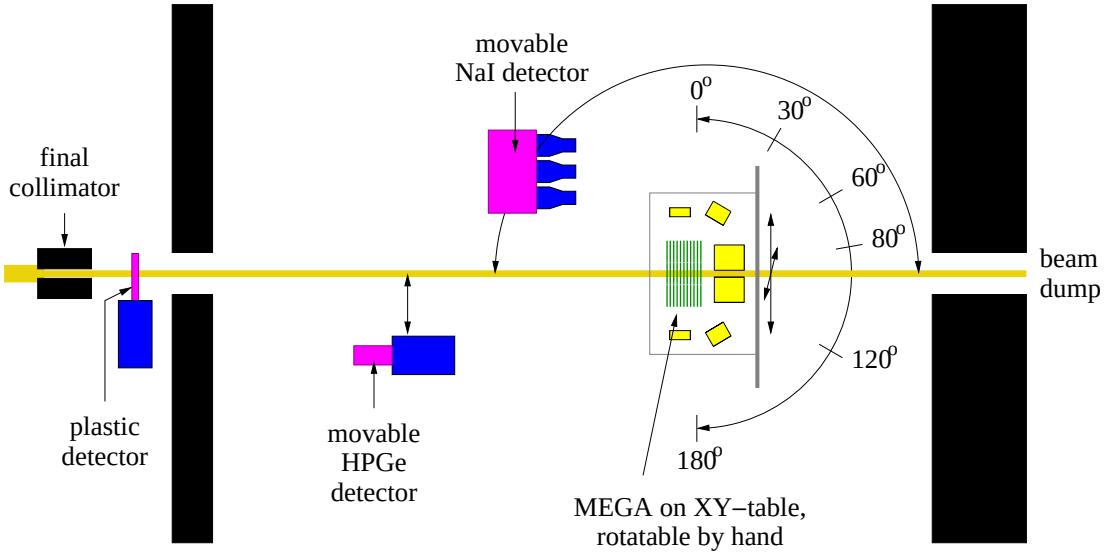

Figure 7.7: Measurement setup of the MEGA prototype at HIGS. The plastic detector monitors the beam intensity. The NaI detector is a stopping detector for calibration of the plastic detector.

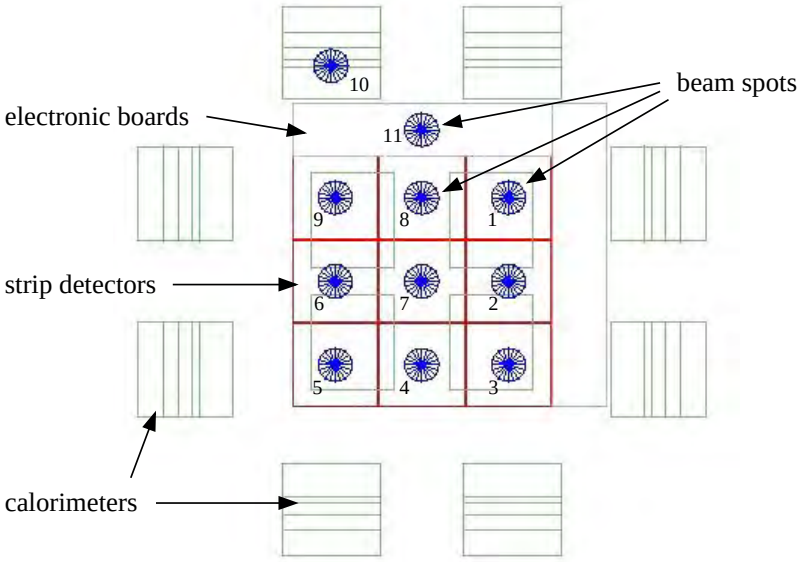

Figure 7.8: Pattern of beam incidences. The markers of the beam spots are to scale with the beam size when the collimator with 2.54 cm diameter is built in.

Figure 7.9: Beam monitor. Left: Plastic scintillator behind collimator and sweeper magnet deflecting charged particles, e.g. from pair creations, out of the beam path. Right: NaI detector in γ-vault.

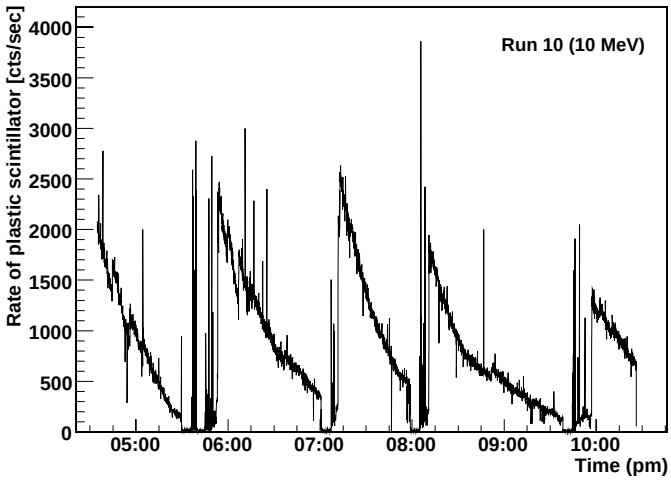

Figure 7.10: Trigger rates of the beam monitor's plastic scintillator. The rates are recorded during a 10 MeV run and illustrate the decay in beam intensity due to the loss of electrons (electrons undergoing a back scatter are not any more in the acceptance range of the storage ring) and the reinjection phases.

The event selection criterion used (valid trigger patterns) was a coincidence of at least one hit in the tracker and one hit in the calorimeter. At beam energies of 10 MeV and higher (except 25 MeV*) the top layer (the one operational only on its p-side) was required to have *no* hit in order to suppress pair creation signatures from events happening in mechanical structures in front of the MEGA tracker.

In addition, *chance* coincidences occur between one beam photon interacting in the tracker and another converting in the calorimeter which would already saturate the readout system. Thus the triggers were blocked of those calorimeter channels which overlap with the γ-ray beam.

*The event selection criterion was changed at the beginning of the first measurement series of a 50 MeV beam because too many events were recorded which had their starting point in (or even in front of) the first layer. The 25 MeV measurement was performed prior to this change (see appendix H.2).

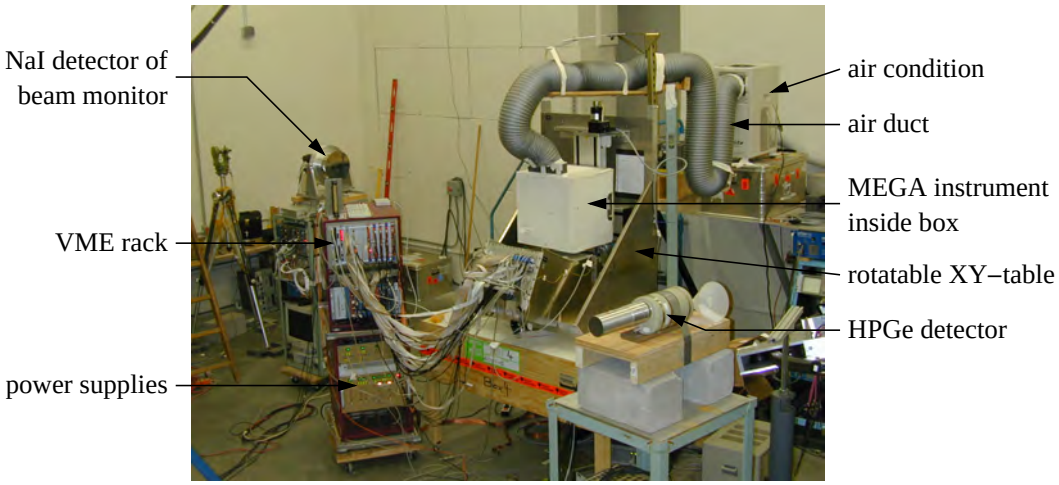

Figure 7.11: Picture of the MEGA setup at HIGS in the γ-vault

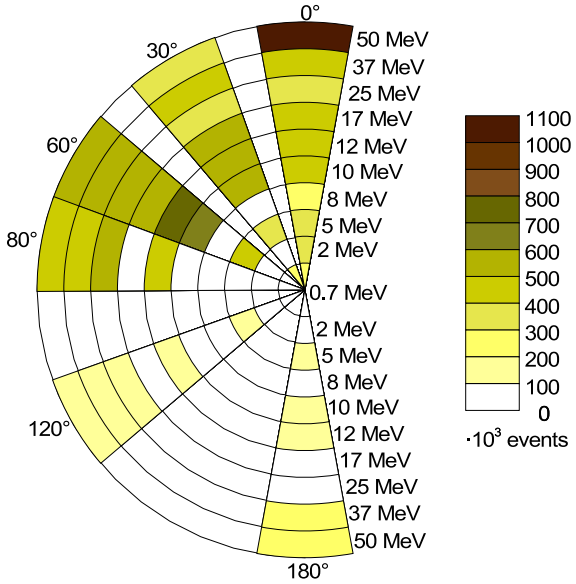

Figure 7.12: Diagram showing the measurement energies and incidence angles. The number of triggered events for each run is color coded. Appendix H.1 lists the numbers.

Chapter 8

Beam Monitor

The beam intensity of the HIGS facility at Duke University varies widely mainly due to the loss of electrons after they have undergone a back scatter interaction. So the photon flux impinging on the MEGA prototype needs to be monitored. No calibrated monitoring system was installed by the operators of the beam, so a dedicated setup had to be assembled. A low-Z detector (plastic scintillator) was put into the beam which has a conversion efficiency on the order of 1%. In order to calibrate the measured plastic scintillator rate, a thick, high-Z (NaI) detector has been used.

The whole beam monitor system including the detectors, readout electronics, and the data acquisition was supplied by collaborators from the University of New Hampshire (UNH) and from Goddard Space Flight Center (GSFC). The evaluation of the acquired data was done as part of this work at MPE.

8.1 The Setup

The low-Z detector in the beam is a plastic scintillator (material: BC 408, size: 5 cm×5 cm×1 cm) read out by a photomultiplier. The high-Z detector consists of a NaI crystal (25 cm diameter, 12.5 cm thick) read out by five 3-inch photomultipliers. Their placement within the whole setup is illustrated schematically and with photos of the detectors in figures 7.7 and 7.9. A detailed drawing of the electrical setup can be found in figure 8.1. Not shown is the VME rack housing a Peak Sensing ADC (C.A.E.N. Mod. 785) and a PCI-to-VMEbus adapter (SBS Mod. 618). The trigger rates of both detectors are acquired by the rate meter (in the center of the drawing) which is read out via a serial interface (RS 232). Additionally the trigger pulses of the plastic detector are fed into MEGA's coincidence electronics where they are counted (redundant to the rate meter) and recorded in the MEGA data stream. The spectrum seen by the NaI is digitized by the Peak Sensing ADC during normal operation, whereas the spectrum of the plastic scintillator is only recorded in a special calibration mode.

8.2 Measurements with the Beam Monitor

The performed measurements could be divided into three groups:

1. The properties of both the plastic and NaI detectors (thresholds and gains) have been determined in measurements with radioactive laboratory sources.
2. For the actual calibration the rates of both detectors for each beam energy are measured (table 8.1).

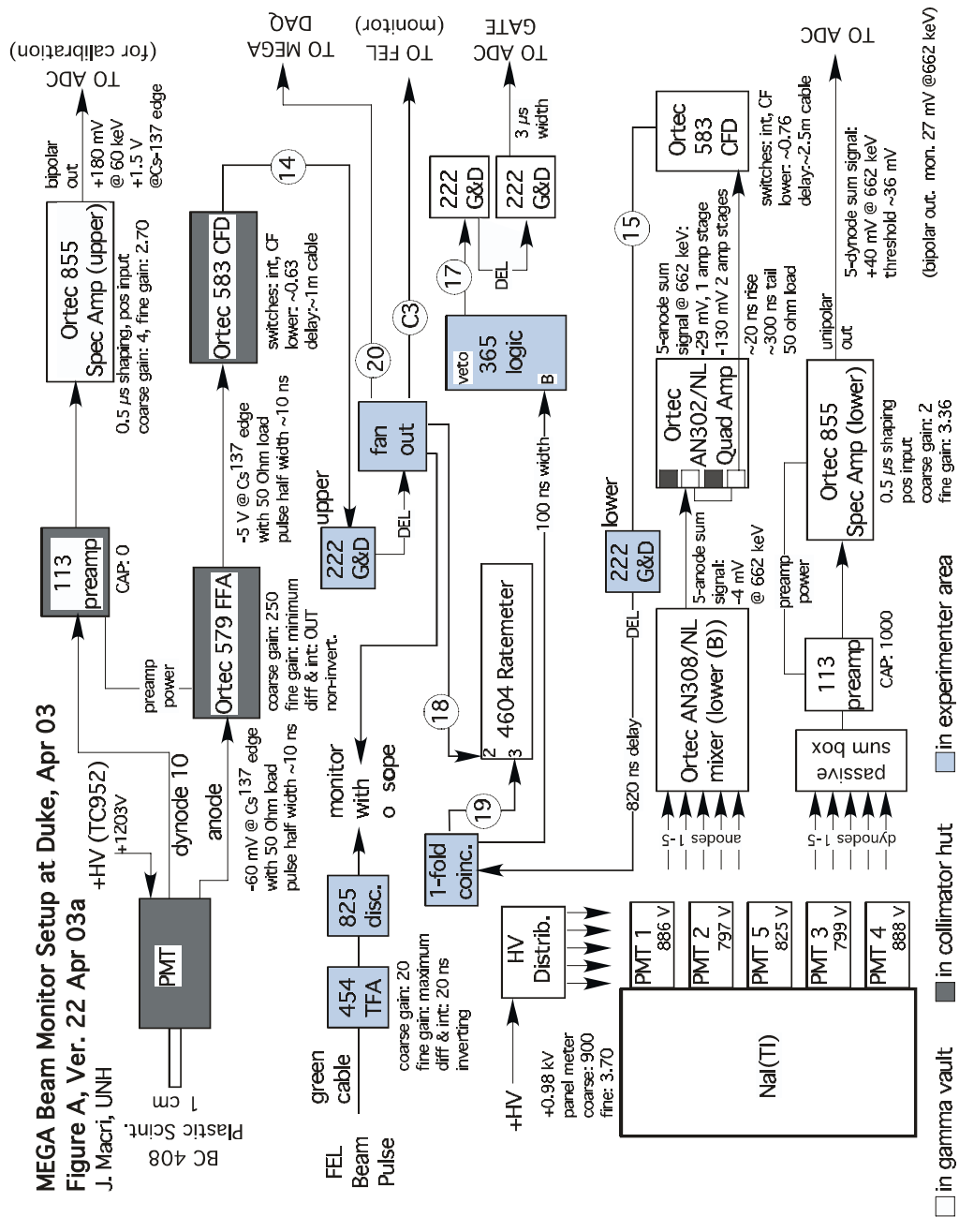

Figure 8.1: Electrical schematic of the beam monitor, figure from [Macri, 2005]. The working principle in few words: From the PMT reading out the plastic scintillator an energy spectrum can be gained from the signal of its last dynode. This signal is amplified, shaped, and given to the ADC. The signal of the PMT's anode is used to derive the trigger rate for monitoring the beam intensity. The anode signal is amplified, discriminated by a constant-fraction-discriminator, and given a constant length. The resulting pulse is distributed to a rate meter, the MEGA DAQ, and to instruments for visual inspection. The five PMTs coupled to the NaI crystal are adjusted to have the same gains by means of their high voltage supplies. The signals of the last dynodes as well as the ones of their anodes are added. Again, the dynodes' signal is used for spectroscopy, and the anodes' signal for measuring a rate so that the processing steps are the same as for the plastic scintillator.

measurement name	beam energy [MeV]	date
Calibration_700keV	0.71	Apr. 23, 2003
Calib_2MeV	2.0	Apr. 22, 2003
Calibration_5MeV	5.0	Apr. 23, 2003
Calibration_8MeV	8.0	Apr. 24, 2003
Calibration_10MeV	10.0	May 6, 2003
*	12.0	May 1, 2003
Calibratio_17MeVC	17.0	May 5, 2003
Calibration_25200keV	25.2	Apr. 28, 2003
*	37.0	May 2, 2003
Calibration_50MeV	48.9	Apr. 29, 2003

Table 8.1: Beam monitor calibration measurements (* calibration data lost due to computer problem)

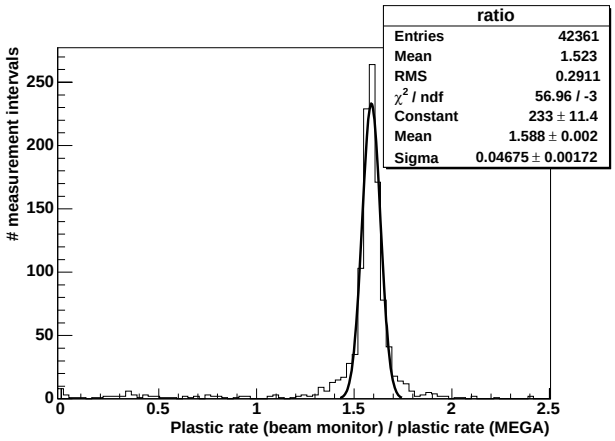

Figure 8.2: Ratio of rates measured by the beam monitor DAQ and the MEGA DAQ. The difference results from a too short pulse on the input of the MEGA DAQ.

3. During the MEGA measurements the beam monitor recorded the plastic rates as a measure of the beam intensity. The NaI was placed behind the MEGA instrument and its data was recorded additionally, but not used. The beam monitor was operated during all beam measurements with MEGA as listed in appendix H.2.

Due to software and computer setup problems of the beam monitor DAQ system one week of data was lost. During this time the plastic rates are available from the MEGA DAQ, but the beam monitor calibration measurements are lost (at energies of 12 MeV, 37 MeV and a second time 48.9 MeV).

The plastic rates counted by the MEGA DAQ need a correction factor due to a too short input pulse. The coincidence electronics runs at a clock of 50 MHz, i.e. 20 ns period. A pulse needed to be applied more than one cycle to be safely recorded (the data is taken over with the rising edge of the clock), but the pulse from the beam monitor DAQ had only a width of $\sim$ 13 ns. A correction factor from measurements with rate data from both DAQ systems is derived to 1.588 (figure 8.2).

8.3 Properties of the Detectors

The trigger rates of the detectors used to measure the beam intensity are depending on their trigger thresholds. For evaluating these thresholds an energy calibration and the lower cut-off of the spectra must be determined.

Run	Energy	$\frac{\text{Trigger rate plastic}}{\text{Trigger rate NaI}}$			$\frac{N_{beam}}{N_{plastic}}$
		measured	calculated	simulated	
1	0.71 MeV	19.4%	-	-	12.2*
2	2 MeV	6.6%	4.9%	6.8%	18.1
3	5 MeV	5.0%	3.0%	3.8%	21.2
4	8 MeV	4.0%	2.3%	3.1%	26.6
10	10 MeV	3.8%	2.1%	2.9%	28.1
5	12 MeV	n/a	1.9%	2.9%	28.0*
9	17 MeV	4.2%	1.7%	2.3%	24.9
6	25 MeV	3.1%	1.5%	2.0%	34.0
8	37 MeV	n/a	1.5%	2.1%	32.8*
7	49 MeV	5.2%	1.4%	2.6%	20.5

Table 8.2: Trigger rate ratios and plastic trigger efficiencies for the different beam energies (* values extrapolated according to simulation). Measured, calculated (assuming some simplifications, see text in chapter 8.4), and simulated values are compared.

For the plastic detector the 59.5 keV line of ^{241}Am is measured to gain an energy calibration. The threshold should be on the order of 60 keV and needs to be raised for the beam measurements. It is adjusted using the Compton continuum in the spectrum of a ^{137}Cs source. Figure 8.3 shows both spectra, the ^{241}Am measurement having a low threshold for energy calibration, and the ^{137}Cs measurement for determining the raised threshold ($\sim$ 75 keV).

The gain of the NaI detector can be easily calibrated by the ^{40}K and ^{208}Tl lines which are clearly evident even during an operating beam (figure 8.4). The threshold for the shown 50 MeV beam measurement is around 850 keV, which is high compared to the other calibration measurements: The thresholds range from $\sim$ 650 to 850 keV (for an unknown reason this appears to be correlated with the beam energy). Additionally a small drop (2 – 3%) of the gain with time has been observed.

A coarse estimate for the efficiency of the plastic detector at the various beam energies can be derived from the ratio of the plastic detector count rate to that of the NaI detector. This ratio directly represents the trigger efficiency of the plastic detector if one assumes the trigger efficiency of the NaI detector to be 100%. The resulting beam monitor efficiencies are listed in table 8.2. Since the NaI has a fairly broad threshold function — in accordance with its energy resolution — and since the beam energy of 710 keV in the first run lies only slightly above the threshold of $\sim$ 650 keV, the NaI counts only a fraction of the beam photons making this calibration measurement of the beam monitor useless. Originally, the 710 keV run was intended to determine the polarization sensitivity of the MEGA prototype only, and the beam monitor was not set up for this low energy.

8.4 Expected Results from Calculation and Simulation

An estimate for the ratio of the plastic to NaI detector rates at a given (monoenergetic) beam energy can be calculated with some of simplifications:

- The trigger efficiency of the NaI detector is assumed to be 100% (the later-discussed simulations show an efficiency of $\sim$ 95%).
- The plastic scintillator is thin enough that only single interactions need to be taken into account.
- Secondary electrons do not escape from the plastic detector without being recorded (interactions near the detector surface could lead to short electron/positron paths in the detector

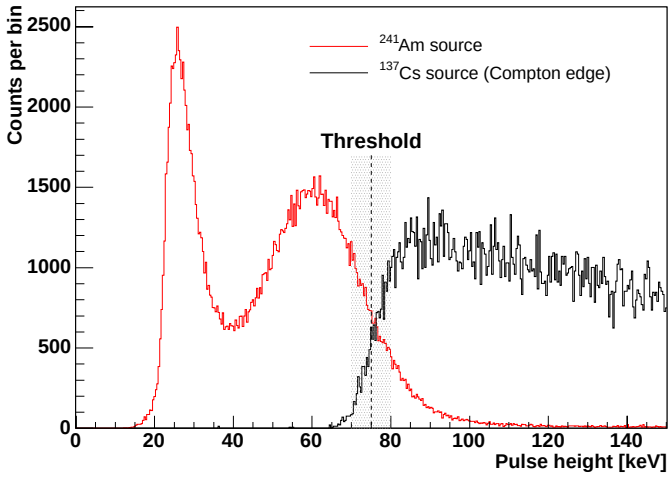

Figure 8.3: Threshold of the plastic detector. The red line shows a ^{241}Am spectrum taken with a low threshold. It was used for energy calibration. The threshold during the beam measurements was set to a higher level which is determined from the Compton distribution of a ^{137}Cs source (black spectrum). The final threshold lies between 70 keV and 80 keV.

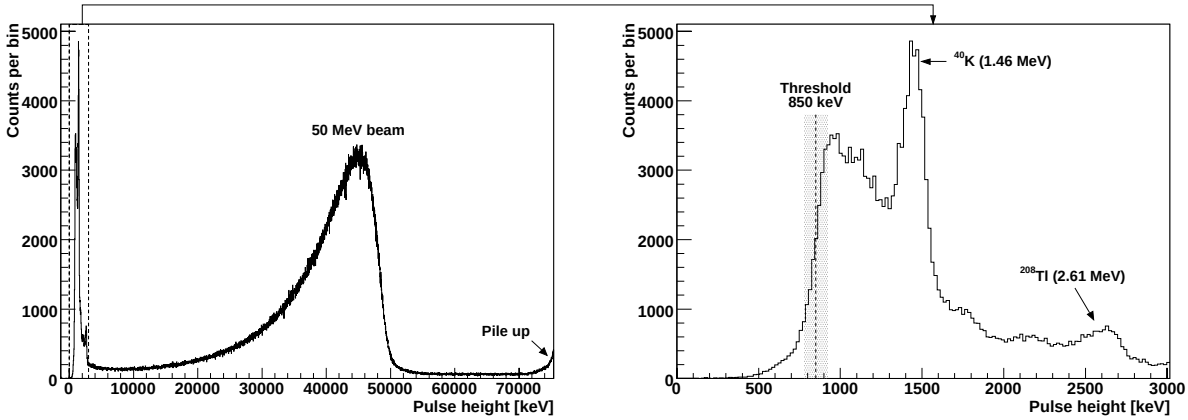

Figure 8.4: Spectrum during a running 50 MeV beam measured with the NaI detector. Left: Full range showing the background, the (incompletely absorbed) beam photons and the beginning of the pile-up. Right: Zoom in the "background region" where the ^{40}K and the ^{208}Tl lines are used for energy calibration. The threshold lies at $\sim$ 850 keV.

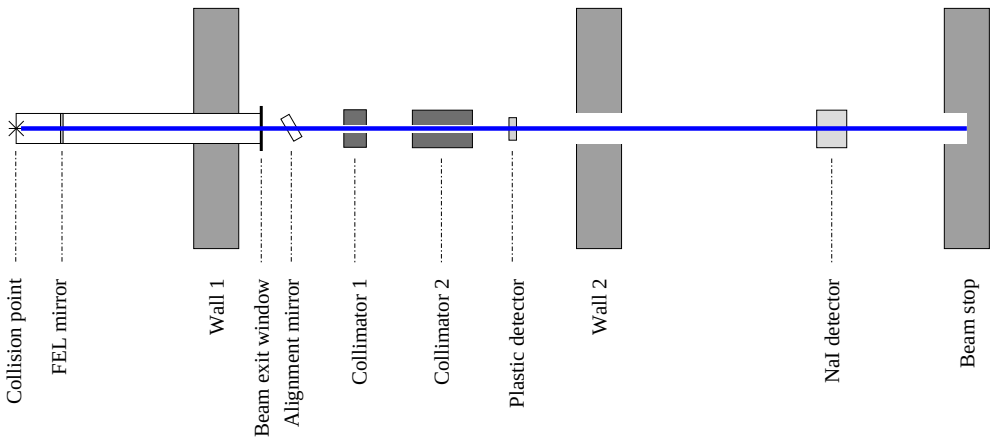

Figure 8.5: Sketch of beam monitor simulation geometry (not to scale, some details are left out). Collimator 2 is only used for energies of 17 MeV and higher.

where not enough energy is deposited to overcome the trigger threshold)

- All passive material is neglected.
- Photo effect is neglected.

Under these assumptions the ratio of the plastic to the NaI detector rate can be calculated by integrating equation 1.6 for energies larger than the threshold energy (contribution from the Compton effect) and adding the (tabulated) pair creation cross section (equation 1.1). The results are listed in table 8.2.

A more detailed analysis is possible with simulations, where the points neglected above are all incorporated. For this task, the GEANT4 simulation package [Agostinelli et al., 2003, Allison et al., 2006] has been used in combination with the front-end tools of the MEGAlib library [Zoglauer et al., 2006]. The simulation geometry is sketched *(*not to scale*)* in figure 8.5. Details such as detector housings are not shown even though they *are* included in the simulation geometry. Collimator 2 has a diameter of 1.27 cm and is removed from the setup for energies of 12 MeV and lower. This has been accounted for also in the simulation. The predicted ratio of the plastic to NaI detector rates can again be found in table 8.2.

8.5 Comparing measurements and simulations

Large discrepancies between the measured, calculated, and simulated values are evident. The ratios obtained from analytic calculations mark only a lower limit since the NaI efficiency is overestimated and "dirt effects" are neglected — e.g. pair creations in passive material, especially in the collimators (these pair creations are responsible for the increasing ratios with energy in the simulation when comparing the 37 MeV with the 49 MeV beam). In an attempt to understand the discrepancies between simulation and measurement several variations of the geometry have been simulated. The most promising variation is a misaligned collimator 2. Such an additional, unintended "target" in the beam effectively produces pairs especially at the higher energies. Also additional material in the beam and around the beam has been introduced. None of these modifications, nor combinations of them, could explain the discrepancy to its full extent without requiring unrealistic misalignments or unrealistic amounts of additional materials. Since the background rates, i.e. when the beam is "off", of both the plastic and the NaI detector are two orders of magnitudes lower than with a turned-on beam, the surplus plastic counts need to originate from the beam, i.e. the beam is not completely clean.

A pollution of the beam with bremsstrahlung photons has been observed especially in the 710 keV beam where a significant fraction of the recorded events had high energies: A reconstructed image from only the *pair* interactions in the MEGA prototype — which cannot be related to the 710 keV photon beam — clearly proves that the beam contains also high-energy photons. They can only originate from storage ring electrons interacting with the residual gas [Zoglauer, 2005]. Since a bremsstrahlung spectrum has roughly a E_γ^{-1} characteristic (figure 1.5), there is a strong low energy component which can be observed in the beam spectra. In figure 8.6 the 8 MeV beam spectrum recorded with a high purity germanium detector is plotted before (left) and after (right) background subtraction. The background lines have (nearly) disappeared* but a strong low energy component remains.

*The exposure times are not available for the Ge-spectra since they were only intended to check the beam quality. The ratio of the background to be subtracted has been (coarsely) chosen so that the background lines disappear. A few lines still appear in the background-subtracted spectrum. They are most likely beam induced. Another reason could be a different detector position in the experimentation hall, i.e. a different distance to a localized hard X-ray / γ-ray source.

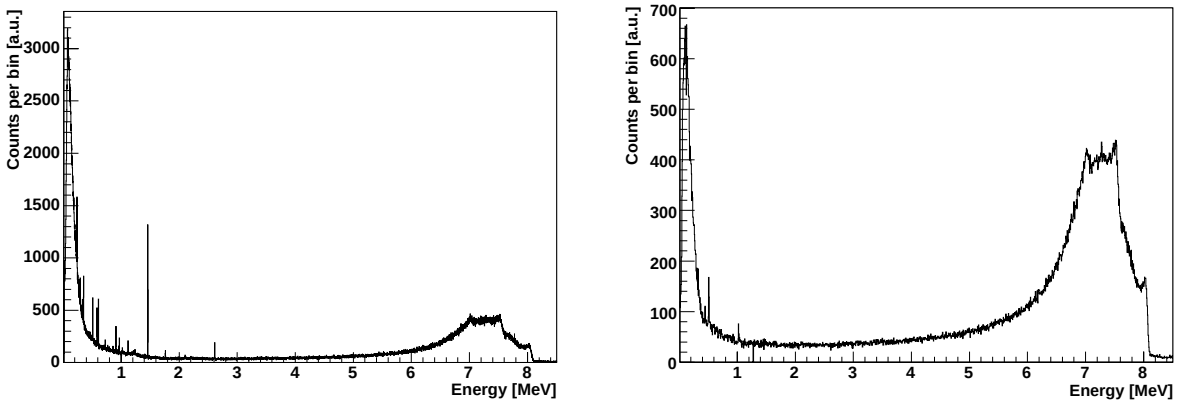

Figure 8.6: Left: Spectrum of the 8 MeV beam taken with a high purity germanium detector. Right: Same spectrum but the room background is subtracted.

Figure 8.6 on the right suggests that the bremsstrahlung component becomes significant below $\sim$ 1 MeV. This energy region is still above the energy threshold of the plastic detector, and below that of the NaI detector, i.e. where the plastic detector registers photons but not the NaI. Moreover, the cross sections for bremsstrahlung interactions of electrons are increasing to lower energies in this range (figure 1.1). A crude estimate of the expected bremsstrahlung triggers in the plastic detector can be obtained as follows: Equation 1.8 for 810 MeV ring electrons[†] and a nitrogen target, integrated between the two thresholds of plastic and NaI detector (60 keV and 750 keV), gives the number of bremsstrahlung photons per electron and target nucleus. Assuming an average beam current of 15 mA, a length of $\sim$ 20 m of one side of the electron storage ring, a gas pressure of 10^{-10} mbar[‡] in the storage ring vacuum system, a geometry factor of 0.1 for the bremsstrahlung photons passing the collimators[§], and an average trigger efficiency of 10% of the plastic detector. This yields a trigger rate of $\sim$ 2000 cts/s, which is on the order of the trigger rate of the plastic detector (figure 7.10). This estimate shows that bremsstrahlung is a significant source for additional photons coming along with the inverse-Compton beam. The estimated amount of bremsstrahlung photons is large enough to account fully for the elevated count rates observed in the HPGe spectra below 1 MeV as well as in the plastic detector.

8.6 Calibration Factors

The bremsstrahlung component depends on many factors and cannot be modeled here — too many unknowns are involved. Instead the bremsstrahlung component is assumed to be a constant fraction of the beam photons for a each beam energy. Calibration factors are used to convert trigger rates of the plastic detector to beam intensities (table 8.2). They are calculated making the following approximations:

- The NaI detector measures the flux seen by the MEGA prototype where a trigger efficiency of the NaI detector of $\sim$ 95% is taken into account. The thresholds of both detectors

[†]For a 50 MeV γ-ray beam 810 MeV electrons circulate in the storage ring. The results change less than 20% if setting in 375 MeV electrons as used for a 10 MeV beam.

[‡]At various places pressures of 10^{-9}–10^{-10} mbar have been measured.

[§]The bremsstrahlung photons are forward beamed, but due to the large distances in the accelerator setup and the small collimators there is still some geometrical effect.

are coarsely the same and the number of photons at energies around the threshold is low compared to the inverse-Compton photons, this is a good approximation.

- All photons above the NaI detector threshold are counted as inverse-Compton photons. The efficiency and effective area of the MEGA prototype is energy-dependent so that photons of other energies than the "beam energy" distort the results. Again, since the number of bremsstrahlung photons above the NaI threshold is low, this is a good approximation.

- The fraction of the inverse-Compton photons in the beam is constant for the varying beam intensities as long as the beam energy does not change. This assumption is not necessarily valid since the beam intensity was not only controlled by the number of electrons in the storage ring but also by adjusting the electron- and photon-beam alignment, i.e. the collision geometry.

- Constant thresholds (of the plastic and NaI detector) are assumed. Variations have been observed in the NaI detector (650 – 850 keV). Such variations can be correlated with time, temperature, beam energy and intensity, and so on. Due to the comparatively low number of photons around the NaI threshold, the fluctuations in the count rate of the NaI detector are low. This does not hold for the plastic detector since the number of breamsstrahlung photon rises exponentially to lower energies and there is already a large amount of photons at the threshold energy of the plastic detector (at 50 MeV half of the count rate is due to bremsstrahlung photons) . Thus changes of the threshold could lead to significant fluctuations in the plastic count rate which are interpreted as changes in the beam flux. Since spectra of the plastic detector are only available at the beginning and the end of the whole campaign, but not during normal operation, there is no handle to even check this issue.

For beam energies of 12 and 37 MeV the beam monitor calibration measurements got lost due to a computer problem. In order to obtain an approximate calibration for these beam energies, the factors from the next-lower energies were scaled according to simulated values.

The assumptions and approximations necessary for deriving the calibration factors lead to unknown **systematic** uncertainties. The **statistical** uncertainties are small since it is merely a counting measurement with a large count rate (assuming a rate of the plastic detector of 1000 cts/s, the statistical error is 0.6% (1σ) already for 30 s of the measurement).

Chapter 9

Characteristics of the Prototype

Most of the prototype's properties that require only knowledge of the beam energy and spatial distribution, plus a detector energy calibration, are already evaluated and discussed in Zoglauer [2005]. These include the energy response, the angular resolution, the field of view, and the polarization sensitivity. For summary the results are repeated shortly here. The set of prototype properties is then completed by the time resolution, and those performance parameters which require a quantitative understanding of incident photon beams — the trigger efficiency and the effective area.

9.1 Energy Response

The spectral response suffers from several shortcomings inherent to the design of the prototype. The low-energy cutoff of the MEGA prototype is defined mostly by the calorimeter's trigger threshold ($\sim 300\,\mathrm{keV}$, chapter 4.1 and 4.2). Another factor influencing the low-energy detection threshold is less obvious; it results from the coincidence window (chapter 6.4): During the open window of $2.2\,\mu\mathrm{s}$ low pulses (i.e. low energy deposits) in the calorimeter may not reach the trigger threshold, since their rise times are $3.5\,\mu\mathrm{s}$ and longer (table 4.1).

Even though each individual channel has a maximum for the measurable energy, there is no hard upper limit for the total measurable energy of an event: The higher the energy, the more interactions are needed to deposit the full energy, i.e. the event distributes its energy over more channels. Thus the individual energy deposits in most cases do not exceed the dynamic range of individual channels (in the tracker as well as in the calorimeter). The calorimeter covers the lower hemisphere of the tracker only to a small fraction ($\sim 30\%$), and its rugged housing contributes with $\sim 40\%$ to the total mass. Consequently, escaping secondaries and absorptions in passive material frequently lead to incompletely measured energies. A restriction to events which are reconstructed to within a 10° radius around the beam incidence helps to reject incompletely measured photons in the Compton regime. This is illustrated in figure 9.1: For the lowest beam energy of $710\,\mathrm{keV}$ the spectra at three stages of the data analysis are shown, (a) directly after energy calibration, (b) after event reconstruction, and (c) after applying the cut on the reconstructed origin. After all cuts an energy resolution of $41\,\mathrm{keV}$ (1σ) is achieved. For larger energies fewer and fewer events are absorbed completely. Figure 9.2 shows the spectra after event reconstruction and restriction of the reconstructed origin. In the pair regime, this does not harm the capability to correctly reconstruct the incident direction of the incoming photon. Almost no fully absorbed photons can be found at photon energies of $8\,\mathrm{MeV}$ and above.

In addition to incomplete absorptions, deficiencies in correctly measuring the individual energy deposits contribute to an influence on the event reconstruction. As mentioned several times in

the detector and electronics-related chapters of this work, the time walk introduced by the trigger mechanism in the front end chip has far-reaching effects. A prominent one is the non-linearity in the energy calibration. Due to the lack of calibration points above 122 keV for the tracker and above 1.275 MeV for the calorimeter, extrapolations are necessary (chapter 3.3.2.1 and 4.4) which leads to systematic errors due to this non-linearity. Another effect concerns only the calorimeter calibration: The time at which the hold to the front-end channels of the calorimeter is applied, is a delayed *calorimeter* trigger during single channel calibration, but it is the delayed *tracker* trigger during coincident readout*! As a consequence, the holds occur at different phases of the shaped pulses for D2 calibration and coincident measurements. This leads to systematically different energy measurements. Finally, it cannot be excluded that the gains of D1 and D2 drifted during the measurement period of more than two weeks.

More details on the energy loss mechanisms can be found in Zoglauer [2005]. There it is shown that the observed spectra can be adequately explained in a full Monte Carlo simulation.

9.2 Angular Resolution and Field of View

In addition to the measured event energy, the angular resolution also heavily depends on the measured individual energy deposits. It is described in the Compton regime by the distribution of the angular distances between the Compton cone and the known source position — the so-called angular resolution measure (ARM). If an electron track is measured from the Compton scatter, the plane of the interaction is known. A second parameter can be derived from the angular deviation of the reconstructed to the real scatter plane — the so-called scatter plane deviation (SPD). This parameter is not discussed here.

As described in detail in Zoglauer [2005], the ARM of the MEGA prototype is far from that of an ideal (but physically possible) detector, which would only be limited by Doppler broadening (chapter 1.1.4.3). In addition to the energy resolution of the detectors, several effects are responsible for the overall broadening of the ARM (table 9.1 shows this for a beam energy of 2 MeV): A finite voxel size limits the position accuracy of the individual energy deposits. The geometry of the detector, including passive materials and wide gaps in the calorimeter, leads to undetected energy deposits and leaking energy from the detector. The same occurs when individual energy deposits are too small to be detected (below the detector thresholds) or the interaction happens in a defective readout channel. Finally there are systematic errors due to remaining non-linearities in the detector calibration. These systematic errors result in a shifted ARM distribution rather than a broadening; the measured ARM distribution has slightly lower values than the simulated one. A better agreement of measured and simulated data can be achieved by introducing a 7% increase of the tracker energies and a 10% decrease of the calorimeter energies below 511 keV.

It is obvious from table 9.1 that for tracked events the energy and depth resolution of the calorimeter has the largest effect on the ARM width. This is not surprising since about half of the incoming photon energy is transferred to the electron (else there would be no track). A fairly low energy is then left for the scattered photon which at the low boundary of the calorimeter range leads to large relative errors.

In the pair regime the limiting factors for the angular resolution are the unknown recoil of the nucleus within whose field the pair creation takes place, and Molière scattering of the electrons and positrons passing the tracker layers. Energy and position resolutions of the prototype are sufficient; they play only a minor role. The angular resolution, expressed in term of the half-angle

*The tracker trigger shows less time-walk due to the shorter shaping time.

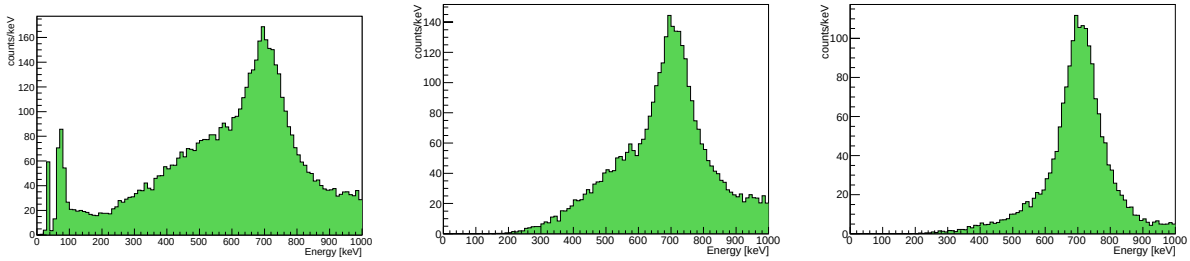

(a) 710 keV, raw energy spectrum

(b) 710 keV beam energy, energy spectrum after event reconstruction

(c) 710 keV, energy spectrum after event reconstruction and origin restricted to 10° around beam direction

Figure 9.1: Measured energy spectra for the 710 keV beam incidenting on-axis (taken from Zoglauer [2005]). Three steps of the analysis are shown: (a) raw spectrum, (b) after event reconstruction, and (c) after restriction to events which are reconstructed to within $\leq 10^{\circ}$ from beam incidence.

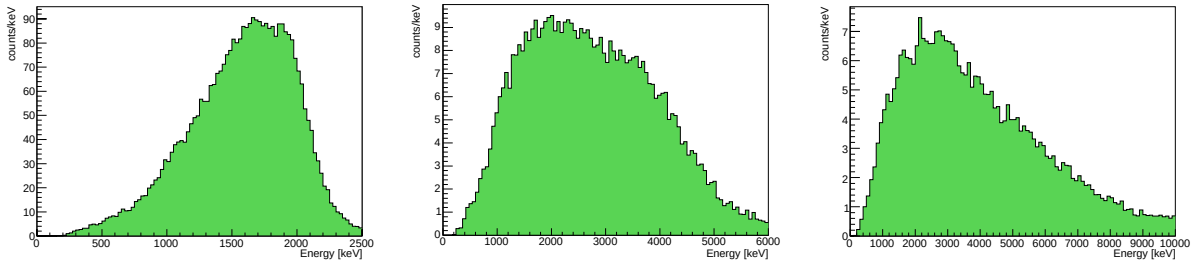

(a) 2 MeV

(b) 5 MeV

(c) 8 MeV

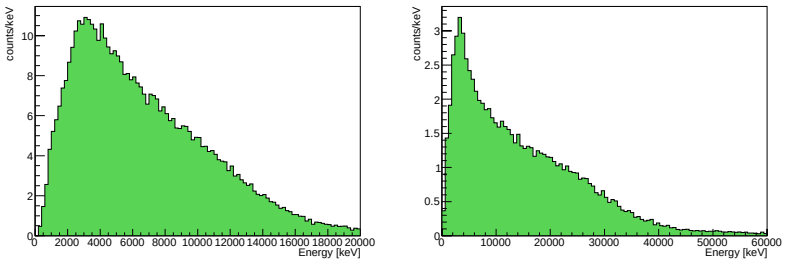

(d) 17 MeV

(e) 50 MeV

Figure 9.2: Measured energy spectra at 2, 5, 8, 17, and 50 MeV beam energies for on-axis beam incidence (taken from Zoglauer [2005]). All data analysis steps have been applied. As discussed in the text, at higher energies no photopeak is evident in the spectra due to incomplete absorption of the incident photon.

Imperfection	FWHM ARM [°] at 2 MeV not tracked events	/	tracked events
Doppler broadening	0.18 ± 0.02	/	0.25 ± 0.02
+ voxelization D1/D2 and incomplete absorption	1.5 ± 0.2	/	1.1 ± 0.1
+ thresholds and defective pixels	1.7 ± 0.2	/	1.3 ± 0.1
+ energy resolution of tracker	2.8 ± 0.3	/	2.7 ± 0.3
+ energy and depth resolution of calorimeter	3.4 ± 0.5	/	9.7 ± 1.1
+ energy shifts	3.7 ± 0.6	/	10.8 ± 1.3

Table 9.1: Impact of the various detector imperfections on the angular resolution of the prototype. One effect after the other has been applied to simulation data. (Table taken from Zoglauer [2005])

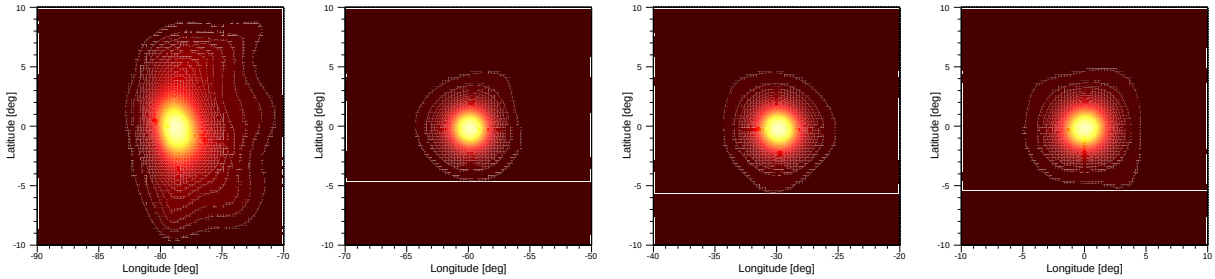

Figure 9.3: Field of view, demonstrated for a beam energy of 50 MeV (taken from Zoglauer [2005]), from left to right: −80°, −60°, −30°, and 0°

of a cone containing 68% of the reconstructed events, is reported to be between 5° for 50 MeV and 14° for 10 MeV beam energy in Zoglauer [2005].

The imaging algorithm (appendix I.2 and references therein) reconstructs the position of the point sources to within 1° and better for the whole field of view which extends to ±80° from on-axis (illustrated in figure 9.3).

Finally it should be mentioned here that of course a Compton and pair imaging instrument such as MEGA can image both point and extended sources. A reconstruction of a rotating radioactive laboratory source is used to demonstrate this in Zoglauer [2005].

9.3 Time Resolution

The time resolution of the prototype is measured using a tagged ^{60}Co source. Figure 9.4 shows a histogram of the time intervals between a trigger of the tagged source and the initiation of a coincident readout (no absolute calibration has been performed; the zero point on the time axis is arbitrary). No cuts have been applied to the data; the background is due to chance coincidences. In principle, the distribution should resemble that obtained in the tracker-only calibrations (figure 3.15). However, the time resolution of 0.53 μs is broader by 0.2 μs. This appears to be a selection effect introduced by the calorimeter: Events with large Compton scatter angles have high electron energies, and thus fast trigger signals. They deposit only a small portion of their energy in the calorimeter. If this amount is below the trigger threshold, these events are not read out resulting in a bias towards lower energy deposits in the tracker and thus later trigger times.

9.4 Polarization Sensitivity

The measurement of the 710 keV beam energy was intended primarily to determine the polarization sensitivity of the prototype. Zoglauer [2005] showed that up to 5 MeV the polarization of the beam

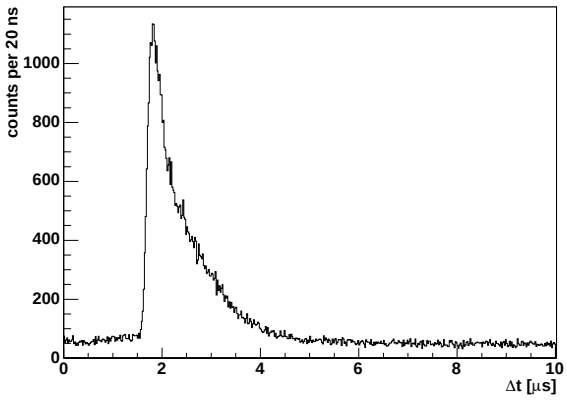

Figure 9.4: Time resolution of the prototype for coincident readout of the tracker and calorimeter measured against the tagged ^{60}Co source. The peak has a width of 0.53 μs FWHM, the zero point of the time axis is arbitrary.

could be detected with the prototype. The details are described there and will not be repeated here.

9.5 Trigger Efficiency and Effective Area

The effective area is a measure for the fraction of the impinging photons which are detected by a given instrument. Determining this critical parameter for the MEGA prototype required several steps:

- Determining the flux of the incoming photon beam (chapter 8).
- Determining the lifetime of the detector. To make this possible, the Coincidence electronics recorded precisely (20 ns resolution) the durations where a readout is ongoing.
- Combining these two values with the number of measured events gives the trigger efficiency. Figure 9.5 (a) gives the numbers separately for the different beam spots on the detector as a function of energy for on-axis incidence.
- Determining the types of the measured events according to Zoglauer [2005]. The result is shown in figure 9.5 (c) where the contribution of the different event types is given in percent. Events are rejected only if they cannot be reconstructed, i.e. no cuts such as restrictions of the incidence angle are applied.
- Scaling from beam spots to a fully illuminated detector front. For **on-axis** incidence the (measured as well as simulated) trigger efficiencies for the nine beam spots impinging on the tracker are averaged and multiplied by the active area of the tracker (9×36 cm^2) resulting in the effective area (figure 9.5 (e)). This is done for each event type individually. It is assumed that the average trigger efficiency of the nine beam spots is the same as over the whole detector active area where geometrical effects are not fully taken into account. Nevertheless the approximation is good compared to the other systematic effects listed later in this section: (1) The beam incidences (sample points for the effective area) cover already significantly different geometries (compare figure 7.8). (2) Passive materials such as the ridges between the individual silicon wafers of the tracker only marginally diminish the effective area since incidences on passive materials are not counted; only events with track could be misinterpreted due to missing hits and alter the trigger efficiency. Since the event reconstruction algorithm can also recognize tracks with missing hits, this is a small effect.

Measurement

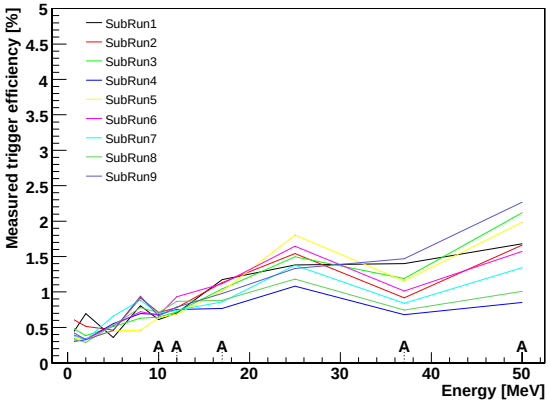

(a)

Simulation

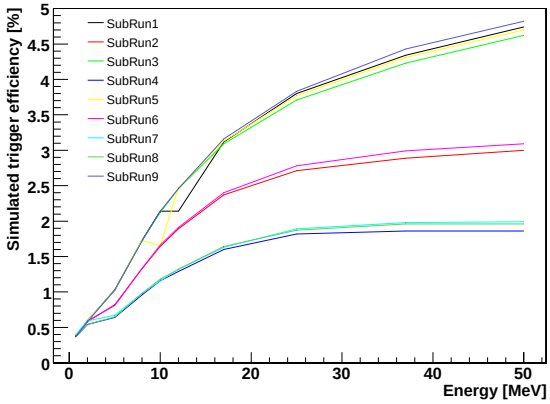

(b)

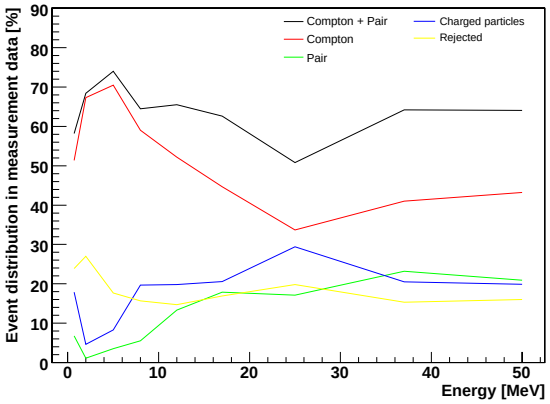

(c)

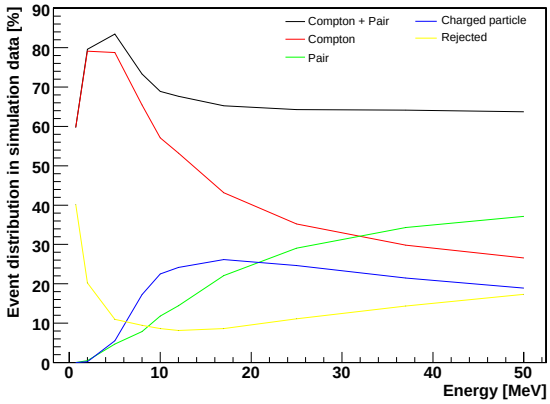

(d)

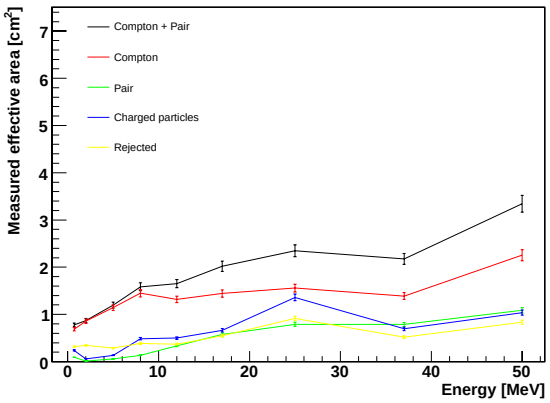

(e)

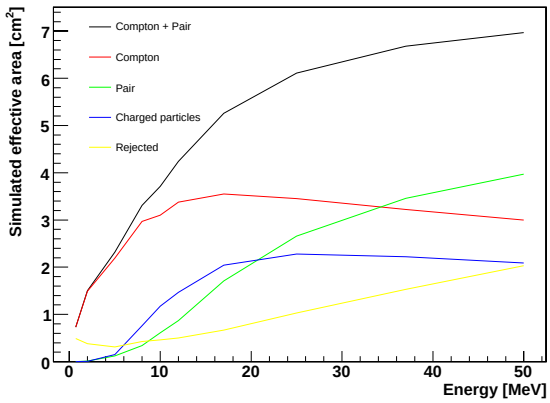

(f)

Figure 9.5: Comparison of measured and simulated properties (left column measured values, right column simulated values). (a), (b) Measured and simulated trigger efficiencies for the nine beam spots (subruns, numbering as in figure 7.8) on the tracker. The "A" marks the measurements where the top layer is used as anticoincidence. (c), (d) Fraction of the different event types as recognized by the event reconstruction algorithm (taken from Zoglauer [2005]). No cuts are applied such as restrictions of the incidence angles. (e), (f) Effective areas. The error bars at the measured values indicate the *statistical* errors only. For details of the computation and the systematic errors see text. All graphs show the values for on-axis beam incidence.

These simplifications are not valid for **off-axis** incidence. Simulations are needed to extrapolate from the beam spots to a fully illuminated detector. They are subject to future work so that effective areas for off-axis cannot be given here. Instead the number of reconstructed pair events at 50 MeV beam energy relative to the number of incident γ rays for incidence angles of up to 80° is presented.

9.5.1 On-axis Beam Incidence

For comparison, simulations of the prototype with on-axis beam incidence have been evaluated [Zoglauer, 2006] as shown in figures 9.5 (b, d, f). Significant differences can be observed (especially in the pair regime above 8 MeV) which will be discussed below, starting with the overall effects followed by the peculiarities depending on the beam energies.

The simulation does not take into account all details. It has not been considered that the triggers of those calorimeter channels which are directly hit by the beam are blocked. Furthermore, the top layer was used in anticoincidence for most of the higher energies (the marked energies in figure 9.5 a) to suppress charged particles; this is not accounted for in the simulation. Implementing an appropriate filter for the simulated data has been tested for the "subrun 1" at a beam energy of 50 MeV (see figure 7.8 for beam incidence). At this energy and beam position the largest effect is expected due to the lowest opening angles of the pairs. Pairs may not leave the beam channel, i.e. no unblocked calorimeter channel is hit and no readout takes place. The trigger efficiency and effective area is reduced by $\sim$25% [Zoglauer, 2006] in this case. For the subruns 2 and 6 this effect should be much smaller and for subruns 4, 7, and 8 negligible because few or no calorimeter crystals are in the beam path. Such a reduction in the simulated trigger efficiency depending on the beam incidence explains that the splitting into three sets of curves in the simulation is not reproduced in the measurement (figures 9.5 b and a).

Unconsidered dead time directly decreases the evaluated trigger efficiency and therefore the effective area. The following significant dead time effect not recorded in the dead time measurement most probably accounts for the generally too low measured values: An interference of the triggering system with the coincidence electronics was not taken into account during the electronics design. When a chip generates a trigger, this trigger pulse is stretched to $\sim 7\,\mu$s (chapter 5.2.1). The pulses are fed directly into the coincidence electronics without any further pulse forming. There, all tracker triggers and all calorimeter triggers are combined by a logical OR into one tracker and one calorimeter trigger for the timing analysis (figure 6.4). A test for a coincidence is started by a tracker trigger (rising edge). However this happens only if the calorimeter trigger is not active, otherwise the tracker trigger is *ignored* (chapter 6.3)! Thus many (non-coincident) calorimeter triggers and overlapping tracker triggers can enhance the dead time significantly as a coarse estimate shows:
Assuming a beam flux of 50 000 γ/s, which corresponds to a beam monitor trigger rate of $\sim$ 2000 s^{-1} at 10 MeV (see figure 7.10 and table 8.2), a conversion efficiency of 4.3% in the tracker (according to the pair creation cross section in 0.55 cm silicon), and a trigger rate in the calorimeter of 25% of the beam photons (the channels of the calorimeter which are in the direct beam path are blocked, thus only secondary particles leaving the primary beam path generate triggers), the number of tracker and calorimeter triggers is 2150 s^{-1} and 12500 s^{-1} respectively. For each second of lifetime, the calorimeter trigger is active for 87 ms. From this follows that around 190 chance coincidences of a tracker trigger and a still active calorimeter trigger occur each second. Overall 8.7% of the tracker triggers are ignored.

Unrecognized coincidences can occur if the calorimeter trigger arrives more than 20 ns before the tracker trigger (compare chapter 6.4). This can happen in pair creation events where the electron or the positron crosses the calorimeter's PIN diode. The large signal in the diode can

generate an earlier trigger than that from the strip detectors despite the longer shaping times in the calorimeter. This is due to the lower thresholds in combination with the time walk problem.

At 710 keV the beam monitor calibration is taken from simulation only since the threshold of the NaI detector is too high for a calibration. Moreover, pollution of the beam by bremsstrahlung was significant at this energy as the reconstructed pairs in the beam clearly prove.

The top layer was not always switched in anti-coincidence (see markers in figure 9.5 a). This explains the comparatively larger measured trigger efficiencies at 25 MeV and the step between 8 and 10 MeV caused by charged particles.

At 12 and 37 MeV the beam monitor calibration data are lost due to a computer problem. The calibration values for the beam monitor efficiency are extrapolations from the simulation adding significant uncertainty to the measurement.

At 50 MeV there is still a large fraction of Compton events. One would expect that the fraction of Compton drops below that of the pairs, as predicted by the simulation. Here the data is polluted by low-energy hits in the tracker and an interaction in the calorimeter (e.g. a pair creation). Such events are reconstructed as Compton events but they are more likely a chance coincidence of a bremsstrahlung photon in the tracker and an interaction of a beam photon in the calorimeter.

A last, important point concerns the **trigger efficiency.** In the simulation, three groups of beam incidences can be distinguished. This is less evident in the measurement, but the trend is the same. The differences between the groups become obvious when looking at the geometry (figure 7.8). The beams leading to the highest trigger efficiencies (subruns 1, 3, 5, and 9) traverse completely a calorimeter block, whereas the others point between blocks. The gap between the blocks is larger where the beams 4, 7, and 8 pass, which results in even lower efficiencies compared to 6 and 2. The smearing out of this effect in the measurement can be attributed to blocked and defective channels. In the simulation the calorimeter crystals directly exposed to the beam are not blocked and the different attributes of a readout channel (e.g. thresholds and defects) are not fixed in position, i.e. for each simulated event a set of randomly chosen attributes is applied with no regard to the interaction location. Additionally it was often necessary in the measurement to block a few more crystals which have not been directly in the beam; this is as well not reflected in the simulation.

Nevertheless the simulation is in agreement with the measurement up to approximately a factor of two. Most of the deviations are expected to result from the mentioned peculiarities of the measurements. This measurement has shown that the simulation is already detailed enough to deliver predictions within a factor of two and better.

9.5.2 Off-axis Beam Incidence

At off-axis beam incidences the beam paths through the detector (figure 9.6) give rise to even more peculiarities. Averaging over the nine beam incidences is not a good assumption any more so that a reasonable number for the effective area cannot be derived directly from the measurements. Instead the fraction of the incoming photons which have been measured and reconstructed (in the following referred as event yield) is given. The following discussion is restricted to measurements at 50 MeV beam energy. At this energy — as already noted for on-axis incidence — the Compton scatter events are polluted by chance coincidences so that the only event yield shown is that of the pair creation events (figure 9.7). Due to the symmetry of the setup the pairs of subruns 1/ 9, 2/6, and 3/5 show nearly identical behavior (for an unknown reason this is not valid for 2/6 at 60° and 3/5 at 30°). Mainly four effects determine the event yield:

1. The amount of conversion material (i.e. silicon of the tracker) traversed by the beam changes

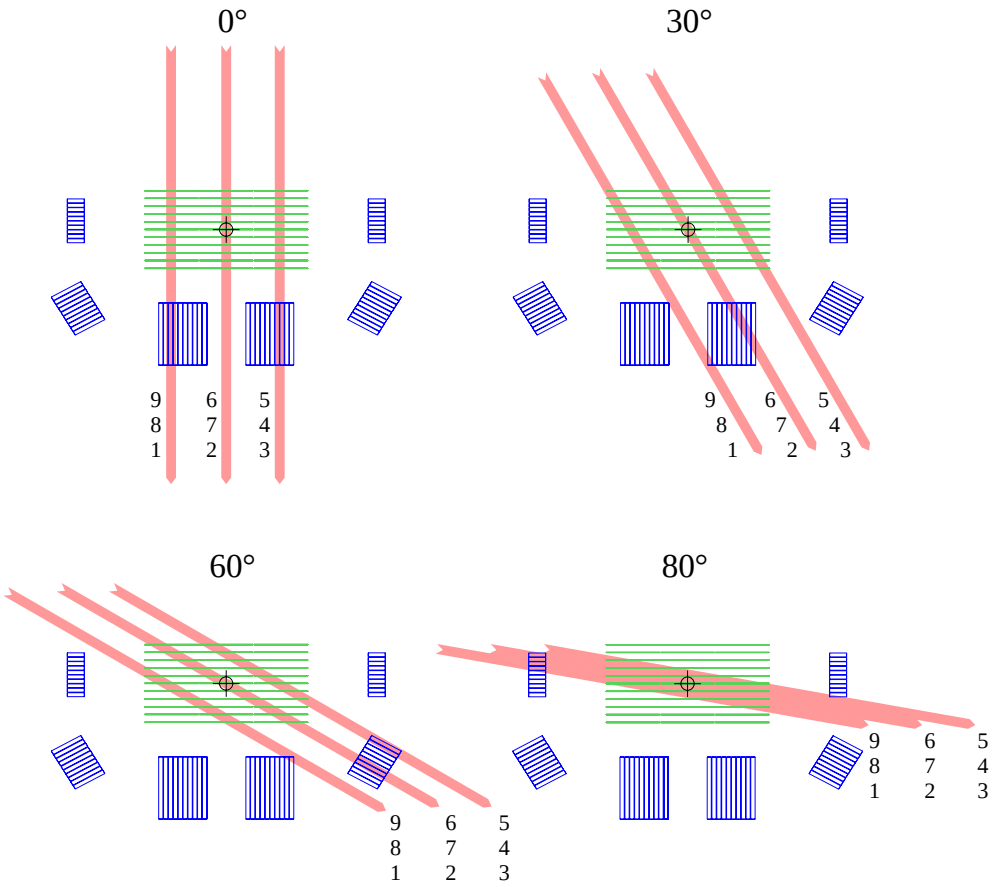

Figure 9.6: Beam paths through the detector for the different incidence angles. The detector is schematically shown from the top of the XY-table omitting two side walls of the calorimeter. The center of rotation of the XY-table is marked by a cross and the subrun numbers are indicated.

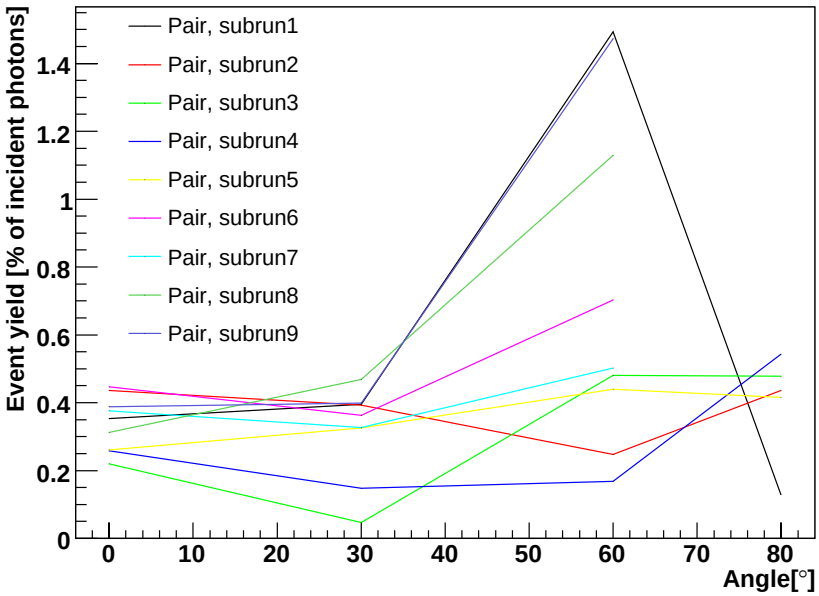

Figure 9.7: Event yields for reconstructed pair events at 50 MeV beam energy at different incidence angles and XY-table positions. Only subruns 1–5 have been measured at 80°.

the interaction probability. The more layers are involved and the steeper the incidence angle the more pairs are generated.

2. Even at 50 MeV beam energy the measurement was set up to accept only events with one or more triggering calorimeter blocks. Thus the trigger efficiency is higher for pairs if there are calorimeter crystals next to the beam channel measuring the electron or positron. This implies that beam paths requiring many blocked channels such as subruns 6 and 2 at 30° have a reduced trigger efficiency.

3. The top layer of the tracker is used as anticoincidence against charged particles. Those beam paths not traversing the top layer have increased trigger efficiencies since conversion in the surrounding passive material (e.g. calorimeter housings) trigger the readout and conversions in the first layer are not discarded any more.

4. At 80° beam incidence the beam is "shielded" for the subruns 1, 2, 6, and 9 by the sidewall calorimeter blocks. A first interaction in those detectors leads to events which are not recognized as pairs (no vertex in the tracker).

The characteristics of the event yield can be explained qualitatively by a combination of these effects. Simulations for a quantitative evaluation are elaborate, especially due to varying trigger conditions. They are subject to future work.

The problems arising from the beam measurement can be circumvented at low energies by measuring radioactive laboratory sources. The evaluation steps necessary for determining the effective area — especially the event reconstruction — depend on a careful single-channel energy calibration. This is also foreseen for future analysis.

9.6 Conclusions

The MEGA prototype is a *demonstrator instrument* for a combined tracking Compton and pair creation telescope. It serves as platform to test the new event reconstruction and imaging methods needed for such an instrument with *real* data. The performance of the prototype's hard- and software is already good or even excellent in terms of polarization sensitivity, field-of-view, and angular resolution: The latter achieved with pair events is better than that of EGRET (at least for energies below 50 MeV); in the Compton regime the prototype is not so far off from COMPTEL in this respect [Zoglauer, 2005].

The budget constraints of a demonstrator instrument of course limit the amount of available detector material, manpower, and development resources. So the energy response suffers from the small amount of scintillator material used for the calorimeter and the effective area is mainly limited by the amount of silicon built into the tracker.

During developing the prototype one had to cope with electronics problems such as a far-from-ideal trigger and energy-measurement concept as this was given by the front-end electronics, detector problems such as the differing depletion voltages of the strip detectors, and thermal problems such as the gain drift of the front-end electronics with temperature. The interplay of all the readout channels became a very complex timing task. At this point, we understand in great detail the instrument's properties — moreover, we know the causes for its behavior and misbehavior as discussed in the following chapter.

Part IV

Achievements and Outlook

Chapter 10

Achievements and Possible Improvements

In the last chapters the current status of the prototype has been described. This fully operational prototype features over $1.5 \cdot 10^6$ voxels (resolution elements) read out by over 10 000 detector channels. During developing and building the MEGA prototype, as well as during measurements and data analysis, a long list of ideas for improvements accumulated. Moreover, new technologies became available in the meantime; the prototype reflects the technological status of 10 years ago. This chapter gives an overview of what has been achieved so far, where the roots of the instrument's shortcomings lie, and how the MEGA telescope concept could be improved, pointing the way towards an instrument that truly could enable a quantum leap in Medium-Energy Gamma-ray Astronomy.

10.1 Principle

In the preceding chapter, reconstructed images of a 50 MeV HIGS beam are shown, other energies and various images of radioactive sources are presented in Zoglauer [2005]. They illustrate the imaging capability of the prototype in the energy band of 0.5 to 50 MeV by measuring Compton interactions as well as pair creations. *Thus the main goal of the prototype, demonstrating the working principle, has clearly been achieved.*

In the pair creation regime, instrumental background plays a minor role. The interaction results in $\bigwedge$-shaped patterns which enable a fairly straightforward reconstruction of the origin of the photon. Moreover, pair creation becomes significant at energies well above most nuclear lines. Nuclear lines are responsible for the instrumental background generated by activation of the detector and satellite materials which is challenging to filter in the Compton regime. Even worse, Compton imaging suffers severely from incompletely measured photons. Depending on the missing quantity, the origin can only be restricted to a cone (missing electron track), an arc of a cone (tracked Compton event), or a section of a great circle (good electron track but imcompletely absorbed scattered photon); the various possibilities are described by Zoglauer [2005]. This means that not only γ rays from activated instrument materials, photons scattered in passive materials, and γ rays generated in the Earth's atmosphere contribute to the background, but also incompletely measured γ rays from celestial sources. A powerful tool for suppressing background from activated materials and from photons from the Earth's atmosphere is the measurement of the time of flight of the scattered photon as realized in COMPTEL. In the compact design of a MEGA-type instrument

this is not yet* possible. The novel information from measuring the electron track instead helps to reduce the background significantly. Simulations of the baseline MEGA satellite instrument by Zoglauer [2005] are very promising; an experimental proof of the suitability of this approach is missing. It could be supplied by a MEGA balloon flight.

Since the basic principle has been proven and the performance of the prototype is known, future steps will be focused on improving the performance of the instrument. In the following each hardware component is analyzed.

10.2 Tracker

The most crucial hardware part is the tracker. A detector with little passive material and a large sensitive area, easily scalable by a factor of four, has been fabricated [Schopper, 2002]. In principle, the physical limit in reconstructing Compton events is the Doppler broadening of the scatter medium (illustrated in [Zoglauer, 2005]). The lower the atomic number of the scatter material, the lower the Doppler broadening. Thus silicon is superior to germanium or CdZnTe in this respect. The tracker of the prototype remains far from this limit†, since its energy resolution of $\sim$ 10 keV (σ at 122 keV) significantly exceeds the Doppler limit which is equivalent to a few keV. Considering the main contributors to the energy resolution as discussed in chapter 5.1.4, there is a lot of room for improvements:

- The large **input capacitance** of the tracker channels due to the connection of long strips with narrow pitch can be decreased by implementing a transistor for each strip. Thus the capacitances do not add up when concatenating several wafers to get a large area. Promissing results of JFET devices compatible with silicon strip detector technologies have been reported by Piemonte et al. [2006].
- The **leakage currents** of a new generation of strip detectors fabricated with improved processing steps could be as low as 100 pA/cm^2.
- The tracker of the MEGA prototype is very sensitive to **induced noise** due to its grounding concept. The p- and n-side electronics need to run at the bias potentials (chapter 3.3.1) and there are three different biasing voltages. This results in four ground levels (one for the connected p-sides and three n-sides) which is a problematic constellation in terms of noise. A common ground for all front-end boards could be achieved by using discrete instead of the detector's built-in capacitors by means of a silicon oxide layer between strip implantation and aluminium readout strip.
- The problems related to the front-end electronics can be circumvented by methods described in chapter 10.4.
- The unidentified noise source measured on the n-side of the tracker layers needs further investigations. Variations of the applied potentials and a temperature scan should give hints for the origin of this noise component.

Altogether an energy resolution of 1 keV (1σ at 122 keV) is expected to be achievable.

*Promising studies have already been done (Fiorini et al. [2004], Castoldi et al. [2004]) and are ongoing.

†The physical limit of the energy resolution of a semiconductor is given by the Fano noise. For silicon at room temperature and 122 keV deposited energy the resolution limit is 225 eV (σ) which is still below the Doppler broadening.

The position resolution of the tracker is good enough to keep its contribution to the angular resolution of the instrument small [Zoglauer, 2005]. Taking into account that a fine position resolution necessitates a large number of readout channels, i.e. high power consumption, a compromise must be found in accordance with the boundary conditions of a satellite instrument. Also, improving the position resolution down to the technically possible would result in rising inter-strip capacitances. Consequently, the energy resolution deteriorates.

The area of the detector wafers could be enlarged from 6 cm × 6 cm to 10 cm × 10 cm since 10″ diameter is currently the standard size of detector wafers. This would result in less holding structure and thus less passive material.

The thickness of the wafers influences the tracking capability for charged particles. The thinner the wafers, the longer the tracks and the lower the small angle scattering (Molière-scattering) in the wafers leading to straighter track beginnings (see, for example, equation 1.9). On the other hand, thinner wafers lead to a significant increase in readout channels (if the amount of conversion material is kept constant), and more power and data processing capability will be needed. One could imagine of thinner layers at the top and thicker ones at the bottom of the tracker.

One method of reducing the number of readout channels uses floating strips, i.e. only every second strip is read out. From charge induction effects it is still possible to derive the energy and position of a hit.

Using drift structures such as a linear drift detector would be another technique to save readout channels. In this detector the electrons drift in a well-tailored field towards one edge of the detector. At the edge readout contacts with the required pitch pick off the charge to a first amplification FET. In contrast to double-sided strip detectors, the back side does not need to have any position resolution because the second dimension is derived from the drift time (the time between the back side and front side signal) of the electrons — similar to a time projection chamber. This demands for good time resolution, but fast timing is desired in any case to achieve a short coincidence window.

10.3 Calorimeter

For the prototype a calorimeter has been built which has the fine segmentation desired for the satellite version and three-dimensional position resolution at its bottom. Thus multiple Compton interactions in many instances are resolved.

The calorimeter limits the overall performance of the MEGA prototype due to its limited energy resolution. A new generation of photon detectors called silicon drift diodes (SDD) are today already established both in X-ray spectroscopy and for reading out scintillators [Fiorini et al., 1997]. The SDD (figure 10.1) is superior to the PIN diode due to the small anode to which the electrons drift in the tailored electric field. The small anode has a very low capacitance (as low as 120 fF has been reported by Lechner, Pahlke, and Soltau [2004]) compared to the PIN diode's (∼ 20 pF of a pixel in the MEGA prototype), resulting in a better signal-to-noise ratio. In order to avoid having a lot of capacitance added by the signal wire connecting the detector with the preamplifier, the first amplification stage (transistor) is implemented directly on the detector.

During design and construction of the prototype it was important that the calorimeter blocks can be disassembled for repairs. Thus the scintillator crystals are coupled by silicone cushions as described in chapter 4.1. In advanced versions, the crystals could be glued to the readout diodes, avoiding light losses due to imperfect optical coupling.

Concerning the position resolution along the crystal axis in the bottom calorimeters, reduced noise will improve the situation. Additional options include treating the surfaces of two sides of

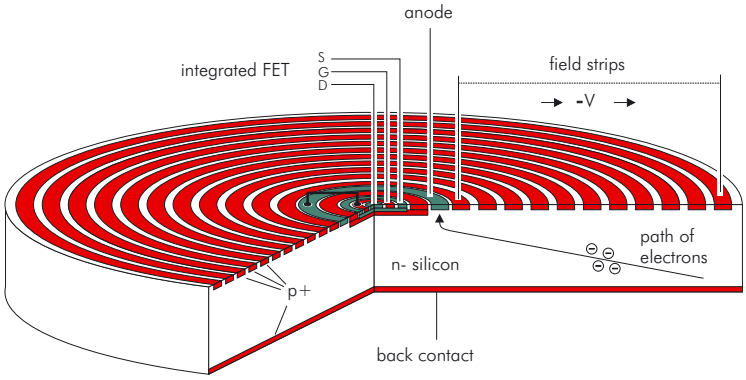

Figure 10.1: Principle of a silicon drift diode (adapted from [Lechner et al., 2001]).

the crystals so that they get milky (e.g. roughening with fine sand paper). The diffuse reflection will increase at the cost of the total reflected component. Consequently the distribution of the light towards the two readout diodes will be more dependent on the interaction position. If the crystal's wrapping into reflective paper is good, the light loss will be low ($\lesssim 5\%$ in the middle of the crystal) and correctable, thus the energy resolution should remain nearly the same.

Another deficiency of the calorimeter is its bad time resolution. The resulting long coincidence window allows for many chance coincidences, especially in case of strong sources. Since the prototype features only a fraction of the detector material of a full instrument, it was feasible to have a sufficiently long coincidence window, but a full instrument will suffer severely from unnecessarily long coincidence windows. There are two approaches solving this problem: The first is improving the readout electronics as described in the next section. The second is using a significantly faster scintillator such as LSO, $LaBr_3$ or similar scintillators with a high (effective) Z and a light output comparable to CsI(Tl).

A very promising combination would be a silicon drift diode reading out a $LaBr_3$ crystal. $LaBr_3$:Ce has been reported in Shah et al. [2003] to have a high light output (60000 photons/MeV), a fast decay time (25 ns) and an excellent energy resolution of 3.2% FWHM at 662 keV (measured by coupling to a PMT).

Last but not least, the calorimeter needs to cover the lower hemisphere around the tracker as tightly and with as little passive material as possible.

10.4 Electronics

For a space application, the most demanding factor of a system with huge numbers of readout channels (100 000 in the case of a baseline MEGA satellite fitting a German Kleinsatellit envelope [Wolter et al., 2000]) is keeping power consumption at a realistically low level. This power not only must be generated by solar cells, but also the dissipated heat has to be radiated away from the satellite. The already-achieved 0.5 mW per channel in the FEE constitutes a low number even by today's standards, but the simplicity of the triggering circuit has a long list of drawbacks with consequences for the detector's entire performance, as already described in the previous chapters.

The pattern of triggered FEE chips needs to be filtered for evaluable events. The data acquisition electronics already features a flexible method of choosing those events within the coincidence electronics. This is crucial for a system with limited readout capacity such as the prototype. For the prototype, patterns have been successfully used which select every coincidence, every coincidence without any hit in the top layer (pattern for the accelerator measurement), or only muons.

For the future one can imagine several improvements:

First of all an improved front-end ASIC is required. There is a small list of new self-triggering chips such as advanced TA chips (general purpose, IDEAS, Oslo), the IKARUS (developed for the PICSIT detector of the IBIS instrument aboard INTEGRAL), the DRAGO (developed for a medical camera), or the RENA (general purpose, NOVA R&D, Riverside). MEGA has some special requirements; most likely only a custom design can fulfill them all. An — admittedly ambitious — approach shall be described briefly:

From each interaction recorded in the individual detector channels a list of quantities should be derived as precisely as possible: the deposited charge, the time of interaction, and ideally (only for the calorimeters) a time constant discriminating between a crystal or diode hit. All three aspects could be derived from a fully sampled pulse (oversampling), on which an analytical function could be fitted as shown in chapter 5.1.6. The timing is uncritical in this case as long as a few samples of the base line are taken (i.e. in front of the pulse), in the rising edge, and in the falling one. Time-walk effects would be eliminated and the start point and pulse height can be determined with a precision better than the sample grids. Such a method would need to be investigated in detail, especially in terms of power consumption.

As already mentioned, the readout capacitance of drift detectors is very low. In order to take advantage of this feature, the first transistor is integrated in the detector so that the capacitance of the signal lines connecting the FEE to the detectors becomes negligible. The designer is now free to place the whole FEE *outside* the detector volume. Significant amounts of passive material between tracker and calorimeter can be eliminated, but more importantly, it gets easier to cool the electronics — likely enabling an increased number of channels given a certain satellite envelope.

The dead time due to the readout procedure limits the data rate of the prototype to below 150 readouts/sec. In order to achieve an event rate one or two orders of magnitude larger, the modularity of the front-end must be kept until after the data reduction. This implies that detector modules must include also the digitalization stage, a data reduction processor, and a data bus interface. Analog optocouplers are not needed any more, the analog-to-digital conversion as well as the data reduction is highly parallelized. Such "intelligent" modules communicate with the central instrument processor by exchanging data and command packages via a bus having a star topology. As a side effect, this approach also results in improved redundancy.

10.5 Structure

The amount and placement of structural components within a Compton camera sensitively influences its performance. Passive material needs to be avoided as much as possible since it causes unrecognized absorptions and scatters. Additionally, nuclear interactions with active or passive material (e.g. neutron captures in aluminium) makes the satellite glow in γ rays. The tracker of the prototype, including its housing, has already been designed with this in mind; the calorimeter still has much room for improvements.

It should be investigated in detail how passive material can be saved. For example, there is no need for a separate light-tight housing for the tracker layers as in the prototype. A common housing for both the tracker and calorimeter would be enough.

Another way of optimizing the structure is to avoid as much as possible materials which are easily activated. For instance, aluminium could be replaced with CRC (carbon-reinforced carbon) at least inside the active detector volume.

10.6 Combination of the Components

In addition to optimizing the individual components, the arrangement and the interplay of these components are crucial points for the overall instrument performance. This has many aspects aiming at an optimum signal-to-background ratio with respect to the mass, power, thermal, telemetry, and cost constraints of a satellite mission. The main tool to approach this optimum is the simulation which has been demonstrated to approximate real measurements within a factor of two.

The main missing topic is the experimental validation of the background model. This was planned to gain from a balloon campaign where large effort was already invested in the extensions necessary for a balloon payload[‡], but it was stopped in 2003. Also the idea of measuring the neutron-induced background by exposing the prototype to a neutron beam was brought up but not realized. Thus the information available from past and present instruments forms the data basis and gathering the peculiarities of a new instrument concepts such as MEGA is postponed until the starting phase of a future γ-ray astronomy mission.

10.7 Final Words

The prototype has shown that timing behavior of the front-end electronics — as it is now — limits the performance in multiple ways, e.g. in the energy calibration of the individual detector channels of the prototype (chapter 3.3.3 and 4.4), in the length of the coincidence window (chapter 6.7), and in the impossibility of background rejection via time-of-flight. Improvements as described above (chapter 10.4), which would effectively and drastically reduce the systematic errors, could have a significant impact on several performance parameters at the same time. *Without improving the electronics, there would be no point in improving the detectors.* However, the development effort will be large; for a satellite mission a compromise will finally be required between power consumption / thermal budget and development speed / enhanced features.

A wide range of applications can benefit from new types of detectors and various developments are ongoing. Developments from other fields of science such as medicine (SPECT and PET cameras), environmental monitoring, or high energy physics (where the current detector and electronic techniques originate from) indicate that the envisioned goal of an instrument with 10 times better sensitivity compared to COMPTEL is achievable. *There is a huge potential in joining those development efforts.* The gained knowledge and techniques achieved by building a next large step of Compton telescopes will in turn be useful for other fields of science. For instance the MEGA prototype tracker has also been used to investigate the performance of a silicon-only PET scanner (appendix B.4 and [Auricchio et al., 2005]).

The *combination* of many tasks, i.e. detectors, readout electronics, and data acquisition, calibration, event reconstruction, imaging, and other high level analysis, made the prototype *work*. The resulting performance already fulfills some of the goals of a satellite mission in the MeV range as described in chapter 2.1. The photomontage in figure 10.2 illustrates this where the beam images at 50 MeV for four incidence angles are plotted "onto the sky". On the one hand, this picture illustrates that the desired large field-of-view has been achieved. On the other hand, it demonstrates the imaging capabilities of the prototype at 50 MeV. In combination with the measurements of beams and radioactive laboratory sources at lower energies down to 0.5 MeV, the prototype instrument operates in the desired wide energy range.

[‡]The mechanical structure and the anticoincidence shield (ACS) are already fabricated, the electronics and software are prepared to handle the ACS, etc.

The hardware is modular so that it is scalable to the dimensions of a satellite instrument which could reach the required effective area. The ultimate measure of a satellite telescope is its *sensitivity*. It depends not only on the effective area, but also on the background prevention and rejection capability, especially important in the Compton regime. A low instrumental background can be achieved e.g. by using materials which do not easily activate, by a thick and tight calorimeter so that incompletely absorbed photons are unlikely, and by a short coincidence window. Background rejection algorithms work more efficient if the energy and position resolution of the individual hits of an event is improved. Simulations proved to be a *reliable* tool for evaluating these aspects at least for photons, electrons and positrons as interacting particles. The most pressing open question concerns the instrumental background, especially the one resulting from material activated by neutrons and protons.

Once the instrumental background is understood, e.g. by performing and evaluating a stratospheric balloon flight of the prototype, reliable predictions for larger configurations can be made. Finally the sensitivity of a space mission can be optimized given the constraints in mass, power consumption, thermal budget, mechanical stability, and — last but not least — in financial budget.

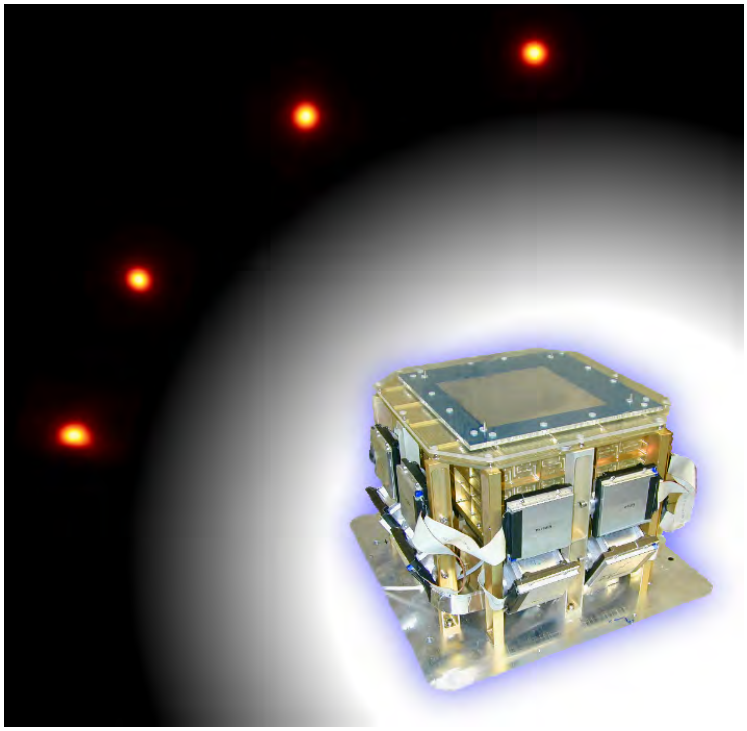

Figure 10.2: The MEGA prototype "observing" the 50 MeV HIGS γ beam under several angles of incidence. It is a photomontage of the images of a 50 MeV beam measurement at four angles of incidence ($0°$, $-30°$, $-60°$, and $-80°$, compare figure 9.3) "onto the sky" with the prototype hardware in the foreground.

COMPTEL taught us that the diversity of astronomical objects shining in MeV γ rays is large, now it is time for a closer look. We have the tools and knowledge at hand to build a worthy successor!

Part V

Appendix

Appendix A

Selected Radioactive Isotopes and their Properties

Several radioactive isotopes and their properties which are of interest in this work are listed below. Only prominent γ-ray line energies are quoted (data taken from the Table of Radioactive Isotopes [Firestone and Shirley, 1996] except for marked numbers: [1][NuDat]).

Isotope	decay	$T_{\frac{1}{2}}$	E_γ[keV]	probability	astrophysical relevance	terrestrial relevance
^{7}Be	EC	53.12 d	477.6	10.5	expected from novae (CO only)	
^{22}Na	β^+	2.6019 y	511 1275	90.5%[1] 99.94%	expected from novae (ONe only)	calibration source
^{26}Al	β^+, EC	$7.17 \cdot 10^5$y	511 1809	81.7%[1] 99.8%	AGB stars, Wolf-Rayet stars, supernovae, possible nova contribution	
^{40}K	β^-	$1.277 \cdot 10^9$y	1460.8	11%	supernovae	natural radioactive background
^{44}Ti	EC	63 y	67.9 78.3	94.4% 96%	supernovae novae Wolf-Rayet stars	
via ^{44}Sc	EC, β^+	3.9 h	511 1157	94.3%[1] 99.9%		

Isotope	decay	$T_{\frac{1}{2}}$	E_γ[keV]	probability	astrophysical relevance	terrestrial relevance
^{56}Co	EC, β^+	77.27 d	511 847 1238 2598	19%[1] 100% 67.6% 17.3%	supernovae	
^{56}Ni	EC	6.077 d	158 812	98.8% 86%	supernovae	
^{57}Co	EC	271.79 d	136 122	10.7% 85.6%	supernovae	calibration source
^{60}Fe	β^-	$1.5 \cdot 10^6$ y	58.6	2%	supernovae	
^{60}Co	β^-	5.2714 y	1173 1332	100% 100%	supernovae	calibration source
^{88}Y	EC	106.65 d	898 1836	93.7% 99.2%		calibration source
^{99m}Tc	γ	6.01 h	140.5	89%		tracer in nucl. med.
^{109}Cd	EC	1.267 y	88	3.6%		calibration source
^{131}I	β^-	8.02 d	364	81.7%		tracer in nucl. med.
^{137}Cs	β^-	30.07 y	662	85.1%		calibration source
^{241}Am	α	432.2 y	59.5	36.0%		calibration source

Appendix B

MeV-Detector Principles and Their Applications Outside Astronomy

There are several terrestrial applications where imaging of γ rays is useful. Nuclear medicine pioneered this field. Molecules which are enriched in e.g. abnormal tissues are marked with a radioactive isotope and incorporated in vivo. The distribution of these tracers are imaged for further medical diagnostics. Different imaging methods are available, some are briefly described below which are the Collimators (B.2), the Compton cameras (B.3) and PET (B.4).

Other terrestrial applications of γ cameras can be found on sectors such as environmental monitoring, industry, military, or homeland security where the camera monitors radioactive waste, leaking radioactivity, nuclear weapons, etc.

Of course position sensitive detectors for photons with energies of $\sim$ 100 keV – several MeV are the central part of all of those cameras.

B.1 Anger Camera Versus Pixel Detector

In principle there are two competing methods to gain positional information from interactions in scintillators. The straight-forward method is to divide the scintillator into pixels of the size corresponding to the desired position resolution and read out each pixel individually (figure B.1b). The other method was introduced by Hal O. Anger [1958]. He coupled several photomultipliers to a block of NaI (figure B.1a). Each photomultiplier measures a fraction of the emitted light, and the position of the interaction can be reconstructed from the distribution of the light.

The main advantage of the Anger camera is the low number of readout channels. In order to achieve a similar position resolution with a pixel detector (when comparing the FWHM position resolution of the Anger camera with the pitch of the pixels) roughly a factor of 10 finer pitch is needed. This advantage of the Anger camera comes at the cost of a complicated reconstruction algorithm and a non-uniform position resolution (interactions tend to be shifted to the nearest detector). Also, resolving multiple interactions occurring simultaneously is problematic. A pixel detector is superior, if photons in the Compton regime are to be measured, which deposit their energy in several discrete locations. The pixel detector can resolve this trivially, whereas the Anger camera measures only (at least without complicated calibrations) the center of gravity.

Optical separation between the individual segments of a pixel detector consumes some volume. In case of the MEGA calorimeter having 120 crystals with a footprint of 5×5 mm and 0.7 mm space for the reflective paper, only 77% of the detector volume is filled with scintillator material. Thus an Anger camera of the same overall volume is superior to the pixel detector in terms of efficiency.

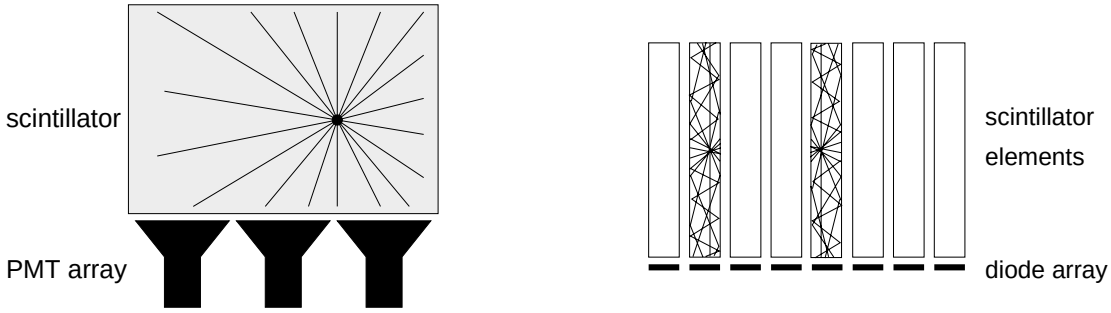

(a) Principle of an Anger camera

(b) Principle of a pixel detector

Figure B.1: Comparison of an Anger camera (left) with a pixel detector (right). The interaction position in an Anger camera needs to be reconstructed from the distribution of the light over the different photomultipliers (PMTs). This saves readout channels — but it is difficult or impossible to resolve multiple interactions.

B.2 Collimators

Hal Anger placed his camera behind a lead pinhole collimator [Anger, 1958]. The efficiency of such a camera is very low and depends mostly on the hole diameter assuming a sufficiently thick detector. Both the hole diameter and the detector's position resolution limit the resolution of the camera. Increased efficiency is gained by combining several cameras; in the extreme case as proposed by Beekman and Vastenhouw [2004] many pinholes are arranged on a cylinder, a second, larger cylinder contains the position sensitive detectors. Radioactive tracers in a small animal such as a mouse can be imaged by this system in three dimensions.

An array of parallel or diverging holes in a lead or tungsten brick is used in the multiple hole collimator (a comparison of different collimator geometries is given in Guru et al. [1996]). Such a setup shields the detector from all radiation not co-axial to the collimating holes (ideally by the photoelectric effect). The efficiency is significantly better than the one of pinhole cameras.

A set of (2D) images taken from different sides of the measured object can be combined to a 3-dimensional image (Single Photon Emission Computed Tomography, SPECT; for examples see Kunyansky [2001] and references therein).

B.3 Compton Cameras

The best efficiency around MeV energies can be achieved — in principle — with a Compton camera since there is no need for an absorbing collimator or mask. Many developments exist for medical Compton cameras since they have been proposed by Todd, Nightingale, and Everett [1974] such as [LeBlanc et al., 1999, Çonka Nurdan et al., 2005]. These cameras are sometimes called "electronic collimators" since the lead collimator is replaced by an electronic device, the scatter detector.

Compton cameras are used in other terrestrial applications as well, for example for homeland security [Hoover et al., 2005, Niedermayr et al., 2005] or for radioactive waste imaging [Martin et al., 1994, King et al., 1994].

B.4 PET

In nuclear medicine the Positron Emission Tomography (PET) is a tool for imaging distributions of tracer molecules. It is based on the annihilation of a positron emitted by a β^+-decaying isotope.

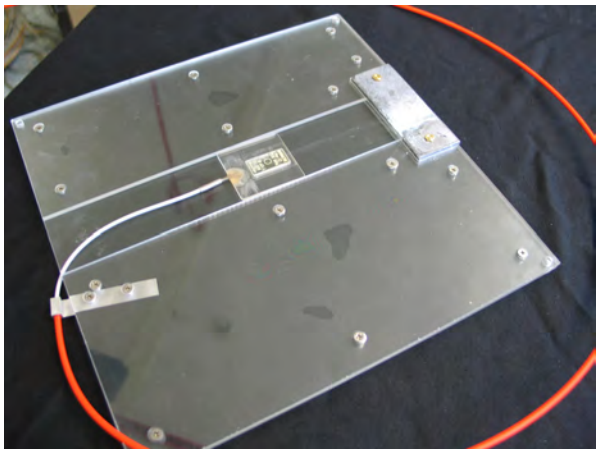

Figure B.2: Source holder for PET setup. The source (^{22}Na) runs on a slide between two plexiglass plates. The slide can be moved by a bowden cable from outside the detector.

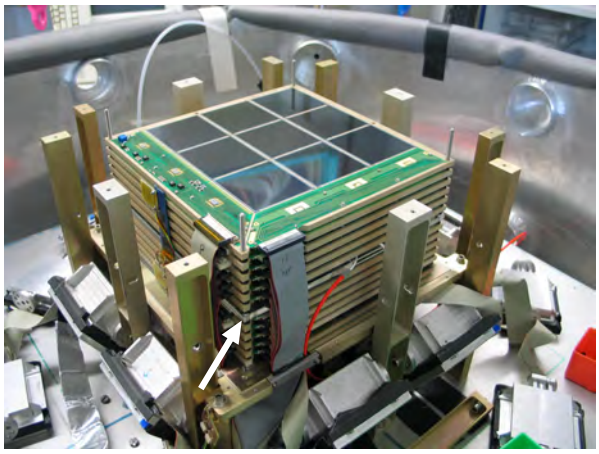

Figure B.3: Placement of the PET source holder in the middle of the tracker

Molecules marked with a β^+ emitter (e.g. ^{38}K) are injected into the organism to be examined. The two annihilation photons (511 keV each) are emitted in opposite directions. Two coincident energy deposits define a line on which the emitter is located. A three dimensional image can be reconstructed from the line densities of different directions with a tomography algorithm (e.g. [Brasse et al., 2004]).

One source of background in PET images results from photon scattering in the body of the test person or animal (for the human body approximately 50% of the events are useful). In order to suppress this kind of background, only events in which the full energy has been detected from both photons are used for imaging. The detector materials are generally crystals (NaI(Tl), BGO, LSO, YAP:Ce) with more or less sophisticated readout. Two main problems limit the position resolution of these systems: (1) multiple Compton scatters in the crystal are likely and (2) the depth-of-interaction is uncertain since the crystal has to be thick enough to provide a sufficient efficiency. Whereas the depth-of-interaction can be measured in principle, the Compton scatters cannot be avoided. A study of the physical limitations on position resolution in scintillators can be found in Zavatini et al. [2005].

The situation can be improved by using the Compton scatter technique, where an inner detector ring made of silicon detectors is the scatter detector and an outer ring of crystal detectors forms an absorber [Park, 2005].

For small animals or small samples, scattering in the test object is negligible and an energy measurement is not necessary any more. For this purpose a PET scanner can consist of several stacked silicon detectors surrounding the test volume without any scintillator crystals. Such a system has been proposed [Auricchio et al., 2005] and proof-of-principle measurements have been conducted with the tracker of the MEGA prototype.

The positron emitter (^{22}Na in this case) is placed between the upper and lower half of the tracker. The tracker housing is large enough so that an additional layer holding the source was built in. The source holder (figure B.2) consists of plexiglass plates with a slide holding the source. This layer is located between the fifth and sixth tracker layer (figure B.3). Events are read out if they show at least one trigger in the upper and one in the lower half of the tracker (adjusted by loading the corresponding trigger patterns into the coincidence electronics, see chapter 6) during a coincidence window of 1 μs.

Only two filters are applied to the data: (1) events showing no hit in the upper or lower half of

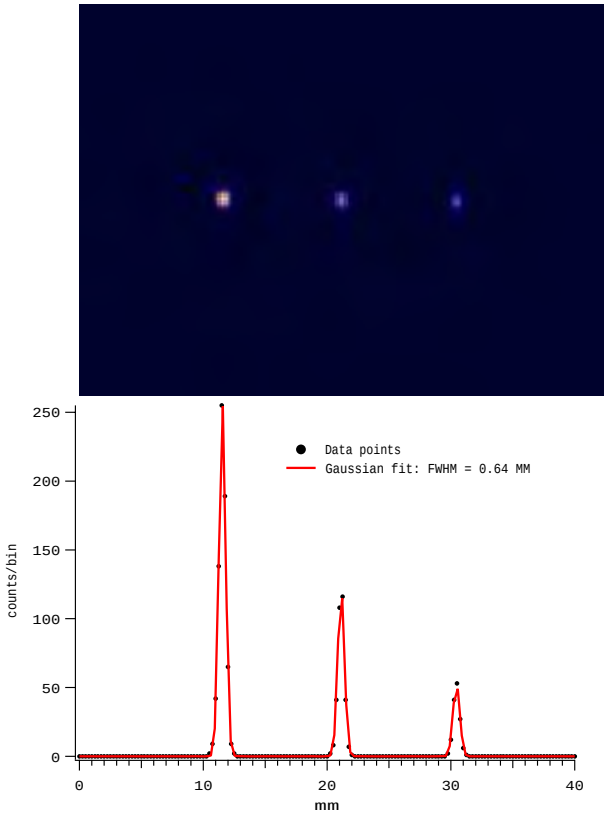

Figure B.4: Central image of the ^{22}Na source in three positions (top) and the profile passing through the three source positions (bottom), figures taken from [Auricchio et al., 2005]. Three measurements taken with the MEGA prototype in PET configuration at MPE have been combined with exposure-time ratios of roughly 4:2:1. For imaging an iterative expectation maximization algorithm has been used.

the tracker are discarded*, and (2) from multiple hits in one of the two tracker halfs always the one nearest to the source is chosen. The results of a measurement with three source positions is shown in figure B.4. A data set combined from three measurements of a ^{22}Na source (source was shifted 1 cm further for each measurement) was reconstructed using an expectation maximization algorithm [Auricchio et al., 2005]. The reconstructed source diameter (0.64 mm FWHM) reflects the dimensions of the source which is a sphere with 0.9 mm diameter (0.636 mm FWHM in projection). Thus the source dimension has been resolved and the position resolution is better than 0.64 mm. A measurement with a source of 0.5 mm diameter is currently in preparation.

*In principle this should not occur since the coincidence electronics does not accept such events. There are, however, some reasons for "losing" hits:

- There is no signal from the n-side. This happens, if the interaction takes place in an defective channel or one of the two wafers which are disconnected on the n-side (compare appendix E.2).
- There is no energy calibration available for the p- or n-side channel. The current algorithm discards such hits. Since there is no energy calibration required as long as multiple hits in one layer are ignored, this problem will be avoided in future.
- The trigger threshold is lower than the noise threshold and the hit is not recognized.

Appendix C

Factors Limiting the Energy Resolution of a Readout Channel

C.1 Noise Sources

There are three sources of electronic noise in detector systems such as the MEGA prototype [Lutz, 1999, Andritschke, 2000, Schopper, 2002]:

1. Thermal noise (Johnson noise): Thermal fluctuations of the electron distribution in a conductor results in a spectral density of the noise voltage U_n in a resistor R of

$$\frac{\mathrm{d}\overline{U_{tn}^2}}{\mathrm{d}f} = 4k_BTR$$

with f the frequency, k_B the Boltzmann constant, and T the absolute temperature.
For field effect transistors (FET) the thermal noise due to the resistance of the channel results in

$$\frac{\mathrm{d}\overline{U_{tn}^2}}{\mathrm{d}f} = \frac{8}{3}\frac{k_BT}{g_m}$$

with g_m the transconductance of the FET.

2. Shot noise: Due to the discrete nature of electric charge there are statistical fluctuations in a flowing current I resulting in a noise contribution of

$$\frac{\mathrm{d}\overline{I_{sn}^2}}{\mathrm{d}f} = 2Ie$$

with e the elementary charge.

3. Low-frequency voltage noise results from widely differing mechanisms depending on the type of the electronic device for example charge trapping effects in the channel of FETs (as described in [Lutz, 1999]). This noise has a power spectrum with an approximated $1/f$ behavior

$$\frac{\mathrm{d}\overline{U_{lfn}^2}}{\mathrm{d}f} \approx \frac{A_n}{f^\alpha}$$

with A_n some constant and $\alpha \approx 1$.

Taking into account the (complex) input susceptance $G_{in} = \frac{1}{R_T} + i2\pi f C_T$ with R_T, C_T the total input resistance and capacitance respectively the noise voltages can be converted to currents

$$\frac{\mathrm{d}\overline{I_{xn}^2}}{\mathrm{d}f} = \frac{\mathrm{d}\overline{U_{xn}^2}}{\mathrm{d}f} \cdot \left(\frac{1}{R_T^2} + 4\pi^2 f^2 C_T^2 \right).$$

Usually the noise in charge measuring circuits is given by the equivalent noise charge (ENC) in electrons

$$ENC = \frac{\sqrt{\overline{I^2{}_n}}}{eB} \text{ [electrons]}$$

with B the bandwidth of the readout circuit.

The influence of the noise on the measured signal is decreased by band-pass filtering, the so-called pulse shaping. There are different shaping methods as described in [Manfredi, 1986]. The technique used in the prototype's front-end electronics is the RC-CR shaping, where a combination of a CR high pass filter and a RC low pass filter form a band pass. The resulting equations describing the noise with the proper filter function included are given in the context of the front-end electronics (chapter 5.1.4).

This ENC noise is determined in a measurement from the rms of the noise fluctuations $\overline{S_n^2}$ (base line fluctuations in units of the ADC) by calibrating the rms values with the defined energy deposit E_0 resulting in a signal amplitude S_0 (in ADC units). Taking into account the effective energy to generate an electron-hole pair in the detector E_{e-h}*, the measured equivalent noise charge is given by

$$ENC = \frac{\sqrt{\overline{S_n^2}}}{S_0} \frac{E_0}{E_{e-h}} \text{ [electrons]} \tag{C.1}$$

In addition to the above-mentioned noise sources, detector systems show some pick-up noise, the amount of which depends on the specific design. Distortions originating in the (laboratory) environment such as spikes on the power line, switching spikes from digital (readout) electronics, radio transmissions, etc. can couple into the extremely sensitive readout electronics or the detector itself in various ways (galvanic, capacitive or inductive). In multi-channel systems a powerful tool to eliminate most of this noise is the so-called common-mode correction. For many situations the pick-up affects all readout channels simultaneously (e.g. bounces of the ground line). Then the noise-induced shift of the base line can be calculated from the channels which do not detect a signal and subtracted.

C.2 Energy Resolution of Semiconductors

Following the measurement chain from the detector itself to the digitized pulse height, each processing step contributes to some extent to the overall energy resolution of the system:

Charge Generation: A deposit of the energy E_0 in the semiconductor by photoelectrons, Compton-scattered electrons, electrons/positrons from a pair creation, atmospheric muons, etc. generates electron–hole pairs and phonons. The mean number of electron–hole pairs N is proportional to the deposited energy $N = \frac{E_0}{E_{e-h}}$. Since this is a statistical process where the deposited energy is divided up between electron–hole pairs and phonons, N varies: $\overline{\Delta N^2} = F \cdot N$ with F the Fano factor†[Lutz, 1995].

*$E_{e-h} = 3.6\,\mathrm{eV}$ for silicon at room temperature

†The Fano factor for silicon is $F = 0.115$ at room temperature.

Charge Collection: The collection of the positive and negative charges at the readout contacts can be incomplete due to recombination, charge trapping at impurities, and insensitive detector parts (e.g. detector edges, defective areas).

Leakage current: Thermally produced electron–hole pairs are responsible for the leakage current. For every 8°-increase in temperature the current doubles. It contributes to the shot noise described above.

Preamplifier Noise: Every amplification stage adds noise to the signal. This is mainly due to effects in the amplifying transistors (e.g. charges trapped in the channel of a FET transistor, low frequency noise). In good amplifier designs, the noise contributions from the stages following the first amplification stage are negligible — the first stage then defines the noise of the front-end system.

Thermal noise: Every component in the readout chain shows thermal noise. Again contributions after the first amplification stage should be negligible.

Capacitances: The input capacitances seen by the preamplifier do not contribute to the noise, but they diminish the signal-to-noise ratio: The signal needs to charge the capacitance. If the capacitance is larger, a lower voltage swing is available for the preamplifier. Since the noise voltages of this stage are independent from the signal, the signal-to-noise ratio decreases with increasing capacitance.

Digitalization Noise: The binning taking place in the digitalization process adds noise. Normally this is negligible compared to the other noise sources.

Induced Noise: The measurement system cannot be completely isolated from its environment. Every wire is an antenna picking up noise, every transformer and optocoupler has a capacitance transferring external interferences into the system. Internal control signals can also couple into the measurement signal path. Different means are used to suppress such noise induction including shielding, star-like ground wiring, differential signal transmission, etc. For noise whose induction cannot be avoided, common-mode correction provides a powerful means of noise suppression in multi channel applications. Its goal is to eliminate the induced fluctuations which disturb several readout channels *by the same amount*, for example all the channels of one front-end chip. For correction, the average over the channels is subtracted.

Systematic Errors in the Measurement Process: In the case of the MEGA readout system the problem of time walk (chapter 5.1.6) introduces additional errors to the measured signal.

Overall Peak Width: Summing up all noise components quadratically gives expected the total peak width ΔE_T

$$\Delta E_T^2 = \Delta E_S^2 + \Delta E_X^2 + \Delta E_E^2 + \Delta E_{sys}^2 \tag{C.2}$$

where $\Delta E_S = 2.35\sqrt{FE_{e-h}E_0}$ (FWHM) represents the semiconductor's inherent statistical fluctuations of the generated charge carriers, E_0 is the energy deposit to be measured, ΔE_X is due to

incomplete charge collection and ΔE_E comprises all broadening from electronic components (leakage currents, preamplifier noise, thermal noise of resistances, digitalization noise, induced noise). The fluctuations due to systematic errors are hard to describe quantitatively (otherwise they could be corrected) and contribute not only to the peak width (expressed by ΔE_{sys}), but also to peak shifts.

C.3 Energy Resolution of Scintillator – Semiconductor Combinations

Light Generation Statistics: The scintillation process is a statistical process where (visible) light is produced proportional to the deposited energy, of course with a statistical fluctuation. A high light output is advantageous to get a good signal-to-noise ratio. Since doped materials (in MEGA the CsI is doped with Tl) emit significantly more light, they are preferred to intrinsic materials. Inhomogeneities in the doping concentration, however, can lead to local variations of the light output. Another source for variations in the light output arises from non-linear responses of the crystal (important for spectra of monoenergetic sources when considering energy deposits which are split into more than one interaction). For this work the effects of crystal inhomogeneities are negligible.

Light Collection Efficiency: The emitted light travels along the crystal and is partly reflected at surfaces. Polished surfaces and reflective covers keep the light in the crystal, optical couplings and antireflective coatings guide the light into the semiconductor. Both mechanisms are of course not perfect, leading to dependencies of the collected light on the interaction location.

Semiconductor Efficiency: After the light is coupled into the semiconductor all the issues mentioned in the previous chapter hold also for this case — except for the electron–hole pair generation. Optical light has not enough energy to produce more than one electron–hole pair, which leads to a modified statistics. Also, the generation of the electron–hole pair takes place in the first micrometers of the semiconductor. This reduces the charge collection efficiency since the first tens of nanometers of the entrance window are implanted contacts, which means that they are passive material.

Overall Peak Width: The total peak width ΔE_T for monoenergetic deposits in the crystal is thus given by

$$\Delta E_T^2 = \Delta E_E^2 + \Delta E_C^2 + \Delta E_I^2 + \Delta E_{sys}^2. \tag{C.3}$$

ΔE_E sums up the electronic noise components of the semiconductor. This component is given as equivalent noise charge in the semiconductor and needs to be corrected by the light yield Y (see chapter 4.4) to get a contribution to the peak width (expressed as keV deposit fluctuation in the crystal): $\Delta E_E = 2.35 \cdot \frac{ENC}{Y}$ (FWHM). ΔE_C represents the statistical fluctuations of the charges measured in the semiconductor including the photon generation statistic, the photon transfer efficiency into the semiconductor (coupling losses), and charge collection inefficiencies in the semiconductor, $\Delta E_C = 2.35 \cdot \sqrt{\frac{E_0}{Y}}$ (FWHM). The intrinsic resolution ΔE_I summarizes effects such as crystal inhomogeneities, peak broadening by leaking (low-energy) particles (X rays, ionization electrons), and non-linear response of the scintillator. Again systematic effects ΔE_{sys} also have to be taken into account.

Appendix D

Algorithm for Fitting Calibration Spectra of Individual Detector Channels

The aim of the described algorithm is to correlate the measured peak height of a signal (in units of the analog-to-digital converter of the hardware) with the deposited energy in the corresponding detector channel. The input is one spectrum per channel, obtained from the measured energy deposits of radioactive laboratory sources. Although the algorithms for evaluating these spectra for the various types of detectors used in the MEGA prototype evolved from the ones described in [Andritschke, 2000, Schopper, 2002], a completely new version has been developed for this work*.

The algorithm has to be optimized for the specific characteristics of both the data-acquisition system and the design of the detector:

- The large number of channels which needed to be evaluated (3840 p-side channels from the tracker, 1920 single-sided and 480 double-sided crystal channels of the calorimeter) necessitated a fully-automated analysis.
- Gains fluctuate between the numerous chips of the front-end electronics and there is a non-uniform quality of the coupling between crystals and readout diodes. Thus variations up to a factor of two in measured pulse heights (ADC units) appear which impede the application of any kind of global restrictions to the calibration parameters.
- The front-end electronic ASIC has a non-linear response resulting from the measurement principle (chapter 5.1) which needs to be accounted for as far as possible.
- For various reasons, the prototype is calibrated in its fully assembled state. A varying exposure over the different detector channels due to shading effects and uneven distances to the calibration sources is a natural consequence. Especially the calorimeter modules show this effect — the outer crystals "shield" the inner ones. For the inner crystals there is also an increased fraction of photons which are scattered once in outer crystals (or passive material) and therefore do not contribute to the photopeak of the inner detector parts, resulting in a lower peak-to-continuum ratio for the shielded crystals.

To overcome these problems the following features are introduced into the algorithm:

- Fixed values such as thresholds or limits are avoided as far as possible in order to deal with varying statistics and gains in an uniform fashion within an automatic process.

*The code is written in C++ and uses extensively the C++ library ROOT [Brun and Rademakers, 1997], see also `http://root.cern.ch/`.

- For the same reason, every channel is treated individually, especially peak position information of previously processed or neighboring channels is *not* used.
- The algorithm handles multiple data sets taken with different sources (^{137}Cs and ^{22}Na for the calorimeter) at once. This reduces the number of parameters, since values shared for one channel by all datasets (such as the offset or the width of the peak[†]) are determined once. Ambiguities are avoided — otherwise the same parameter would have been determined twice — and run-always of parameters to senseless values (mainly due to the low statistics of the calibration measurements) are diminished which leads to a more robust algorithm.
- A "background" for the calibration is made up of interactions not contributing to the photopeak which includes incompletely absorbed photons (Compton edge) and photons which already had an interaction somewhere else, e.g. in other crystals or passive material. They are taken into account for two reasons: 1. In multiple line spectra the lower-energy photopeak often coincides with the energy deposits of Compton-scattered photons. 2. The Compton edge contains information of use for the energy calibration. It helps to account for the non-linearities, which mostly are largest at low energies.

These requirements lead to an algorithm which fits all measured spectra for each channel simultaneously. The fit function has components for the photopeaks, for the Compton edges, and for photons Compton-scattered into the considered channel from the surrounding material.

For the calorimeter channels featuring double-sided readout, in addition the z-dependence (the position along the crystal) has to be taken into account. This is implemented in the algorithm by including a simple model for the light transport along the crystal (appendix D.3). The resulting pulse height histogram has three dimensions (x: pulse height of first readout diode, y: pulse height of second readout diode, z: number of events) and consequently a surface has to be fitted.

D.1 Procedure

Since the (final) fit has many parameters and the data have low statistics, the starting values are crucial to avoid a run-away of the parameters. Thus the pulse height histograms (i.e. the uncalibrated spectra) are processed in several steps. Some of these steps do not depend on the detector type; many differ just slightly. Consequently there is a single program for all three detector types (strip detectors, single-sided calorimeters and double-sided calorimeters) where (C++) classes represent the various steps:

1. Sufficient number of counts: If any single histogram has less than 400[‡] entries, the channel is marked as defective and no further processing is performed.
2. Projection (only for channels of double-sided calorimeters): For the first processing steps of the double-sided channels the 3-dimensional pulse height histogram is reduced to two 2-dimensional ones. The first is a projection onto the square-sum of the signals $S_{sum} = \sqrt{S_i^2 + S_o^2}$ (with S_i and S_o the signals of the two readout diodes), the second a projection

[†]The dependence of the peak width on the energy is neglected in the calibration of single channels. The approximation of a constant peak width simplifies and speeds up the algorithm through reduction of the number of parameters. Although small deviations are observable, no impact on the procedure is found.

[‡]This value is somewhat arbitrary. It especially depends on the duration of the measurement and the exposure, but a spectrum can be evaluated if it contains $\gtrsim 1000$ entries. 400 turned out to be a practical value to discriminate operating channels from defective ones.

onto a parameter reflecting the ratio between the two signals called $\eta = \frac{S_i - S_o}{S_i + S_o}$. The projection on the sum is processed in the following steps the same way as the histograms of the single-sided readout channels. The η-projection is used to recognize channels with one defective diode (i.e. η is around +1 or -1) and to determine a medium η value.

3. Photopeak identification: A given number of photopeaks (one or two for the radioactive laboratory sources used in this work, the algorithm is designed to handle an arbitrary number of isolated peaks) is located in a couple of steps:

   (a) All local maxima are determined by calculating the second derivative of the histogram.

   (b) One maximum after the other is eliminated starting with the lowest amplitude until three times the needed number of peaks is left over for further processing.

   (c) From the remaining peaks the one with the highest ADC value is identified with the most energetic line of the source.

   (d) If this is a multiple-line source, the remaining peaks are associated with best-matching energies (nearest neighbor to the peak position guessed from the first peak's energy and ADC value).

   (e) Every peak is fitted with a pure Gaussian giving the start parameters for later fit stages.

4. Background: All entries from histogram bins above the highest photopeak are regarded as background. The average of the considered bin entries are used as start parameter for later fit stages.

5. Spectrum: The spectrum is fitted (at this point multiple spectra are not yet combined, in the channels of the double-sided calorimeters still the one-dimensional spectrum is processed). The fit functions are described in the next section.

6. Spectra (except for channels of double-sided calorimeters): If there are spectra of multiple sources, a simultaneous fit of the different spectra is performed where the energy calibration and the peak width are common parameters. This step is omitted for double-sided readout channels because the overall fit will be in the 3-dimensional histogram.

7. 3D-Spectrum (only for channels of double-sided calorimeters): The 3-dimensional spectrum (again at this point multiple spectra are not yet combined) is fitted. The fit surface is a combination of the fit function used in item 5 and the model for the z-dependence described later in this appendix (D.3).

8. 3D-Spectra (only for channels of double-sided calorimeters): Analog to item 6, multiple spectra are fitted with common parameters in this step (if available).

9. Output: The calibration parameters (a subset of the fit parameters) are stored in a format, which is used by the data-acquisition program "MEGAlyze".

In the case of the tracker channels there are only two calibration sources (^{241}Am and ^{57}Co) available and any Compton edge of the corresponding source lies below the trigger threshold. The applied fit function is simple and fitting both spectra simultaneously is not required.

In order to be able to check and intervene — if necessary — every parameter can be changed by hand after each step and the step can be repeated with the new values. Additionally a log of every step is generated so that corrections can be applied also after a fully automatic run. The latter feature was used for the calorimeter channels because the fitting procedure is time consuming even on modern personal computers. About 10–20% of the p-side channels on the tracker needed

manual intervention. In the calorimeter the need to intervene depends on the individual module. Between 8% and 56% of the channels in modules having single-sided readout (average 26%) and 42% of the ones with double-sided readout needed corrective actions (in most cases the position of the 1.275 MeV line of ^{22}Na was not fitted correctly due to low statistics).

D.2 Fit Functions

In order to accurately model source spectra over a wide energy band, appropriate (fit) functions are a necessity. The interactions included in the model are the photoelectric and Compton effect. Pair creation has no impact in this case since the used source energies are below 1.3 MeV.

D.2.1 Simplifications

The geometry of the detector setup is not taken into account. Instead a homogeneous exposure to the source photons during calibration measurements with radioactive laboratory sources is assumed.

The energy resolution of an individual channel is assumed to be constant over the considered energy range. Since the energy resolution is dominated by electronic noise which is independent from the measured signal height, and since the calibration energies cover only a small part of the dynamic range (compare chapters 3 and 4), the variation can be neglected.

D.2.2 Cross Sections for Compton Scattering and Absorption

The shape of the different components of the spectrum is defined by the cross sections differential in the deposited energy (i.e. the electron energy) $\frac{\mathrm{d}\sigma}{\mathrm{d}E_d}$.

In a photoelectric effect the whole photon energy is absorbed in the medium. This leads to

$$\frac{\mathrm{d}\sigma_p}{\mathrm{d}E_d} = \sigma_p(E_i) \cdot \delta(E_d - E_i) \tag{D.1}$$

with σ_p the total cross section for photoelectric effect (chapter 1.1.4.2) as a function of energy, $\delta(x)$ the delta distribution, E_i the energy of the incoming photon and E_d the deposited energy in the detector channel.

In a Compton interaction the energy of an incoming photon E_i is distributed between the energy of the recoil electron E_e and the scattered photon E_g. The cross sections defining the energy distributions of the scattered electrons and the scattered photons respectively are given by equations 1.6 and 1.7.

Since the (differential) cross section is defined as the number of scattered particles with energy E_x per second and per incident particle flux, the contribution of the photoelectric effect to the spectrum is given by

$$\frac{\mathrm{d}N}{\mathrm{d}E_x} = n \cdot \frac{\mathrm{d}\sigma}{\mathrm{d}E_x} \cdot \frac{\rho}{m_{atom}}$$

with n the number of incident particles during the measurement time per unit area, ρ the material's density and m_{atom} the mass of one atom.

D.2.3 Nonlinearities

Due to the time-walk problem of the front-end electronics (chapter 5.1) the function connecting measured signal amplitudes s (in units of the analog-to-digital converter) with deposited energy E_d shows deviations from linearity. This is taken into account by interpolation between the calibration points (i.e. photopeak positions) consisting of the line energies ($E_{line,\,i}$) and the (fitted) peak positions ($p_{line\,position,\,i}$) resulting in a function

$$s = s(E_d)$$

which is either a polygon for linear inter- and extrapolation (used for the tracker channels and for the calorimeter crystals with single-sided readout) or a spline function (calorimeter crystals with double-sided readout).

D.2.4 Noise

The detector noise is included in the energy spectrum $\frac{\mathrm{d}N_d}{\mathrm{d}s}(s)$ by convolving the theoretical distribution of energy deposits $f(s)$ (as stated in D.2.2) with a Gaussian[§]:

$$\frac{\mathrm{d}N_d}{\mathrm{d}s}(s) = \frac{1}{\sqrt{2\pi}\cdot p_{sigma}} \int_{s_i} f\,(s) \cdot \exp\left(-\frac{(s-s_i)^2}{2p_{sigma}}\right) \mathrm{d}s_i \tag{D.2}$$

with p_{sigma} the energy resolution (in analog-to-digital converter units) of the considered channel.

D.2.5 Function for Spectra Taken with Tracker Channels

Since the Compton edges for the available calibration sources of the tracker are below the trigger threshold a relatively simple fit function can be applied. It has three components:

1. **Photopeak:** Equation D.1 inserted into equation D.2 gives

$$\frac{\mathrm{d}N_{photo}}{\mathrm{d}s}(s) = p_{photo\,height} \cdot \frac{\sigma_p}{\sqrt{2\pi}\cdot p_{sigma}} \cdot \exp\left(-\frac{(s-p_{line\,position})^2}{2p_{sigma}}\right)$$

   with the fit parameter $p_{photo\,height}$ representing the photopeak height.

2. An exponential function represents **the noise**

$$\frac{\mathrm{d}N_{noise}}{\mathrm{d}s}(s) = p_{noise\,height} \cdot e^{-p_{noise\,exp}\cdot s}.$$

3. a constant for **the background**, resulting from interactions from room background (e.g. ^{40}K, muons)

$$\frac{\mathrm{d}N_{background}}{\mathrm{d}s}(s) = p_{background}$$

with $p_{photo\,height}$, $p_{line\,position}$, p_{sigma}, $p_{noise\,height}$, $p_{noise\,exp}$, $p_{background}$ the particular fit parameters.

[§]The one-dimensional expression is given here. The two-dimensional case for the two-sided calorimeters is analogous and uses two independent σ_d for the two diodes.

D.2.6 Function for Spectra taken with Calorimeter channels

The spectrum of an individual calorimeter channel exhibits several components. For every γ-ray line emitted by a source there are four major components to be considered:

1. The **photopeak** (equation D.1)
2. The deposited energies by the **recoil electrons** of photons not completely absorbed in the calorimeter's crystals (Compton edge, equation 1.6):

$$\frac{\mathrm{d}N_{recoil}}{\mathrm{d}E_e} = p_{compton\,height} \cdot \frac{\mathrm{d}\sigma_C}{\mathrm{d}E_e}$$

   Since the scattered photon could be absorbed in the *same* crystal, a portion of this component is subtracted and added to the photopeak component. This fraction is calculated from the absorption probability of the scattered photon in 0.5 cm CsI.

The (active as well as passive) material surrounding the considered crystal (Compton) scatters source photons. These lower-energy photons can be absorbed in the considered crystal, but can also be Compton-scattered again.

3. The component describing **scattered photons** which are **absorbed** has the following distribution

$$\frac{\mathrm{d}N_{scatter\,absorbed}}{\mathrm{d}E_d} = p_{scatter} \cdot \int_{E_g} \frac{\mathrm{d}\sigma_C}{\mathrm{d}E_g} \cdot \frac{\mathrm{d}\sigma_p}{\mathrm{d}E_d}\mathrm{d}E_g$$

4. The energy deposits of **scattered photons** which are **scattered again** contribute

$$\frac{\mathrm{d}N_{scatter\,Compton}}{\mathrm{d}E_d} = p_{scatter} \cdot \int_{E_g} \frac{\mathrm{d}\sigma_C}{\mathrm{d}E_g}(E_i, E_g) \cdot \frac{\mathrm{d}\sigma_C}{\mathrm{d}E_d}(E_g, E_d)\mathrm{d}E_g$$

For each line a set of the four components is introduced and summed up. Then the non-linearities and the noise are taken into account. The last component added to the fit is a constant representing the background.

D.3 Model of the z-Dependence

In case of the calorimeter blocks with readout on both ends of the crystals, additionally the dependence of the two signals from the depth of interaction has to be taken into account. A simple model based on a one-dimensional cellular automaton is used here.

The crystal is divided into 100 cells along the crystal axis (figure D.1). Light can travel up- or downwards through each cell. Inside a cell a percentage $p_{passing}$ of the light keeps its direction and is transferred to the next cell. This includes photons without any interaction and totally reflected ones. Another percentage $p_{diffusive\ reflection}$ is reflected diffusively, representing mainly light exiting the crystal and being reflected by the covering reflective paper. Finally the percentage $p_{abs} = 1 - p_{passing} - p_{diffusive\ reflection}$ is absorbed. Both ends of the crystal are special cells representing the diodes. There the absorption probability is 1.

In order to calculate the distribution of signals onto both diodes for a certain depth of interaction in the crystal, the corresponding cell is filled with a unit amount of photons, 50% in upward and 50% in downward direction. This is the starting point for the recursion of the cellular automaton which addresses in an iteration each cell and redistributes the light according to the probabilities

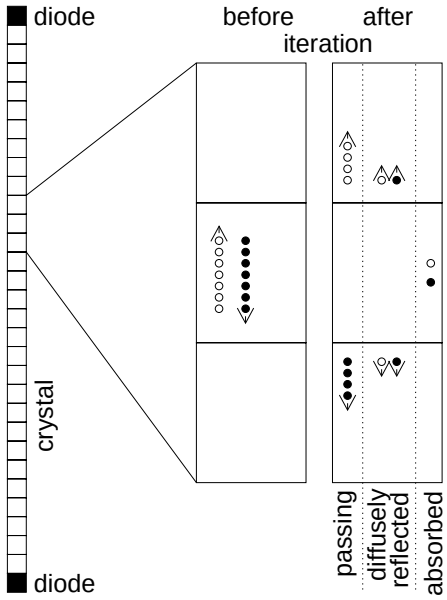

Figure D.1: Model for z-dependence of the signals for two-sided read-out

$p_{passing}$ and $p_{diffusive\ reflection}$. The recursion is stopped when less than 10^{-6}units of light are left over traveling through the crystal, i.e. being not absorbed.

Combining the results for each cell as starting point with the spectrum described in D.2.6, introducing non-linearities, and adding noise, finally yields the fit surface.

D.4 Improvements and Comments

In most cases where the automatic process fails (already mentioned in appendix D.1) the fit did not converge. Since the most time consuming part of the calibration is the correction of false fits, significant improvements could be expected from tuning of the ROOT fitting routines or introducing a better-matching fit algorithm.

In principle the non-linearities could be eliminated by measuring the pulse shapes and trigger thresholds of each channel (chapter 5.1.6). This would allow a reduction of the number of fit parameters, increasing the stability of the algorithm.

If the peak width is modeled as the sum of a constant component from the electronics[¶] and an energy-dependent component of the photon statistics (in case of the calorimeter channels), the fit algorithm might be better able to handle weak peaks (the 1.275 MeV line compared to the 511 keV in case of ^{22}Na).

[¶]which includes preamplifier noise as well as detector leakage current

Appendix E

Performance of the Tracker in Detail

This appendix gives an overview over the performance of the 8448 tracker channels in a sequence of plots. They illustrate the necessity for individual treatment of each channel and describe some issues in detail which were beyond the scope of the main text. All the data plotted here, except for the rise times measurement, have been taken during the campaign at the HIGS facility, a total of 83 measurements. This keeps the fluctuations in the operating conditions of the detector at a minimum since the detector (especially the front-end chip) is very sensitive to environmental changes, especially ambient temperature. Each graph in this chapter displays values for all 768 channels of a layer, first the 384 channels of the n-side followed by the 384 channels of the p-side.

E.1 Operating Parameters

Every measurement is started with an initialization phase (chapter 5.2.5). Here the whole detector is read out at random times. First, the **baseline offset** (figure E.1) of each channel is determined. Except for a few channels, the offset is roughly stable over the different measurements. A handful of channels show extreme offsets; presumably they are defective and always in saturation. The large variation especially from chip to chip results in a significant reduction of the usable ADC range (up to 40%). In the current design, no possibility exists to compensate this.

The second parameter determined in the initialization phase is the **noise** of each channel. One part of the noise can be subtracted, which is the induced noise seen by all channels of a chip called common-mode noise. For each readout the mean of all 128 channels of a front-end chip is subtracted after the base line correction (i.e. subtracting the baseline offsets) chip-by-chip. The RMS of the remaining fluctuations are shown in figure E.2. Many factors influence this distribution; the main sources are the detector leakage currents and the front-end chip. The variations observable between the various chips result partly from the different gains (apparent in the photopeak positions, figure E.6). Partly they reflect the differences of the connected wafers, where the various wafers have individual amounts of leakage currents in intact strips. The channels with high and widely varying noise are due to leakage currents (mostly impurities or crystal defects at the detector surface). Some channels show significantly lower noise values than their neighbors. Possible explanations are defective bonds to the detector strips, defective readout electronics, and saturated preamplifiers. One would expect that these channels should show a noise level near zero, but due to the common-mode correction a certain amount of fluctuations is introduced artificially.

During each readout of the detector a **common-mode** value for each front-end chip is calculated and histogrammed. The distribution obtained from many readouts is centered around zero (otherwise the offset would have been miscalculated or there is some crosstalk coupling into the chip)

and the width of the distribution shows the amount of induced noise onto the front-end (the RMS values are plotted in figure E.3 bottom for each chip and one entry per measurement). It is obvious that the n-side chips (the first three of the six chips of a layer) show often wider distributions. This is due to the the ground wiring. All p-side electronics is connected to a common ground whereas the electronic grounds on the n-side are only connected for layers with the same bias voltage*.

After the initialization phase the normal data taking process takes place and the detector is only read out upon a valid trigger. Six times the noise (calculated in the fashion described above) is used as threshold to discriminate detector channels with interactions from empty ones, i.e. data reduction after readout. This threshold sets the lower limit for the **dynamic range**. The upper limit is defined by saturation effects mainly in the front-end chips. In order to evaluate the saturation point, the maximum signal from each measurement and for each channel is determined and plotted in figure E.4 (values are not corrected for varying gains). The saturation is then given as the maximum of this distribution. In combination with the baseline offset values the ADC range (0–1023) is used nearly to full capacity.

Due to the trigger and readout mechanism of the front-end chips the **rise time** of the signals causes problems. The pulse shapes of a channel (figure 5.4) are determined in a dedicated measurement as described in chapter 5.1.6 (for the consequences see also this chapter). The rise times of each measured pulse are plotted in figure F.5. They distribute not uniform, neither between channels nor within a single channel, and there is a large dependency on the chip. The within a single channel depends to some extent on the pulse height, as larger pulses are slower. For noisy channels the peak search and fit algorithm fails; those channels show "lines" as distribution.

In order to obtain an energy information, the **gain** has to be determined. Calibration measurements are performed with radioactive laboratory sources and the photopeak position of the emitted γ-ray line is determined as described in chapter 3.3.2. The result for the 122 keV line of ^{57}Co is shown in figure E.6.

The single-channel calibration algorithm automatically delivers the peak width (figure E.7), i.e. the **energy resolution** of the channels. In spite of the large differences in the operating parameters of the chips, the energy resolution at the 122 keV line of ^{57}Co depends on the individual strip rather than on the chip, i.e. the achieved energy resolution is (nearly) independent of the chip settings.

E.2 Tracker Layers Illuminated With a ^{57}Co Source

The dead areas on the tracker layers are illustrated best with a hit distribution statistic for the detector layers. The sequence of images in figure E.8 shows the hit statistics of all ten operational tracker layers from a measurement with a ^{57}Co source placed directly below the tracker. The number of hits is grey-scale coded (maximum 10 counts), no energy cuts are applied, and the order of images follows the sequence of layers in the stack from top to bottom. The x-direction corresponds to the n-side channels, the y-direction to the p-side. The white regular grid observable in all layers is the spacing of the mounting frame. All other dead areas are defective strips. The detectors called "Apoll" and "Ikarus" have each the back corner wafer in the n-side chain disconnected†, because these wafers do not fully deplete and show only huge noise but no signals. That the disconnected areas also exhibit few counts result from misinterpretations in the case of

*The electronic of the tracker layers has to run at bias voltage levels in spite of the integrated AC coupling on the detector wafers. This is due to the fact that a broken oxide of the AC coupling connects a front-end chip input to the bias potential. The chip stops working if it sees too large an input potential, it even might be damaged.

†The hits seen in the disconnected wafer on "Ikarus" are artifacts of noisy p-side strips due to misinterpretations in the reconstruction of the interaction position.

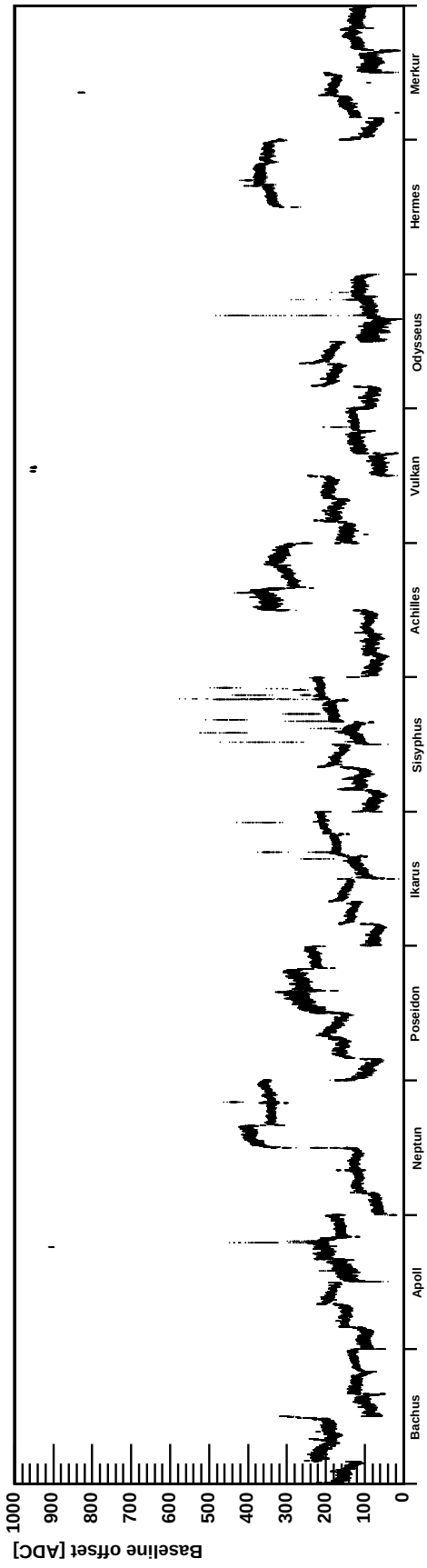

Figure E.1: Baseline offsets for all channels of the tracker layers. The 83 data points for each channel represent the measurements at the HIGS facility. Within one layer first n-side channels and then p-side channels are shown. The detector "Hermes" has unconnected front-end electronics on the n-side.

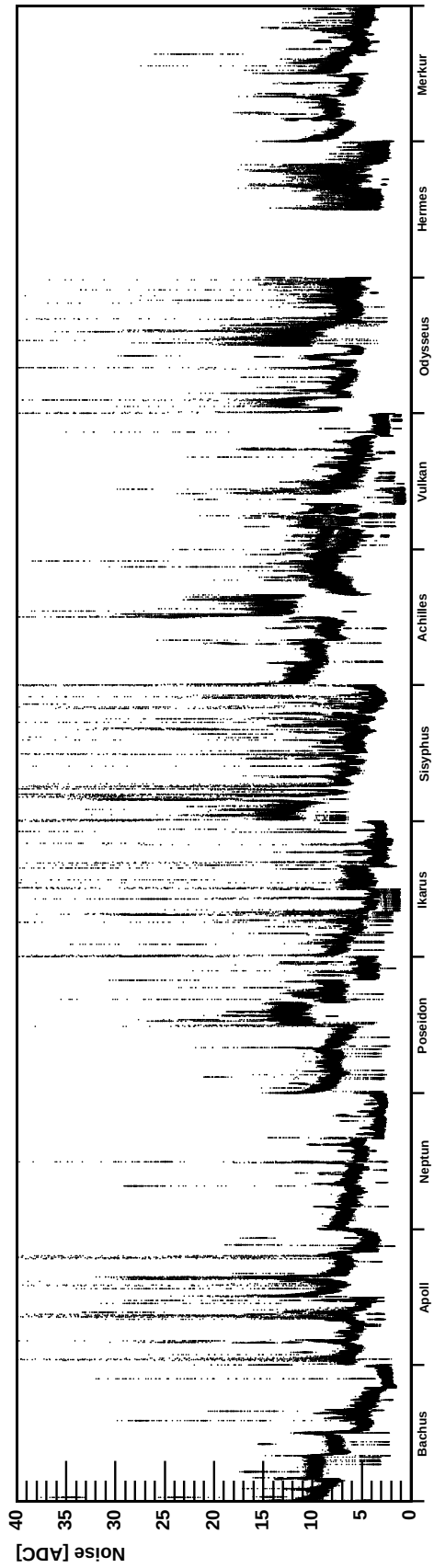

Figure E.2: Noise of the tracker layers. The noise is given in uncalibrated units. Within one layer first n-side channels and then p-side channels are shown.

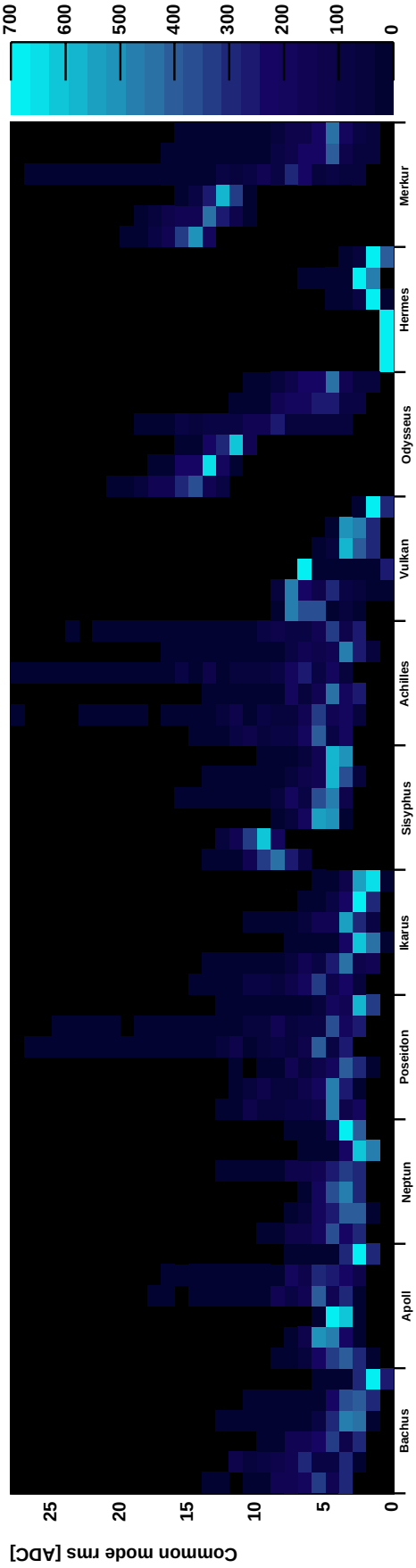

Figure E.3: Widths (rms) of the common mode distributions. (See text.) Within one layer first n-side channels and then p-side channels are shown.

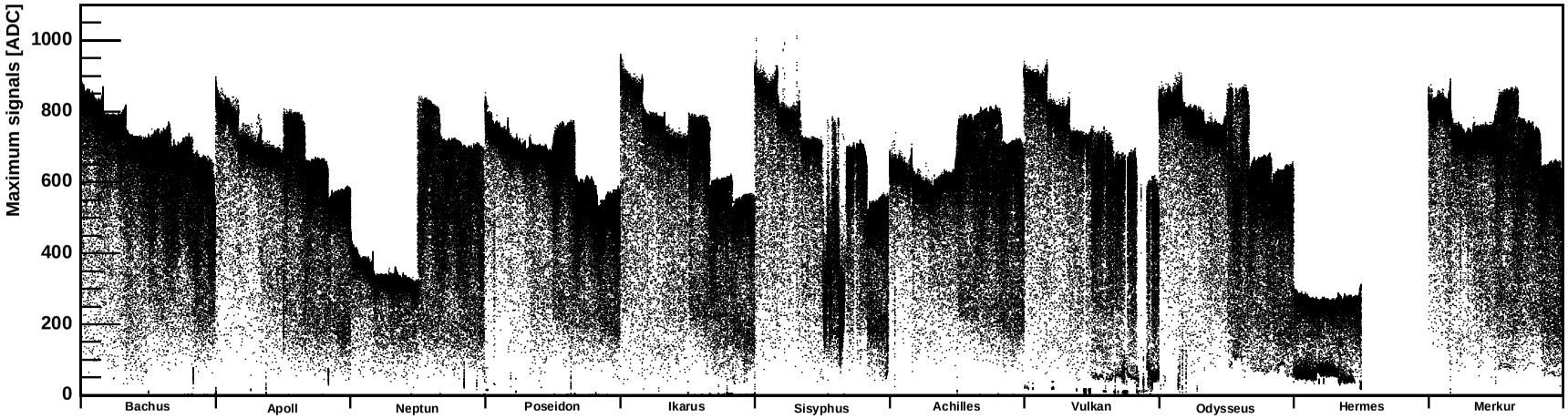

Figure E.4: Maximum signals in a measurement for the channels of the tracker layers. Within one layer first n-side channels and then p-side channels are shown.

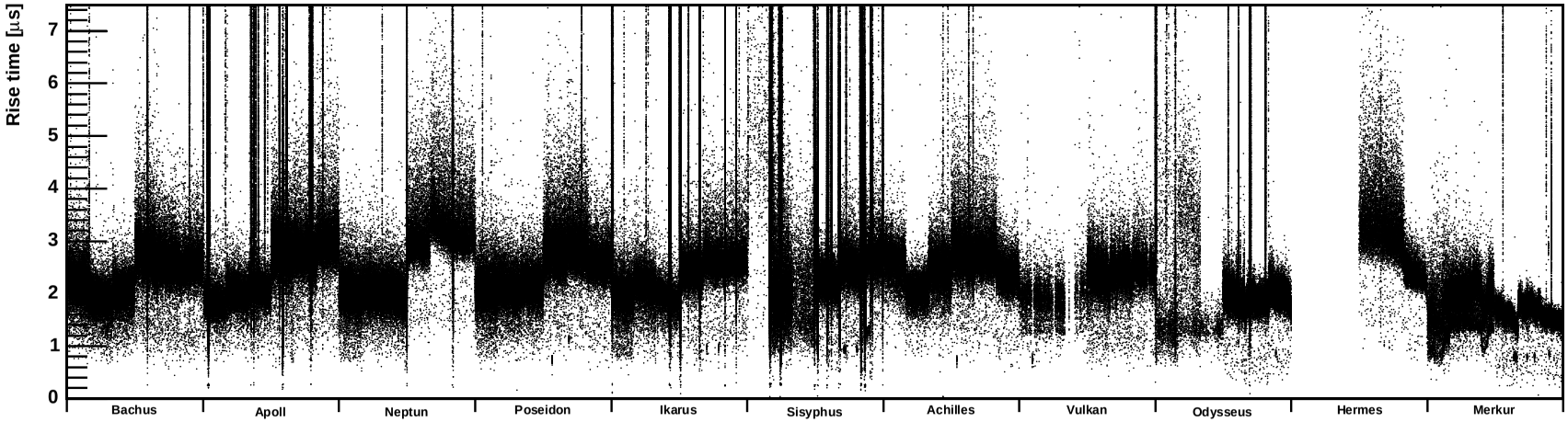

Figure E.5: Rise times of the 8448 channels of the tracker layers. A couple of sources was placed around the detector and for each channel the analog output was sampled. For each recognized pulse the rise time was determined and included in the plot. Channels having black vertical lines are noisy where the algorithm fits many "noise peaks". Within one layer first n-side channels and then p-side channels are shown.

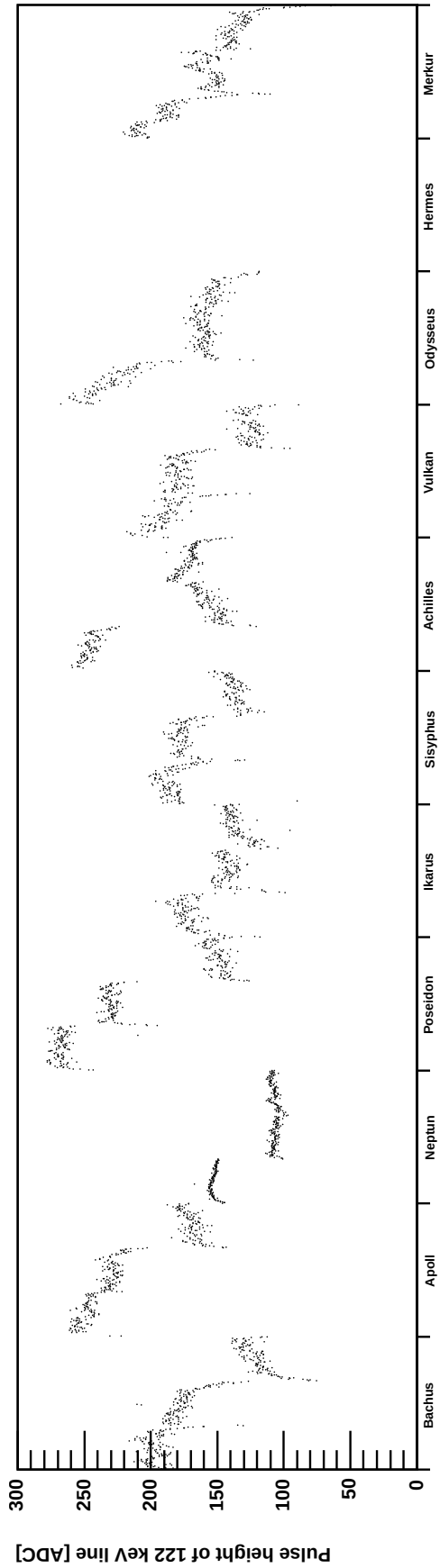

(a) p-side

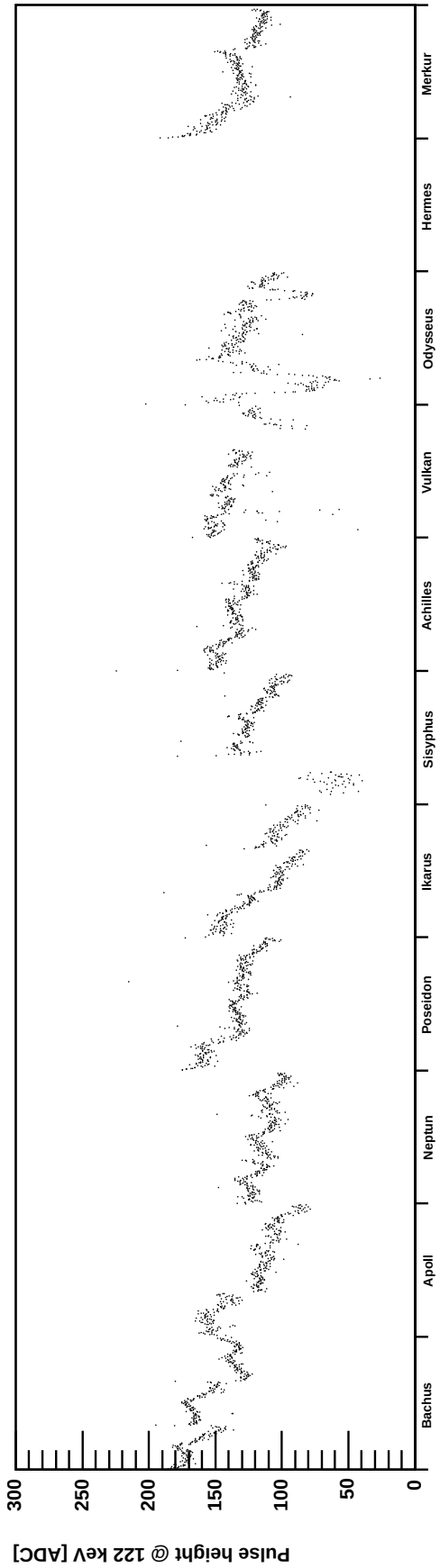

(b) n-side

Figure E.6: Pulse heights for 122 keV signals.

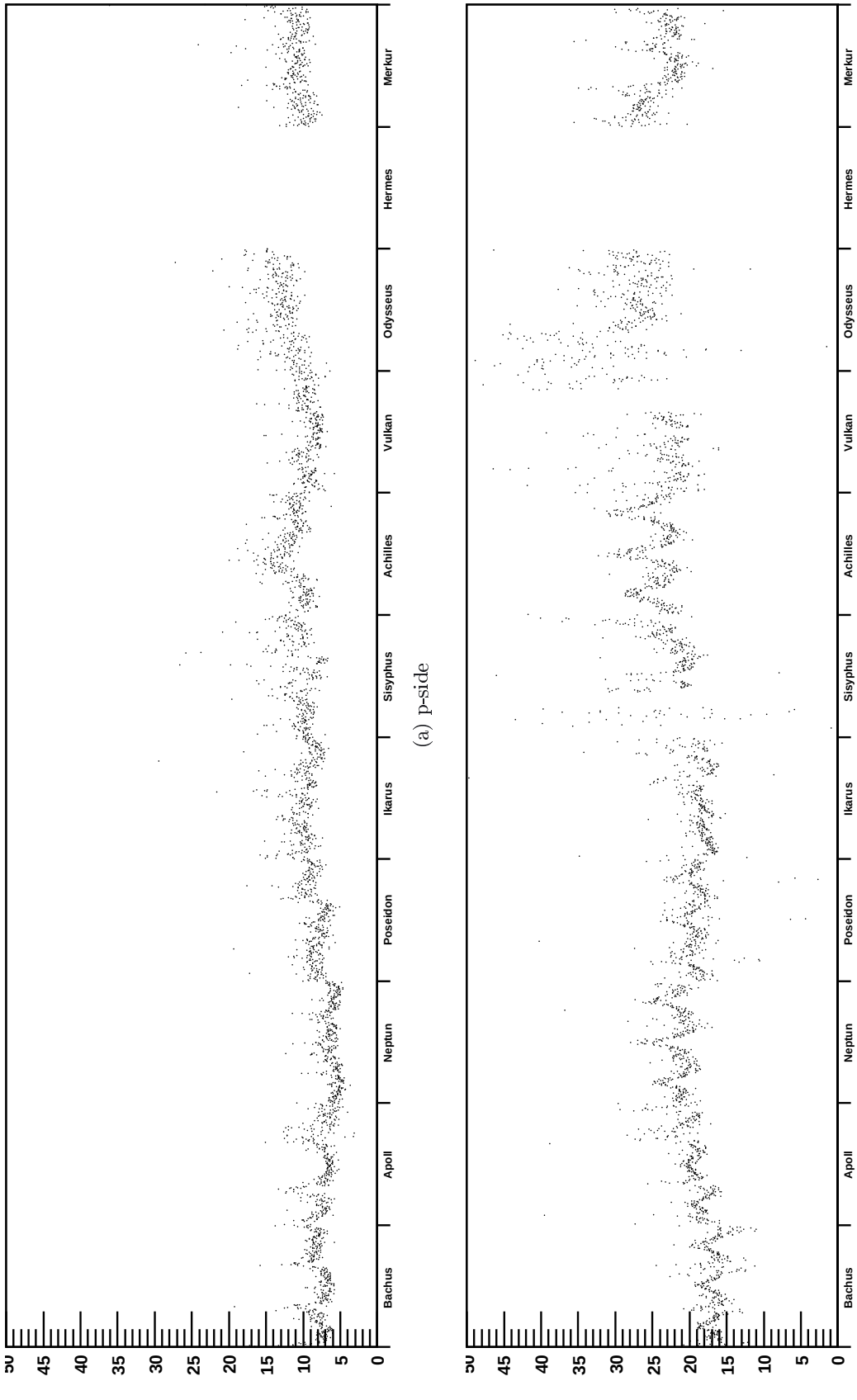

(a) p-side

(b) n-side

Figure E.7: Energy resolutions for 122 keV signals.

ambiguities. The dependency of the source intensity on the source-to-plane distance can be seen clearly. The order is from top ("Bachus", furthest from the source) to bottom ("Vulkan").

The reason for dead strips can be derived for most cases from the noise of the individual channels (figure E.2 top). A few reasons can keep a channel from working:

- Mainly inoperative channels exhibit much noise, presumably due to surface impurities or defects. If the energy of a hit does not exceed the noise threshold, it is filtered out. Additionally, in the case of noisy p-side channels the trigger had to be blocked and no calibration is available (only p-side channels are allowed to trigger in the prototype). Hits in uncalibrated channels cannot be processed further, so they are ignored.
- The channel itself could have a defect (either something is broken on the detector or on the front-end chip).
- One of the wire bonds between the detector and the input of the front-end chip could be open (low-noise channels).
- A defect in the oxide layer of a wafer can connect the readout wire (aluminium) and the implant. This short can saturate the channel and the channel shows a low noise.
- There is an adjustable feed-back resistor of the charge-sensitive amplifier in the front-end chip which has a common voltage input for all 128 channels of a chip. If this resistance is chosen too high, some channels can saturate and a low noise is measured from these channels.

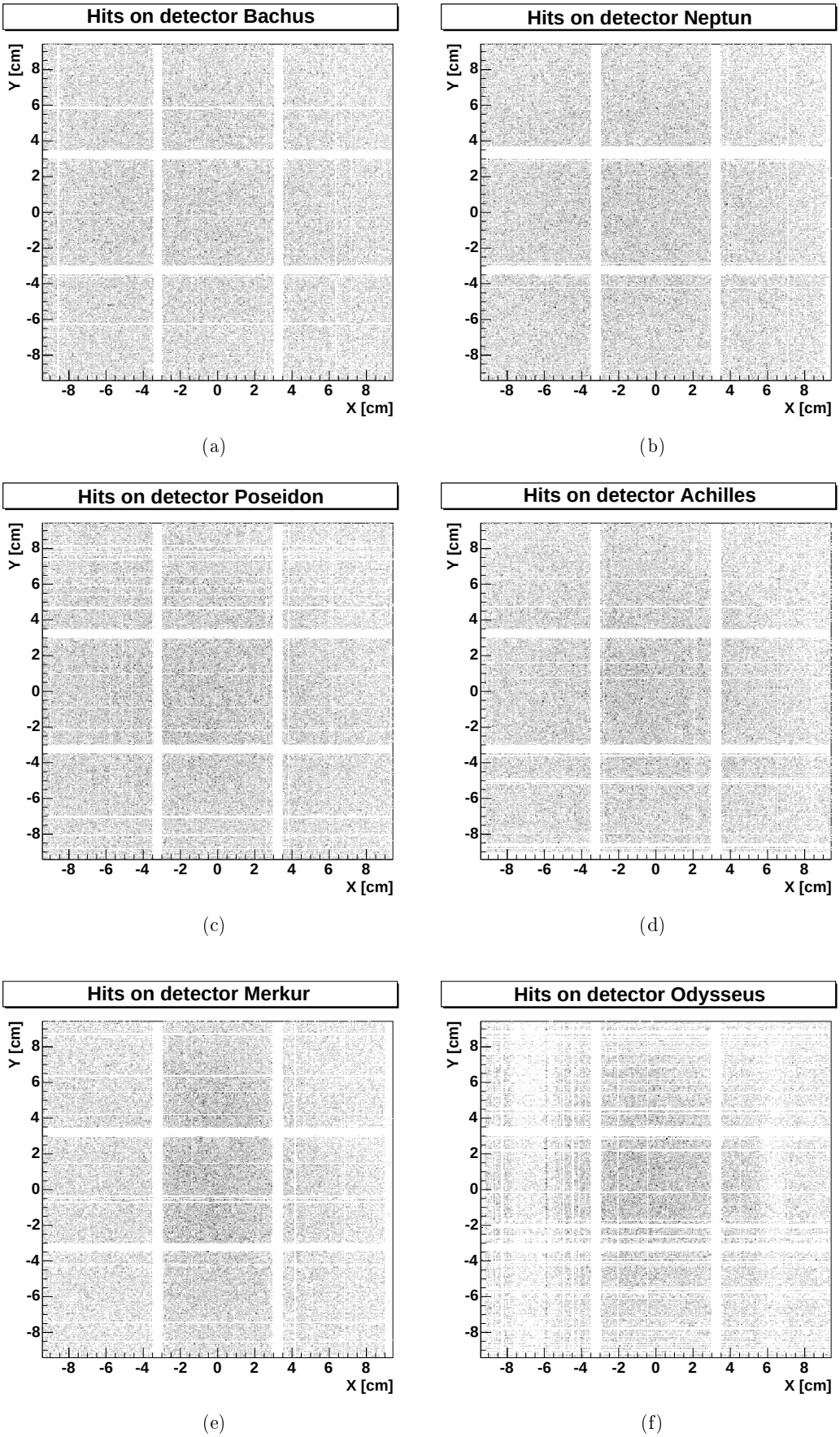

(a) (b)

(c) (d)

(e) (f)

Figure E.8: Hit distribution for the tracker layers

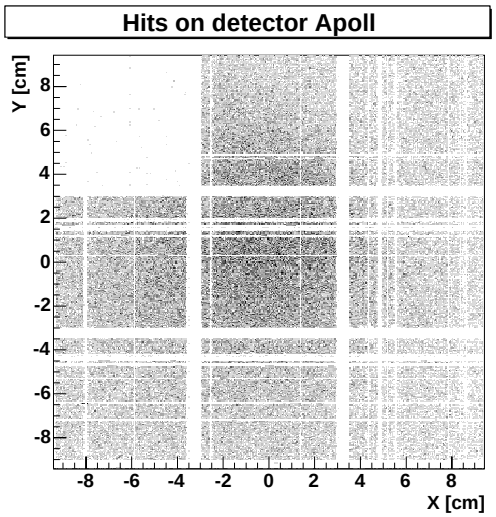

(g)

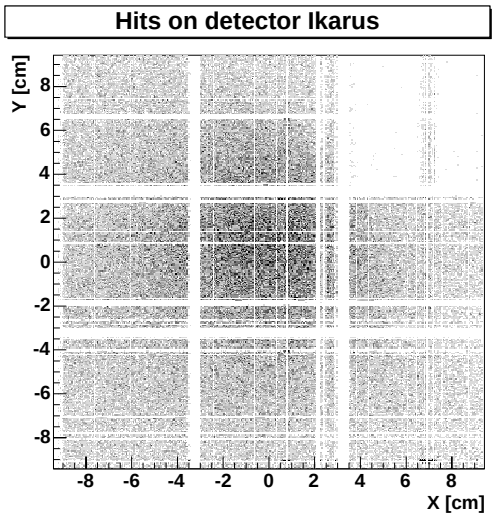

(h)

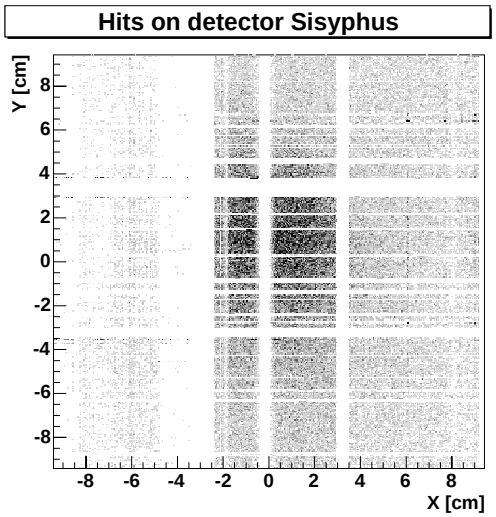

(i)

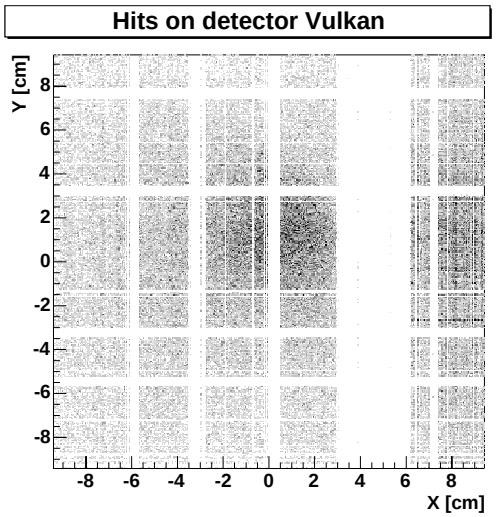

(j)

Figure E.9: Hit distribution for the tracker layers (continued)

Appendix F

Detailed Performance of the Calorimeter

As was done in the previous appendix for the tracker channels, this appendix gives an overview over the performance of the calorimeter channels. There are 1920 crystals with single-sided and 480 with double-sided readout. Due to the stability problem of the electronics the presented data are derived exclusively from measurements at the HIGS facility except for the rise time and ^{241}Am measurements, which — due to time constraints at HIGS — were taken afterwards back at MPE's laboratory.

F.1 Operating Parameters

Since the readout electronics of the PIN-diode arrays are identical to those of the strip detectors most of the points discussed for the tracker channels also apply to the calorimeter channels. These similarities will be mentioned without repeating the arguments, differences will be emphasized:

The **baseline offsets** (figure F.1) show the same behavior as in the case of the tracker channels. The (electronic) **noise** (figure F.2) is significantly smaller* and more homogeneous. Lower bias voltages, a smaller detector area per readout channel ($25\,\mathrm{mm}^2$ versus $84.6\,\mathrm{mm}^2$), and a simpler detector design lead to lower leakage currents. The encapsulation in the aluminium housings of each block forms a good shield. The bias and ground concept is simple because the photodiodes need only readout on one polarity, etc. These points lead to low leakage currents and insensitivity to crosstalk, resulting in low noise. This is even more evident in the **common-mode** (figure F.3) which is nearly non-existent. The **saturation** (figure F.4) behaves similar to that of the tracker. No reason for the early saturation of the detectors "Fortuna", "Diane" and "Persephone" could be identified. The **rise times** (figure F.5) are significantly larger, as is necessary for reading out the crystals. Here two types of interaction can be distinguished, which have peaking times differing by $\sim 1\,\mu$s. The slower, strong component are the interactions in the crystal. Their pulses have larger rise times due to the long time constant of the CsI crystal in comparison to the diode interactions which form the faster and weaker component. The **gain** is determined by evaluating the photopeak amplitudes. In case of the single-sided calorimeter blocks (figure F.6 shows the peak amplitudes of the 662 keV line of ^{137}Cs) the gain varies up to a factor of five. The large differences result from the varying operating conditions of the front-end chips. This becomes clear when comparing

*The noise values in figure F.2 are given in uncalibrated units. For a correct comparison these values have to be calibrated with the amplification in the front-end chips. The electronic noise (expressed in equivalent noise charge as described in chapter 3.3.3 and 4.2) is still lower in the calorimeter than in the tracker. One should keep in mind that this applies only for interactions in the semiconductor! The number of charges generated by scintillation light in the crystal are about one order of magnitude lower. Thus the uncertainties induced by electronic noise translate to larger energy uncertainties in the crystal than the ones in the tracker.

these pulse heights with the ^{241}Am measurement of the PIN-diode arrays (figure F.11). The latter show the same large steps between chips but are mostly homogeneous between the channels of a single chip. The remaining fluctuations in the photopeak amplitudes of the 662 keV line reflect inhomogeneities in the optical coupling of the crystals to the diodes. In the case of the double-sided calorimeters, the dependence of the readout signals on the interaction location along the crystal has to be corrected first. The resulting peak positions are shown in figure F.8. They are more homogeneous than in the single-sided case because the position correction already takes into account and thus averages over the different gains of the two readout diodes. The **energy resolutions** (figures F.7 and F.9) show no obvious correlation to any other parameter, which agrees with the idea that the main contribution are crystal inhomogeneities and systematic effects from the electronics, as stated in chapter 4.4. Additionally the energy resolution of the two-sided readout crystals is approximately the same as in the single-sided case (compare also tables 4.1 and 4.2) because the larger crystal inhomogeneities are compensated by the position correction. The expected factor of $\sqrt{2}$ increase in electronic noise due to the second readout diode is negligible compared to the systematic effects. In the **z-resolution** of the double-sided modules (figure F.10) no striking pattern can be observed. Such a pattern would indicate problems with distributing the contact pressure. Instead, the pattern looks random, suggesting varying production qualities of the hand-polished crystals and hand-made coupling cushions responsible for the wide spread of the observed z-resolutions.

F.2 Parameters of the PIN Diodes

In order to be able to differentiate between effects from the electronics and from the crystal including its coupling, ^{241}Am measurements have been performed. At 60 keV, the highest photon energy of this source, only interactions in the diodes are recorded (trigger threshold). The photopeak amplitudes (figure F.11) show large steps between chips but only smaller variations between the channels of a single chip. The corresponding peak widths (figure F.12) are between 1 and 2 keV except for the detectors "Aetna", "Thetis", and "Circe". The chips of these three detectors have a very low gain. As a result of peak heights of ~ 30 ADC, the noise spread of the peak position is only a few ADC. While for peaks at $\gtrsim 80$ ADC the noise peak width is $\gtrsim 5$ ADC FWHM and digitalization noise becomes negligible, for a peak at 30 ADC the noise peak width is $\lesssim 2$ ADC FWHM; digitalization noise becomes a significant contributor. The additional noise contribution is also observed in the electronic noise expressed in equivalent noise charge (figure F.13). Where the majority of chips shows a noise of $250 - 350\,e^-$ENC, the chips with low gains have noise values of $350 - 550\,e^-$ENC. By combining the ^{241}Am and ^{137}Cs measurements, one can calculate the number of electrons measured in the diodes per keV deposited energy in the crystal. This parameter combines all leakage mechanisms of the measurement; it is called **light yield** and is plotted in figure F.14. The values peak around $18\,e^-$/keV (compare figure 4.10). The differences between the chips are small compared to other parameters such as the gain. There are no crystals with a light yield larger than $25\,e^-$/keV, but values of $40\,e^-$/keV and better have been reported(see chapter 4.4). Thus systematic problems such as ballistic deficit due to too short shaping times are very likely to be responsible for the comparatively low light yield.

F.3 Calorimeter Illuminated with a Source

For calibration the calorimeter is exposed to radiation from radioactive laboratory sources. Figure F.15 shows the hit statistics of a calibration measurement. The position of the radioactive source

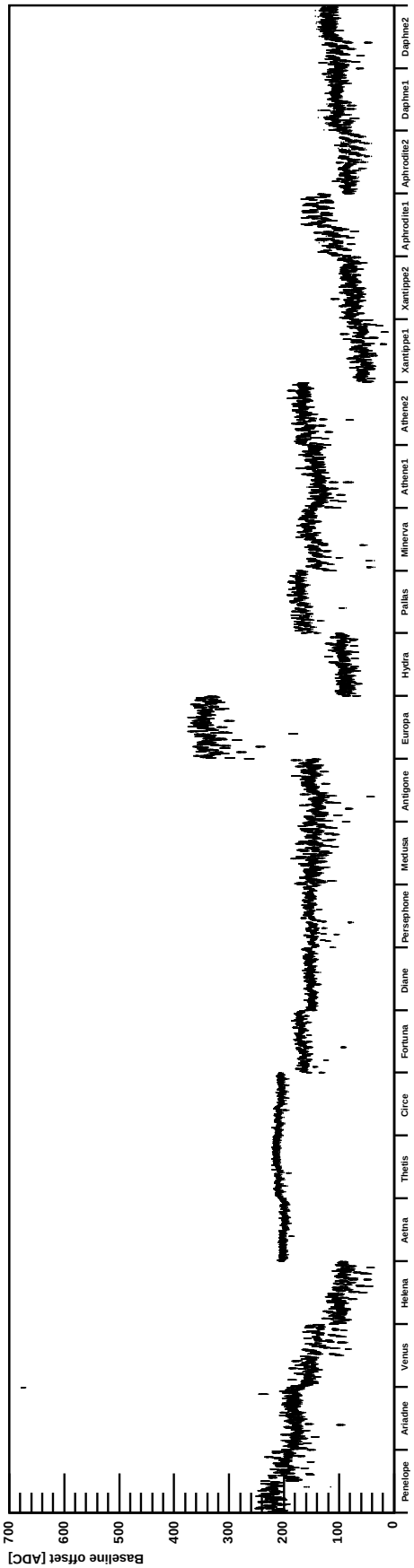

Figure F.1: Baseline offsets of the calorimeter blocks

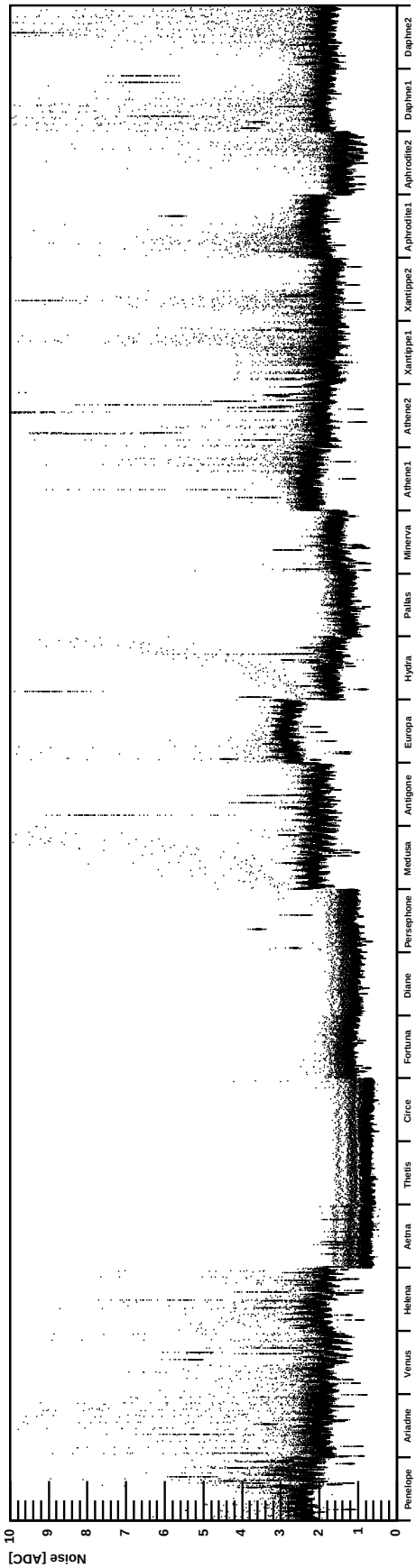

Figure F.2: Noise of the calorimeter blocks in uncalibrated units. The block of detectors from Aetna to Persephone shows low noise in ADC units due to their low gains (compare figure F.6).

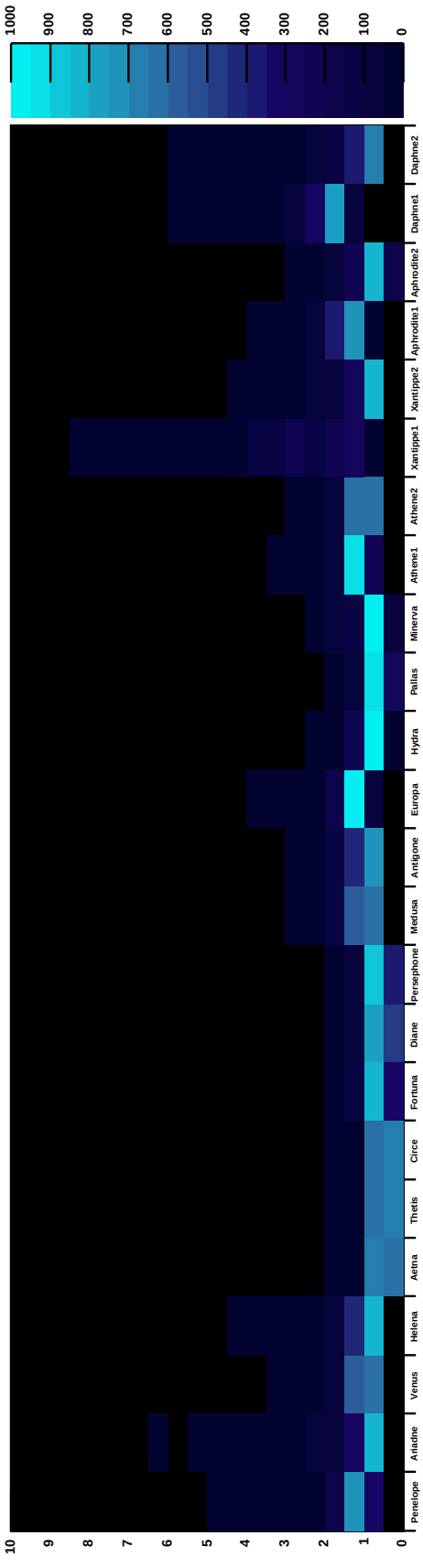

Figure F.3: Widths (rms) of the common mode distributions

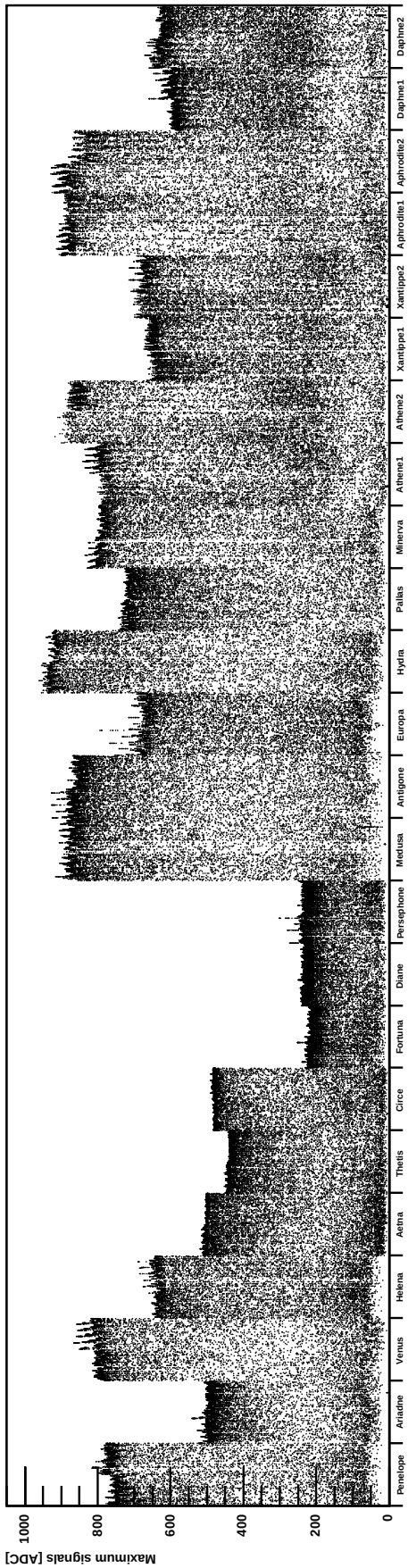

Figure F.4: Maximum signals of the calorimeter blocks

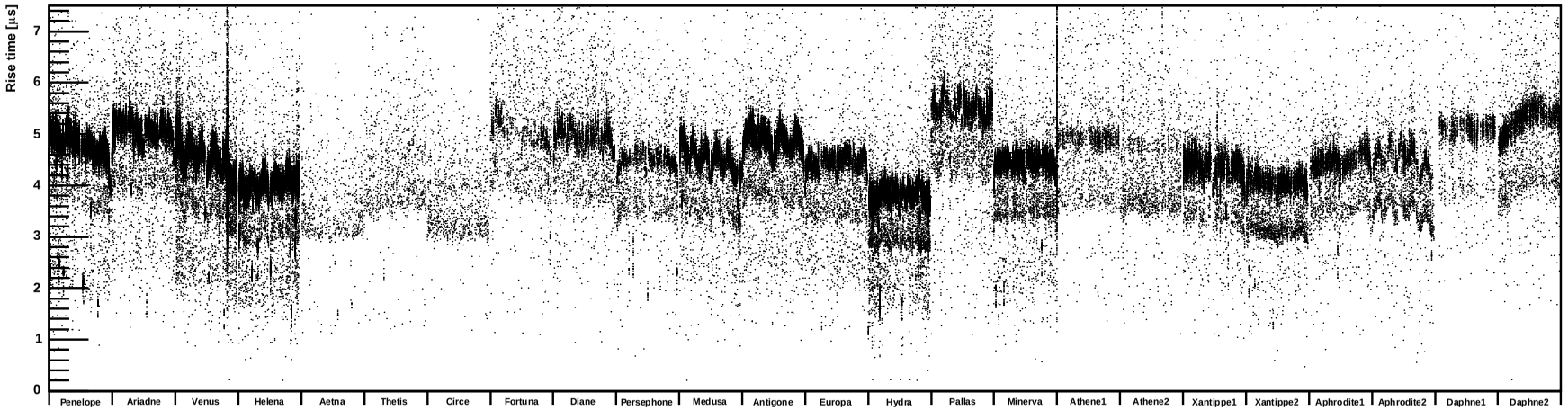

Figure F.5: Rise times of the 2880 channels of the calorimeter. For the measurement method see the corresponding measurement of the tracker (chapter **??**).

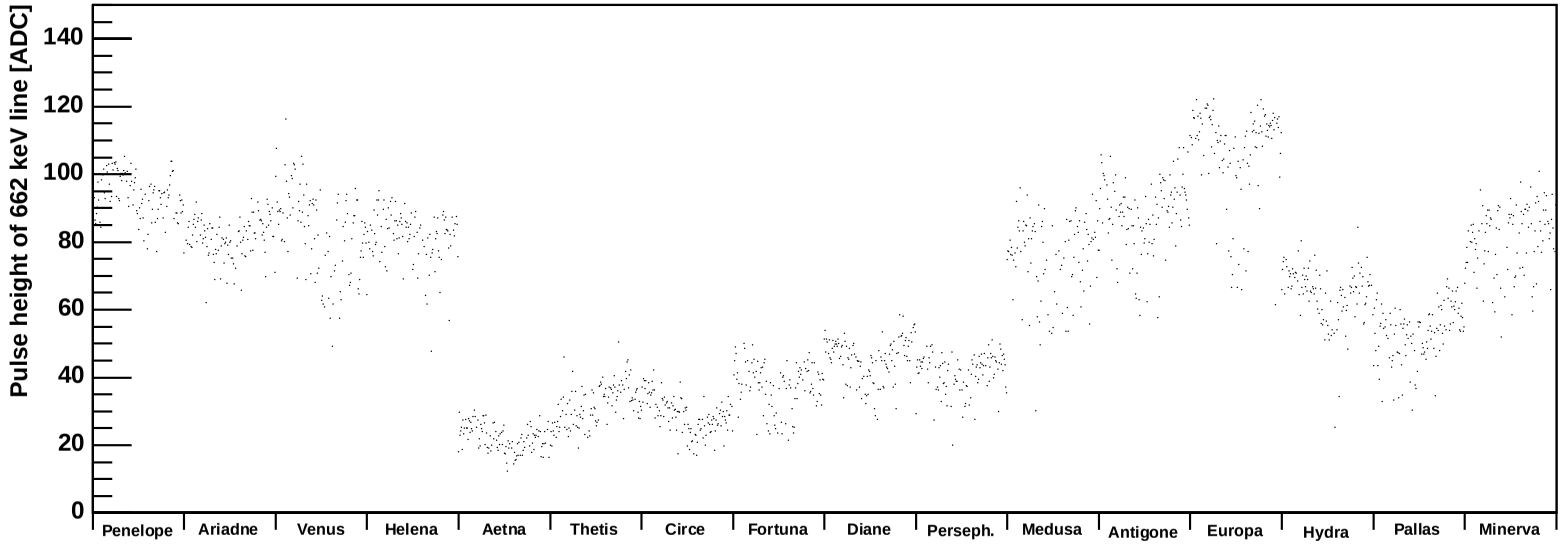

Figure F.6: Photopeak pulse height for 662 keV line, single-sided calorimeter blocks

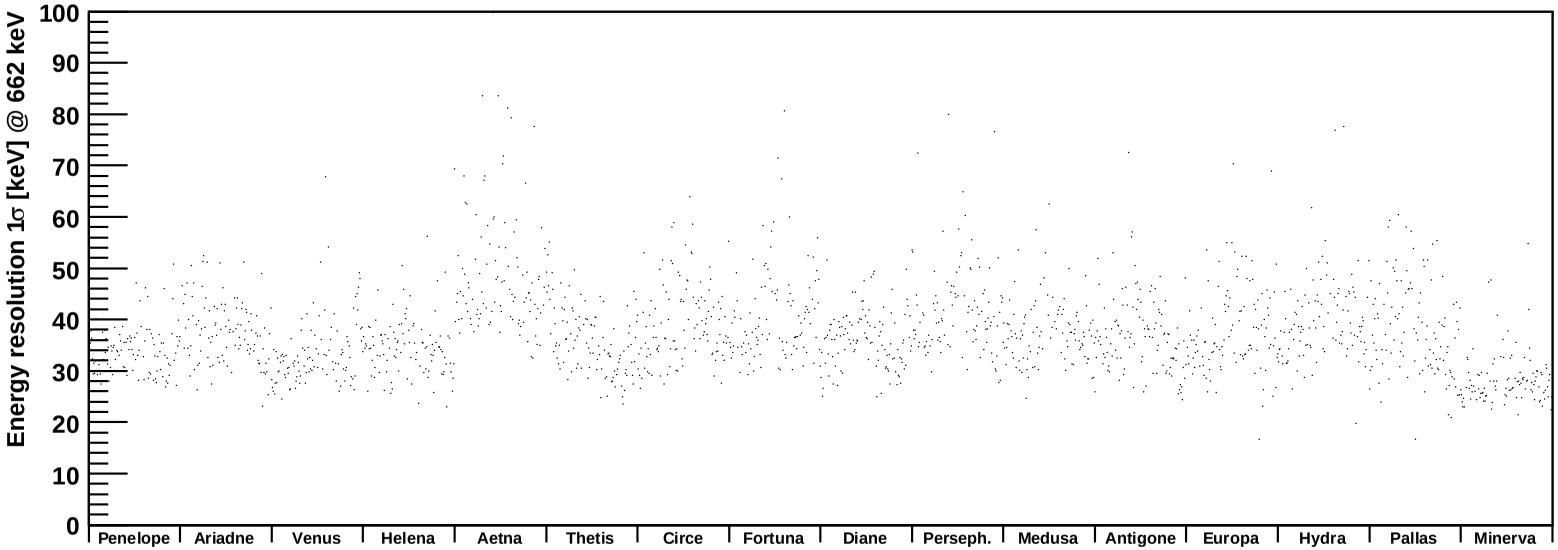

Figure F.7: Energy resolution of the 662 keV line, single-sided calorimeter blocks

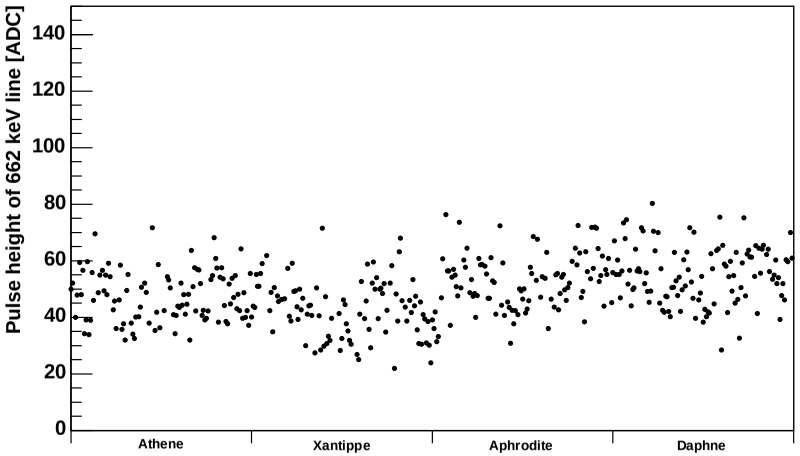

Figure F.8: Photopeak pulse height for the 662 keV line, double-sided calorimeter blocks

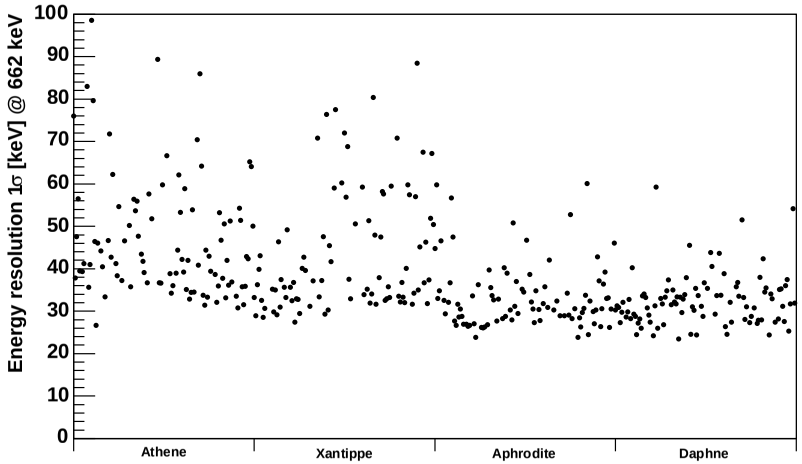

Figure F.9: Energy resolution for the 662 keV line, double-sided calorimeter blocks

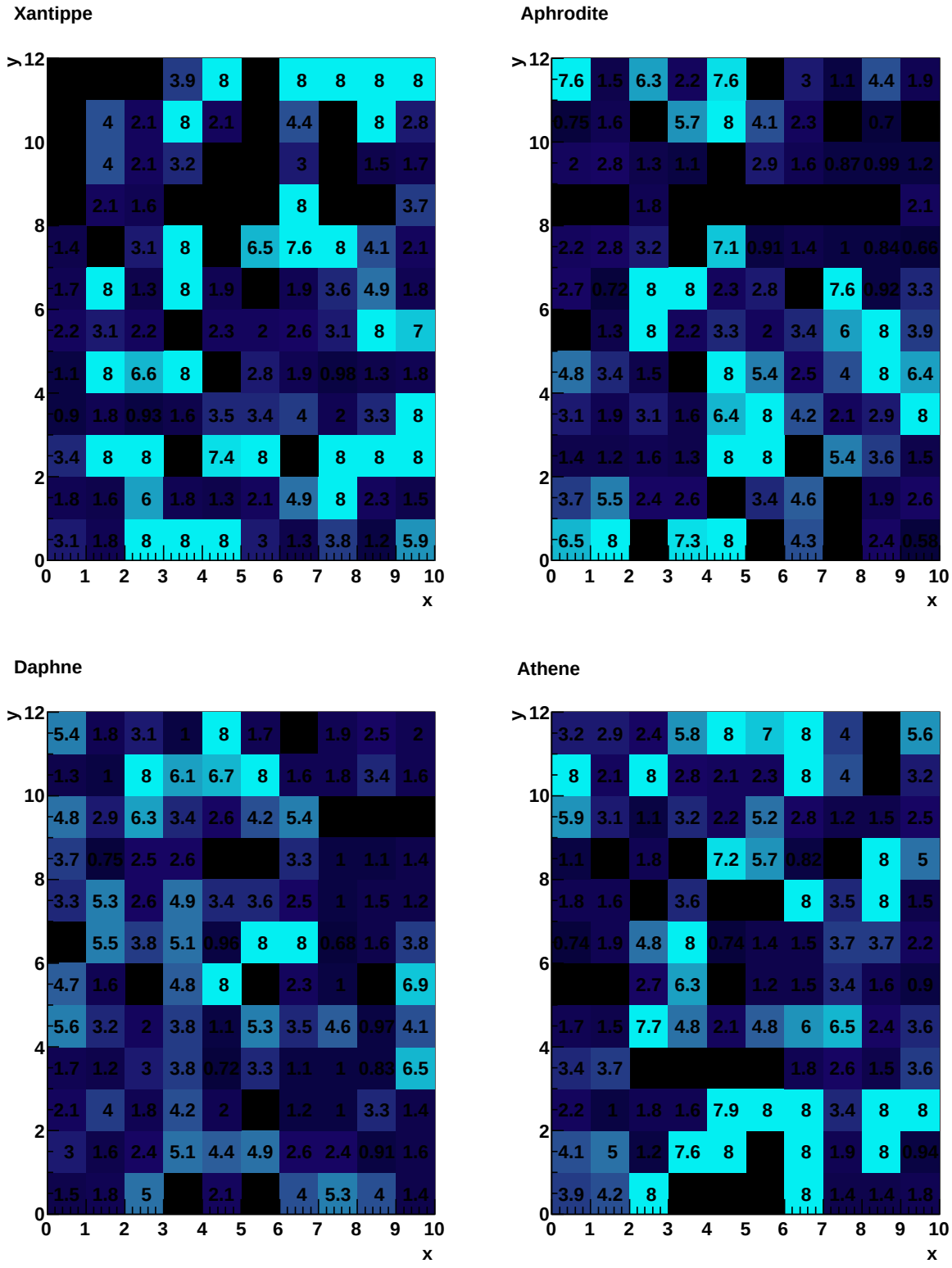

Figure F.10: Calculated z-resolutions of the double-sided calorimeter blocks for 1 MeV energy deposits (the numbers in the boxes are in cm and are directly related to the colors). For the black pixels no z-resolution could be calculated because one or both of the read-out diodes are detective.

Figure F.11: Photopeak pulse height of 59 keV line interacting in the PIN diodes

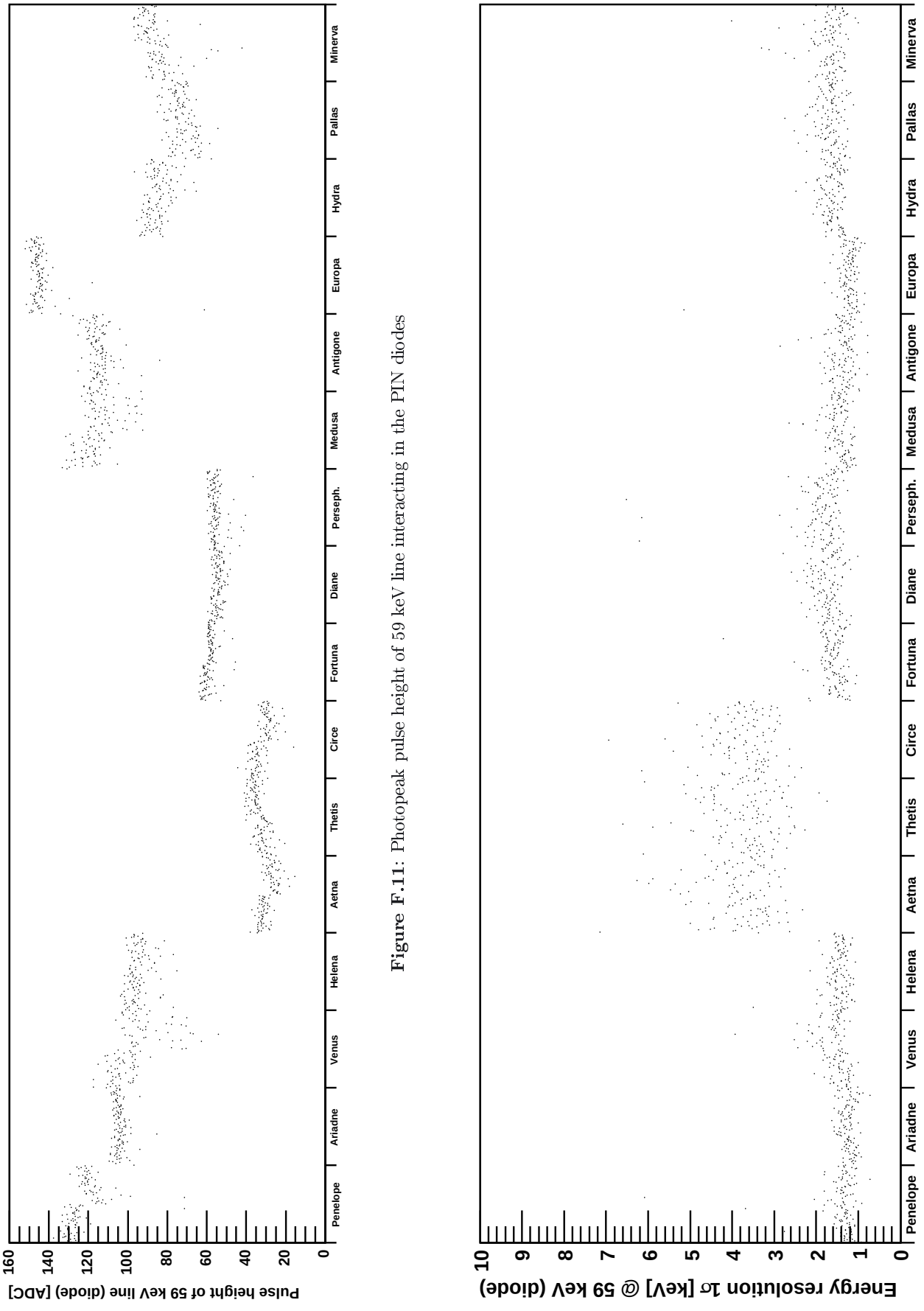

Figure F.12: Energy resolutions of the PIN diodes at 59 keV

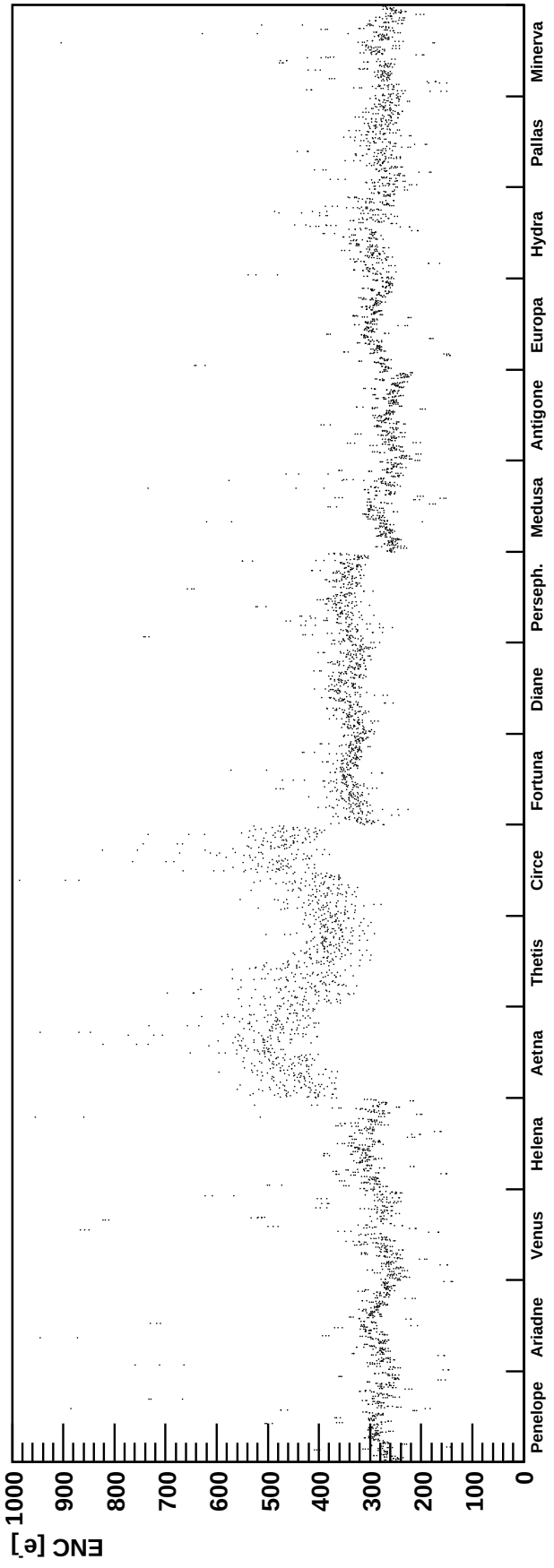

Figure F.13: Equivalent noise charge (ENC) of the PIN diode arrays

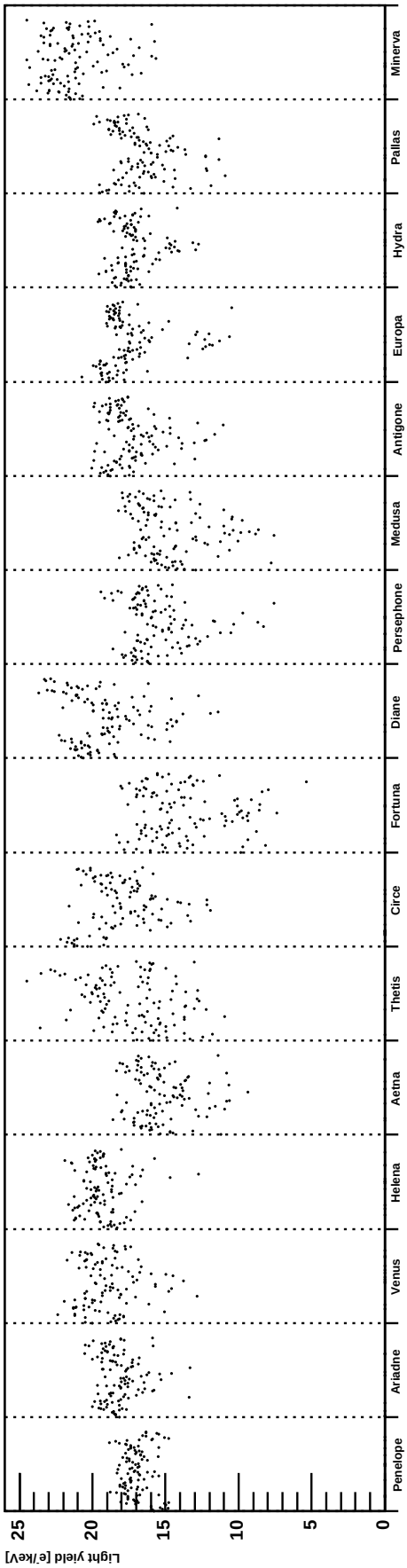

Figure F.14: Light yields of the single sided calorimeter crystals

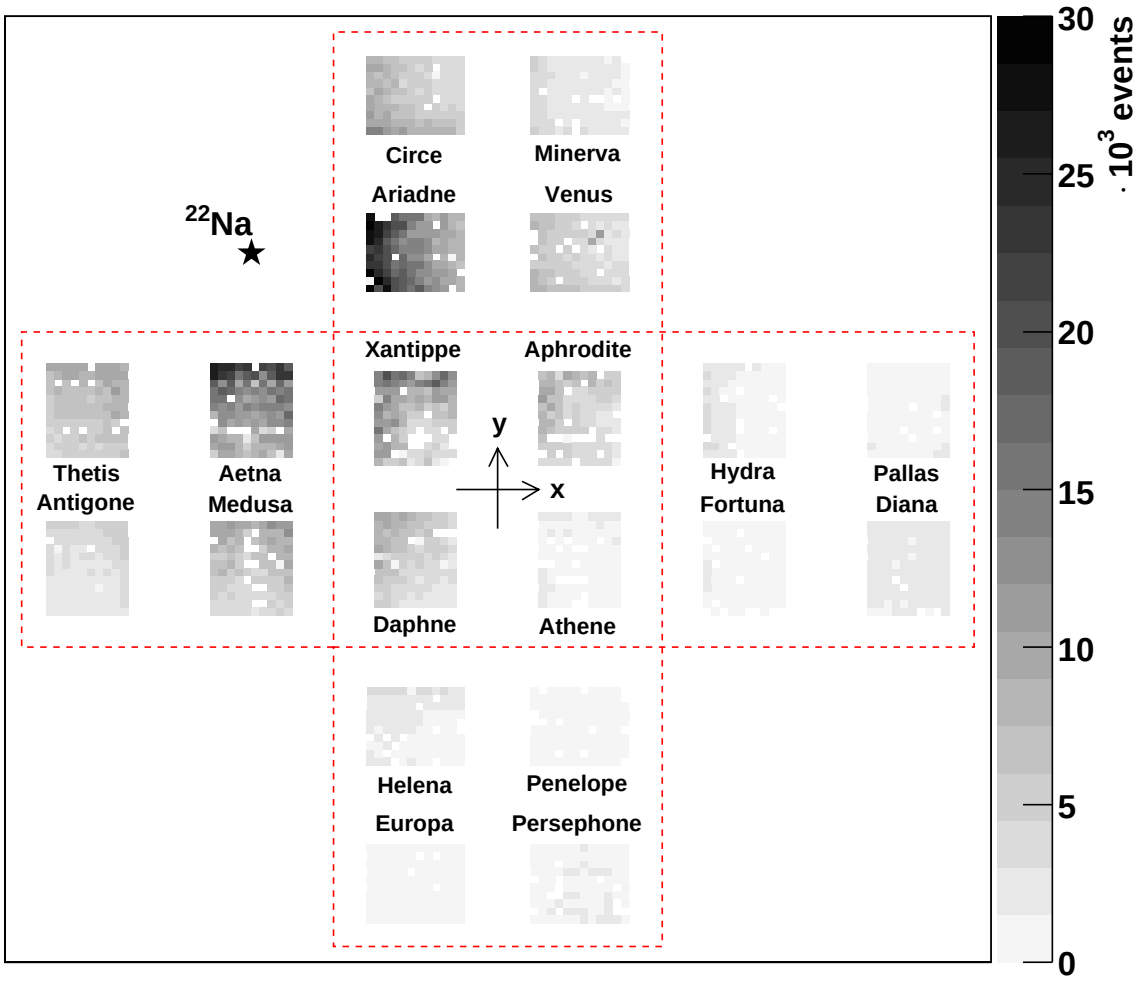

Figure F.15: Hit statistics of the calorimeter modules. The calorimeter is illuminated with a ^{22}Na source from one corner of the prototype. In this illustration the side blocks are projected onto the ground plane. Raw counts are used, i.e. no data cuts have been applied.

is indicated; the side walls of the calorimeter are projected onto the ground plane. There are no cuts applied accounting for example for the varying thresholds.

The number of hits decreases quickly with distance from the source not only due to the decreasing solid angle, but also due to shading of inner crystals by outer ones. The empty pixels (white squares in figure F.15) are dead channels which do not show a regular pattern except for one pixel, which is known to have a shortened diode due to an error in the production. There are several reasons for defective channels:

- The diode itself is defective. The specification for the production was less than 3 defective diodes per array.
- The diode is noisy. A few diodes exhibit significantly more leakage currents than the others. In order to achieve a reasonably low trigger threshold for a given chip these few diodes are blocked. Since the implemented calibration method requires a triggered pulse height histogram, a blocked channel cannot be calibrated and is marked as defective.
- The diode's bond contact is defective. The top aluminium layer of the diode arrays is very sensitive. Too many bonding tries can short the contacts to ground (the contacts are surrounded by a ground layer to avoid cross talk), or the contact itself can be damaged to the point where no bond is possible.
- The bond to the printed circuit board is broken due to mechanical stress or suboptimal bond parameters.
- The bond from the printed circuit board to the input of the front-end chip is broken.
- The analog path of the readout channel in the front-end chip is defective.
- The trigger part of the channel is defective. For the same reason mentioned for noisy diodes these channels marked as defective.
- A bug in the software truncated a few calibration spectra; unfortunately for the affected channels no calibration was possible any more.
- The coupling of the crystal to the diode is bad. If the crystal is shorter than its neighbors the contact to the coupling grid could be loose. Then the signal is too low to generate an analyzable spectrum.

Overall, 154 pixels (8% of all) on the single-sided calorimeter blocks are defective. In 39 (2% of all) cases the diode itself is defective, in 85 cases (4.4%) a bond or the readout channel is broken. The double-sided blocks have 57 (11.8%) defective pixels. The larger number is due to the fact that every pixel has two diodes connected. In principle, a pixel could deliver results also with only one diode working, but usually the calibration fails[†]. Additionally a good coupling is crucial because the signal height is roughly half of that obtained with single-sided readout. The crystal length, however, differs (the crystal bars for the MEGA prototype are hand-polished), resulting in inhomogeneous quality of the coupling. The crystals of one of the 8 cm blocks (Daphne) were milled with a diamond fly cutter to the same length in order to test a method for avoiding this problem. This particular block shows significantly less bad pixels (7) than the others (16-18).

[†]Principally, a pixel with double-sided readout having one defective diode could be treated as a pixel with single-sided readout. The quality of the spectra is significantly worse compared to a "real" single-sided readout with reflective paper at one end of the crystal. This due to the loss of the light coupled into the defective diode instead of being reflected back into the crystal. Thus about half of the scintillation light is not collected, and the dependence on the interaction position along the crystal is large smearing out the signals. In most cases the calibration algorithm is unable to identify the photopeaks.

Appendix G

The Anti-Coincidence Shield

The Earth's atmosphere is continuously bombarded by particles, mainly protons, in addition to photons. They are believed to originate from outside the solar system. When the (primary) cosmic rays penetrate into the Earth's atmosphere, they produce secondary particles, e.g. electrons, positrons, muons, and neutrons. In the orbit of a satellite the primary and secondary particles pass the spacecraft (a measurement and modeling work has been performed for GLAST [Mizuno et al., 2004]. Their interactions affect the payload, the γ-ray telescope in our case, and would be recorded along with γ rays. A large fraction of those unwanted events result from charged particles impinging onto the detector. Charged-particle events can be rejected by surrounding the whole detector with a plastic scintillator, a so-called Anti-Coincidence Shield (ACS). Every charged particle which crosses the shield results in a pulse which can be used to suppress the readout of the detector.

The same problem holds also for stratospheric balloon payloads. Since a balloon flight with the MEGA prototype was planned in preparation for the envisioned satellite mission, the full prototype is equipped also with an ACS.

The prototype's ACS consists of two parts, a top cover (figure G.1) and a bottom plate (not shown, it resides below the detector's ground plate). The scintillation light of the plastic detector plates is collected with wavelength shifting fibers which are glued into grooves of the plastic. The fibers guide the light onto photomultipliers. The signals from the PMTs are converted to digital veto pulses by the attached electronics. The veto pulses are fed into the Coincidence electronics (chapter 6).

Flight spare units of the EGRET telescope (aboard CGRO, figure 1.9) were available for this ACS. Four PMTs read out the four sides of the upper dome; two of them are coupled to the lower plate, giving some redundancy. The attached electronic boxes are flight spare modules as well, one is the Main Electronic Box (MEB, responsible for the pulse forming) and the other is the Low Power Control (LPC). The interconnection scheme for the MEGA balloon ACS is shown in figure G.2. The PMT modules and the MEB have built-in command interfaces over which the units can be controlled and the housekeeping data can be acquired. The coincidence electronics not only evaluates the veto pulses; it also incorporates the logic to drive the command interfaces.

The coincidence electronics provides two types of veto inputs, an absolute veto and a programmable one (chapter 6.3). The veto of the lower plate is defined as "programmable" to avoid the self-veto of high-energy pair creation events; the side-wall vetos are connected to the absolute input.

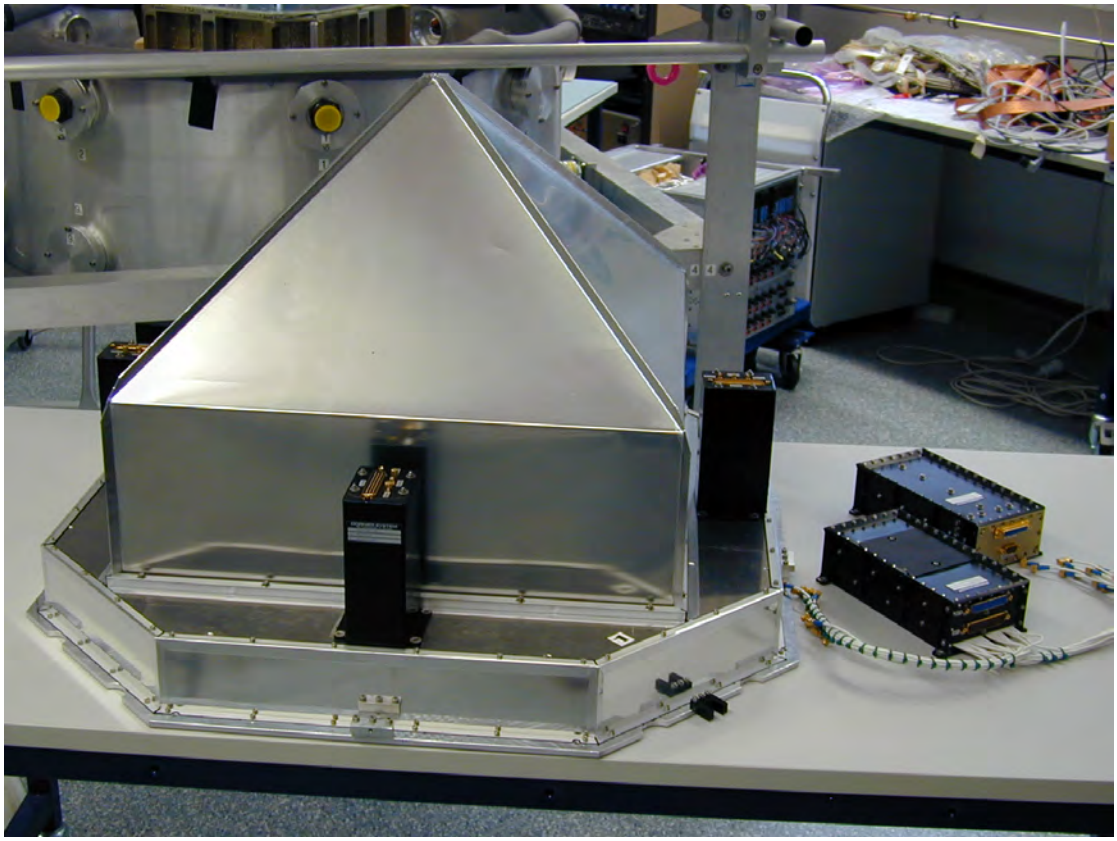

Figure G.1: ACS hardware: dome and electronics boxes (the two black boxes on the right, no cable harness)

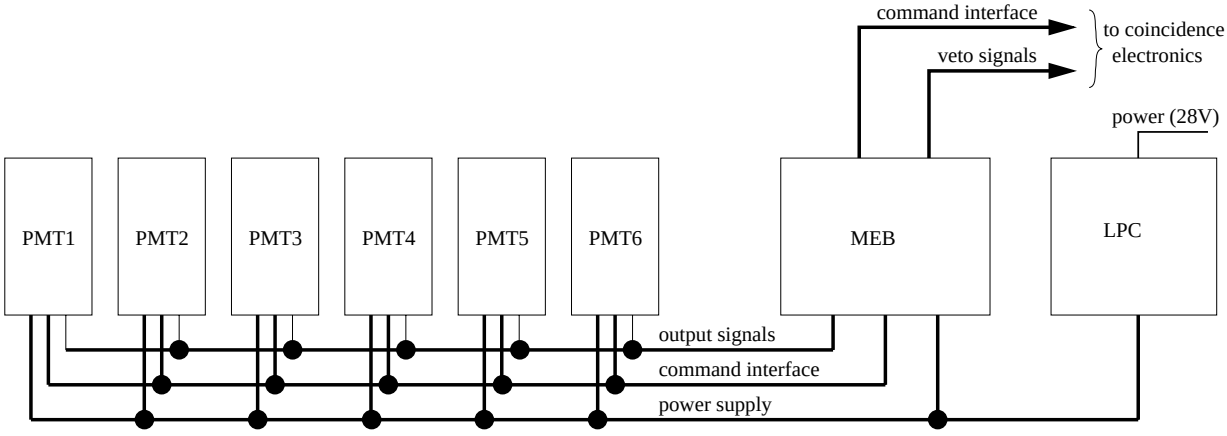

Figure G.2: Connection scheme of the ACS for the MEGA balloon payload

Appendix H

Matrix of Measurements

H.1 Calibration Measurements

Number	Isotope	X [cm]	Y [cm]	Z [cm]	Detector	Name
1	^{22}Na	-24	24	4	D2	20030422_050426_Na22Calibration
2	^{57}Co	0	0	42	D1	20030423_055922_Calibration_CO57
3	^{241}Am	0	0	≈50	D1	20030424_062337_D1_Calibrun_Am241
4	^{57}Co	0	0	42	D1	20030425_042544_D1_CalibRun_Co57
5	^{57}Co	0	0	42	D1	20030429_055927_D1Calib_Co57
6	^{22}Na	24	-24	5	D2	20030430_042925_Na22Calibration
7	^{57}Co	0	0	42	D1	20030501_045249_D1Calib_Co57
8	^{57}Co	0	0	10	D1	20030502_041124_D1Calib_Co57
9	^{22}Na	10	10	4	D2	200300503_041332_Na22Calibration
10	^{22}Na	-10	-10	4	D2	20030503_164656_Na22Calibration
11	background				D2	20030504_043336_GammaVaultBackground_D2
12	^{137}Cs	-10	10	2	D2	20030506_041702_D2_Cs137_CalibRun
13	^{137}Cs	10	-10	3	D2	20030507_045507_D2_Cs137_CalibRun

X, Y, and Z are the source positions, the point of origin in X and Y is the center of the active tracker area; Z=0 is defined by the base plate.

H.2 Beam Measurements

Measurement name	E [MeV]	Trigger	Angle	Triggers [$\times 10^3$]
20030422_174946_Run2_Pos0	2	D1-D2	0°	40
20030422_224407_Run2_Pos0b	2	D1-D2	0°	40
20030423_023131_Run1_Pos0Small	0.7	D1-D2	0°	140
20030423_041205_Run1_Pos0Smallb	0.7	D1-D2	0°	90
20030423_151720_Run1_Pos0Smallc	0.7	D1-D2	0°	90
20030423_160413_Run1_Pos30Small	0.7	D1-D2	−30°	108
20030423_172036_Run1_Pos30Smallb	0.7	D1-D2	−30°	108
20030423_205605_Run3_Pos30	5	D1-D2	−30°	345
20030423_234045_Run3_Pos60a	5	D1-D2	−60°	255
20030423_234045_Run3_Pos60b	5	D1-D2	−60°	255

Measurement name	E [MeV]	Trigger	Angle	Triggers [$\times 10^3$]
20030424_033611_Run3_Pos120	5	D1-D2	$-120°$	120
20030424_154853_Run3_Pos180	5	D1-D2	$-180°$	90
20030424_171121_Run3_Pos0q	5	D1-D2	$0°$	345
20030424_223548_Run4_Pos0b	8	D1-D2	$0°$	255
20030428_182704_Run6_Pos0	25	D1-D2	$0°$	345
20030428_210532_Run6_Pos30	25	D1-D2	$-30°$	390
20030429_003630_Run6_Pos60	25	D1-D2	$-60°$	570
20030429_013441_Run6_Pos60	25	D1-D2	$-60°$	570
20030429_034217_Run6_Pos120	25	D1-D2	$-120°$	540
20030429_170835_Run7_Pos0	50	D1$\overline{\text{h}}$-D2	$0°$	345
20030429_194341_Run7_Pos30	50	D1$\overline{\text{h}}$-D2	$-30°$	390
200304223316_Run7_Pos60	50	D1$\overline{\text{h}}$-D2	$-60°$	570
20030430_013839_Run7_Pos120	50	D1$\overline{\text{h}}$-D2	$-120°$	165
20030430_025757_Run7_Pos180	50	D1$\overline{\text{h}}$-D2	$-180°$	120
20030430_035536_Run7_Pos0_LowFlux	50	D1$\overline{\text{h}}$-D2	$0°$	22.5
20030430_170337_Run5_Pos0	12	D1$\overline{\text{h}}$-D2	$0°$	435
20030430_210218_Run5_Pos30	12	D1$\overline{\text{h}}$-D2	$-30°$	525
20030501_000824_Run5_Pos60	12	D1$\overline{\text{h}}$-D2	$-60°$	705
20030501_032939_Run5_Pos120	12	D1$\overline{\text{h}}$-D2	$-120°$	165
20030501_151433_Run5_Pos80	12	D1$\overline{\text{h}}$-D2	$-80°$	250
20030501_162605_Run5_Pos180	12	D1$\overline{\text{h}}$-D2	$-180°$	90
20030501_201348_Run7_Pos0_B	50	D1$\overline{\text{h}}$-D2	$0°$	390
20030501_222732_Run7_Pos80	50	D1$\overline{\text{h}}$-D2	$-80°$	480
20030501_234752_Run7_Pos180	50	D1$\overline{\text{h}}$-D2	$-180°$	120
20030502_003604_Run7_Pos0_C	50	D1$\overline{\text{h}}$-D2	$0°$	390
20030502_155128_Run8_Pos0	37	D1$\overline{\text{h}}$-D2	$0°$	435
20030502_184737_Run8_Pos30	37	D1$\overline{\text{h}}$-D2	$-30°$	480
20030502_223916_Run8_Pos60	37	D1$\overline{\text{h}}$-D2	$-60°$	570
20030503_011409_Run8_Pos80	37	D1$\overline{\text{h}}$-D2	$-80°$	250
20030502_022309_Run8_Pos180	37	D1$\overline{\text{h}}$-D2	$-120°$	120
20030502_031910_Run8_Pos180	37	D1$\overline{\text{h}}$-D2	$-180°$	90
20030505_180452_Run9_Pos0	17	D1$\overline{\text{h}}$-D2	$0°$	435
20030505_205830_Run9_Pos30	17	D1$\overline{\text{h}}$-D2	$-30°$	525
20030506_001130_Run9_Pos60	17	D1$\overline{\text{h}}$-D2	$-60°$	540
20030506_Run10_Pos0B	10	D1$\overline{\text{h}}$-D2	$0°$	435
20030506_2000600_Run10_Pos30	10	D1$\overline{\text{h}}$-D2	$-30°$	525
20030506_233111_Run10_Pos60	10	D1$\overline{\text{h}}$-D2	$-60°$	525
20030507_033711_Run10_Pos180	10	D1$\overline{\text{h}}$-D2	$-180°$	145
				Σ =14933.5

Angle: Angle of incidence of the beam with respect to the telescope axis. Trigger: Two different trigger patterns were used at HIGS. The first (D1-D2) has at least one D1 hit and one D2 hit. The second pattern (D1$\overline{\text{h}}$-D2) additionally requires the top layer (Hermes) to have NO trigger, i.e. this layer is used in anti-coincidence eliminating charged particles impinging on the detector.

Appendix I

Event Reconstruction and Imaging

I.1 Event Reconstruction

The energy of a measured photon in the Compton and pair creation regime is deposited over several discrete interactions and thus spread over different detector channels. From the pattern of interaction points and the deposited energies the type of interaction, the temporal sequence*, and finally the energy and origin of the incoming photon has to be reconstructed. This problem must be solved by applying the laws of physics as well as statistical considerations as described in great detail in Zoglauer [2005]. The various steps of event reconstruction are briefly summarized here:

- In the first step, interactions in two or even more *neighboring* voxels† (e.g. charge sharing between neighboring strips of the tracker) are recombined.
- Next, pair events are filtered from the data stream. The algorithm looks for characteristic "⋀"-shaped patterns characteristic for the vertices of a pair creation. If a pair is recognized, the electron and positron paths are traced to their end points.
- If no pair is found, the interactions are examined for straight tracks in the tracker which are trajectories of high-energy charged particles. Such events are marked and used for special analyses, e.g. the determination of the position resolution of the strip detectors with muon tracks, but disregarded in normal photon analysis.
- The remaining events are most likely Compton events. Thus the data is first scanned for Compton recoil electron tracks. All hits belonging to one electron track are isolated and the direction of motion is determined.
  Interaction points in subsequent tracker layers are a priori considered to form a track. In contrast to high-energy charged particles, Compton electrons do not follow straight paths due to Molière scattering (multiple small-angle scatters) in the silicon. Frequently, electrons bounce back into the previous layer ("U-turn") at the end of the track. In these cases, the electron's trajectory is ambiguous. Surplus hits from detector noise, chance coincidences, bremsstrahlung, or defective detector channels are often present, making track reconstruction even more ambiguous. Consequently the track reconstruction algorithm must examine all possible paths of the electron and decide on a most likely sequence.
  Several aspects help to identify the direction of motion of the recoil electron:

*The time of the individual interaction cannot be resolved accurately enough in the prototype to directly determine an interaction sequence from it.

†A voxel is a resolution element in the detector such as the strip detector volume corresponding to the intersection of one p- and one n-side strip.

1. The Molière scattering increases with decreasing electron energy.
2. Along the track, i.e. with decreasing electron energy, the energy deposits increase on average (according to Bethe-Bloch equation, figure 1.4).
3. The electron loses notably little energy in the first layer, i.e. the layer of the Compton interaction, where the electron does not pass the whole wafer.
4. A comparatively large fraction of the electron's energy is deposited in an U-turn.

Using this knowledge, all possibilities of composing a track are rated (and there are always at least two, forward and backward). Two principally different rating algorithms are compared in Zoglauer [2005]: The first uses analytically calculated quality factors which are increasing if the energy deposits and scatter angles increase along the track, i.e. correlations between the position number along the track and the energy deposit respectively the scatter angle. The second algorithm uses Bayesian statistics to assign each possible track a probability. This method relies on a broad data base (the event reconstruction response) generated on the basis of extensive simulations. The version of the track with the highest quality factor, respectively the highest probability, is chosen as the correct one.
If tracks were found in this step, they are reduced to their starting point, scatter direction, and total electron energy.

- Now the photon itself needs to be traced, i.e. the sequence of the interaction sites of Compton interaction(s) and photoelectric absorption has to be determined. Similar to the electron tracking, a quality factor ("classical" approach) or a probability (Bayesian approach) is assigned to each possible order of the interaction sites and the "best" is taken. Depending on the number of interaction points, complications arise:
  For single Compton events without an electron track (i.e. one hit in the tracker and one hit in the calorimeter) it is possible to clearly exclude either the forward or the backward direction[‡] only in a few cases. In these cases, more energy would have been transferred to the recoil electron than in a Compton backscatter (of a photon with the measured total energy). The sequence is either physically impossible or the photon is not fully absorbed; such an ordering of a 2-hit sequence is rejected.
  If there is an electron track and one hit in the calorimeter, all parameters of the Compton event are known and only one of the two possible sequences should fit the data, assuming a fully absorbed event.
  In the case of multiple Compton scatters within one event, redundant scatter information provide the means to correctly order the interactions and to decide whether the initial photon is fully absorbed or not. However, limited position and energy resolution especially in the calorimeter gives rise to ambiguities. Additional information such as the electron track direction and absorption probabilities is often necessary.

Subsequently, higher-level data analysis can be performed using the reconstructed events or a selected subset, such as spectroscopy, polarimetry, and imaging.

[‡]Time-of-flight measurement is impossible in the prototype.

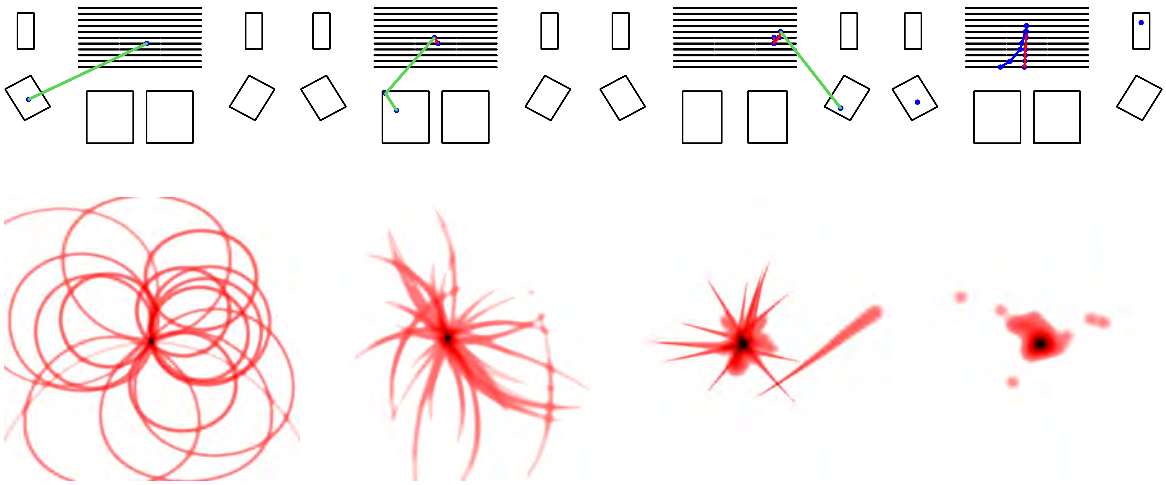

(a) Untracked Compton events

(b) Tracked Compton events

(c) High-energy tracked Compton events with incomplete absorption

(d) pair events

Figure I.1: The various event types, the imaging algorithm has to cope with (from Zoglauer, 2005). Top row: Measured events. Bottom row: Reprojections of the events into the image space.

I.2 Imaging

In an ideal world, the origin of an incoming photon could be directly calculated from the complete measured information of the Compton scatter. In reality, only a distribution can be determined for the origin: Lack of the electron direction for some events allows to restrict the origin only to a cone whose width reflects the energy and position resolution of the detectors (figure I.1a). This happens frequently for low-energy photons. Even if the electron direction is known, Molière scattering does not allow to reduce the cone to a point, only to a segment of this cone (figure I.1b). This segment gets smaller at higher energies, leading to a better definition of the scatter plane, but with increasing photon energy the events are more and more likely incompletely absorbed. In this case the area of origin is a segment of a great circle, defined by the scatter geometry in the scatter plane (figure I.1c). Pair events can be directly reconstructed, but the original direction is smeared out, again by Molière scattering of the electron and the positron, as well as by the unknown recoil of the nucleus (figure I.1d).

The problem of reconstructing the source distribution is — expressed in a mathematical abstract way — to invert this measurement process

$$\mathbf{y} = \mathcal{T} \times \lambda + \mathbf{b} + \mathbf{n}$$

The measurement data $\mathbf{y}$ correspond to a convolution of a source intensity distribution λ with the detector response $\mathcal{T}$ and adding background $\mathbf{b}$ and noise $\mathbf{n}$. Specialized image deconvolution algorithms have been developed for this deconvolution task. The one applied on the MEGA data is described briefly in the following.

The unbinned maximum-likelihood algorithm called *list-mode maximum-likelihood expectation-maximization method* is ideally suited for MEGA. It was originally developed for medical imaging with SPECT (Single Photon Emission Computer Tomography) cameras [Wilderman et al., 1998] and later adapted for use in astrophysics [Zoglauer, 2000].

A fundamental property of this algorithm is that the events are stored in a list rather than in a binned data space. Modern Compton telescopes measure many parameters of an event so that the data space and detector response required for binned-mode analysis becomes huge. The amount of

corresponding bins would exceed the number of events by several orders of magnitude. Thus storing the events in a list and calculating the detector response functions "on-the-fly" is significantly more efficient than binned data space algorithms and pre-determined response matrices. In addition the full accuracy of the measured data is kept.

The maximum-likelihood method determines the most probable source distribution by maximizing the underlying likelihood function which represents the probability that an assumed source distribution resulted in the measured data. The maximization is a non-trivial, iterative process as detailed by Zoglauer [2000].

Appendix J

Abbreviations and Constants

symbol	quantity	value
E_i	energy of incoming photon	
E_g	energy of Compton scattered photon	
E_e	kinetic energy of an electron	
E_p	kinetic energy of a positron	
$\underline{E}_i$, $\underline{E}_g$, $\underline{E}_e$	energies in units of electron rest masses	
E_{e-h}	effective energy for generating an electron-hole pair in a semiconductor	e.g. $E_{e-h}(\mathrm{Si}) = 3.6\,\mathrm{eV}$
p_e	momentum of an electron	
$\underline{p}_e$	momentum in units of $m_e c$	
A_{av}	effective (average) atomic mass in compound materials	e.g. $A_{av}(\mathrm{CsI}) = \frac{55+53}{2} = 54$
Z	atomic number	
ρ	mass density	
m_e	rest mass of the electron	$0.511\,\mathrm{MeV}/c^2 = 9.11 \cdot 10^{-31}\,\mathrm{kg}$
e	charge of the electron	$1.60 \cdot 10^{-19}\,\mathrm{C}$
$1\,\mathrm{u}$	unified atomic mass unit	$931\,\mathrm{MeV}/c^2 = 1.66 \cdot 10^{-27}\,\mathrm{kg}$
k_B	Boltzmann constant	$1.38 \cdot 10^{-23}\,\mathrm{J/K} = 8.62 \cdot 10^{-5}\,\mathrm{eV/K}$
F	Fano factor	0.115 (for silicon @ 20°C)
σ_x	cross section	
X_0	Radiation length	9.36 cm for silicon
c	speed of light	$3 \cdot 10^8$ m/s

List of Figures

List of Tables

References

S. Agostinelli et al. Geant4—a simulation toolkit. *NIM A*, 506:250–303, 2003.

F. A. Aharonian and C. W. Akerlof. Gamma-ray astronomy with imaging atmospheric Čerenkov telescopes. *Annu. Rev. Nucl. Part. Sci.*, 47:273–314, 1997.

F. A. Aharonian et al. Discovery of very high energy gamma rays associated with an X-ray binary. *Science*, 309:746–749, 2005.

J. Ahrens, L. S. Ferreira, and W. Weise. Photonuclear dispersion relation and δ excitations in nuclei. *Nucl. Phys. A*, 485:621–631, 1988.

D. E. Alexandreas et al. The CYGNUS extensive air-shower experiment. *Nucl. Instr. Meth. A*, 311:350–367, 1992.

J. Allison et al. Geant4 developments and applications. *IEEE Trans. Nucl. Sci.*, 53(1):270–278, 2006.

R. Andritschke. Aufbau und Eichung der Kalorimeter für das Gammateleskop MEGA. Diplomarbeit, Fakultät für Physik, Technische Universität München, Apr. 2000.

H. O. Anger. Scintillation camera. *Rev. of Scient. Instr.*, 29:27–33, 1958.

R. Atkins et al. Evidence for TeV emission from GRB 970417a. *Astrophys. J.*, 533:L119–L122, 2000a.

R. Atkins et al. Milagrito, a TeV air-shower array. *Nucl. Instr. Meth. A*, 449:478–499, 2000b.

N. Auricchio, N. Cesca, G.Di Domenico, E. Moretti, N. Sabba, M. Gambaccini, G. Zavatini, R. Andritschke, G. Kanbach, and F. Schopper. SiliPET: design of an ultra high resolution small animal PET scanner based on stacks of semiconductor detectors. *IEEE Nuclear Science Symposium Conference Record*, 5: 3010–3013, 2005.

C. Baixeras et al. Commissioning and first test of the MAGIC telescope. *Nucl. Instr. Meth. A*, 518:188–192, 2004.

S. D. Barthelmy et al. The burst alert telescope (BAT) on the SWIFT MIDEX mission. *Space Sci. Rev.*, 120:143–164, 2005.

F. J. Beekman and B. Vastenhouw. Design and simulation of a high-resolution stationary SPECT system for small animals. *Phys. Med. Biol.*, 49:4579–4592, 2004.

B. L. Berman and S. C. Fultz. Measurements of the giant dipole resonance with monoenergetic photons. *Rev. Mod. Phys.*, 47:713–761, 1975.

G. Bertone, A. Kusenko, S. Palomares-Ruiz, S. Pascoli, and D. Semikoz. Gamma-ray bursts and the origin of galactic positrons. *Phys. Let. B*, 636:20–24, 2006.

H. A. Bethe. Molière's theory of multiple scattering. *Phys. Rev.*, 89(6):1256–1266, 1953.

D. Bhattacharya, T. J. O'Neill, A. Akyüz, J. Samimi, and A. D. Zych. Prototype TIGRE Compton γ-ray balloon-borne telescope. *New Astr. Rev.*, 48:287–292, 2004.

G. F. Bignami, G. Boella, J. J. Burger, P. Keirle, H. A. Mayer-Hasselwander, J. A. Paul, E. Pfeffermann, L. Scarsi, B. N. Swanenburg, B. G. Taylor, W. Voges, and R. D. Wills. The COS-B experiment for gamma-ray astronomy. *Space Sci. Instr.*, 1:245–268, 1975.

A. Bird, T. Carter, A. Dean, D. Ramsden, and B. Swinyard. The optimisation of small CsI(Tl) gamma-ray detectors. *Trans. Nuc. Sci.*, 40:395, 1993.

P. M. S. Blackett and G. P. S. Occhialini. Some photographs of the tracks of penetrating radiation. *Proc. Roy. Soc.*, 839:699–727, 1933.

S. D. Bloom. Broadband properties of candidate blazar counterparts of unidentified EGRET sources. *ASP Conf. Ser.*, 350:128–130, 2006.

P. Bloser et al. Development of silicon strip detectors for a medium energy gamma-ray telescope. *Nucl. Instr. Meth. A*, 512:220–228, 2003.

P. F. Bloser. private communication, 2002.

S. E. Boggs. The Advanced Compton Telescope. NASA Vision Mission Concept Study Report, Dec. 2005. available from http://www.ssl.berkeley.edu/act/ACTreport_final.pdf or astro-ph/0608532.

W. V. Boynton, W. C. Feldman, et al. Distribution of hydrogen in the near surface of mars: Evidence for subsurface ice deposits. *Science*, 297:81–85, 2002.

C. Braig and P. Predehl. X-ray astronomy with ultra-high-angular resolution. *Proc. SPIE*, 5488:601–612, 2004.

D. Brasse, P. E. Kinahan, R. Clackdoyle, M. Defrise, C.Comtat, and D. W. Townsend. Fast fully 3-D image reconstruction in PET using planograms. *IEEE Trans. Med. Imag.*, 23:413–425, 2004.

R. Brun and F. Rademakers. ROOT - an object oriented data analysis framework. *Nucl. Instr. Meth. A*, 389:81–86, 1997. Proceedings AIHENP'96 Workshop, Lausanne, Sept. 1996.

A. Burrows, R. Walder, C. D. Ott, and E. Livne. Rotating core collapse and bipolar supernova explosions. *ASP Conf. Ser.*, 332:350–362, 2005.

A. Castoldi, E. Gatti, and C. Guazzoni. Fast triggering in silicon drift detectors by means of holes' induction. *Nucl. Instr. Meth. A*, 518:429–432, 2004.

T. Çonka Nurdan, K. Nurdan, A. H. Walenta, I. Chiosa, B. Freisleben, N. A. Pavel, and L. Strüder. First results on Compton camera coincidences with the silicon drift detector. *IEEE Trans. Nucl. Sci.*, 52: 1381–1385, 2005.

W. Collmar. New blazar detections at MeV energies by COMPTEL. *ASP Conf. Ser.*, 350:120–123, 2006.

A. Comastri. AGN models for the X and γ-ray backgrounds. *Astrophys. Let. Comm.*, 39:181–188, 1999.

A. H. Compton. A quantum theory of the scattering of X-rays by light elements. *Phys. Rev.*, 21:483–502, 1923.

A. H. Compton and A. W. Simon. Relation between the direction of a recoil electron and that of the scattered X-ray quantum. *Phys. Rev.*, 26:289–299, 1925.

W. Cui. Very energetic gamma rays from microblazars. *Science*, 309:714–715, 2005.

S. A. Cummer, Y. Zhai, W. Hu, D. M. Smith, L. I. Lopez, and M. A. Stanley. Measurements and implications of the relationship between lightning and terrestrial gamma ray flashes. *Geophys. Res. Lett.*, 32:L08811, 2005.

C. Davisson and R. Evans. Gamma-ray absorption coefficients. *Rev. Mod. Phys.*, 24:79–107, 1952.

R. Diehl, H. Halloin, K. Kretschmer, et al. Radioactive ^{26}Al from massive stars in the Galaxy. *Nature*, 439:45–47, 2006.

R. Diehl and F. X. Timmes. Gamma-ray line emission from radioactive isotopes in stars and galaxies. *Astron. Soc. Pac.*, 110:637–659, 1998.

J. Dyks, A. K. Harding, and B. Rudak. Relativistic effects and polarization in three high-energy pulsar models. *Astrophys. J.*, 606, 2004.

R. Enomoto et al. A search for sub-TeV gamma rays from the Vela pulsar region with CANGAROO-III. *Astrophys. J*, 638:397–408, 2006.

R. D. Evans. *The Atomic Nucleus.* McGraw-Hill, 1955.

R. Fender and T. Maccarone. High energy emission from microquasars. In K. S. Cheng and G. E. Romero, editors, *ASSL Vol. 304: Cosmic Gamma-Ray Sources*, pages 205–224, Oct. 2004. also available as astro-ph/0310538.

C. E. Fichtel, R. C.Hartman, D. A. Kniffen, D. J. Thompson, G. F. Bignami, H. Ögelman, M. E. Özel, and T. Tümer. High-energy gamma-ray results from the second small astronomy satellite. *Astrop.J.*, 198:163–182, 1975.

C. E. Fichtel and J. I. Trombka. *Gamma-Ray Astrophysics.* NASA Reference Publication 1386. NASA, Oct. 1997.

C. Fiorini, A. Gola, A. Longoni, F. Perotti, and L. Strüder. Timing properties of silicon drift detectors for scintillation detection. *IEEE Trans. Nuc. Sci.*, 51(3):1091–1097, 2004.

C. Fiorini, A. Longoni, F. Perotti, C. Labanti, P. Lechner, and L. Strüder. Gamma ray spectroscopy with CsI(Tl) scintillator coupled to silicon drift chamber. *Trans. Nuc. Sci.*, 44:2553, 1997.

R. B. Firestone and V. S. Shirley, editors. *Table of Isotopes.* John Wiley & Sons, Inc., 1996. also available at http://isotopes.lbl.gov/education/isotopes.htm.

G. J. Fishman, B. N. Bhat, R. Mallozzi, J. M. Horack, T. Koshut, C. Kouveliotou, P. N. Pendleton, C. A. Meegan, R. B. Wilson, W. S. Paciesas, S. J. Goodman, and H. J. Christian. Discovery of intense gamma-ray flashes of atmospheric origin. *Science*, 264:1313–1316, 1994a.

G. J. Fishman et al. The first BATSE gamma-ray burst catalog. *Astrophys. J. Suppl.*, 92:229–283, 1994b.

W. Friedrich, P. Knipping, and M. von Laue. Interferenz-Erscheinungen bei Röntgenstrahlen. *Ber. Bayer. Akad. Wiss.*, pages 303–322, 1912.

GEANT3. *GEANT — Detector Description and Simulation Tool.* CERN Geneva. CERN Program Library Long Writeup W5013.

N. Gehrels. Use of νF_ν spectral energy distributions for multwavelength astronomy. *Il Nuovo Cimento B*, 112:11–15, 1997.

M. M. González, M. Carrillo-Barragán, B. L. Dingus, Y. Kaneko, and R. D. Preece. Spectroscopy of the brightest bursts up to energies of 200 MeV. *AIP Conf. Proc.*, CP836:612–615, 2006.

P. D. Group. Review of particle physics. *Phys. Let. B*, 592(1–4):1–1109, 2004.

C. Grupen. *Teilchendetektoren.* BI-Wiss.-Verl., Mannheim, 1993.

N. Guessoum, P. Jean, and W. Gillard. The lives and deaths of positrons in the intestellar medium. *Astron. Astrophys.*, 436:171–185, 2005.

S. V. Guru, Z. He, G. F. Knoll, R. H. Redus, and M. R. Squillante. portable high energy gamma ray imagers. *Nucl. Instr. Meth. A*, 378:612–619, 1996.

H. Halloin. *CLAIRE: Premières Liminères d'une Lentille Gamma.* PhD thesis, Université Paul Sabatier de Toulouse III, 2003.

B. A. Harmon, G. J. Fishman, et al. The burst and transient source experiment earth occultation technique. *Astrophys. J. Suppl.*, 138:149–183, 2002.

M. J. Harris, J. Knödlseder, P. Jean, E. Cisana, R. Diehl, G. G. Lichti, J.-P. Roques, S. Schanne, and G. Weidenspointner. Detection of γ-ray lines from interstellar ^{60}Fe by the high resolution spectrometer SPI. *Astron. Astrophys.*, 433:L49–L52, 2005.

M. Hernanz and J. José. γ-rays from classical novae: expectations from present and future missions. *New Astr. Rev.*, 48:35–39, 2004.

W. Hillebrandt and J. C. Niemeyer. Type Ia supernova explosion models. *Annu. Rev. Astron. Astrophys.*, 38:191–230, 2000.

W. Hofmann et al. Status of the H.E.S.S. project. In *International Cosmic Ray Conference*, pages 2785–2788, Aug. 2001.

J. Holder et al. The first VERITAS telescope. *Astrop. Phys.*, 25:391–401, 2006.

A. S. Hoover, R. M. Kippen, J. P. Sullivan, M. W. Rawool-Sullivan, W. Baird, and E. B. Sorensen. The LANL prototype Compton gamma-ray imager: Design and image reconstruction techniques. *IEEE Trans. Nucl. Sci.*, 52:3047–3053, 2005.

G. J. Hurford et al. The RHESSI imaging concept. *Sol. Phys.*, 210:61–86, 2002.

IDE. *The TA1 Specifications.* Oslo, Norwegen.

M. Igashira, H. Kitazawa, M. Shimizu, H. Komano, and N. Yamamuro. Systematics of the pygmy resonance in keV neutron capture γ-ray spectra of nuclei with $n \approx 82 - 126$. *Nucl. Phys. A*, 457:301–316, 1986.

A. F. Iyudin, R. Diehl, H. Bloemen, W. Hermsen, G. G. Lichti, D. Morris, J. Ryan, V. Schönfelder, H. Steinle, M. Varendorff, C. de Vries, and C. Winkler. COMPTEL observations of ^{44}Ti gamma-ray line emission from Cas A. *Astron. and Astrophys.*, 284:L1–L4, 1994.

A. F. Iyudin, O. Reimer, V. Burwitz, J. Greiner, and A. Reimer. Resonant absorption troughs in the gamma-ray spectra of QSO. *Astron. and Astrophys.*, 436:763, 2005.

W. N. Johnson, R. L. Kinzer, J. D. Kurfess, et al. The Oriented Scintillation Spectrometer Experiment: Instrument description. *Astrophys. J. Suppl.*, 86:693–712, 1993.

G. Kanbach et al. The project EGRET on NASA's Gamma-Ray Observatory GRO. *Space Science Reviews*, 49:69–84, 1988.

U. Kilgus, R. Kotthaus, and E. Lange. Prospects of CsI(Tl)-photodiode detectors for low-level spectroscopy. *Nucl. Instr. Meth. A*, 297:425–440, 1990.

S. E. King, G. W. Phillips, P. S. Haskins, J. E. McKisson, R. B. Piercey, and R. C. Mania. A solid-state Compton camera for three-dimensional imaging. *Nucl. Instr. Meth. A*, 353:320–323, 1994.

R. L. Kinzer, P. A. Milne, J. D. Kurfess, M. S. Strickman, W. N. Johnson, and W. P. Purcell. Positron annihilation radiation from the inner galaxy. *Astrophys. J.*, 559:282–295, 2001.

O. Klein and Y. Nishina. Über die Streuung von Strahlung durch freie Elektronen nach der neuen relativistischen Quantendynamik von Dirac. *ZS. f. Phys.*, 52:853–868, 1929.

G. F. Knoll. *Radiation Detection and Measurement*. Wiley, 1988.

J. Knödlseder. Prospects in space-based gamma-ray astronomy. *Exp. Astron.*, in press, 2006.

J. Knödlseder, P. Jean, V. Lonjou, G. Weidenspointner, N. Guessoum, W. Gillard, G. Skinner, P. von Ballmoos, G. Vedrenne, J.-P. Roques, S. Schanne, B. Teegarden, V. Schönfelder, and C. Winkler. The all-sky distribution of 511 keV electron-positron annihilation emission. *Astron. Astroph.*, 441:513–532, 2005.

H. W. Koch and J. W. Motz. Bremsstrahlung cross-section formulas and related data. *Rev. Mod. Phys.*, 31(4):920–956, 1959.

C. Kouveliotou, C. A. Meegan, G. J. Fishman, N. P. Bhat, M. S. Briggs, T. M. Koshut, W. S. Paciesas, and G. N. Pendleton. Identification of two classes of gamma-ray bursts. *Astrophys. J.*, 413:L101–L104, 1993.

W. Kraushaar, G. W. Clark, G. P. Garmire, H. Helmken, P. Higbie, and A. Agogino. Explorer XI experiment on cosmic gamma rays. *Astroph. J.*, 141(3):845–863, 1965.

W. L. Kraushaar, G. W. Clark, G. P. Garmire, R. Borken, P. Higbie, C. Leong, and T. Thorsos. High-energy cosmic gamma-ray observations from the OSO-3 satellite. *Astroph. J.*, 177:341–363, 1972.

L. A. Kunyansky. A new SPECT reconstruction algorithm based on the Novikov explicit inversion formula. *Inverse Problems*, 17:293–306, 2001.

D. Lazzati, G. Ghirlanda, G. Ghisellini, L. Nava, C. Firmani, B. Morsony, and M. C. Begelman. Long gamma-ray bursts as standard candles. *AIP Conf. Proc.*, CP836, 2006.

J. W. LeBlanc, N. H. Clinthorne, C. Hua, W. L. Rogers, D. K. Wehe, and S. J. Wilderman. A Compton camera for nuclear medicine applications using ^{113m}In. *Nucl. Instr. Meth. A*, 422:735–739, 1999.

P. Lechner, C. Fiorini, R. Hartmann, J. Kemmer, N. Krause, P. Leutenegger, A. Longoni, H. Soltau, D. Stötter, R. Stötter, L. Strüder, and U. Weber. Silicon drift detectors for high count rate X-ray spectroscopy at room temperature. *Nucl. Instr. Meth. A*, 458:281–287, 2001.

P. Lechner, A. Pahlke, and H. Soltau. Novel high-resolution silicon drift detectors. *X-Ray Spectrom.*, 33: 256–261, 2004.

R. P. Lin, B. R. Dennis, G. J. Hurford, D. M. Smith, A. Zehnder, et al. The Reuven Ramaty high-energy solar spectroscopic imager (RHESSI). *Sol. Phys.*, 210:3–32, 2002.

V. Litvinenko et al. Gamma-ray production in a storage ring free-electron laser. *Phys. Rev. Let.*, 78(24): 4569–4572, 1997.

V. Litvinenko and J. Madey. High power inverse Compton γ-ray source at Duke storage ring. *SPIE*, 2521: 55–77, 1995.

V. Litvinenko, S. Park, I. Pinayev, and Y. Wu. Performance of the OK-4/Duke storage ring FEL. *Nucl. Instr. Meth. A*, 470:66–75, 2001.

N. Lund et al. JEM-X: The X-ray monitor on INTEGRAL. *Astro. Lett. and Comm.*, 39:339–345, 1999.

G. Lutz. Silicon radiation detectors. *Nucl. Instr. Meth. A*, 367:21–33, 1995.

G. Lutz. *Semiconductor Radiation Detectors.* Springer, Berlin, 1999.

A. I. MacFadyen and S. E. Woosley. Collapsars: Gamma-ray bursts and explosions in "failed supernovae". *Astrophys. J.*, 524:262–289, 1999.

J. Macri. private communication, 2005.

G. M. Madejski and M. Sikora. High energy observations of blazars: the future. *ASP Conf. Ser.*, 350: 215–224, 2006.

D. Malesani, S. Covino, E. M. Rossi, D. Lazzati, a. De Luca, P. Filliatre, and G. Tagliaferri. Open issues in gamma-ray bursts: polarimetry and dark GRBs. *Il Nuovo Cimento C*, 28:515–520, 2005.

E. G. P. Manfredi. *Processing the Signals from Solid-State Detectors in Elementary Particle Physics*, volume 9. La Rivista del nuovo Cimento, 1986.

J. B. Martin, N. Dogan, J. E. Gormley, G. F. Knoll, M. O'Donnell, and D. K. Wehe. Imaging multi-energy gamma-ray fields with a Compton scatter camera. *IEEE Trans. Nucl. Sci.*, 41:1019–1025, 1994.

S. M. Matz, G. H. Share, M. D. Leising, E. L. Chupp, W. T. Vestrand, W. R. Purcell, M. S. Strickman, and C. Reppin. Gamma-ray line emission from SN1987A. *Nature*, 331:416–418, 1988.

C. A. Meegan, G. J. Fishman, R. B. Wilson, W. S. Paciesas, G. N. Pendleton, J. M. Horack, M. N. Brock, and C. Kouveliotou. Spatial distribution of γ-ray bursts observed by BATSE. *Nature*, 355:143–145, 1992.

P. F. Michelson. GLAST: A detector for high-energy gamma rays. In B. D. Ramsey and T. A. Parnell, editors, *Proc. SPIE Vol. 2806, p. 31-40, Gamma-Ray and Cosmic-Ray Detectors, Techniques, and Missions, Brian D. Ramsey; Thomas A. Parnell; Eds.*, pages 31–40, Oct. 1996.

T. Mizuno, T. Kamae, G. Godfrey, T. Hanada, D. J. Thompson, D. Lauben, Y. Fukazawa, and M. Ozaki. Cosmic-ray background flux model based on a gamma-ray large area space telescope balloon flight engineering model. *Astrophys. J.*, 614:1113–1123, 2004.

D. J. Morris, K. Bennett, H. Bloemen, R. Diehl, W. Hermsen, G. G. Lichti, M. L. McConnell, J. M. . Ryan, and V. Schönfelder. Reassessment of the ^{56}Co emission from SN 1991T. *API Conf. Proc.*, CP410: 1084–1088, 1997.

R. J. Murphy, G. H. Share, J. E. Grove, W. N. Johnson, R. L. Kinzer, J. D. Kurfess, M. S. Strickman, and G. V. Jung. Accelerated particle composition and energetics and ambient abundances from gamma-ray spectroscopy of the 1991 June 4 solar flare. *Astrophys. J.*, 490:883–900, 1997.

P. V. R. Murthy and A. W. Wolfendale. *Gamma-ray astronomy.* Cambridge University Press, 2nd edition, 1993.

T. Niedermayr, K. Vetter, L. Mihailescu, G. J. Schmid, D. Beckendahl, J. Blair, and J. Kammeraad. Gamma-ray imaging with a coaxial HPGe detector. *Nucl. Instr. Meth. A*, 553:501–511, 2005.

NuDat. NuDat 2.2. available at http://www.nndc.bnl.gov/nudat2. web interface for querying nuclear data, data source: National Nuclear Data Center, Brookhaven National Laboratory.

A. Pais. *Inward Bound.* Oxford University Press, 1986.

S.-J. Park. *A very high resolution small animal PET based on the Compton PET concept.* PhD thesis, University of Michigan, 2005.

L. E. Peterson. Radioactivity induced in sodium iodide by trapped protons. *J. Geophys. Res.*, 70(7): 1762–1765, 1965.

L. E. Peterson and R. L. Howard. Gamma-ray astronomy in space in the 50_keV to 3_MeV region. *IRE Trans. Nucl. Sci.*, NS-8:21–29, 1961.

D. Petry. The Earth's gamma-ray albedo as observed by EGRET. *AIP Conf. Proc.*, 745:709–714, 2005. also available from astro-ph/0410487.

M. M. Phillips. Type Ia supernovae as distance indicators. *ASP Conf. Ser.*, 342:211–216, 2005.

C. Piemonte, G.-F. Dalla Betta, M. Boscardin, P. Gregori, N. Zorzi, and L. Ratti. An improved fabrication process for si-detector-compatible jfets. *Nucl. Instr. Meth. A*, 568:314–321, 2006.

C. Pittori. The gamma-ray imaging detector AGILE: Scientific goals and instrument performance. *Chin. J. Astron. Astrophys.*, 3:517–522, 2003.

S. Plüschke. ^{26}Al-*Ursprung und OB Assoziationen*. Doctoral thesis, Fakultät für Physik, Technische Universität München, July 2001. also published as MPE Report 276, 2001.

N. Prantzos. On the intensity and spatial morphology of the 511 keV emission in the Milky Way. *Astron. Astrophys.*, 449:869–878, 2006.

Y. Rasera, R. Teyssier, P. Sizun, M. Cassé, P. Fayet, B. Cordier, and J. Paul. Soft gamma-ray background and light dark matter annihilation. *Phys. Rev. D*, 73:103518 1–10, 2006.

R. C. Reedy, L. G. Evans, J. . Brückner, K. J. Kim, and W. V. Boynton. Gamma Rays in a Spectrum from the Mars Odyssey Gamma-Ray Spectrometer. In S. Mackwell and E. Stansbery, editors, *Lunar and Planetary Institute Conference Abstracts*, page 1592, Mar. 2003.

J. P. Roques et al. SPI/INTEGRAL in-flight performance. *Astron. Astrophys.*, 411:L91–L100, 2003.

M. Ruffert and H.-T. Janka. Colliding neutron stars. *Astron. Astrophys.*, 338:535–555, 1998.

T. Sakamoto et al. Gamma-ray bursts: Huge explosion in the early Universe. *Nature*, 440:164, 2006.

G. C. Schmidt. Ueber die von den Thorverbindungen und einigen anderen Substanzen ausgehende Strahlung. *Ann. d. Phys.*, 301:141–151, 1898.

F. Schopper. *Entwicklung eines Teleskops zur Abbildung von Gammastrahlung mittels Comptonstoß und Paarerzeugung*. Doctoral thesis, Fakultät für Physik, Technische Universität München, Aug. 2002.

V. Schönfelder, editor. *The Universe in Gamma Rays*. Springer, 2001.

V. Schönfelder, H. Bloemen, W. Collmar, R. Diehl, W. Hermsen, J. Knödlseder, G. G. Lichti, S. Plüschke, J. Ryan, A. Strong, and C. Winkler. ^{44}Ti gamma-ray line emission from Cas A and RXJ0852-4622/GROJ0852-4642. *AIP Conf. Proc.*, CP510:54–59, 2000a.

V. Schönfelder et al. Instrument description and performance of the imaging gamma-ray teleskope COMPTEL aboard the Compton Gamma-Ray Observatory. *Astroph. J. Suppl. Series*, 86:657–692, 1993.

V. Schönfelder et al. The first COMPTEL source catalogue. *Astron. Astrophys. Suppl.*, 143:145–179, 2000b.

V. Schönfelder, A. Hirner, and K. Schneider. A telescope for soft gamma ray astronomy. *Nucl. Instr. and Meth.*, 107:385–394, 1973.

K. S. Shah, J. Glodo, M. Kluferman, W. W. Moses, S. E. Derenzo, and M. J. Weber. $LaBr_3$: Ce scintillators for gamma-ray spectroscopy. *IEE Trans. Nucl. Sci.*, 50(6):2410–2413, 2003.

G. K. Skinner. Diffractive/refractive optics for high energy astronomy. *Astron. and Astrophys.*, 375:691–700, 2001.

D. M. Smith. Gamma-ray line observations with RHESSI. In *Proc. 5$^{\text{th}}$ INTEGRAL Science Workshop*, volume SP-552, pages 45–50. ESA, Oct. 2004.

D. M. Smith, L. I. Lopez, R. P. Lin, and C. P. Barrington-Leigh. Terrestrial gamma-ray flashes observed up to 20 MeV. *Science*, 307:1085–1088, 2005.

R. K. Smither. New method for focusing x rays and gamma rays. *Rev. Sci. Instrum.*, 53:131–141, 1982.

SolPhys. *Solar Physics*, volume 210, 2002.

J. A. Sorenson and M. E. Phelps. *Physics in Nuclear Medicine*. Grune & Stratton, 1987.

K. Z. Stanek et al. Spectroscopic discovery of the supernova 2003dh assiciated with GRB 030329. *Astrophys. J.*, 591:L17–L20, 2003.

F. W. Stecker. *Cosmic Gamma Rays*, volume SP-249. NASA, 1971.

A. W. Strong, R. Diehl, H. Halloin, V. Schönfelder, L. Bouchet, P. Mandrou, F. Lebrun, and R. Terrier. Gamma-ray continuum emission from the inner Galactic region as observed with INTEGRAL/SPI. *Astron. Astrophys.*, 444:495–503, 2005.

SUZAKU. The Suzaku Technical Description. available at http://www.astro.isas.ac.jp/suzaku/doc/suzaku_td.pdf, 2005.

F. X. Timmes, S. E. Woosley, D. H. Hartmann, and R. D. Hoffman. The production of ^{44}Ti and ^{60}Co in supernovae. *Astrophys. J.*, 464:332–341, 1996.

R. W. Todd, J. M. Nightingale, and D. B. Everett. A proposed γ camera. *Nature*, 251:132–134, 1974.

O. Toker, S. Masciocchi, E. Nygøard, A. Rudge, and P. Weilhammer. VIKING, a CMOS low noise monolithic 128 channel frontend for Si-strip detector readout. *Nuc. Instr. Meth. A*, 340:572–579, 1994.

P. Ubertini, F. Lebrun, et al. The gamma-ray imager on board INTEGRAL. *Astro. Lett. and Comm.*, 39: 331–338, 1999.

C. M. Urry and P. Padovani. Unified schemes for radio-loud active galactic nuclei. *Pub. Astron. Soc. Pacific*, 107:803–845, 1995.

P. v. Ballmoos, H. Halloin, et al. CLAIRE's first light. *New Astr. Rev.*, 48:243–249, 2004.

G. Vedrenne, V. Schönfelder, et al. The INTEGRAL spectrometer SPI. *Astro. Lett. and Comm.*, 39: 325–329, 1999.

A. von Kienlin, C. A. Meegan, G. G. Lichti, et al. The GLAST burst monitor. In G. Hasinger and M. J. L. Turner, editors, *Proceedings of the SPIE*, volume 5488, pages 763–770, Oct. 2004.

K. Watanabe, D. H. Hartmann, M. D. Leising, and L.-S. The. The diffuse gamma-ray background from supernovae. *Astrophys. J.*, 516:285–296, 1999.

G. Weidenspointner, C. R. Shrader, J. Knödlseder, P. Jean, V. Lonjou, N. Guessoum, R. Diehl, W. Gillard, M. J. Harris, G. K. Skinner, P. von Ballmoos, G. Vedrenne, J.-P. Roques, S. Schanne, P. Sizun, B. J. Teegarden, V. Schönfelder, and C. Winkler. The sky distribution of positronium annihilation continuum emission measured with SPI/INTEGRAL. *Astron. Astroph.*, 450:1013–1021, 2006.

J. I. Weise. Photon splitting in the electromagnetic vacuum. *Phys. Rev. D*, 69:105017 1–16, 2004.

R. Wielebinski. The characteristics of (normal) pulsars. *MPE Report*, 278:167–170, 2002. in Proceedings of the 270. WE-Heraeus Seminar.

S. J. Wilderman, W. L. Rogers, G. F. Knoll, and J. C. Engdahl. Fast algorithm for list mode back-projection of Compton scatter camera data. *IEEE Trans. Nucl. Sci.*, 45:957–962, 1998.

D. Wolter, W. Engel, U. Haubenreisser, S. Ochs, and G. Lichtenauer. MEGA Pre-Phase A Study. available from http://www.mpe.mpg.de/gamma/instruments/mega/www/documents/studies/DJO_FinalReport.pdf, June 2000.

S. Woosley and T. Janka. The physics of core-collapse supernovae. *Nature Physics*, 1:147–154, 2005.

C. B. Wunderer. *Imaging with the Test Setup for the Coded-Mask INTEGRAL Spectrometer SPI.* Doctoral thesis, Fakultät für Physik, Technische Universität München, Dec. 2002. also published as MPE Report 282, 2003.

G. Zavatini, A. Del Guerra, N. Cesca, G. Di Domenico, M. Gambaccini, E. Moretti, and N. Sabba. High Z and medium Z scintillators in ultra-high-resolution small animal PET. *IEEE Trans. Nucl. Sci.*, 52: 222–230, 2005.

A. A. Zdziarski. Contribution of AGNs and SNe Ia to the cosmic X-ray and gamma-ray backgrounds. *Mon. Not. R. Astron. Soc.*, 281:L9–L13, 1996.

A. Zoglauer. Methoden der Bildrekonstruktion für das Comptonteleskop MEGA. Diplomarbeit, Fakultät für Physik, Technische Universität München, July 2000.

A. Zoglauer. *First Light for the Next Generation of Compton and Pair Telescopes.* Doctoral thesis, Fakultät für Physik, Technische Universität München, Dec. 2005. also published as MPE Report 289, 2006.

A. Zoglauer, 2006. private communication.

A. Zoglauer, R. Andritschke, and F. Schopper. MEGAlib — the Medium Energy Gamma-ray Astronomy library. *New Astr. Rev.*, 50:629–632, 2006.

Danksagung — Acknowledgments

Einen so aufwendigen Prototypen, wie den hier beschriebenen, zu bauen und die gelieferten Daten auszuwerten, setzt viel gegenseitige Unterstützung und Zusammenarbeit voraus. Hier möchte ich mich bei all den vielen fleißigen Händen, den Köpfen voller Erfahrungen mit Detektoren, Astrophysik, Elektronik, Datenauswertung, Mechanik und Computern, den guten Organisatoren und allen, die für ein gutes Arbeitsklima am Institut sorgten und sorgen, bedanken.

Einigen Leuten möchte ich hier explizit danken:

- Prof. Volker Schönfelder, der den MEGA Prototypen und damit diese Arbeit ermöglichte und sie auch noch in seinem Ruhestand bis zum Ende begleitet hat.
- Gottfried Kanbach für seinen unerschütterlichen Einsatz für das Projekt, seinen Optimismus, seine guten Ideen und Überredungskunst. Das Fortschreiten und die Qualität (und Quantität) der Arbeit sind mit sein Verdienst.
- Jochen Greiner für seinen Einsatz, eine MEGA-artige Mission zu verwirklichen. Das hat die Motivation für diese Arbeit aufrechterhalten, da das Schicksal eines "Schubladendaseins" nicht schon besiegelt wurde, *bevor* sie fertiggestellt war.
- Meinem Mitstreiter Andreas Zoglauer, ohne ihn wäre ich nicht einmal halb so weit gekommen. Unermüdlich (d.h. 24/7) schuf er mit seinen Programmierkünsten eine Datenaufnahme-, Simulations- und Datenauswertesuite, ohne die eine funktionierende Hardware nichts wert wäre. Nicht nur das, in ihm findet man auch stets einen guten Diskussionspartner, Reisegefährten, Korrekturleser, oder jemanden, bei dem man sich den Frust von der Seele reden kann. Wir waren über viele Jahre hinweg ein Spitzenteam, und das vom allerersten Tag unseres Studiums an!
- Florian Schopper, der mir das Handwerkszeug beigebracht hat, das die Arbeiten im Labor und am Computer voranbringen. In Hardwarefragen konnte man immer am besten mit ihm diskutieren. Mit vielen Ideen, Diskussionen und Korrekturlesen hat er diese Arbeit unterstützt. Und er hat dem Prototypen nochmal "neues Leben" eingehaucht, nämlich als PET-Kamera.
- Fritz Schrey, ohne dessen Hilfe vieles bei weitem nicht so reibungslos verlaufen wäre, hätte er sich nicht darum gekümmert. Dabei war es egal, ob er selbst mit angepackt hat, oder es sich um mechanische, elektronische oder rein organisatorische Dinge handelte, wie die umfangreichen Ballonvorbereitungen, das ganze "Drumherum" um die Beschleunigermessung(en) und so vieles mehr. Zudem sind Kampagnen halb so kurzweilig, wenn er mit dabei ist!
- Peter F. Bloser, der hier am Institut für zwei Jahre war. Teils bis spät in die Nacht hinein hat er mit am Prototypen gewerkelt und war auf allen Kampagnen mit von der Partie. Seit dieser Zeit hängt er an MEGA, an München, den Alpen und am Kletterseil!

- Cornelia Wunderer, unserer Trixi, die sich sehr für uns MEGAs engagiert hat — sei es mit vielen Diskussionen und Ideen, als "Kummerkasten" oder als kritische und zugleich flotte Korrekturleserin. Insbesondere hat sie mir gezeigt, wie schön fern Detektorprobleme sein können beim Erklimmen einer Felswand.
- Allen Mitgliedern der Gammagruppe für das entspannte und kollegiale Klima, für die stets offenen Türen bei Fragen, für die Diskussionen in kleiner und großer Runde — und natürlich für die Kuchen, Eiscrems und Eiskaffees! Und wenn's mit dem Computer mal wieder knifflig wurde, Karsten Kretschmer und Alexander Stefanescu halfen weiter.
- Den zahlreichen Werksstudenten und Praktikanten, die mit viel Fleiß, Gedult und Freude an der Sache mitgeholfen haben.
- Prof. Trümper, daß er seine schützende Hand über MEGA gehalten hat.

Besonderen Anteil am Prototypen haben natürlich die Werkstätten des MPE:

- Die Elektronikwerkstatt vollbringt echte Handwerkskunst, ich denke da vor allem an die faszinierenden "Kunstwerke" von Herrn Rupprecht, den Koinzidenzkartenprototyp (mit dem übrigens die Beschleunigermessung durchgeführt wurde!) und die D1-Biasbox.
- Dem steht die mechanische Werkstatt und Konstruktion in nichts nach, man schaue sich nur die filigranen Detektorgehäuse oder die Ballongondel an.
- Die Kunstwerke von Leo Pichl und Georg Deuschle aus dem Kunststofflabor verstecken sich meist in Gehäusen, so wie die Koppelkissen auf den PIN-Diodenarrays oder das Antikoinzidenzschild für den Ballonflug.

Mein Dank ist nicht auf Garching beschränkt:

- Herrn Schenkl, der mit seinen Repeaterkarten dafür gesorgt hat, daß wir "ruhig" messen konnten. Er hat mir klar gemacht, daß meine Probleme mit der Ausleseelektronik systeminherent sind (und nicht vor dem System stehen).
- Lothar Strüder gab mir die Chance, an vorderster "Detektorfront" mitzuarbeiten, und hat damit auch die finanzielle Dürreperiode beendet. Die notwendige Zeit zum Abschließen der Arbeit bekam ich darüberhinaus dank der Gedult meiner Kollegen am HLL.
- Vladimir Litvinenko and his crew supported us with a nice γ-ray beam going at the limits of the machine — and now everybody knows: "Yes, we see polarization!"
- The HIGS measurement campaign has also been supported by the people from UNH and GSFC with their beam monitor and measurement support.

Zu guter Letzt gilt aber mein größter Dank meinen Eltern. Ohne ihre Unterstützung und Förderung von Anfang an hätte ich es nicht schaffen können. Leider kann mein Vater meinen Abschluß nicht miterleben, er wäre sicher der stolzeste von allen gewesen!